

AD-A137 186

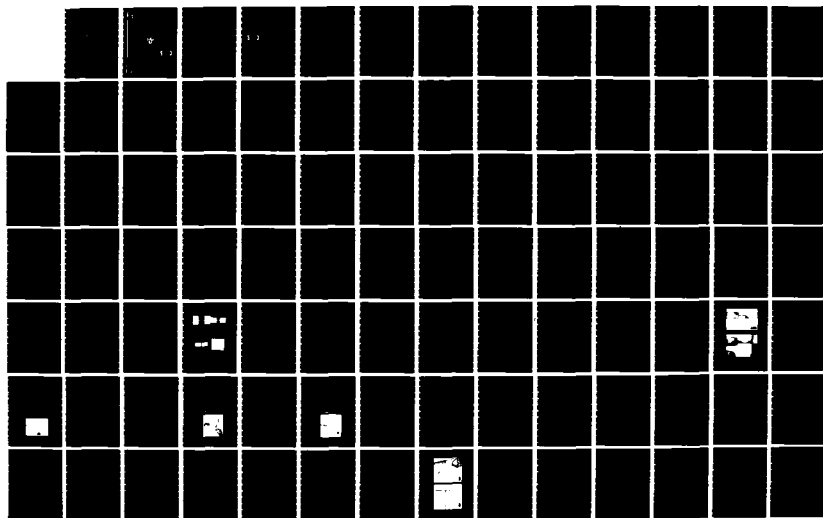
A FAR-INFRARED LASER STUDY OF SMALL-AREA
SUPERCONDUCTING TUNNEL JUNCTIONS(U) HARVARD UNIV
CAMBRIDGE MA DIV OF APPLIED SCIENCES W C DANCHI OCT 83
DAS-TR-22 N00014-83-K-0383

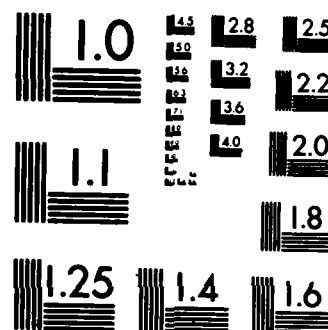
1/3

UNCLASSIFIED

F/G 20/12

NL





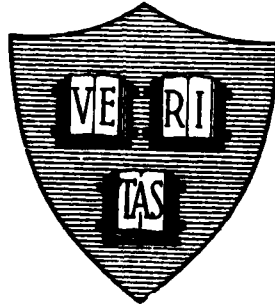
MICROCOPY RESOLUTION TEST CHART
NATIONAL BUREAU OF STANDARDS-1963-A

AD A137186

12

Office of Naval Research
Contract N00014-83-K-0383 NR-319-116
Contract N00014-75-C-0648 NR-372-812

**A FAR-INFRARED LASER STUDY OF SMALL-AREA
SUPERCONDUCTING TUNNEL JUNCTIONS**



By

William C. Danchi

October 1983

Technical Report No. 22

DTIC
ELECTE
S JAN 25 1984 D
A B

This document has been approved for public release
and sale; its distribution is unlimited. Reproduction in
whole or in part is permitted by the U. S. Government.

DTIC FILE COPY

Division of Applied Sciences
Harvard University Cambridge, Massachusetts

84 01 23 017

Unclassified

SECURITY CLASSIFICATION OF THIS PAGE (When Data Entered)

REPORT DOCUMENTATION PAGE		READ INSTRUCTIONS BEFORE COMPLETING FORM
1. REPORT NUMBER Technical Report No. 22	2. GOVT ACCESSION NO. AD-A137 186	3. RECIPIENT'S CATALOG NUMBER
4. TITLE (and Subtitle) A FAR-INFRARED LASER STUDY OF SMALL-AREA SUPER-CONDUCTING TUNNEL JUNCTIONS		5. TYPE OF REPORT & PERIOD COVERED Interim Report
		6. PERFORMING ORG. REPORT NUMBER
7. AUTHOR(s) William C. Danchi		8. CONTRACT OR GRANT NUMBER(s) N00014-83-K-0383 N00014-75-C-0648
9. PERFORMING ORGANIZATION NAME AND ADDRESS		10. PROGRAM ELEMENT, PROJECT, TASK AREA & WORK UNIT NUMBERS
11. CONTROLLING OFFICE NAME AND ADDRESS Division of Applied Sciences Harvard University Cambridge, MA 02138		12. REPORT DATE October 1983
14. MONITORING AGENCY NAME & ADDRESS (if different from Controlling Office)		13. NUMBER OF PAGES 221
		15. SECURITY CLASS. (of this report) Unclassified
		15a. DECLASSIFICATION/DOWNGRADING SCHEDULE
16. DISTRIBUTION STATEMENT (of this Report) Reproduction in whole or in part is permitted for any purpose of the United States Government. Approved for public release; distribution unlimited.		
17. DISTRIBUTION STATEMENT (of the abstract entered in Block 20, if different from Report)		
18. SUPPLEMENTARY NOTES → This document		
19. KEY WORDS (Continue on reverse side if necessary and identify by block number) Far-infrared laser study Superconducting tunnel junctions Josephson effect quasiparticle tunneling		
20. ABSTRACT (Continue on reverse side if necessary and identify by block number) We report the first observations of photon-assisted quasiparticle tunneling and AC Josephson effect in superconducting tunnel junctions irradiated with far-infrared (FIR) radiation. Radiation at 246 GHz ($\lambda = 1.22$ mm) and 604 GHz (496 μ m) from an optically-pumped FIR laser source was used. Tin-tin oxide-lead junctions of ~ 1 (μ m) ² area were fabricated on crystal quartz substrates with integral planar dipole antennas of resonant length at the frequency of the incident radiation. The observed photon-assisted tunneling features are in excellent agreement with the Tien-Gordon theory, and the inferred responsivity approaches		

DD FORM 1 JAN 73 1473

EDITION OF 1 NOV 65 IS OBSOLETE
S/N 0102-014-6601

Unclassified

SECURITY CLASSIFICATION OF THIS PAGE (When Data Entered)

the quantum limit at low temperatures for photon energies less than the gap. At 604 GHz, with a 176 ohm junction, we have seen 7 Josephson steps, comparable to point contact performance. The variation of the step widths with laser power is found to agree quite well with both the RSJ model and the Werthamer theory. For low resistance junctions (e.g., 16 ohms), we find the Josephson steps to be flat and to agree well with the shape predicted by the RSJ model without noise rounding, while noise rounding is very evident with the higher resistance junctions.

The step shape is in reasonable agreement with the theory of P.A. Lee, using a noise temperature of 20-25 K, attributed to shot noise at finite voltage, with an appropriate small junction capacitance. A computer simulation has been developed which models the effects of the voltage-dependent (shot) noise and the nonlinear quasiparticle resistance of the junctions, assuming $T=2K$. Reasonably good agreement is obtained between the simulated I-V curves for un-irradiated but noise affected junctions, reproducing the observed fall-off in the I_{Cn} product with increasing junction resistance. For irradiated junctions, we also obtain good agreement with the observed noise rounding of the ac Josephson steps. Finally, we have coupled FIR radiation into a 7 Ω niobium-silicon-niobium junction and have observed three Josephson steps and one photon-assisted tunneling step.

DTIC
ELECTE
S JAN 25 1984 D
B

Accession For	
NTIS GRA&I	<input checked="" type="checkbox"/>
DTIC TAB	<input type="checkbox"/>
Unannounced	<input type="checkbox"/>
Justification	
By	
Distribution/	
Availability Codes	
Dist	Avail and/or Special
A-1	



Unclassified

Office of Naval Research

Contract N00014-83-K-0383 NR-319-116

Contract N00014-75-C-0648 NR-372-012

A FAR-INFRARED LASER STUDY
OF SMALL-AREA SUPERCONDUCTING TUNNEL JUNCTIONS

By

William C. Danchi

Technical Report No. 22

Reproduction in whole or in part is permitted for any purpose of the United States Government. Approved for public release; distribution unlimited.

October 1983

The research reported in this document was made possible through support extended the Division of Applied Sciences, Harvard University, by the Office of Naval Research, under Contract N00014-83-K-0383 and Contract N00014-75-C-0648.

Division of Applied Sciences
Harvard University • Cambridge, Massachusetts

ABSTRACT

We report the first observations of photon-assisted quasiparticle tunneling and AC Josephson effect in superconducting tunnel junctions irradiated with far-infrared (FIR) radiation. Radiation at 246 GHz ($\lambda=1.22$ mm) and 604 GHz (496 μm) from an optically-pumped FIR laser source was used. Tin-tin oxide-lead junctions of ~ 1 (μm)² area were fabricated on crystal quartz substrates with integral planar dipole antennas of resonant length at the frequency of the incident radiation. The observed photon-assisted tunneling features are in excellent agreement with the Tien-Gordon theory, and the inferred responsivity approaches the quantum limit at low temperatures for photon energies less than the gap. At 604 GHz, with a 176 ohm junction, we have seen 7 Josephson steps, comparable to point contact performance. The variation of the step widths with laser power is found to agree quite well with both the RSJ model and the Werthamer theory. For low resistance junctions (e.g. 16 ohms), we find the Josephson steps to be flat and to agree well with the shape predicted by the RSJ model without noise rounding, while noise rounding is very evident with the higher resistance junctions.

The step shape is in reasonable agreement with the theory of P. A. Lee, using a noise temperature of 20-25 K, attributed to shot noise at finite voltage, with an appropriate small junction capacitance. A computer simulation has been developed which models the effects of the voltage-dependent (shot) noise and the non-linear quasiparticle resistance of the junctions, assuming $T=2\text{K}$. Reasonably good agreement is

obtained between the simulated I-V curves for un-irradiated but noise affected junctions, reproducing the observed fall-off in the $I_c R_n$ product with increasing junction resistance. For irradiated junctions, we also obtain good agreement with the observed noise rounding of the ac Josephson steps. Finally we have coupled FIR radiation into a 7Ω niobium-silicon-niobium junction and have observed three Josephson steps and one photon-assisted tunneling step.

TABLE OF CONTENTS

	page
ABSTRACT	i
TABLE OF CONTENTS	iii
LIST OF FIGURES	vi
LIST OF TABLES	xii
CHAPTER I: INTRODUCTION	1
CHAPTER II: THEORETICAL OVERVIEW	8
2.1 Introduction	8
2.2 Tunneling Hamiltonian/Werthamer Theory	8
2.3 The RSJ Model	22
2.4 Noise Effects	26
2.5 Discussion	36
CHAPTER III: EXPERIMENTAL TECHNIQUES	39
3.1 Introduction	39
3.2 Sample Fabrication	40
3.2.1 Mask Fabrication--Commercial Masks	40
3.2.2 Mask Fabrication at Harvard	43
3.2.3 Photoresist Stencils	46
3.2.4 Junction Evaporation/Oxidation Sequence	49
3.3 Antenna Coupling to FIR Laser Source	60
3.3.1 Introduction	60
3.3.2 Dipole Antennas on Thin Substrates	61

3.3.3	Power Patterns of Current Elements and Dipoles	62
3.3.4	Design Decisions	71
3.4	Far-Infrared Laser Source	77
3.4.1	Introduction	77
3.4.2	Qualitative Theory	77
3.4.3	Operation and Performance	81
CHAPTER IV: DATA ANALYSIS		89
4.1	Introduction	89
4.2	DC Characteristics	90
4.3	AC Josephson Effect Analysis	102
4.4	Photon-Assisted Tunneling Analysis	115
4.5	Noise Effects	125
4.5.1	The Lee Analytic Approximation	127
4.5.2	Computer Simulation	130
4.5.3	Discussion	147
CHAPTER V: SUMMARY AND CONCLUSIONS		149
APPENDIX A: DETAILED SAMPLE FABRICATION PROCEDURES		156
A.1	Introduction	156
A.2	Photolithographic Procedures	156
A.3	Evaporation Procedures	165
A.4	Substrate Cleaning Procedures	170
A.5	Etches	172
APPENDIX B: OTHER DATA AND ANALYSIS		174
B.1	Introduction	174
B.2	Low Resistance Junctions Fabricated at Bell Labs	174
B.3	Point Contact Edge-Aligned Junctions	182

B.4 SNAP Junctions	191
REFERENCES	199
ACKNOWLEDGEMENTS	206

LIST OF FIGURES

	page
FIG. 1.1 (a) Schematic illustration of the dc electrical measurement of an SIS tunnel junction. (b) DC current-voltage (I-V) curve of a 16Ω Sn-SnO-Pb tunnel junction taken at $T=1.4$ K.	3
FIG. 1.2 (a) Effect of 32 GHz microwave radiation on superconducting weak link, illustrating the flat current steps from the ac Josephson effect. (b) Effect of 38 GHz microwave radiation on an Al-oxide-Pb junction, illustrating the photon-assisted tunneling current steps.	6
FIG. 2.1 Real and imaginary parts of the response functions $j_1(\omega)$ and $j_2(\omega)$, at $T=0$.	14
FIG. 2.2 (a) Critical current $I_c(T)$, normalized to $I_c(0)$, vs. the reduced temperature T/T_c for a Sn-Sn tunnel junction. (b) Critical current, $I_c(T)$, normalized to $I_c(0)$, vs. the reduced temperature T/T_c for a Sn-Pb tunnel junction.	19
FIG. 2.3 Schematic illustration of the current biased RSJ model.	24
FIG. 2.4 Mechanical analogy of the RSJ model with a particle moving in a tilted periodic potential.	31
FIG. 2.5 Effect of noise on the RSJ model I-V curve for $\beta_c \rightarrow 0$.	33
FIG. 3.1 (a) Section of the commercial mask containing a tunnel junction pattern and a pad pattern. (b) A close-up of the central region of (a) showing the tunnel junction pattern. (c) Another section of the mask, this time with a tunnel junction pattern with long leads. (d) Section of mask containing a long microbridge pattern.	42
FIG. 3.2 Illustration of the sequence of steps used to make a mask.	44
FIG. 3.3 Photoresist exposure/development procedure beginning with the photoresist/ Al/photoresist trilayer and ending with the suspended photoresist bridge which is used to make the junction.	48

	page
FIG. 3.4 (a) SEM micrograph of a photoresist bridge suspended over a polished sapphire substrate, made with the mask in Figure 3.1(c), following the procedure of Fig. 3.3. (b) SEM micrograph of a suspended photoresist bridge used in fabricating a small-area junction at the center of a dipole antenna.	50
FIG. 3.5 (a) Evaporation/oxidation steps for Sn-SnO-Pb overlap junctions. (b) SEM micrograph of a junction made with this procedure.	52
FIG. 3.6 (a) Evaporation/oxidation procedure for resist-aligned junctions. (b) SEM micrograph of a sample made with this procedure.	55
FIG. 3.7 (a) Evaporation/oxidation procedure for edge-aligned junctions. (b) SEM micrograph of junction made with this procedure.	57
FIG. 3.8 (a) Reduction factor, α , as a function of the effective thickness, t_{eff} , for different values of ϵ_r . (b) Values of α for $t_{eff} > 0.15$ for the values of ϵ_r in (a). (c) E-plane and H-plane antenna patterns for a dipole antenna on a thin substrate.	63
FIG. 3.9 (a) Current element at an air-dielectric interface. (b) E-plane and H-plane power patterns from this current element.	66
FIG. 3.10 (a) H-plane power pattern of a resonant dipole antenna at an air-dielectric interface for different values of ϵ_r . (b) E-plane power pattern of the resonant dipole of (a) for the same values of ϵ_r .	70
FIG. 3.11 Detail of transverse optical access dewar. FIR laser radiation is focussed by the TPX lens onto the cone, through the back side of the substrate, onto the junction-antenna structure.	72
FIG. 3.12 (a) SEM micrograph of a typical sample with a dipole antenna of $\sim 183 \mu\text{m}$ length and $\sim 5 \mu\text{m}$ line width. At the center of the dipole is the tunnel junction. (b) Close-up of the junction region in (a).	73
FIG. 3.13 Methyl fluoride energy-level diagram. The CO_2 pump line coincides with the $v=0-1$, $J=11$, $K=2$ transition. The $496 \mu\text{m}$ FIR lasing transition is the $v=1$, $K=2$, $J=12-11$ transition.	78
FIG. 3.14 Optically-pumped FIR laser set-up.	82

	page
FIG. 3.15 A 24 minute recording of the free-running FIR laser output power.	87
FIG. 4.1 Typical I-V curves of a low resistance ($\sim 2 \Omega$), larger area ($\sim 4.5 \times 10^{-8} \text{ cm}^2$), tunnel junction for decreasing temperatures.	91
FIG. 4.2 The square of $2\Delta_{Sn}$, measured from data such as that presented in Fig. 4.1, versus the temperature T.	96
FIG. 4.3 (a) The critical current at a temperature T, normalized to the critical current at 1.4 K, $I_C(T)/I_C(0)$, versus the reduced temperature, $t=T/T_C$. (b) The critical current at a temperature T, normalized to the estimated zero temperature critical current, $I_C(0)=1.2 \pm 0.1 \text{ mV}$, $\{I_C(T)/I_C(0)\}_{\text{est}}$ versus $t=T/T_C$.	98
FIG. 4.4 Critical current, I_C , vs. the normal resistance, R_n , for the junctions studied in this work. Data shown by solid circles falls below the dashed line, $I_C R_n = 1.2 \text{ mV}$ for $R_n > 10 \Omega$. The computer simulation solid line and open circles, closely follows the data. Error bars indicate bounds of simulated I_C for a given I_n .	101
FIG. 4.5 (a) Typical I-V curves of a low-resistance sample for increasing laser power. Here, $V_g = (\Delta_{pb} + \Delta_{Sn})/e$. (b) Typical I-V curves of a high-resistance junction for increasing laser powers.	103
FIG. 4.6 Effect of the polarization of the FIR laser output relative to the antenna axis. Parallel polarization, //, couples well, whereas perpendicular polarization, \perp , does not, as expected.	105
FIG. 4.7 Normalized step width as a function of the laser voltage in the junction compared with the Bessel function $ J_n $ dependence and the Werthamer theory $ W_n $, for a composite of data from two low resistance junctions.	109
FIG. 4.8 Normalized step width as a function of the laser voltage in the junction, compared with the Bessel function $ J $ dependence and the Werthamer theory, $ W $. The data is from a high-resistance (176Ω) junction irradiated by 604 GHz laser radiation.	111
FIG. 4.9 Normalized step width as a function of laser voltage in the junction, compared with the Bessel function dependence, $ J $, and the Werthamer theory, $ W $. The data shown is from a 156Ω junction irradiated by 246 GHz laser radiation.	113

	page
FIG. 4.10 I-V curves of two different junctions, each with suitable antenna length, irradiated at 604 and 246 GHz at 1.4 K. The dashed curves are obtained from the Tien-Gordon theory. This accounts for the photon-assisted tunneling steps at $\pm V_G \pm k\hbar\omega_L/e$ where k is an integer and $V_G = (\Delta_{pb} + \Delta_{sn})/e$, leaving only local voltage displacements near the Josephson steps labeled by $n=0,1,2,\dots$	117
FIG. 4.11 (a) Superposed dc I-V curves for different values of the normalized FIR laser-induced voltage $\alpha = eV_L/\hbar\omega_L$ for a 176 Ω junction at 4.2 K and a laser frequency of 604 GHz. (b) Comparison between the voltage dependence of dV/dI computed theoretically for various FIR power levels and that obtained by digital differentiation of the experimental I-V curves in (a).	118
FIG. 4.12 Change in the dc current with laser power ($\sim \alpha^2$) at selected dc bias voltages. Points are experimental data; curves are computed theoretically from the zero-power I-V curve.	120
FIG. 4.13 Plot of current responsivity normalized to the quantum limit ($e/\hbar\omega$) vs. dc bias voltage. Inset shows computed frequency dependence of $R/(e/\hbar\omega)$ at $T=0, 1.4$ and 4.2 K, for a bias of $V=V_G$, and experimental points at 246 and 604 GHz at 4.2 K.	122
FIG. 4.14 Fit to the shape of the 2nd Josephson step on a 16 Ω junction illuminated with 604 GHz laser radiation.	126
FIG. 4.15 Fits to the shape of the 4th Josephson step on a 176 Ω sample at 604 GHz for different values of the fitting parameters I_4^0 , T_{eff} , and C .	129
FIG. 4.16 (a) Simulated I-V curve with noise but no ac currents. Switching at critical current shown by dashed lines. Critical currents from simulation (for 5 runs) fall within bounds indicated by dotted lines. (b) I-V curve from the 176 Ω junction (data).	136
FIG. 4.17 Zeroth and first step simulated behavior for a junction with rf and dc bias but no noise.	138
FIG. 4.18 Simulated step at $2\alpha=4.0$ Arrow labeled by I_C^0 is the unfluctuated critical current estimated from the nominal $I_C R_n$ product. The critical current with noise is also shown, as well as the estimated errors on the simulated critical current, i.e., the error bars drawn.	140

	page
FIG. 4.19 (a) I-V curve of a 176Ω junction at $\alpha=2.0$; Josephson steps are labelled by the integers $n=2$, $n=3$, and $n=4$. (b) Simulation of the data shown in (a), which includes noise and photon-assisted tunneling steps. (c) Simulation, dashed lines in (b), compared with data from (a) illustrating the excellent quality of the fit.	143
FIG. 4.20 Fourth Josephson step fits at two laser power levels, $2\alpha=4.0$ and $2\alpha=5.75$. On the left are the simulated step shapes, measured from the step center, solid circles, compared with the data, solid line. On the right is the same data, but the simulation now includes the photon-assisted tunneling effect.	145
FIG. 5.1 Input impedance of a bow-tie antenna as a function of bow angle for an antenna on a fused quartz substrate. Solid lines are calculated values, crosses are values measured from a 10 GHz microwave modelling experiment.	153
FIG. A.1 Illustration of cross-section of plexiglass contact printing sample holder.	163
FIG. B.1 A typical high current-density sample showing depressed gap structure from quasiparticle injection at 6 temperatures. At 1.4 K a scaled I-V curve from a high-resistance junction is drawn in dashed lines for comparison. The three upper curves are drawn with a scale twice as sensitive as the lower three curves.	177
FIG. B.2 An I-V curve for a Sn-SnO-Sn junction (Ref. 116) showing the same sort of gap depression phenomena observed in this work on Sn-SnO-Pb junctions.	178
FIG. B.3 Voltage difference, V_g , between the dashed curve and solid curve in Fig. B.1 at $T=1.4$ K versus the current in the junction.	180
FIG. B.4 Voltage difference, V_g , between gap structure of low resistance and high resistance junctions, computed in the same way as Fig. B.3, for the Sn-SnO-Sn junctions of Ref. 116 as a function of JG , which is proportional to the current through the junction.	181
FIG. B.5 I-V curves of a 0.55Ω edge-aligned point contact type sample at $2\alpha=0$, and $2\alpha=0.8$, the maximum power coupled to the junction, where $2\alpha \equiv 2eV_L/\hbar\omega_L$. The curve at $2\alpha=0.8$ clearly shows a step at 1.25 mV, labelled $n=1$.	185

- FIG. B.6 I-V curves at several laser powers for a 14Ω point contact edge-aligned sample showing gap structure at $(\Delta_{pb} + \Delta_{Sn})/e$ at $2\alpha=0$, and up to five Josephson steps at $2\alpha=6.7$. Note the presence of the half-harmonic step, labelled $n=\frac{1}{2}$, not previously seen in point contact data in the FIR. 187
- FIG. B.7 Step-widths as a function of normalized laser induced voltage in the junction, 2α , for the steps shown in Fig. B.6. Solid lines are scaled Werthamer functions, $|W|$, and the dashed lines are scaled Bessel functions, $|J|$. 188
- FIG. B-8 Maximum value of the normalized laser induced voltage in the junction, $2\alpha=2eV_L/\hbar\omega_L$, versus the normal resistance, R_n . 190
- FIG. B.9 SEM micrographs of a SNAP junction. (a) Low magnification view of sample, displaying dc leads--vertical parallel lines in the Figure--and pads to which gold wires are bonded. (b) Close-up of antenna region of (a), showing $10 \mu\text{m}$ linewidth antenna, $\sim 180 \mu\text{m}$ long. The junction is at the center of the antenna, dc leads are to the left of the center. (c) Close-up of junction region at the center of (b) taken with SEM stage tilted. The junction is the smallest area at the center of the two larger squares. (d) Close-up of junction region but without a tilt on the SEM stage, the junction is the $\sim 1 \mu\text{m}$ by $\sim 1 \mu\text{m}$ region at the center of the Figure. 193
- FIG. B.10 I-V curves of the SNAP junction in Fig. B.9, irradiated with 604 GHz ($\lambda=496 \mu\text{m}$) laser radiation, at normalized laser induced voltages, $2\alpha=0$, and the highest voltage coupled, $2\alpha=1.7$. We see three Josephson steps at $V_n=n(\hbar\omega_L/2e)$ where n is an integer, and a single photon-assisted tunneling step at $V_g+(\hbar\omega_L/e)$ where $V_g=2\Delta_{Nb}$, as labelled in the Figure. 195
- FIG. B.11 Step half-widths as a function of normalized laser induced voltage, 2α , for the Josephson steps of Fig. B.10, at two temperatures $T=4.2 \text{ K}$ (crosses), and $T=1.4 \text{ K}$ (solid circles). Solid line denotes Werthamer function fits, $|W|$, and dashed lines denote Bessel function fits, $|J|$. 197

LIST OF TABLES

	page
Table 3.1 FIR Laser Lines and Mesh Constants	84
Table 4.1 Parameters of Low Resistance Junctions	92
Table 4.2 Parameters of High Resistance Junctions Measured in the Far-Infrared	99
Table B.1 Parameters of Point-Contact Type Junctions	184

CHAPTER 1

INTRODUCTION

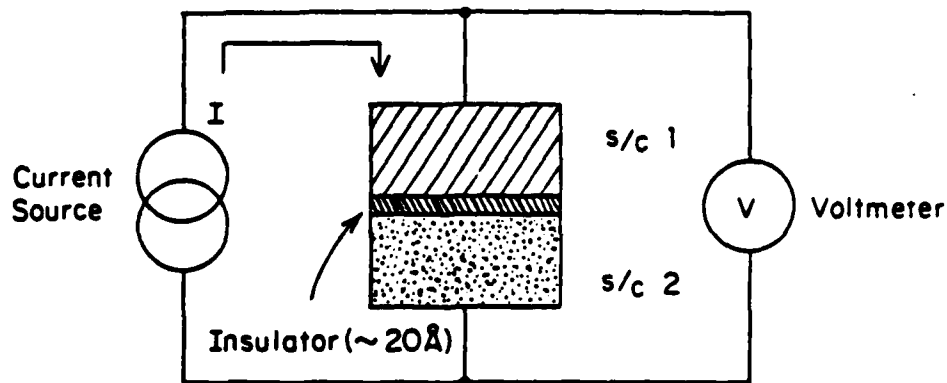
In the 26 years since the development of the microscopic theory of superconductivity by Bardeen, Cooper, and Schrieffer¹, research in superconductivity has followed two divergent paths. One path has brought the development of high transition temperature (T_c), high critical magnetic field (H_{c2}) superconducting materials for use in large scale applications such as beam magnets for high energy proton and electron accelerators, or magnetic confinement "mirrors" for fusion applications². These developments depended critically on the discovery of A15 compounds by Hulm, Matthias, and Kunzler³. The second path of research in superconductivity relied on two discoveries related to the problem of electrons tunneling between two superconductors separated by a thin layer of insulator. The first discovery was of quasiparticle or single electron tunneling between superconductors by Giaever⁴, the second was the discovery of the tunneling of Cooper pairs of electrons by Josephson⁵. The work reported here contributes to this second path by making a systematic study of electron tunneling between superconductors irradiated in the far-infrared (FIR) region of the spectrum.

We will start by giving a qualitative description of the dc electrical behavior of a superconductor-insulator-superconductor (SIS) tunnel junction. The current-voltage (I-V) characteristics of the SIS tunnel junction have two distinct branches. Fig. 1.1(a) shows schematically such a tunnel junction while Fig. 1.1(b) shows its I-V

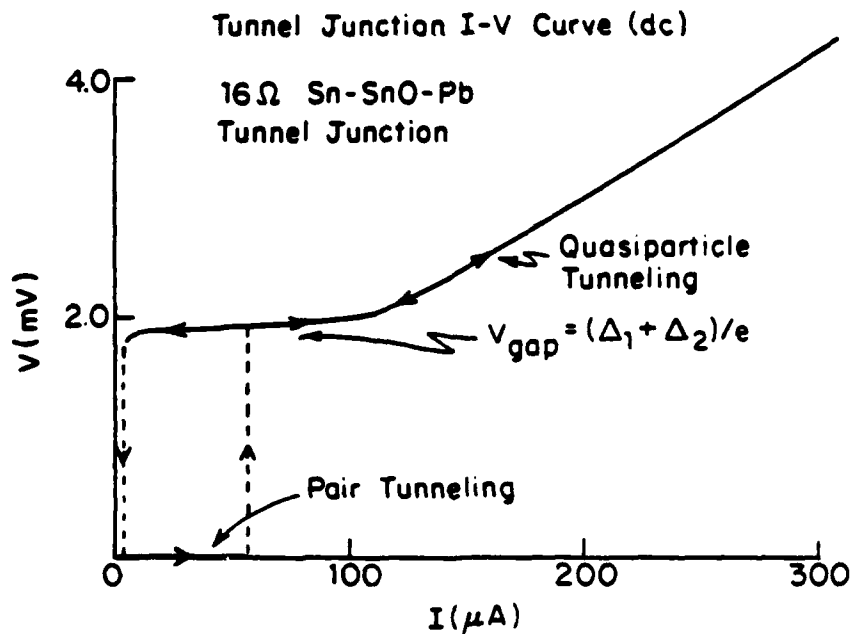
curve. In the current-biased dc behavior, as we increase the bias current, we find a portion of the I-V curve in which there is zero voltage for finite currents. This is the case until the current exceeds a characteristic current called the critical current, I_c , at which point the junction switches to the finite voltage state. At high currents the junction I-V curve becomes approximately linear. As the current is reduced towards zero the junction voltage stays approximately constant at a characteristic voltage called the gap voltage or $V_{\text{gap}} = (\Delta_1 + \Delta_2)/e$. This effect comes from the high differential conductance resulting from the divergence in the density of states of the quasiparticle excitations at the superconducting energy gap. Finally as the current approaches zero, the junction voltage suddenly becomes zero. Usually a large hysteresis loop, beginning where the junction initially goes to the finite-voltage state to where it drops back into the zero-voltage state, is found. It is the ability of the junction to switch rapidly between two states which makes SIS devices attractive for high-speed computing applications⁶.

Other interesting effects occur when an SIS tunnel junction is illuminated by high frequency electromagnetic radiation. One effect depends on the Cooper pairs and is called the ac Josephson effect in which constant voltage "steps" appear on the I-V curve at multiples of a characteristic voltage, $\hbar\omega_L/2e$, shown in Fig. 1.2(a). These steps are due to the mixing of the ac supercurrent with the applied high frequency electromagnetic field in the junction. A second effect comes from the interaction of the quasiparticles with the external field, and is called

dc Electrical Measurement of a Tunnel Junction



(a)



(b)

FIG. 1.1 (a) Schematic illustration of the dc electrical measurement of an SIS tunnel junction. (b) DC current-voltage (I-V) curve of a 16 Ω Sn-SnO-Pb tunnel junction taken at $T=1.4$ K.

the photon-assisted tunneling effect. Due to this effect, "steps" appear on the I-V curve at characteristic voltages $\pm V_{\text{gap}} + n(\hbar\omega_L/e)$ where n is a positive or negative integer. This effect is shown schematically in Fig. 1.2(b). The photon-assisted tunneling (PAT) effect was discovered in 1962 by Dayem and Martin⁷ and explained in 1963 by Tien and Gordon⁸.

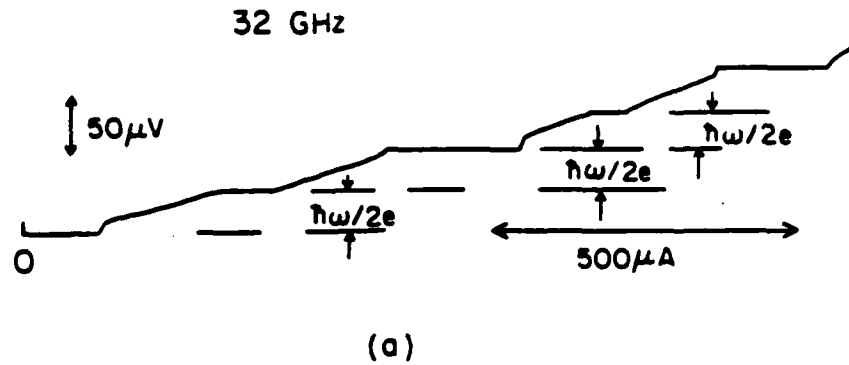
The complete frequency-dependent theory of the SIS tunnel junction, including the PAT effect and the ac Josephson effect was developed by Werthamer⁹ in 1966. Because the tunnel junction is so sensitive to external electromagnetic fields due to the above-mentioned effects, tunnel junctions and other superconducting devices have been proposed for use as sensitive detectors of millimeter and submillimeter wavelength radiation¹⁰.

In this report we will be concerned with the quantitative measurement of the Josephson effect and the photon-assisted tunneling effect in the sub-millimeter wavelength region of the spectrum, particularly near and above the superconducting energy gap. The measurements described herein are the first reported measurements in the far-infrared (FIR) on these effects on fabricated thin-film tunnel junctions¹¹. Prior to this work the only data available on superconducting devices¹² in the FIR were on point-contact devices which are mechanically unstable and known to have a large variety of I-V curves¹³.

Using small-area superconducting tunnel junctions we have observed the ac Josephson effect and the photon-assisted tunneling effect at frequencies up to 604 GHz, the highest frequency reported to date. We have seen a maximum of seven ac Josephson steps¹², up to 8.75 mV, a result comparable to that of point contacts. We have made a systematic study of the ac Josephson effect and the PAT effect and found good agreement between our data and the predictions based on fundamental theory. On high resistance junctions, $R > 100 \, \Omega$, we have observed rounded Josephson steps. We have shown that the rounding is due to shot noise¹⁴, in contrast to the results on point contacts which were consistent with thermal noise from joule heating of the point contact at high dc bias voltages¹².

This report is organized into five chapters and two appendixes, beginning with this brief introductory Chapter. Chapter II begins with a detailed theoretical review, describing the fundamental frequency-dependent theory of the ac Josephson effect, the photon-assisted tunneling effect, and the fundamental theory of noise effects in these devices. After this theoretical discussion, we briefly describe the important experimental results obtained prior to this work. In Chapter III we describe the experimental techniques which were used to make our measurements, including the fabrication of the samples which were made at Harvard, the means of coupling FIR radiation to the small-area tunnel junctions, and the FIR laser system used to irradiate the junctions. Chapter IV is a detailed analysis of these measurements, the Josephson effect results, the photon-assisted tunneling effect

ac Josephson Effect



Photon-Assisted Tunneling Effect

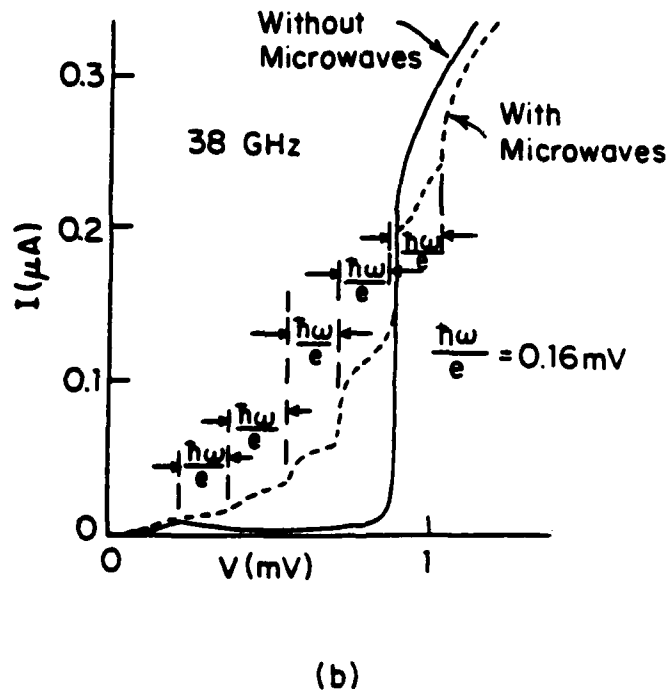


FIG. 1 2 (a) Effect of 32 GHz microwave radiation on superconducting weak link, illustrating the flat current steps from the ac Josephson effect. (b) Effect of 38 GHz microwave radiation on an Al-oxide-Pb junction, illustrating the photon-assisted tunneling current steps. [After Ref. 3.]

results, and noise effects. The main body of the report ends with Chapter V, which discusses the results of the FIR measurements as a whole, proposes a set of experiments to do in the future, and briefly discusses the implications of this work for FIR mixers and direct detectors.

The two appendixes are organized as follows. In Appendix A we give complete details of the fabrication process including the photolithography, substrate cleaning procedures, and chemical etches for the various metals used. Appendix B begins by describing measurements on high-current density junctions made at Bell Labs which showed unusually large amounts of gap suppression due to heavy quasiparticle injection. Following this, data on point-contact type junctions and preliminary results from Nb-Si-Nb junctions made at Sperry Research Labs, are presented.

CHAPTER II

THEORETICAL OVERVIEW

2.1 Introduction

This Chapter is concerned with the quantitative, fundamental theory of the phenomena described previously in Chapter I, that is, why a SIS tunnel junction has a non-linear I-V curve with two distinct branches, and why the I-V curve develops ac Josephson steps and photon-assisted tunneling steps when the junction is irradiated by high-frequency radiation.

We will sketch the main features of the theory of the tunnel junction, relevant to this experiment, beginning in Section 2.2. In Section 2.2 the tunneling Hamiltonian formalism will be described as well as its specific predictions for the dc and ac voltage biased tunnel junction cases. The RSJ model, a commonly used low-frequency version of the theory, is presented in Section 2.3, while the effects of noise on the dc and high-frequency behavior of the junction are outlined in Section 2.4. The Chapter ends with a brief discussion of the experimental results obtained by others prior to this work.

2.2 Tunneling Hamiltonian/Werthamer Theory

The original calculation of the frequency dependence of the tunneling current in a superconducting tunnel junction is due to Werthamer.⁹ Werthamer's calculation in turn is based on the tunneling Hamiltonian method used originally by Bardeen,¹⁵ and by Cohen, Falicov, and Phillips,¹⁶ and the calculations of Ambegaokar and Baratoff,¹⁷ and

of Josephson.⁵

The Hamiltonian for a tunnel junction is given by

$$H = H_L + H_R + H_T \quad (2.1)$$

where H_L and H_R are the complete Hamiltonians of the left and right superconductors, and H_T is the term which couples the left and right superconductors.

The tunneling term, H_T , is given by

$$H_T = \sum_{k,q\sigma} \left[T_{k,q} c_{k\sigma}^\dagger d_{q\sigma} + (T_{k,q})^* d_{q\sigma}^\dagger c_{k\sigma} \right] \quad (2.2)$$

where $c_{k\sigma}$, and $d_{k\sigma}$ are the destruction operators for the electrons in the left and right superconductors, respectively, and σ is a spin index for the electrons. The number operators for the left and right metals are

$$N_L = \sum_{k\sigma} c_{k\sigma}^\dagger c_{k\sigma} \quad (2.3)$$

$$N_R = \sum_{q\sigma} d_{q\sigma}^\dagger d_{q\sigma}$$

The tunneling Hamiltonian formalism has several important assumptions built into it.¹⁸ First, the spins of the electrons are unchanged as they are transferred across the barrier. Second, the tunneling of the electrons occurs instantaneously. Another important assumption is that the distribution functions describing the thermal distribution of the quasiparticles are equilibrium distribution functions. Third, the voltage drop is pictured as occurring entirely

within the barrier. And finally, the matrix elements, $T_{k,q}$, and $T_{-k,-q}^*$, are equal by time reversal symmetry.

If a time dependent voltage $V(t)$, which can have a dc term in it, is applied to the left electrode, such that it is positive relative to the right one, the Fermi levels for the left and right electrodes are related by $\mu_L - \mu_R = -eV$. Here $e = |e|$, the absolute value of the electric charge. The Hamiltonian of the left electrode is $H_L(V) = H_L(0) - eVN_L$, where N_L is the number operator for the left side, given by Eq. (2.3a), i.e., the voltage, $V(t)$, only modulates the energy of each electron on the left electrode.

The calculation for the current through the junction, outlined below, assumes an interaction representation in which the time dependence of the operators is derived from the unperturbed Hamiltonian, $H_0 = H_L(V) + H_R$, whereas the time evolution of the eigenstates comes from the perturbation term, H_T , the tunneling Hamiltonian. Therefore if, $\hat{c}_{k\sigma}(t)$ is the destruction operator for an electron on the left side of the barrier with the voltage applied, then its time dependence can be calculated from the Heisenberg equations of motion; it depends only on the Hamiltonian for the left electrode, $H_L(V)$, and is.

$$i\hbar \frac{d}{dt} \hat{c}_{k\sigma}(t) = [\hat{c}_{k\sigma}(t), H_L(V)] \quad (2.4)$$

The solution of Eq. (2.4) is

$$\hat{c}_{k\sigma}(t) = e^{i\phi(t)/2} c_{k\sigma}(t) \quad (2.5)$$

where

$$\frac{d\phi}{dt} = \frac{2e}{\hbar} V(t) \quad (2.6)$$

the effect of $H_L(V)$ being a modulation of the phase of the destruction operator. The tunneling current operator is given by the rate of change of the electron number operator N_L

$$\hat{I}(t) = -e\dot{N}_L \quad (2.7)$$

As for the case of the destruction operators $\hat{c}_{k\sigma}(t)$, the rate of change of the number of electrons on the left side of the barrier is calculated from the Heisenberg equations of motion using the total Hamiltonian, H , in Eq. (2.1). The only piece of H which does not commute with N_L is the tunneling Hamiltonian, H_T , which gives a non-zero commutator:

$$\dot{N}_L = \frac{i}{\hbar} [H_T, N_L] \quad (2.8)$$

The expectation value of the current operator $I(t)$ is calculated to first order in the tunneling Hamiltonian, H_T using linear response theory (or first order perturbation theory), and is given by:

$$I(t) = \langle \hat{I}(t) \rangle = \frac{-2e}{\hbar} \text{Re} \sum_{kq\sigma} T_{kq} \int_{-\infty}^t d\tau e^{n\tau} \times \langle [c_{k\sigma}^+(t) d_{q\sigma}(t), H_T(\tau)] \rangle_0 \quad (2.9)$$

where $\langle \rangle_0$ denotes an expectation value referred to the unperturbed Hamiltonian. The factor $e^{n\tau}$, comes from the adiabatic turn on of the perturbation assumed in the perturbation calculation. Here, $n \rightarrow 0^+$.

Werthamer⁹ evaluated Eq. (2.9) for a general time dependent voltage $V(t)$ across the barrier, and his result is reprinted below:

$$I(t) = \text{Im} \left[\int_{-\infty}^{\infty} d\omega d\omega' \{ W(\omega) W^*(\omega') e^{-i(\omega-\omega')t} j_1(\omega' + \frac{1}{2}\omega_0) \right. \\ \left. + W(\omega) W(\omega') e^{-i(\omega+\omega')t + i\phi + i\alpha_0} j_2(\omega' + \frac{1}{2}\omega_0) \} \right] \quad (2.10)$$

In Werthamer's notation, the time dependent voltage $\hat{V}(t)$ contains no dc part, $\hat{V}(t) = V(t) - V_0$, where V_0 is a dc voltage. The functions, $W(\omega)$, are related to $\exp\{(-ie/\hbar) \int_{-\infty}^t \hat{V}(t') dt'\}$ by a Fourier transform:

$$\exp\left\{\frac{ie}{\hbar} \int_{-\infty}^t \hat{V}(t') dt'\right\} = \int_{-\infty}^{\infty} d\omega W(\omega) e^{-i\omega t} \quad (2.11)$$

The phase ϕ contains the time dependence from the dc bias voltage, V_0 ,

$$\phi = \frac{2e}{\hbar} V_0 t = \omega_0 t \quad (2.12)$$

and the phase α_0 is the initial phase difference between the two electrodes. The frequency-dependent current amplitudes $j_1(\omega)$ and $j_2(\omega)$ are defined by

$$j_1(\omega) = 2e \sum_{kq\sigma} \int_{-\infty}^{\infty} d\omega_1 d\omega_2 \left[f^-(\omega_1) - f^-(\omega_2) \right] |T_{k,q}|^2 \\ \times A_k(\omega_1) A_q(\omega_2) \left[\omega_1 - \omega_2 - \omega + i\eta \right]^{-1} \quad (2.13)$$

$$e^{i\alpha_0} j_2(\omega) = 2e \sum_{kq\sigma} \int_{-\infty}^{\infty} d\omega_1 d\omega_2 \left[f^-(\omega_1) - f^-(\omega_2) \right] T_{k,q} T_{-k,-q}^* \\ \times B_k(\omega_1) B_q(\omega_2) \left[\omega_1 - \omega_2 - \omega - i\eta \right]^{-1}$$

where $f^-(\omega) = [e^{+\beta\omega} + 1]^{-1}$

is the Fermi distribution function, $\beta = (kT)^{-1}$ and $\hbar = 1$. The terms $A_k(\omega)$, and $B_k(\omega)$, and $\bar{B}_k(\omega)$ are the spectral weight functions¹⁹ for the superconductor on the left side

$$\begin{aligned} A_k(\omega) &= \frac{1}{2} \left[(1 + (\epsilon_k/E_k)) \delta(\omega - \epsilon_k) + (1 - (\epsilon_k/E_k)) \delta(\omega + \epsilon_k) \right] \\ B_k(\omega) &= \frac{-i}{2} (\Delta_k/E_k) \left[\delta(\omega - E_k) - \delta(\omega + E_k) \right] \\ \bar{B}_k(\omega) &= (\Delta_k^*/\Delta_k) B_k(\omega) \end{aligned} \quad (2.14)$$

E_k is the energy of the quasiparticle excitation and is given by the usual expression:

$$E_k = (\epsilon_k^2 + \Delta_k^2)^{\frac{1}{2}} \quad (2.15)$$

where Δ_k is the superconducting energy gap and ϵ_k is the kinetic energy of the quasiparticle relative to the Fermi energy.

When the temperature T is raised above the superconducting transition temperatures of the two junction electrodes the spectral weight function $B_k(\omega) \rightarrow 0$ since $B_k(\omega) \sim \Delta_k$, and $A_k(\omega) \rightarrow \delta(\omega - \epsilon_k)$, the spectral weight function for an electron in a normal metal.

The current amplitudes $j_1(\omega)$ and $j_2(\omega)$ are computed by substituting Eqs. (2.14) into Eqs. (2.13), and doing the ω_1 and ω_2 integrals. The sums over wave vectors are replaced by integrals. The resulting integrals can be done only by numerical integration at finite temperatures; however at $T=0$ they can be evaluated analytically. Fig. 2.1 displays the real and imaginary parts of $j_1(\omega)$ and $j_2(\omega)$ at $T=0$

Tunnel Junction Response Functions

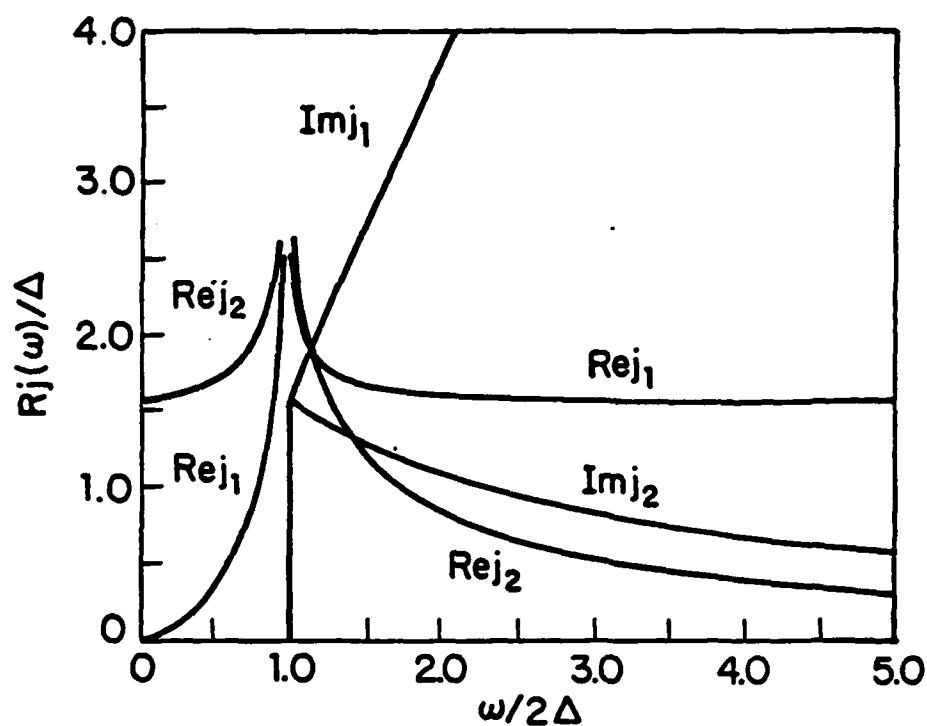


FIG. 2.1 Real and imaginary parts of the response functions $j_1(\omega)$ and $j_2(\omega)$, at $T=0$. The peak in $\text{Re}[j_2(\omega)]$ at $\hbar\omega/2\Delta=1$ is the Riedel peak. $\text{Re}[j_2(\omega)]$ is the pair response function, while $\text{Im}[j_1(\omega)]$ is the quasiparticle I-V curve. [Adapted from Ref. 9.]

and for a junctions with both electrodes made of the same superconducting material. At $\hbar\omega/2\Delta=1$ there is a peak in the real part of $j_2(\omega)$ and $j_1(\omega)$. The peak in $\text{Re}[j_2(\omega)]$ is the peak first described by Riedel,²⁰ while the sharp rise in $\text{Im}[j_1(\omega)]$ at $\hbar\omega/2\Delta=1$ is the gap structure first seen in the I-V curve of a tunnel junction by Giaever.⁴

2.3 Results From the Werthamer Theory

The main result of the Werthamer theory, Eq. (2.10) is rather formidable looking, however, we can make sense of it by analyzing it in specific cases of interest. We begin with the case of $\hat{V}(t)=0$, i.e. only a dc voltage on the junction. Eq. (2.11) implies $W(\omega)=\delta(\omega)$ since $\hat{V}(t)=0$. Inserting this value of $W(\omega)$ in Eq. (2.10) we obtain

$$I(t) = \text{Im}\left[j_1\left(\frac{\omega_0}{2}\right)\right] + \text{Im}\left[j_2\left(\frac{\omega_0}{2}\right)\right] \cos(\phi + \alpha_0) \\ + \text{Re}\left[j_2\left(\frac{\omega_0}{2}\right)\right] \sin(\phi + \alpha_0) \quad (2.17)$$

where $\omega_0=2eV_0/\hbar$, $\phi = \omega_0 t$, and α_0 is the initial phase value, using Eq. (2.12). The real and imaginary parts of j_1 and j_2 , written in Eq. (2.17), can be rewritten in standard notation^{2,5} as follows:

$$I_{qp}(V_0, T) = \text{Im}\left[j_1(eV_0/\hbar)\right] \\ I_{J1}(V_0, T) = \text{Re}\left[j_2(eV_0/\hbar)\right] \\ I_{J2}(V_0, T) = \text{Im}\left[j_2(eV_0/\hbar)\right] \quad (2.18)$$

where $V_0=V_{dc}$. Eq. (2.17) becomes

$$I(t) = I_{qp}(V_0, T) + I_{J2}(V_0, T) \cos(\phi + \alpha_0) \\ + I_{J1}(V_0, T) \sin(\phi + \alpha_0) \quad (2.19)$$

As $V_0 \rightarrow 0$, $I_{qp}(V_0, T) \rightarrow 0$ and $I_{J2}(V_0, T) \rightarrow 0$, and we are left with the term $I_{J1}(0, T) \sin(\phi + \alpha_0)$, the dc Josephson effect. I_{qp} and I_{J2} can be written in terms of conductances,

$$\begin{aligned} I_{qp} &= \sigma_0(V_0, T) V_0 \\ I_{J2} &= \sigma_1(V_0, T) V_0 \end{aligned} \quad (2.20)$$

so that Eq. (2.19) becomes

$$I(V_0, T; t) = I_{J1}(V_0, T) \sin \phi(t) + \{\sigma_1(V_0, T) \cos \phi(t) + \sigma_0(V_0, T)\} V_0 \quad (2.21)$$

where $\phi(t) = \phi(t) + \alpha_0$. Eq. (2.21) is the result obtained by Josephson⁵ in 1962.

The factor $I_{J1}(V_0, T)$ at $V_0=0$ is called the critical current. The notation is $I_{J1}(0, T) = I_c(T)$ and it can be evaluated¹⁷ to find a simple form for the case of a tunnel junction with two identical superconductors for any temperature T , with energy gap $\Delta(T)$ and normal resistance R_n :

$$I_c(T) = \frac{\pi \Delta(T)}{2eR_n} \tanh\left(\frac{\Delta(T)}{2kT}\right) \quad (2.22a)$$

For dissimilar metals, at $T=0$, with gaps $\Delta_1(0)=\Delta_1$, and $\Delta_2(0)=\Delta_2$, an analytic form has been found^{17,95}

$$I_c(0) = \frac{2}{eR_n} \left(\frac{\Delta_1 \Delta_2}{\Delta_1 + \Delta_2} \right) K\left(\frac{|\Delta_1 - \Delta_2|}{\Delta_1 + \Delta_2} \right) \quad (2.22b)$$

where K is the complete elliptic integral of the first kind. At finite temperatures, the expression for the critical current of a tunnel

junction is written in terms of a series expansion.¹⁷ Fig. 2.2(a) displays the critical current as a function of T for a Sn-Sn junction, while Fig. 2.2(b) shows the critical current as a function of temperature for a Sn-Pb junction.¹⁷ As $T \rightarrow T_c$, for the Sn-Sn junction $I_c \propto (1-t)$ where $t = T/T_c$.

It is relatively straightforward to find the effect of a dc bias voltage and an ac voltage. In this case $V(t) = V_0 + V_L \cos(\omega_L t)$ and the Josephson relation $2eV(t) = \hbar d\phi(t)/dt$ implies

$$\phi(t) = \left(\frac{2eV_0}{\hbar}\right)t - \left(\frac{2eV_L}{\hbar\omega_L}\right)\sin \omega_L t \quad (2.23)$$

and

$$\begin{aligned} \exp\left(\frac{ieV_L}{\hbar\omega_L} \sin \omega_L t\right) &= \int_{-\infty}^{\infty} d\omega W(\omega) e^{-i\omega t} \\ &= \sum_{k=-\infty}^{\infty} J_k\left(\frac{eV_L}{\hbar\omega_L}\right) e^{ik\omega_L t} \end{aligned} \quad (2.24)$$

where we have used the relation

$$\exp(-ix \sin(\theta)) = \sum_{n=-\infty}^{\infty} J_n(x) e^{-in\theta} \quad (2.25)$$

where J_n is the n th order Bessel function. The W function becomes

$$W(\omega) = \sum_{k=-\infty}^{\infty} J_k\left(\frac{eV_L}{\hbar\omega_L}\right) \delta(\omega + k\omega_L) \quad (2.26)$$

Substituting Eq. (2.26) into Eq. (2.10) we obtain:

$$\begin{aligned} I(t) = \text{Im} & \left[\sum_{k,k'=-\infty}^{\infty} J_k(\alpha) J_{k'}(\alpha) j_1(-k'\omega_L + \frac{1}{2}\omega_0) e^{-i(k'-k)\omega_L t} \right. \\ & \left. + \sum_{k,k'=-\infty}^{\infty} J_k(\alpha) J_{k'}(\alpha) j_2(-k'\omega_L + \frac{1}{2}\omega_0) e^{i(k'+k)\omega_L t + i\omega_0 t + i\alpha_0} \right] \end{aligned} \quad (2.27)$$

where $\alpha = eV_L / \hbar \omega_L$ is the normalized ac voltage in the junction and $\omega_0 = 2eV_0 / \hbar$. The dc I-V curve for the dc plus ac voltage sources is calculated from Eq. (2.27) and is:

$$I(V_0) = \sum_{k=-\infty}^{\infty} J_k^2(\alpha) \operatorname{Im}\{j_1(-k\omega_L + eV_0/\hbar)\} \\ + \sum_{n \geq 0} \left| \sum_{k=-\infty}^{\infty} J_k(\alpha) J_{n-k}(\alpha) \operatorname{Re}\{j_2((k - \frac{1}{2}n)\omega_L)\} \right| \delta(V_0 \pm n(\frac{\hbar\omega_L}{2e})) \quad (2.28)$$

Eq. (2.28) is the fundamental, experimentally verifiable result of the frequency-dependent theory of the Josephson tunnel junction.²¹ In this equation, the imaginary part of j_1 is the dc I-V curve - $\operatorname{Im}(j_1(\omega)) = I_{dc}(\hbar\omega/e) = I_{qp}(\hbar\omega/e)$, while the real part of j_2 contains the frequency dependence of the Josephson effect, and is rewritten in terms of the response function I_{J1} , $\operatorname{Re}[j_2(\omega)] = I_{J1}(\hbar\omega/e)$. Eq. (2.28) is rewritten as:

$$I(V_0) = \sum_{k=-\infty}^{\infty} J_k^2(\alpha) I_{qp}(V_0 + k(\frac{\hbar\omega_L}{e})) \\ + \sum_{n \geq 0} \left| \sum_{k=-\infty}^{\infty} J_k(\alpha) J_{n-k}(\alpha) I_{J1}((k - \frac{1}{2}n)\frac{\hbar\omega_L}{e}) \right| \delta(V_0 \pm n(\frac{\hbar\omega_L}{2e})) \quad (2.29)$$

Eq. (2.29) contains two terms. The first term comes from the interaction of the electromagnetic field in the junction with the quasiparticles, and is the mathematical description of how the photon-assisted tunneling effect changes the shape of the whole I-V curve. This term reproduces the result of the Tien-Gordon⁸ theory of the photon-assisted tunneling effect. The photon-assisted tunneling

Temperature Dependence of the Critical Current

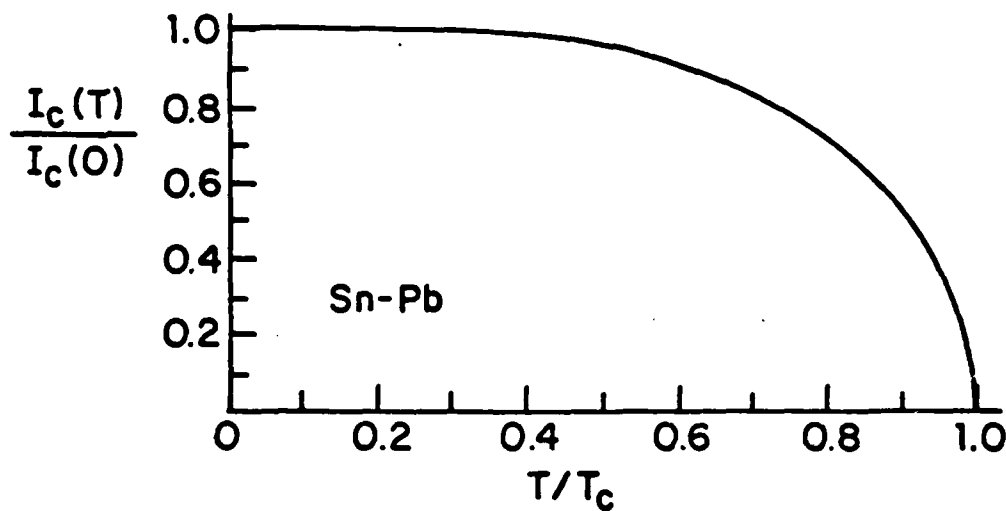
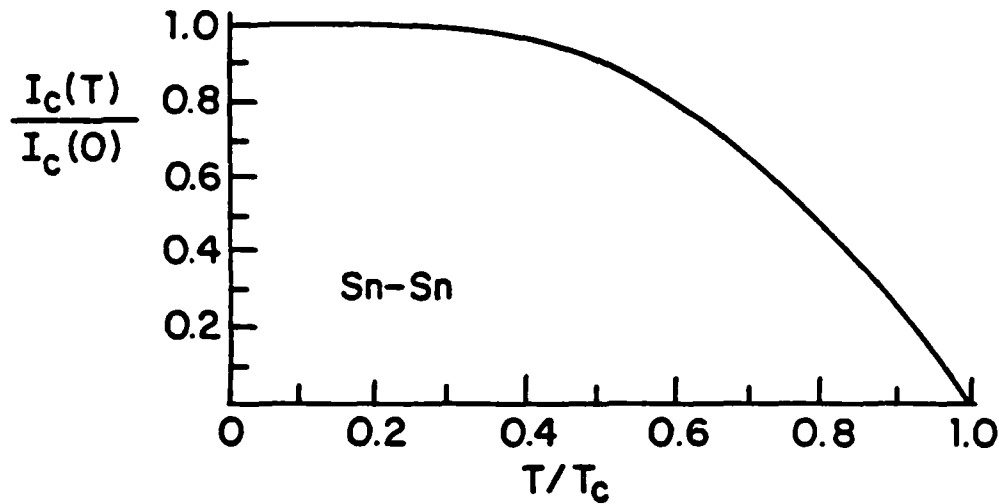


FIG. 2.2 (a) Critical current $I_c(T)$, normalized to $I_c(0)$, vs. the reduced temperature T/T_c for a Sn-Sn tunnel junction. (b) Critical current, $I_c(T)$, normalized to $I_c(0)$, vs. the reduced temperature T/T_c for a Sn-Pb tunnel junction. [After Ref. 21.]

steps or Dayem-Martin⁷ steps occur at $\pm V_{\text{gap}} + k(\hbar\omega_L/e)$ as can be seen from Eq. (2.29) by observing that a feature which is significant on the I-V with no applied radiation, i.e. the gap structure on the dc I-V curve (Fig. 1.1(b)) will appear at the voltage $k(\hbar\omega_L)/e$ away from the original structure, but modulated in amplitude by the squares of Bessel functions, $J_k^2(\alpha)$.

The second term, unlike the first one, has an effect only at discrete voltages, $V_0 = n(\hbar\omega_L/2e)$, producing "spikes" on the I-V curve at these voltages. When the junction is dc current biased the "spikes" become flat regions on the I-V. This second term describes the ac Josephson effect. Figs. 1.2a and 1.2b previously illustrated these effects, and the reader is urged to look at these figures again. The frequency dependence of the Josephson effect, first obtained by Werthamer, is displayed in this term through the dependence of the step amplitudes on I_{J1} , the pair response function.

The frequency dependence of the Josephson effect, observable as an enhancement of the step amplitudes at the Riedel peak, was first tested by Hamilton and Shapiro²³ in 1971, using 20-26 GHz microwave radiation. Their results were however limited to frequencies only within ~5% of the Riedel peak. Buckner, Finnegan, and Langenberg²⁴ studied Sn-SnO-Sn junctions at 135 GHz, and also observed the effect of the Riedel peak, but their work was also limited to frequencies within a few percent of the Riedel peak. Weitz, Skocpol, and Tinkham²⁵ first observed the Riedel peak in the far-infrared directly, by measuring the enhancement of the size of the first Josephson step at the peak and its subsequent

fall-off. They used Nb-Nb point contacts for this work. While their work showed an overall consistency with prior work, and they observed a fall-off in step amplitudes with roughly the right frequency dependence, the observed step amplitudes were a factor of two smaller than expected from theory, even with corrections for reductions in the step size from heating or noise. It is at present an open question whether there are irreducible differences between tunnel junctions and point contacts, due to the unknown nature of the contact, although significant progress has been made recently on this question.²⁶

The Werthamer result, Eq. (2.10), for a general time-dependent voltage is very difficult to solve, and is appropriate only to a voltage biased situation. Harris²⁷ recast the Werthamer theory from the frequency domain description of Eq. (2.10) to a time domain formulation. He developed general techniques for digitally computing the behavior of a junction connected to an arbitrary circuit. These methods, however, require considerable computer time, and have not been used extensively in analyzing data on tunnel junctions. A more common, simpler approach, in wide use is a model of the junction, called the resistively shunted junction (RSJ) model developed by Stewart²⁸ and McCumber.²⁹ This model is essentially a low frequency or low voltage approximation to Eqs. (2.10) and (2.19) and is discussed in the following section.

2.3 The RSJ Model

The RSJ model can be derived from the microscopic theory result of Eq. (2.19) by assuming first that the pair response function whose imaginary part gives an $I_J(V,T)$ which is not frequency (voltage) dependent. So for $I_J(V,T)$, the maximum dc supercurrent at the junction temperature, $I_c(T)$, is substituted. The quasiparticle current, $I_{qp}(V,T)$, is modelled as either a voltage dependent conductance $G(V)$, i.e. $I_{qp}=G(V)V$, or even more drastically as simply a resistor with the value of the normal state conductance G_n , $I_{qp}=VG_n$. The $\cos(\phi)$ term is ignored.³⁰ Finally, the capacitance of the junction can be included in the equations by a term $\propto C(dV/dt)$. The external circuitry which drives the junction is modelled as a dc current source, plus a time dependent (ac) source if needed. The equation which results if these substitutions are inserted into Eq. (2.19) is:

$$I_T = G(V)V + I_c \sin\phi + C \frac{dV}{dt} \quad (2.30)$$

where $I_c=I_c(T)$, and $V=(\hbar/2e)d\phi/dt$. The total bias current, I_T , through the device is written as.

$$I_T = I_{dc} + I_L \sin\omega_L t + \hat{I}_N(t) \quad (2.31)$$

where a noise term, \hat{I}_N , has been included to model thermal fluctuations in the resistor, R_n , or an external noise source. Inserting the equation for the junction voltage $V=(\hbar/2e)\dot{\phi}$ into Eq. (2.30), the result is:

$$\frac{d^2\phi}{dt^2} + G\left(\frac{\hbar}{2e}\dot{\phi}\right) \frac{1}{C} \frac{d\phi}{dt} + \left(\frac{2eI_c}{\hbar C}\right) \sin\phi = \frac{2eI_T}{\hbar C} \quad (2.32)$$

where I_T is given by Eq. (2.31). Eq. (2.32) is a very general RSJ model, although not nearly as complex as the original Werthamer equation, it still retains solutions of considerable complexity depending on specific choices for $G(V)$, C , and the rf drive term $I_L \sin(\omega_L t)$. Fig. 2.3 schematically illustrates the RSJ model. Fig. 2.3(a) is a schematic of Eq. (2.30), where the Josephson element defined by the symbol, Φ , in the Figure, is shunted by the capacitor C , and the conductance $G(V)$, and driven by the current I_T . Fig. 2.3(b) shows that the conductance can be pictured as the normal conductance of the junction or the non-linear quasiparticle conductance, while Fig. 2.3(c) illustrates the total current can be viewed as a dc bias current, an ac current source, and a noise current.

We can easily determine the effect of an ac voltage source on the junction I-V curve using the RSJ model. We take a voltage source with dc and ac terms $V(t) = V_0 + V_L \cos(\omega_L t)$. The phase ϕ becomes $\phi(t) = (2eV_0/\hbar) t + (2eV_L/\hbar \omega_L) \sin(\omega_L t) + \phi_0$. We use $G(V) = G_n$, and $C=0$. Eq. (2.30) becomes

$$I_T = G_n V(t) + I_c \sin \phi(t) \quad (2.33)$$

The second term of Eq. (2.33), $I_p = I_c \sin \phi(t)$, becomes

$$I_p = I_c \sum_{n=-\infty}^{\infty} J_n\left(\frac{2eV_L}{\hbar \omega_L}\right) \cos(\omega_0 + n\omega_L)t \quad (2.34)$$

where $\phi_0 = \pi/2$ to maximize the zero voltage critical current, and standard trigonometric identities were used to arrive at the result. $J_n(2\alpha)$ is the Bessel function of order n , and $\alpha = eV_L/\hbar \omega_L$ as before. The

Resistively Shunted Junction (RSJ) Model [Current Biased]

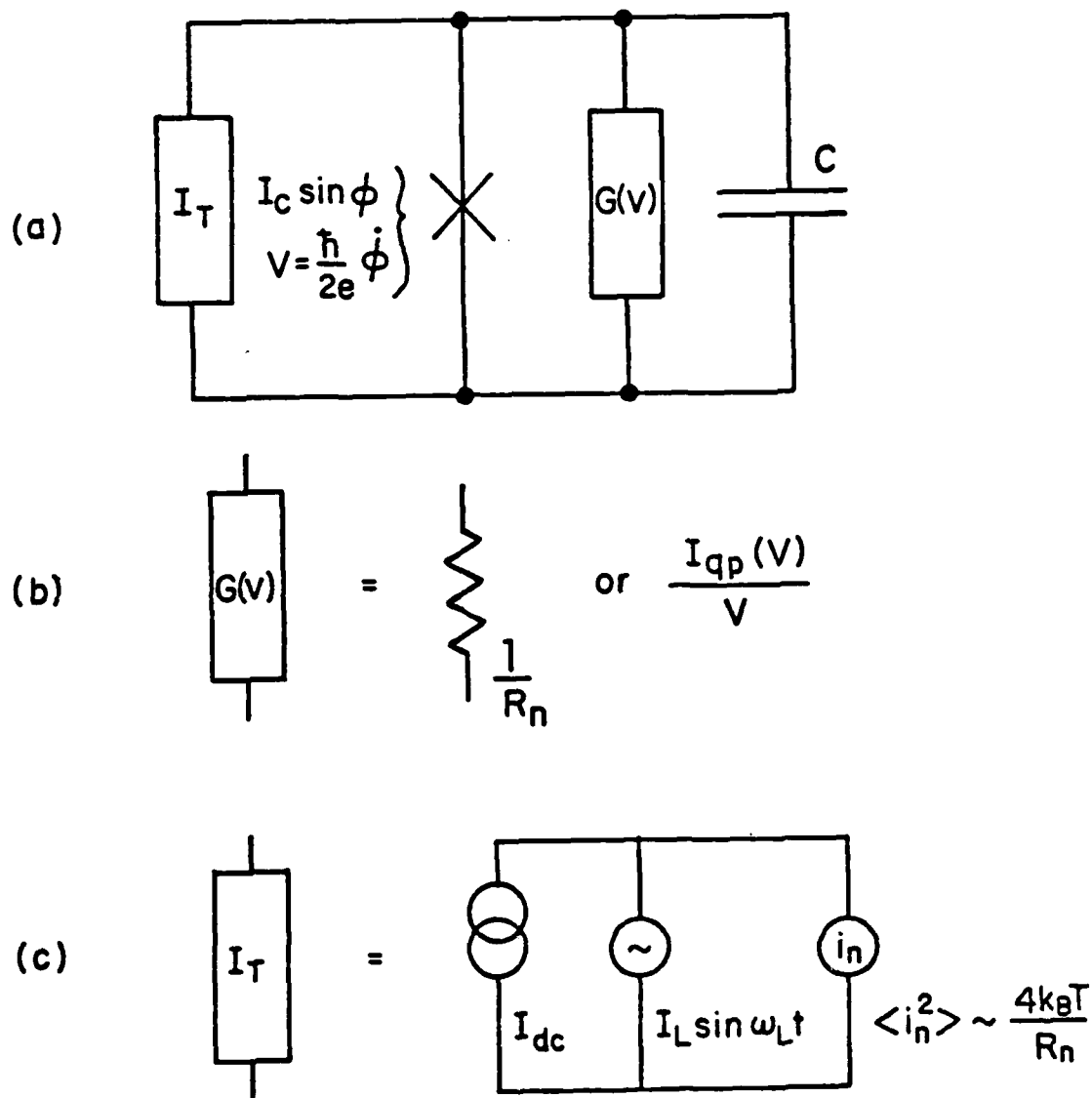


FIG. 2.3 (a) Schematic illustration of the current biased RSJ model. I_T is the total current through the junction, C is the junction capacitance, $G(V)$ is the quasiparticle conductance, the \times denotes the Josephson element. (b) The quasiparticle conductance can be linearized, i.e. represented as $(R_n)^{-1}$, or left non-linear. (c) The total current, I_T through the junction is the sum of a dc term, I_{dc} , an ac drive term, $I_L \sin \omega_L t$, and a noise term, I_N .

time-averaged dc current becomes

$$\langle I_T \rangle = G_n V_0 + I_c \sum_{n=-\infty}^{\infty} J_n(2\alpha) \delta(\omega_0 + n\omega_L) \quad (2.35)$$

since the second term of Eq. (2.34) contributes only if $\omega_0 = -n\omega_L$ where n is an integer. Therefore, "steps" appear on the I-V curve at dc voltages which are integer multiples of $\hbar\omega_L/2e$ as observed before. In this case the full width of the n th step is $I_n = 2I_c J_n(2\alpha)$, instead of the complicated structure of Eq. (2.29). The second term of Eq. (2.29) reduces to the second term of Eq. (2.35) in the limit of $\hbar\omega_L/2e \rightarrow 0$. In this case $I_J((k-n/2)\hbar\omega_L/e) \sim I_c$, and

$$\sum_{k=-\infty}^{\infty} J_k(\alpha) J_{n-k}(\alpha) = J_n(2\alpha),$$

so that the term is

$$I_c \sum_{n \geq 0} J_n(2\alpha) \delta(V_0 \pm n(\hbar\omega_L/e)).$$

The term $\sum_{k=-\infty}^{\infty} J_k^2(\alpha) I_{qp}(V_0 + k(\hbar\omega_L/e))$ reduces to $V_0 G_n$ if the I-V curve is linear, since the term $(V_0 + k(\hbar\omega_L/e))$ is compensated for by a term in the sum with $(V_0 - k(\hbar\omega_L/e))$, leaving

$$\sum_{k=-\infty}^{\infty} J_k^2(\alpha) [V_0 G_n] = V_0 G_n \quad (2.36)$$

since $\sum_{n=-\infty}^{\infty} J_n^2(\alpha) = 1$. The resulting equation is:

$$I(V_0) = G_n V_0 + I_c \sum_{n \geq 0} J_n(2\alpha) \delta(V_0 \pm n(\frac{\hbar\omega_L}{2e})) \quad (2.37)$$

and is equivalent to Eq. (2.35).

This discussion demonstrates how the Werthamer theory reduces to the RSJ model only in the limit of low frequencies. This point is important since it indicates that for junctions which are sensitive to frequencies approaching the energy gap frequency, caution must be applied in using results from the RSJ model when interpreting experimental data.

We now discuss the effects of noise sources intrinsic to the junctions on their I-V curves for both the transition out of the zero-voltage state assuming a dc current bias, and the rounding of the ac Josephson steps.

2.4 Noise Effects

The intrinsic noise in electronic devices such as transistors, resistors and superconducting tunnel junctions is described by the power spectrum for current or voltage fluctuations.³¹ In superconducting tunnel junctions the noise could come from fluctuations in the quasiparticle (or pair) current, for example. The power spectrum for quasiparticle current fluctuations, at a constant dc bias voltage V_0 , first calculated by Dahm et al.³², is given by

$$P_I(\omega) = \frac{e}{2\pi} \left\{ I_{qp}(V_0 + \frac{\hbar\omega}{e}) \coth\left(\frac{\beta}{2}(eV_0 + \hbar\omega)\right) + I_{qp}(V_0 - \frac{\hbar\omega}{e}) \coth\left(\frac{\beta}{2}(eV_0 - \hbar\omega)\right) \right\} \quad (2.38)$$

where $I_{qp}(V_0)$ is the quasiparticle current in the junction, defined in

Eq. (2.18). The power spectrum is defined as the Fourier transform of the current-current auto-correlation function:

$$\text{Re } \overline{I(t+\tau) I(t)} = \int_{-\infty}^{\infty} P_I(\omega) \cos \omega \tau d\omega \quad (2.39)$$

where the autocorrelation function is

$$\overline{I(t+\tau) I(t)} = \lim_{T \rightarrow \infty} \frac{1}{2T} \int_{-T}^T \overline{I(t+\tau) I(t)} dt \quad (2.40)$$

In this notation the angular brackets imply a statistical and quantum mechanical average, and the bar indicates a time average.³³ The mean-square current fluctuation (noise), $\langle i_N^2 \rangle$, can be calculated from the power spectrum by integrating over all frequencies

$$\langle i_N^2 \rangle = \int_{-\infty}^{\infty} P_I(\omega) d\omega \quad (2.41)$$

The power spectrum, Eq. (2.38), while rather complicated can be understood simply in certain limiting cases. If the bias voltage, V_0 , is small compared to kT/e , i.e. $eV_0 \ll kT$, and the frequency ω is small, $\hbar\omega \ll kT$, eV_0 , the power spectrum reduces to

$$P_I(\omega) = \frac{e}{2\pi} (4kT) \frac{I_{qp}(V_0)}{V_0} \quad (2.42)$$

Eq. (2.42) reduces to the standard Johnson-Nyquist result

$$P_I(\nu) = 4kT/R_n \quad (2.43)$$

by converting the frequency measure from radians to Hz using

$P_I(\nu) = 2\pi P_I(\omega)$, and the fact that $I_{qp}(V_0)/V_0 = (R_n)^{-1}$, if the junction is

in its normal state (linear I-V). If the junction is below the transition temperatures of the two electrodes, its I-V curve is non-linear. At low dc voltages, i.e., $V_0 \rightarrow 0$, $I_{qp}(V_0) \sim (dI/dV)V_0$, and $I_{qp}(V_0)/V_0 \sim (R_d)^{-1}$ where $R_d = (dI/dV)^{-1}$, the dynamic resistance of the junction at low voltages.

At high bias voltages, $eV_0 \gg kT, \hbar\omega, \Delta$, regardless of whether or not the junction is superconducting, the power spectrum, Eq. (2.38), reduces to

$$P_I(\omega) = \frac{e}{\pi} I_{qp}(V_0) \quad (2.44)$$

in agreement with the usual expression for shot noise, $P_I(\nu) = 2eI_{qp}(V_0)$, after conversion to frequencies in Hz.

The mean-square voltage noise $\langle v_N^2 \rangle$ is related to the current noise by the dynamic resistance, R_d :

$$\langle v_N^2 \rangle = R_d^2 \langle i_N^2 \rangle = R_d^2 \int_{-\infty}^{\infty} P_I(\omega) d\omega \quad (2.45)$$

Eq. (2.38) was used first by Dahm, et al.³² to calculate the linewidth of the Josephson radiation emitted by a tunnel junction, in a calculation based on FM noise theory.

The power spectrum of Eq. (2.38), while an important result, because it is derived with the assumption of a constant dc bias voltage, is of limited usefulness in studying the detailed dynamics of a tunnel junction. In the usual experimental configuration the junction is dc current biased with noise and without rf, or dc current biased and rf

voltage or current biased. In practice the RSJ model and the limit of Eq. (2.38) for low voltages has been used as an approximate scheme, with reasonable success, for calculating the effects of noise on a junction. In the low capacitance limit, $\beta_C \rightarrow 0$, appropriate to shunted tunnel junctions or metallic weak links, analytic solutions to the RSJ model with a white noise source such as for the power spectrum of Eq. (2.43), are available. We will now give a brief description of the results of Ambegaokar and Halperin (AH)³⁴, for $\beta_C \rightarrow 0$, and Lee,³⁵, for $\beta_C < 1$.

Eq. (2.32) can be simplified by rewriting it in terms of normalized units. Frequencies are normalized to ω_J , where $\omega_J = (2eI_C/\hbar C)^{1/2}$ is the junction plasma frequency. Currents are divided by I_C , the critical current, and voltages by the $I_C R_n$ product, where, for example, $I_C R_n = \pi \Delta(0)/2e$ for a junction with equal gaps at $T=0$. The resulting equation is

$$\frac{d^2\phi}{d\tau^2} + g\left(\frac{d\phi}{d\tau}\right) + \sin\phi = \rho_{dc} + \rho_L \sin\Omega\tau + \hat{\rho}_N \quad (2.46)$$

where $\tau = t \omega_J$ is the normalized time, $g(d\phi/d\tau) = I_{qp}((\hbar/2e)d\phi/d\tau)/I_C$ is a function of the normalized frequency (voltage), $d\phi/d\tau$. The normalized ac current and frequency are $\rho_L = I_L/I_C$, and $\Omega = \omega_L/\omega_J$, respectively. The noise term is $\hat{\rho}_N = \hat{I}_N/I_C$. If $G(V) = (R_n)^{-1}$ then $g(d\phi/d\tau)$ becomes $g(d\phi/d\tau) = (\beta_C)^{-1/2} d\phi/d\tau$ which is the situation described by AH, and Lee. The parameter $\beta_C = (\omega_J R_n C)^2 = 2eI_C R_n^2 C/\hbar$ is called the Stewart-McCumber parameter, and is used to describe the hysteresis on the I-V curve of the junction. The β_C parameter is small,

$\beta_C \ll 1$, in the low capacitance, low hysteresis limit used by AH, and Lee.

The noise term $\hat{\rho}_N$ is described by its autocorrelation function in the time domain:

$$\langle \hat{\rho}_N(\tau+\tau') \hat{\rho}_N(\tau') \rangle = \frac{4}{\gamma \beta_C^{1/2}} \delta(\tau) \quad (2.47a)$$

where $\beta_C = (2eI_C R_n^2 C) / \hbar$, and $\gamma = \hbar I_C / ekT$, is calculated from the unnormalized autocorrelation function

$$\langle \hat{I}_N(t+\tau) \hat{I}_N(t) \rangle = \frac{4kT}{R_n} \delta(\tau) \quad (2.47b)$$

appropriate to the resistance of the junction in the low voltage Johnson noise limit. For an nonlinear I-V curve in the low voltage limit, β_C is replaced by $\beta_C' = (2eI_C R_d^2 C) / \hbar$ and γ remains the same in Eq. (2.47a), or equivalently R_n is replaced by R_d in Eq. (2.47b). All terms on the left hand side of Eq. (2.46) remain the same since we have used the general form for the normalized quasiparticle current, $g = g(d\phi/d\tau)$.

The RSJ model can be rewritten in terms of the mechanical model of a particle in a tilted, periodic potential. If we consider the case where the conductance $G(V)$, is simply $G_n = (R_n)^{-1}$, then the middle term of the left hand side of Eq. (2.46), $g(d\phi/d\tau)$, is $(\beta_C)^{-1/2} [\dot{\phi}]$. We take for the moment $\hat{\rho}_N = 0$, then Eq. (2.46) becomes:

$$\frac{d^2 \phi}{d\tau^2} + \frac{1}{\sqrt{\beta_C}} \frac{d\phi}{d\tau} + \frac{\partial}{\partial \phi} U(\phi) = 0 \quad (2.48)$$

where $U(\phi) = (-\rho_{dc}\phi - \cos\phi)$ is the tilted periodic potential the particle is sliding in. A particle is trapped in a well at position A in Fig. 2.4. Friction or damping is modelled by the second term of Eq.

Particle in a Tilted Periodic Potential (Junction Analogy)

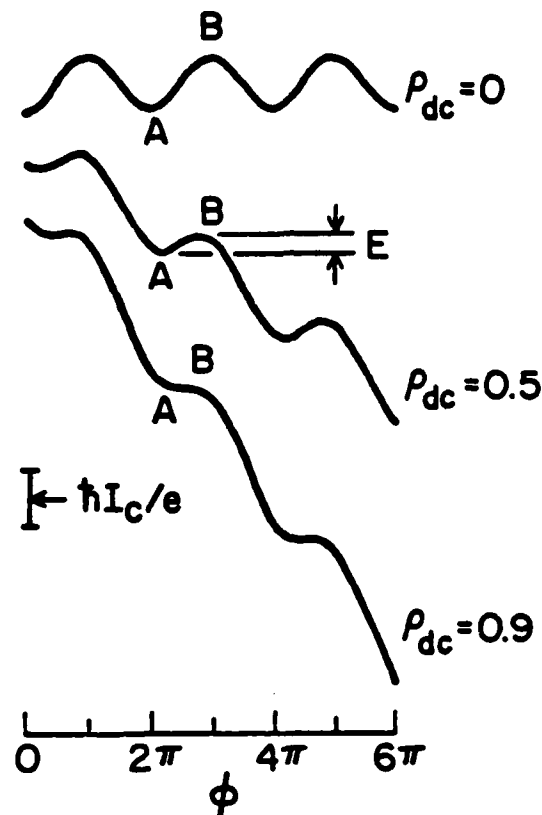


FIG. 2.4 Mechanical analogy of the RSJ model with a particle moving in a tilted periodic potential. As the dc current is increased from zero the particle trapped in a well at A can escape prematurely from the well by jumping over the energy barrier E, and begin sliding down the potential. [After Ref. 37.]

(2.48). With no noise the particle remains trapped in the well until the tilt is great enough for the particle to become dislodged and roll down the hill. As the tilt decreases, the particle continues rolling until the tilt reaches a minimum value which depends on the frictional term. If the friction is large, i.e. low β_c , then the particle comes to rest when the tilt is larger than it would for the low friction, large β_c , case. This means that the hysteresis of the junction I-V is less for the low β_c junction than for the high β_c junction. Noise can cause the particle to roll out of the well at a lower tilt than it would without noise. Noise can kick the particle out of the bottom of the well at A, over the barrier B, causing the particle to roll down the hill. The phase then changes with time, or the junction has a voltage.

Ambegaokar and Halperin used Eq. (2.46) in the limit of $\rho_L=0$, and $\beta_c \ll 1$, and $g(d\phi/d\tau) = (\beta_c)^{-1/2}(d\phi/d\tau)$. AH found that the critical current was depressed and the transition out of the zero voltage state was rounded as the parameter $\gamma = \hbar I_c / ekT$ was decreased from large values to zero, as is shown in Fig. 2.5. The parameter γ measures the strength of the coupling of the junction from the Josephson effect, against kT , the thermal energy tending to destroy the phase coherence of the junction. We can get a feeling for the significance of various values of γ if we compute it for real parameters. Inserting values of e , \hbar , k into the equation for γ , we obtain $\gamma = 47.68 [I_c (\mu A) / T(K)]$. If $I_c = 1 \mu A$ in the absence of fluctuations, and $T = 1 K$, then $\gamma \sim 48$. From Fig. 2.5 we observe that the critical current would be depressed by $\sim 20\%$ by the thermal fluctuations. In the limit of $\gamma \rightarrow 0$, the noise-rounded I-V

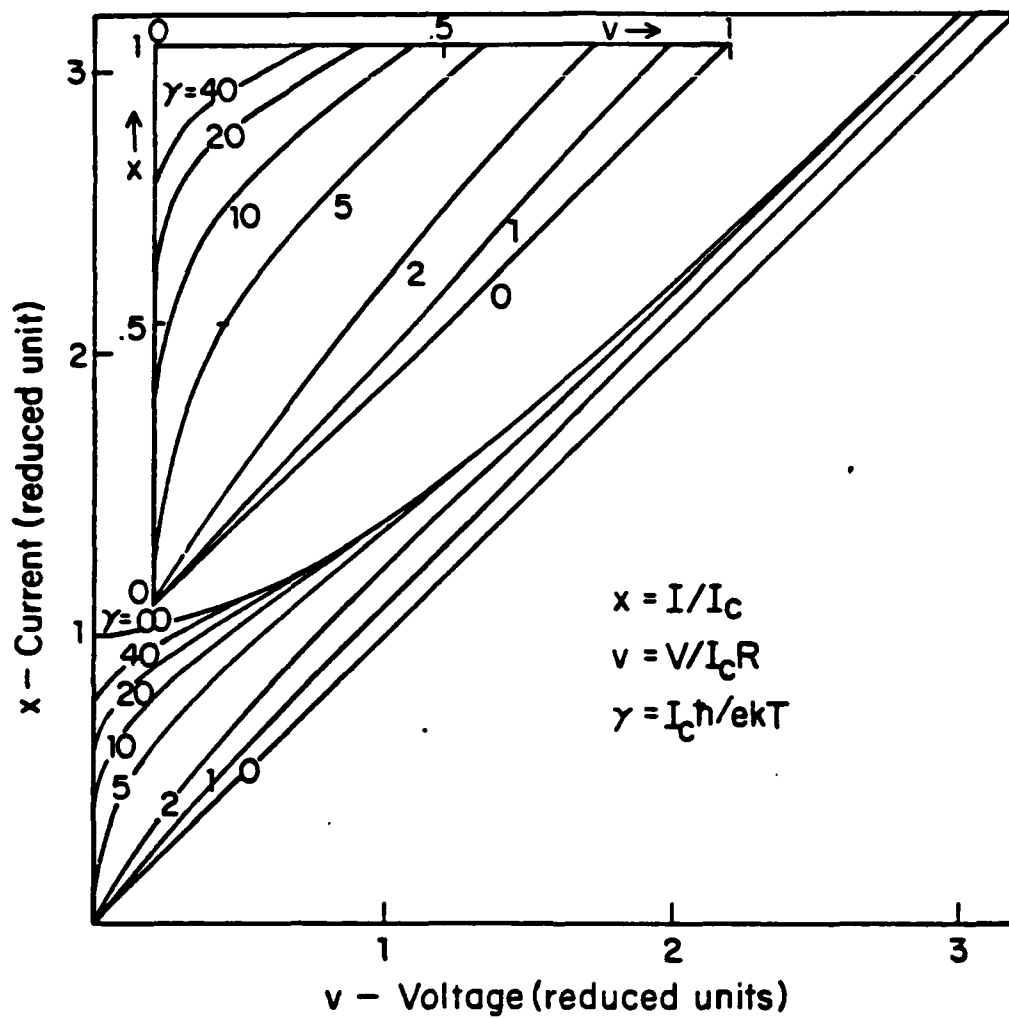


FIG. 2.5 Effect of thermal noise on the RSJ model I-V curves in the limit of $\beta_c = (2eI_c R^2 C) / \hbar \rightarrow 0$, at different values of the noise parameter, $\gamma = \hbar I_c / e k T$. [After Ref. 34.]

curve of the junction would, in fact, be linear. The critical current (Josephson effect) would be completely destroyed by the thermal noise.

P. A. Lee's result is more general, and is written below for the situation in which the junction is driven by an ac signal, for the n th Josephson step:

$$\Delta V = \frac{2}{\gamma} R_d I_n^0 (1 - e^{-\pi \gamma' \alpha}) T_1^{-1} (1 + \beta_c (T_2/T_1)) \quad (2.49)$$

where the arguments of this equation are as follows. ΔV is the dc voltage measured from the step center, $\alpha = \Delta I / I_n^0$, where ΔI is the current along the step measured from the step center, and I_n^0 is the step half-width without noise and R_d is the dynamic resistance at the step center without radiation. The current and voltage at the step center are I_0 and V_0 respectively, $\gamma' = \gamma (V_0 / I_0 R_d)$ where $\gamma = \hbar I_n^0 / e k T_{\text{eff}}$, and finally $\beta_c = (2e I_n^0 R_d^2 C) / \hbar$. T_1 and T_2 are integrals given by

$$\begin{aligned} T_1 &= \int_0^{2\pi} d\phi I_0 \left[\gamma' \sin(\phi/2) \right] \exp(-\frac{1}{2} \gamma' \alpha \phi) \\ T_2 &= \int_0^{2\pi} d\phi \sin(\phi/2) I_1 \left[\gamma' \sin(\phi/2) \right] \exp(-\frac{1}{2} \gamma' \alpha \phi) \end{aligned} \quad (2.50)$$

where I_0 and I_1 are modified Bessel functions. Eq. (2.49) in the limit of $\beta_c = 0$, agrees with the AH result if $\alpha = I / I_c$, $\gamma' = \gamma \hbar I_c / e k T$, $R_d = R_n$, and $\beta_c = (2e I_c R_n^2 C) / \hbar$, etc.

Henkels and Webb,³⁶ and Weitz¹² used a simplified version of Eq. (2.49), appropriate for $\beta_c = 0$, in their analyses of the noise rounding of Josephson steps at microwave and FIR frequencies, respectively, on point contacts. In Chapter IV, we will describe fits to step shapes on high

resistance tunnel junctions, using Eq. (2.49), the Lee result. We will also describe a more complete analysis, using a computer simulation of the junction dynamics, of both the noise rounding of the Josephson steps and the reduction of the critical current from noise, based on the model of Eq. (2.46).

Lee also calculated the effect of noise rounding in the limit of large β_c . His result was used by Fulton and Dunkleberger³⁷ in their studies of the lifetime of the zero-voltage state of Sn-Sn and Pb-Pb tunnel junctions. The inverse lifetime or probability per unit time of switching is

$$\tau^{-1} = (\bar{\omega}_J/2\pi) \exp(-E/kT) \quad (2.51)$$

where $E = (\hbar I_c/2e)[\alpha(2\sin^{-1}\alpha - \pi) + 2\cos(\sin^{-1}\alpha)]$ is the energy barrier in the presence of current,

with $\alpha = I/I_c$, and $\bar{\omega}_J = \omega_J(1-\alpha^2)^{1/4}$ is the angular attempt frequency. If the bias current is swept at a rate dI/dt , Eq. (2.51) can be used to compute the probability per unit current $P(I)$ of the junction switching.

$$P(I) = (\tau(I) \frac{dI}{dt})^{-1} \exp\{-\int_0^I dI' (\tau(I') \frac{dI'}{dt})^{-1}\} \quad (2.52)$$

This probability, measured by Fulton and Dunkleberger, was used by inversion of Eq. (2.52) to compute the lifetime $\tau(I)$ for their tunnel junctions. They found very good agreement with the expression for $\tau(I)$ Eq. (2.51) for their junctions in the temperature range from 4.2K down to 1.5K.

2.5 Discussion

Although the theory presented in Sections 2.2-2.4 is rather well established and considerable experimental work has been done to confirm it in one aspect or another, as pointed out in the text, much experimental work and theoretical work remains to be done, particularly at the limits of very low (~ 1 mK) temperatures for the transition out of the zero voltage state, and at high frequencies (FIR) for the Werthamer theory and the noise rounding of the Josephson steps at finite voltages. We will begin this section by discussing the problem of the transition out of the zero voltage state.

As the temperature of a tunnel junction is lowered into the mK range it is expected that the thermally activated process described by Eq. (2.51) will be frozen out. Instead as the current is swept towards the critical current, the transition out of the zero-voltage state is expected to occur by quantum mechanical tunneling through the energy barrier. Voss and Webb³⁸ performed experiments on high β_c ($\beta_c \sim 50-5000$, or low current density, $J_c \sim 16-160$ A/cm²) all-Nb junctions and found basically good agreement with the theory of Caldeira and Leggett³⁹, but they found a value of 5 for a parameter which should have been of order 1. Like many all Nb junctions their junctions had a significant normal conductance below the gap, which should not occur in a tunnel junction which follows the behavior described by the Werthamer theory. In high current density junctions ($J_c \sim 5 \times 10^5$ A/cm²), Jackel et al.⁴⁰ found evidence for macroscopic quantum tunneling at temperatures from 2.2K down to 1.6K. These experiments suggest that macroscopic quantum

tunneling effects are probably not important for the junctions used in this experiment ($\beta_c \sim 6$, $J_c \sim 10^3$ A/cm²) in the temperature range ($T \sim 1.4$ K) used, but these effects may become important on higher current density junctions which will be used in future experiments. It would be interesting to find out if Sn-SnO-Sn or Pb-PbO-Pb junctions would have a closer agreement with the theory of Caldeira and Leggett, since these junctions have dc I-V curves which are nearly ideal, i.e., follow the behavior expected from tunneling theory.

At high frequencies, Weitz et al.²⁵ observed the fall-off of the ac Josephson effect above the Riedel peak. They found the shape of the fall-off was in agreement with the theory but that the theory predicted the step widths to be a factor of 2 larger than the observed step widths even after correction for heating and noise rounding effects. A comprehensive theory for the dc I-V curve of point contacts has not been found, so the fact that the step widths were smaller than expected may have more to do with the nature of the point contact than any problem with the Werthamer theory, especially considering the reasonable agreement found near the Riedel peak by Hamilton and Shapiro,²² and Buckner et al.²³, working with classical tunnel junctions.

Weitz et al.^{12,41} found Josephson steps at high voltages on high resistance junctions to be rounded by noise. They were able to explain the observed rounding in terms of thermal noise at a temperature elevated above the bath temperature, essentially caused by Joule heating of the point contact. The temperatures found, however, were considerably (a factor of 2) lower than the temperature that would

correspond to the shot noise predictions of the noise theory of Dahm et al.³² Vernet, Heneaux, and Adde⁴² measured Josephson step linewidths as a function of dc voltage for point contacts and found good agreement with the theory of Dahm et al.³² At low dc voltages, Dahm et al.³² found good agreement with their theory from linewidth measurements on Sn-Sn and Pb-Pb tunnel junctions. Crozat, Vernet, and Adde⁴³ found good agreement with the theory of Dahm et al.³² on microbridges using a direct noise measurement technique, but direct noise measurement techniques on point contacts performed by Claassen, Taur, and Richards^{43a} showed considerably less noise than expected from the tunnel junction noise theory of Ref. 32.

It is clear from this discussion that considerable experimental work needs to be done to clear up these discrepancies. It is particularly important that well characterized tunnel junctions, for which the theory of Sections 2.2-2.4 is appropriate, be used. The experiments described in the Chapters which follow are on Sn-SnO-Pb junctions having good gap structure, small-area, and moderate current densities. These junctions were made by photolithographic techniques which were not yet developed when the experiments described above were performed. The experiments of this work attempt to address the questions raised about the size of the ac Josephson steps and the intrinsic shot noise in the junction.

CHAPTER III

EXPERIMENTAL TECHNIQUES

3.1 Introduction

During the course of this work three types of tunnel junction samples were made. The first samples were small-area junctions designed for experiments on gap suppression induced by high quasiparticle current injection, and consisted of Sn-SnO-Pb overlap tunnel junctions fabricated by the method of Dolan⁴⁴ and Dunkleberger⁴⁵. This work will be described in Appendix B. The second set of samples were small-area junctions fabricated at the centers of dipole antennas for use in the FIR measurements which make up the bulk of this work. These junctions were made primarily by the "resist-aligned" scheme of Howard,⁴⁶ et al., although some samples were fabricated by the "edge-aligned" method. The third type of samples were fabricated at Sperry Research Labs. The Sperry samples consisted of Nb-Si-Nb SNAP⁴⁷ (Selective Niobium Anodization Process) junctions at the centers of dipole antennas. Our results on the Sperry samples are reported in Appendix B.

Because the fabrication of these samples is rather involved we will devote most of this chapter to this problem. We begin by describing the mask making techniques used for the first two types of samples, and will then discuss the three methods of junction making used at Harvard. In order to keep the discussion to a reasonable length we will leave the complex, but critically important, details of the substrate cleaning procedures, mask and sample fabrication, and etches used to Appendix A. Following this we will discuss the problem of coupling the FIR laser

radiation to the samples and the particular method we used. We will end the chapter with a brief description of the FIR laser system, its operation, and performance.

3.2 Sample Fabrication

3.2.1 Mask Fabrication--Commercial Masks

The first set of samples were made using a mask fabricated by a local firm (Advance Reproductions, North Andover, MA). This mask was used in a contact printing procedure to produce photoresist stencils, which in turn were utilized in the thin film evaporation/oxidation sequence used to fabricate the actual samples.

The mask made by Advance Reproductions contained the patterns for a set of tunnel junctions at the centers of superconducting strips of varying lengths, designed to study the non-equilibrium effects in the superconducting strips created by the presence of the high-current density tunnel junction at its center. The mask can be best described by imagining viewing it under a microscope as the magnification is increased. With no magnification six strips of chrome 0.3 mm wide and 4.8 mm long are seen. There are four notches on five of the strips and five notches on one of them. Three of the long strips contain tunnel junction patterns, while the other three have long microbridge patterns. A close-up of a notch area of the strip (the white areas between the two large dark areas) with five notches is shown in Fig. 3.1(a). The dark areas in Fig. 3.1 are covered by chrome, while the white areas are

clear on the mask. The central portion of Fig. 3.1(a) is magnified in Fig. 3.1(b). The region of the Figure with the small white tab and the small black bridge defines where the tunnel junction will be in the completed sample. Fig. 3.1(c) displays a pattern for a tunnel junction at the center of a superconducting strip, taken with the same magnification as Fig. 3.1(b). A long microbridge pattern is shown in Fig. 3.1(d). This mask was made using an Electromask Pattern Generator/Image Repeater system. The desired sample geometry was decomposed into a set of rectangles of varying center positions (x,y) and widths and heights (w,h) . The widths and heights of these rectangles had to be greater than a minimum value of $5\text{ }\mu\text{m}$, and less than a maximum value of 1.5 mm . These limits on the rectangle dimensions depended on the particular pattern generator we used. Large areas which were to be clear on the mask were then decomposed into many rectangles of this maximum size. The results of this procedure, the set of numbers (x,y,w,h) for the whole pattern, were recorded on 9 track, 800 bpi (bits per inch) tape in Extended Binary Coded Decimal Interchange Code (EBCDIC).⁴⁸ This tape was produced at Lincoln Labs using the pattern generating software available there.

The pattern generator works by taking a soda-lime glass substrate coated with chrome and photoresist and projecting rectangles of varying widths and heights onto it at locations defined by the (x,y) coordinates on the tape by using a precision x-y translation stage.⁴⁹ The resulting mask, after developing the photoresist and etching the chrome, was a $10\times$ mask (or reticle) if the minimum dimensions for the final mask were to

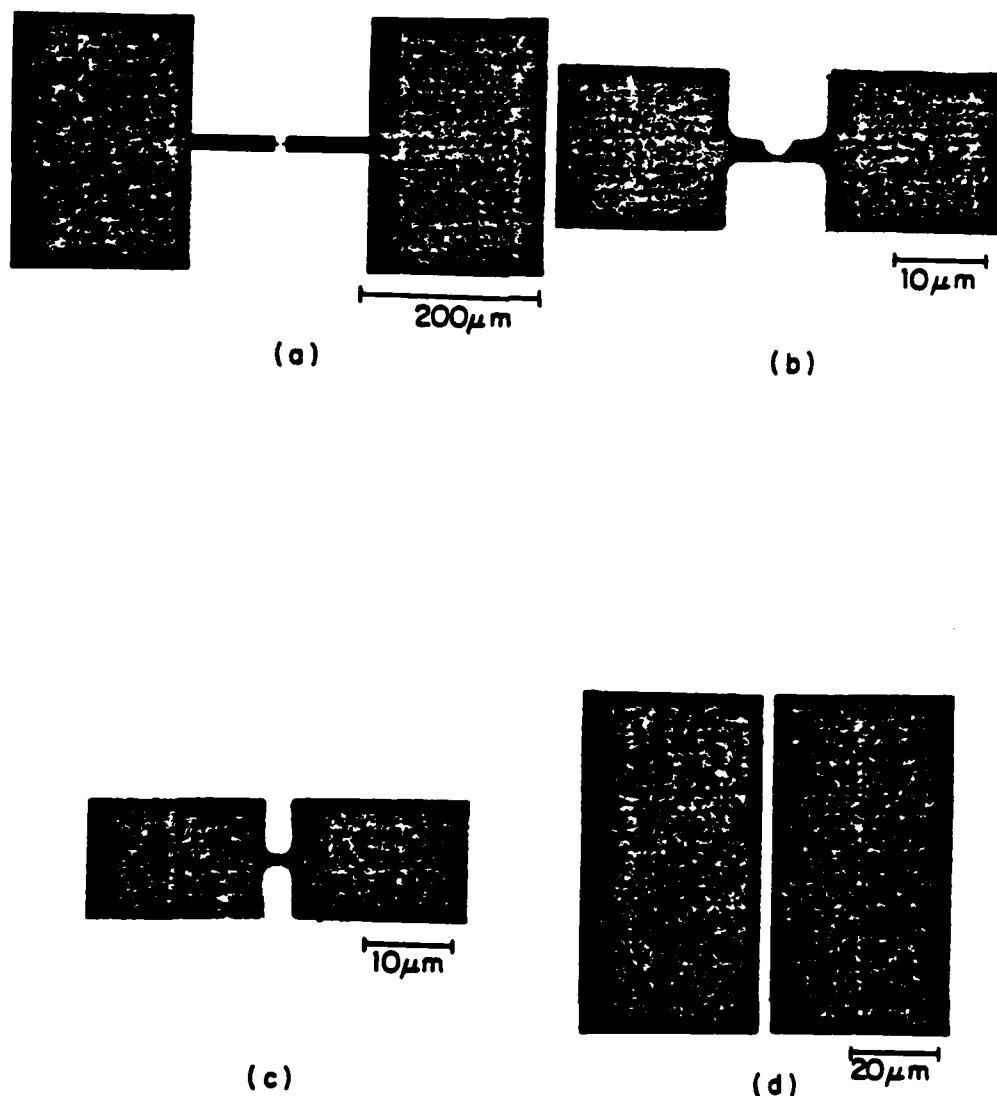


FIG. 3.1 (a) Section of the commercial mask containing a tunnel junction pattern and a pad pattern. See text for details. The black regions have Cr on them in the mask. (b) A close-up of the central region of (a) showing the tunnel junction pattern, the narrow black region in the center will be used to make the photoresist bridge which is used to form the junction. (c) Another section of the mask, this time with a tunnel junction pattern with long leads. (d) Section of mask containing a long microbridge pattern. The width of the white line is only $\sim 2\mu\text{m}$.

be below 5 μm . Otherwise this mask would have been the master mask. The minimum final dimension we used was 2 μm , so we had the reticle projected (and reduced by 10 in size) onto another photomask blank to produce the final master mask. We made working copies by contact printing from this master mask. These copies were later discarded when damaged.

The mask fabrication procedure outlined above is commonly used in the present day electronics industry. Because of the need to produce a magnetic tape, which requires considerable software, and because of the high cost per mask, we developed a method for making our own masks at Harvard. Our method is based on relatively simple techniques that were used in the electronics industry in the 1960's but which were abandoned after the invention of reliable computer-controlled pattern-generating equipment.

3.2.2 Mask Fabrication at Harvard

All of the fabrication work at Harvard, reported here below, was performed in a clean room in which all personnel using the room were required to wear disposable talc-free gloves, and lint-free gowns. All the photolithographic work was performed under laminar-flow hoods. Surfaces not under these hoods, which could collect dust and grease, were wiped off with ethanol before work was begun every day.

Masks were fabricated at Harvard by a sequence of steps outlined in Fig. 3.2. We began with sheets of clear acetate upon which pieces of

Mask Fabrication Procedure

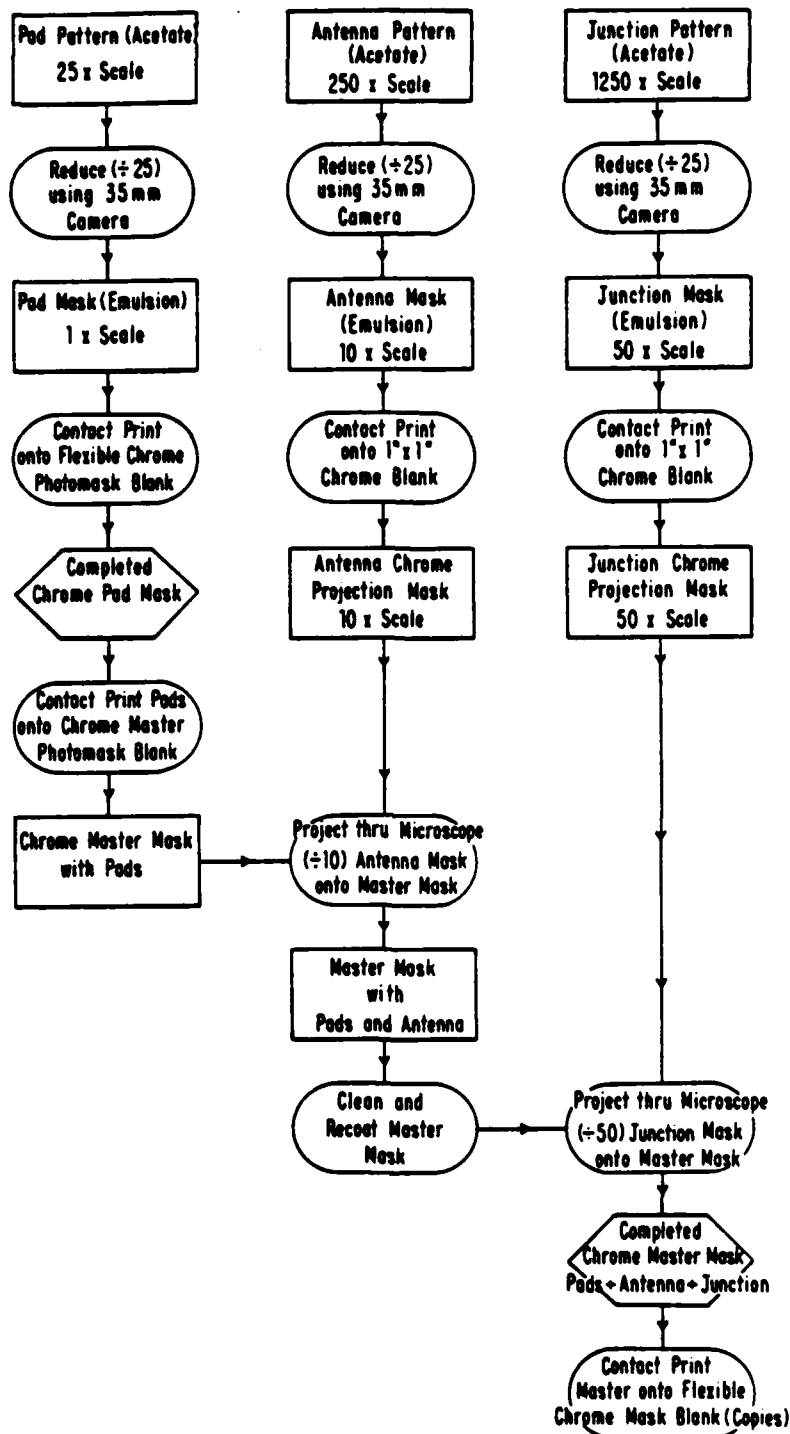


FIG. 3.2 Illustration of the sequence of steps used to make a mask. The rectangular boxes indicate intermediate products, circular-edged boxes display a process, while the boxes with triangular corners show completed products.

black tape were placed where we wanted metal in the completed sample. Three sets of acetate sheets were used because the field of view of the microscope diminishes as the magnification is increased. For the largest areas on the sample, a 25x scale pattern was made for the pad mask. A second acetate sheet plus tape pattern, prepared at a 250x scale, defined the FIR antenna and dc connections to the pads. The third pattern was at a 1250x scale and contained the junction and its connection to the antenna.

The patterns prepared in this way were taped to a lightboard which illuminated them from the back in order to produce the highest possible contrast between the light and dark areas on the pattern. The patterns were then photographed with a high quality 35 mm camera on high-contrast fine-grained Kodak Kodalith Ortho film type 6556. The resulting film (emulsion mask) had the features of the original acetate patterns but reduced in size by a factor of 25. The pad mask was therefore at its final size and was contact printed onto a photoresist plus chrome coated flexible photomask blank (dimensions 2"x2"x0.010"). This mask in turn was used to contact print the pad pattern onto a thicker chrome photomask blank (2.5"x2.5"x0.060") which after a few more steps became the master mask. The emulsion pad mask could be contact printed directly onto the master mask blank; however, the life of the emulsion mask was extended because it was only used occasionally, i.e. when it was contact printed onto the flexible mask blank.

The 10x antenna emulsion mask and 50x junction emulsion mask were contact printed onto 1"x1"x0.030" projection mask blanks. These

projection masks fit onto the x-y stage of the projection attachment⁵⁰ to the lab's Zeiss Universal Microscope. After the pads were contact printed onto the thick photomask blank, the antenna mask pattern was projected onto the pad mask at the proper location; the exposed mask was then developed and etched. Because the widths of the developed regions increased with continued development, we found that stripping the mask of the old photoresist and recoating with 0.3 μm thick photoresist produced the best results. Using this freshly recoated mask with the pads plus antenna, the junction was next projected onto the center of the antenna region. If the junction area looked good after the development, the mask was etched. This mask was copied onto thin flexible photoresist coated chrome photomask blanks. These flexible masks in turn were used to produce the photoresist stencils which were used to make the tunnel junctions.

3.2.3 Photoresist Stencils

Photoresist stencils were fabricated following the procedure of Dolan⁴⁴ and Dunkleberger⁴⁵. Initially 1.5 μm of Shipley AZ 1350J photoresist⁵¹ was spun at 5500 RPM onto a clean 1"x0.5"x0.010" thick z-cut crystal quartz substrate. The substrates were then baked in a hot plate oven for 25 \pm 5 minutes at 80°C. After cooling for 10-15 minutes in the laminar flow hood, the substrates were exposed to UV light for 2.5-3.0 minutes at a distance of 2' from the 200 watt high pressure mercury UV light source. Following this, a thin ($\sim 500 \text{ \AA}$) layer of aluminum was evaporated onto the photoresist. Finally a layer of 1.0 μm

thick Shipley AZ 1370 photoresist was spun onto the photoresist/aluminum sandwich and baked at $\sim 70^{\circ}\text{C}$ for 20 ± 5 minutes. The resulting photoresist/aluminum/photoresist sandwiches were stored in tightly sealed sample storage boxes until needed for the photoresist stencils.

The photoresist coated substrates were now ready for the exposure and development sequence, summarized in Fig. 3.3. The substrates were placed in a vacuum contact printing holder consisting of a piece of 0.5" thick plexiglass with a slot milled to a depth of 0.001" beyond the sample thickness. Holes were machined in the plexiglass to connect this slot to a vacuum port. A flexible chrome mask was placed chrome side down on the substrate, a vacuum valve was opened and the flexible mask was then pressed down against the photoresist by atmospheric pressure⁵². The sample/holder combination was then placed 2' away from the UV light source and exposed for ~ 90 seconds. The top layer of photoresist was then developed for 30-60 seconds in high resolution photoresist developer (5 parts water to 1 part Shipley AZ 351 developer), and rinsed with distilled water. Next the aluminum layer was etched. Finally the bottom layer of photoresist was developed for a few seconds beyond the point at which it was clear that all the photoresist had been developed away from the substrate. (The bottom layer of photoresist could be seen where it had been exposed to the developer by the etching of the Al layer.) This procedure resulted in a $\sim 5 \mu\text{m}$ undercut all around the edges of the photoresist and produced the overhanging photoresist bridge used in making the junctions. SEM micrographs of undercut resist profiles are shown in Fig. 3.4. Fig. 3.4(a) displays a photoresist

Photoresist Exposure/Development Sequence

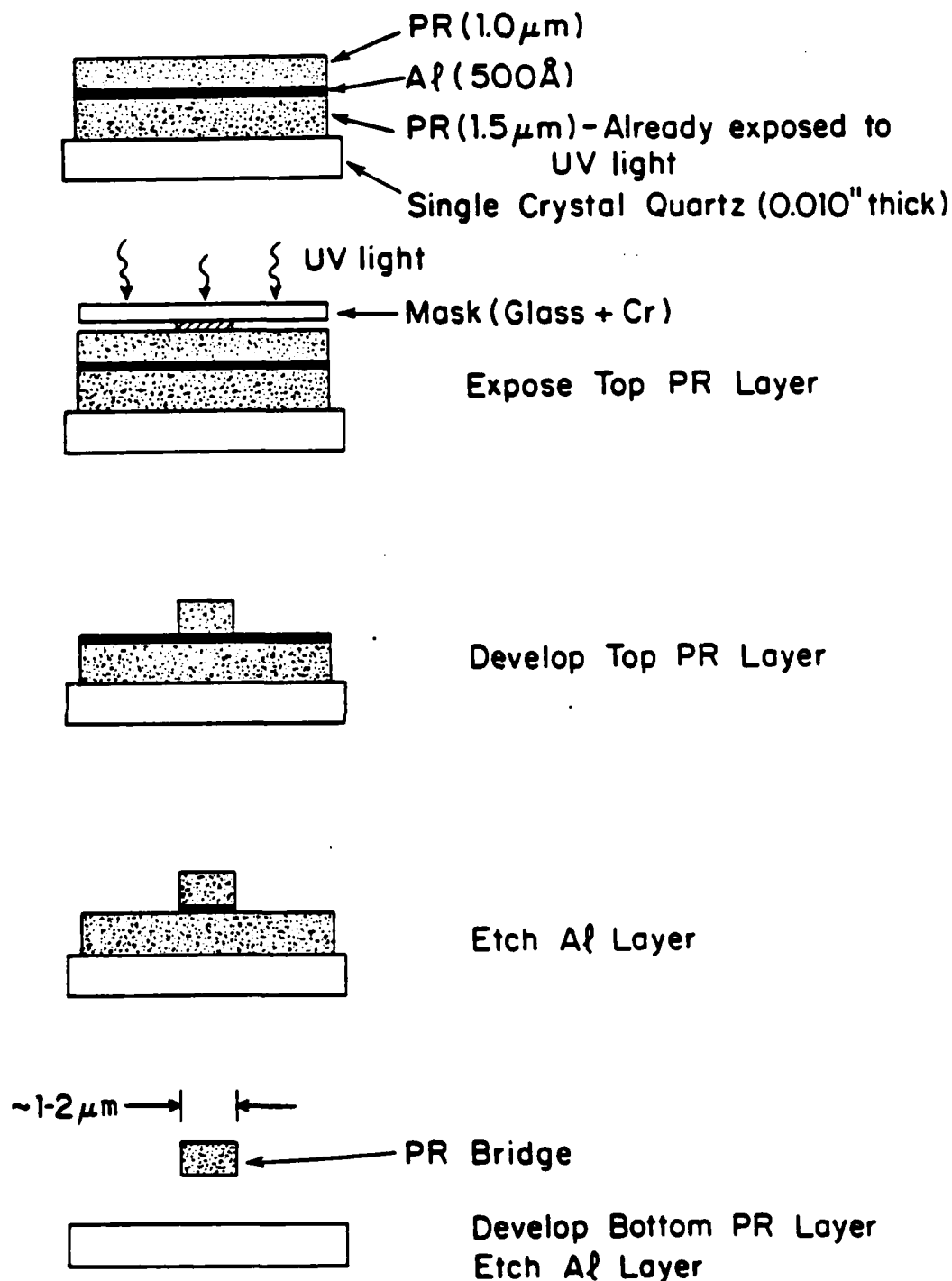


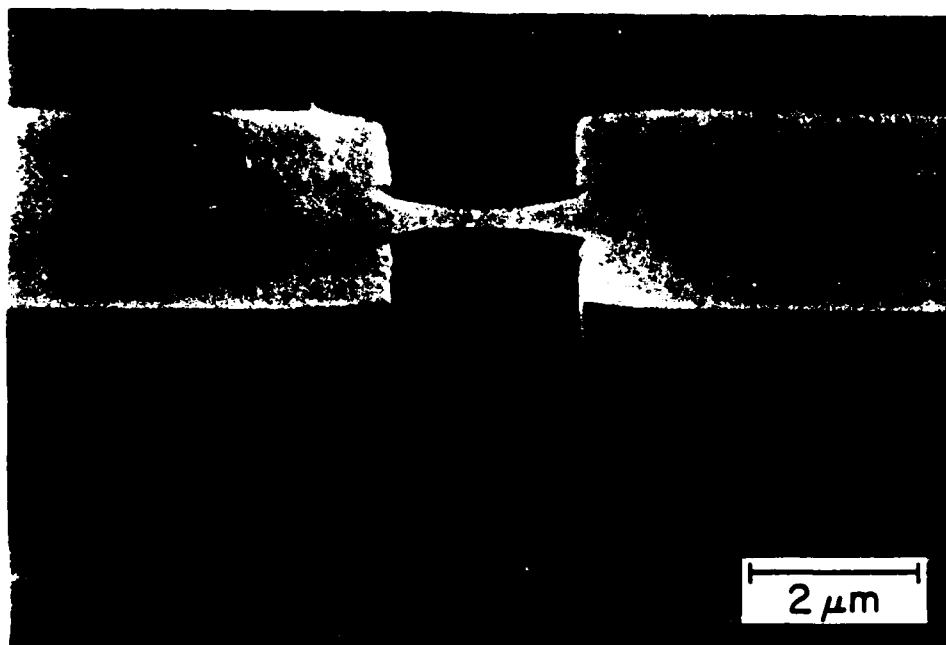
FIG. 3.3 Photoresist exposure/development procedure beginning with the photoresist/ Al/photoresist trilayer and ending with the suspended photoresist bridge which is used to make the junction.

bridge fabricated using the commercial mask described in Section 3.2.1, and schematically displayed in Fig. 3.1(c). A photoresist bridge used in fabricating tunnel junction at the center of a dipole antenna is shown in Fig. 3.4(b). This micrograph was taken with the SEM stage at an $\sim 80^\circ$ tilt, viewed along the antenna axis. Going off to the left are the parts of the stencil used to make the dc leads. Note the vertical sidewalls indicating good contact was made between the mask and the photoresist.

3.2.4 Junction Evaporation/Oxidation Sequence

There are three ways to make tunnel junctions using the overhanging photoresist bridge shown in Fig. 3.4. The first technique was developed at Bell Labs by Dolan⁴⁴ and Dunkleberger⁴⁵. We call their original technique the "overlap" technique. This sequence begins with the deposition of the base electrode material (Sn) at an angle to the substrate normal ($+55^\circ$), followed by a glow discharge of the base electrode, and ends with the evaporation of the counter electrode (Pb) at an angle of -50° . For this evaporation sequence, substrates were placed on a rotatable sample holder which was cooled to liquid nitrogen temperature in a cryopumped evaporator at a base pressure of 2×10^{-7} torr. The base electrode (always Sn) was oxidized by a dc glow discharge in 99.9999% pure oxygen at a pressure of 30 mtorr for 30-60 seconds with 12 mA of current at 1.1 kV. Fig. 3.5(a) shows schematically the evaporation sequence, while Fig. 3.5(b) displays an SEM micrograph of a sample made with this procedure. Typically this

FIG. 3.4 (a) SEM micrograph of a photoresist bridge suspended over a polished sapphire substrate, made with the mask in Figure 3.1(c), following the procedure of Fig. 3.3 . The micrograph was taken with a $\sim 80^\circ$ tilt on the SEM stage. (b) SEM micrograph of a suspended photoresist bridge used in fabricating a small-area junction at the center of a dipole antenna. The micrograph was taken with an $\sim 80^\circ$ tilt on the SEM stage; the view is from along the antenna axis. DC leads will be on the left in the completed sample.



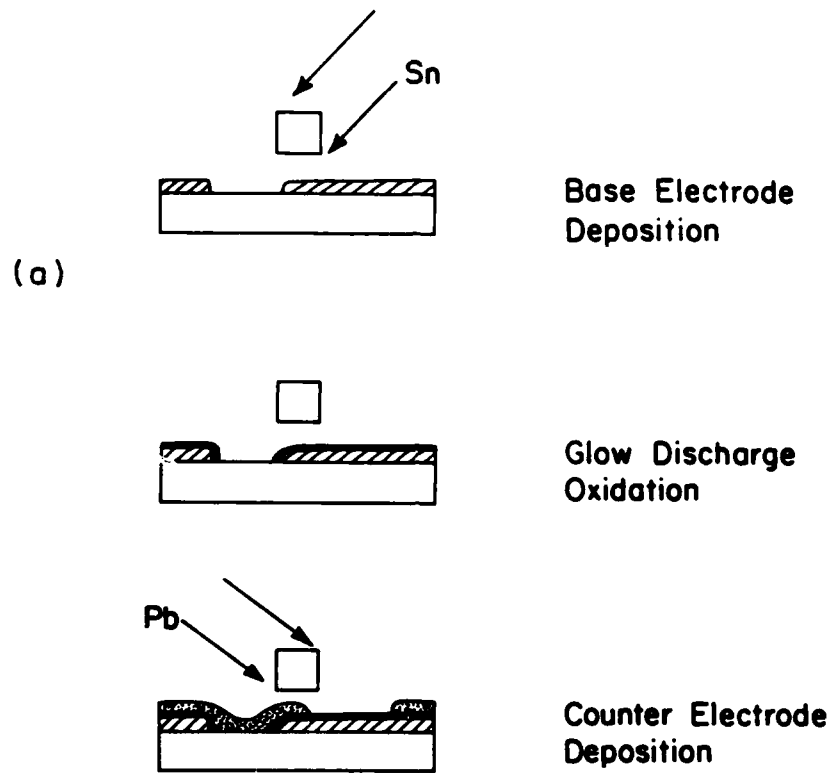
(a)



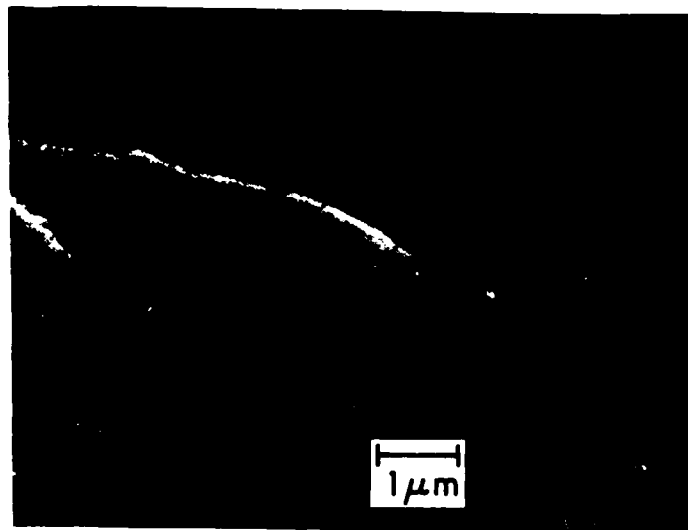
(b)

FIG. 3.5 (a) Evaporation/oxidation steps for Sn-SnO-Pb overlap junctions. (b) SEM micrograph of a junction made with this procedure. The lighter colored metal on the left is Pb, while the darker metal on the right is Sn.

Overlap Junction Technique



(b)



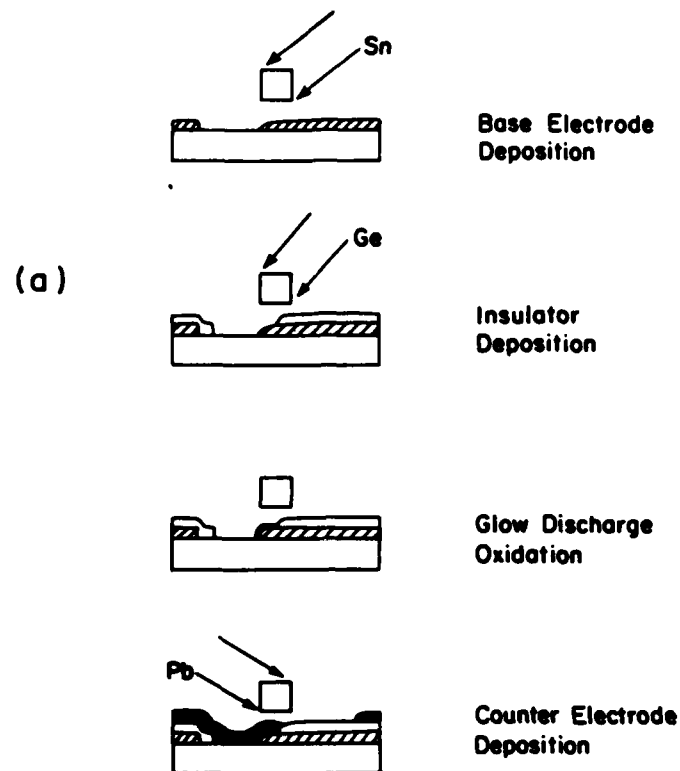
technique produces junctions with areas from $2\text{-}10\ \mu\text{m}^2$.

There are two variants on this method, developed by Howard et al.⁴⁶ which can produce junctions with somewhat smaller areas. These two variants are called the "resist-aligned" scheme, shown schematically in Fig. 3.6(a), and the "edge-aligned" scheme, shown in Fig. 3.7(a). In the resist-aligned sequence, the area of the junction is reduced from that of the overlap junction by the deposition of an insulating layer of Ge after the base electrode deposition at an angle ($\sim 42^\circ$ for example) which is slightly less than the angle of the base electrode deposition. In Fig. 3.6(b) we see an SEM micrograph of a junction produced this way. The final variant of the overlap technique, the edge-aligned technique, begins with the evaporation of Sn at normal incidence. The Ge layer is evaporated at an angle such that it breaks over the Sn edge; the junction is glow discharge oxidized as before, and the Pb counter electrode is evaporated at a shallow angle to insure it touches the Sn-SnO surface. In Figure 3.7(b) we display an SEM micrograph of a sample produced using this scheme. We clearly see that the Ge broke over the Sn edge and was deposited on the substrate surface.

The smallest area junctions produced by optical lithography are those made using the edge-aligned technique. These could have areas as small as $\sim 0.2\ \mu\text{m}^2$ or $\sim 2 \times 10^{-9}\ \text{cm}^2$ with the $\sim 2\ \mu\text{m}$ minimum linewidth lithography we use. Unfortunately, we were not able to make many good samples using this technique. In fact, almost all of the junctions tested in the FIR were fabricated using the resist-aligned scheme. Areas ranged from $0.5\text{-}2.5\ \mu\text{m}^2$ with resistances from $16\text{-}380\ \Omega$ for these

FIG 3.6 (a) Evaporation/oxidation procedure for resist-aligned junctions. (b) SEM micrograph of a sample made with this procedure. The bright metal is Pb, while the material between the two Pb tips is Ge. Under the Pb in the lower part of the photo is the tunnel junction. On the left are the dc leads.

Resist-Aligned Junction Technique



(b)

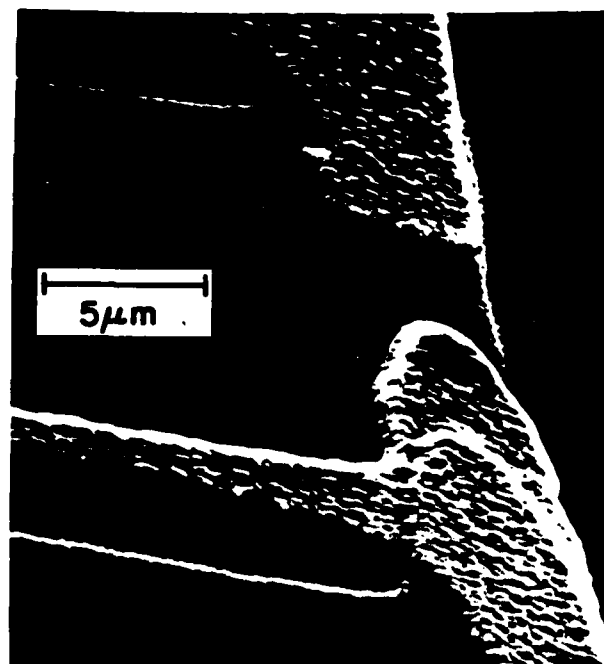
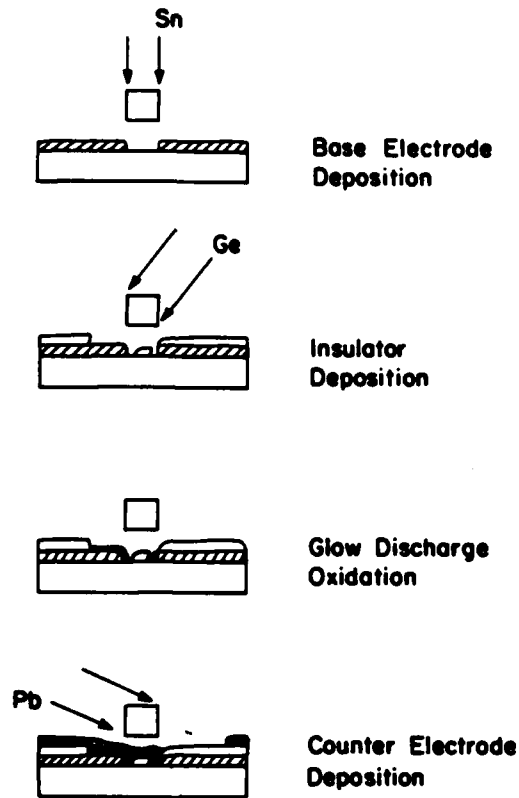


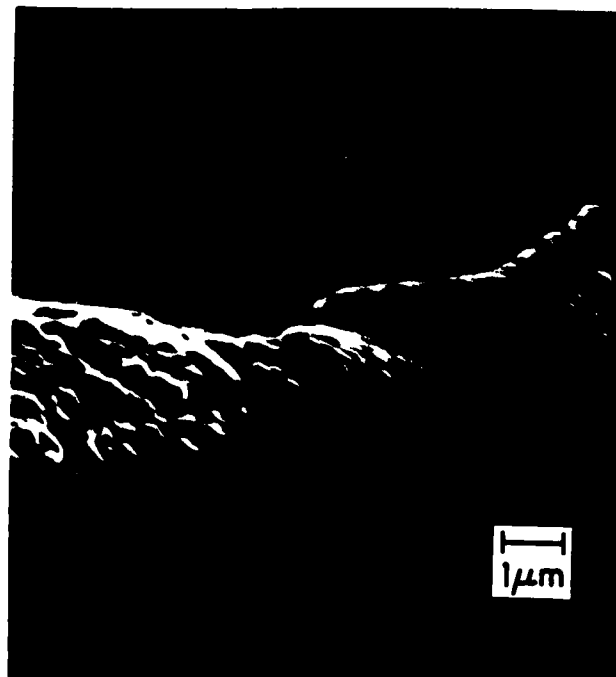
FIG. 3.7 (a) Evaporation/oxidation procedure for edge-aligned junctions. (b) SEM micrograph of junction made with this procedure. On the left is the Pb layer contacting the SnO on the edge of the Sn layer. The Ge layer is on the substrate, underneath the Pb, but close to the Sn layer, and the Ge is also on the surface of the Sn.

Edge-Aligned Junction Technique

(a)



(b)



resist-aligned junctions.

Unfortunately, good junctions alone do not couple significantly to submillimeter laser radiation. In the next section we will describe the design of the dipole antenna used to couple the Gaussian free space output mode of the FIR laser to the junction.

3.3 Antenna Coupling to the FIR Laser Source

3.3.1 Introduction

Thin film tunnel junctions, unlike point contacts, can be reliably made and can have excellent thermal cycling characteristics and stability. Unfortunately, the dielectric substrate, essential to planar microfabrication technology, makes coupling a FIR laser gaussian output mode to the junction much more difficult than coupling it to a point contact. A point contact makes a good long wire antenna by virtue of the fact that it is a long (~ 5 mm), thin (~ 75 μ m) wire sharpened at the tip in contact with a metal ground plane. This natural antenna produces an antenna pattern, cylindrically symmetrical about the wire axis, with its maximum at a polar angle close to that axis.^{53,54} The output mode of a FIR laser can couple quite efficiently to such an antenna pattern.⁵⁵

The simplest antenna structure one could fabricate on a dielectric substrate is a dipole antenna. In fact, planar dipole antennas were fabricated for the 337 μ m HCN FIR laser line by Javan's group in 1974.⁵⁶ Using a Ni-oxide-Cr thin film diode at the center of a dipole antenna, they were able to detect the HCN laser radiation using the non-linearity of the diode I-V curve. Gradually shortening the length of the antenna by trimming it with a diamond knife, they found its resonant length to be $(\sim 1/3)\lambda$ instead of $(\sim 1/2)\lambda$ as would be expected; the difference is due to the presence of the dielectric substrate.⁵⁶

Since the pioneering work of Javan's group there have been several other attempts at coupling FIR radiation efficiently to antennas on dielectric substrates.⁵⁷⁻⁶² Besides dipole antennas, other groups have constructed slot antennas⁵⁸, V antennas⁵⁹, bow-tie antennas⁶⁰, long-wire antennas⁶¹, and dielectric antennas⁶². For the purposes of this work it is necessary to discuss only dipole antennas, since that was the only configuration used. In the final chapter we will describe the possible advantages of bow tie antennas for certain kinds of experiments. The discussion of antennas which follows here is separated into three parts. The first reviews microwave modelling experiments on dipole antennas on thin substrates. In the second section the radiated power pattern of a current element on a thick substrate is derived and theoretical results on the power pattern of a resonant dipole on thick substrates of different dielectric constants are presented. The final part of this section presents our design for the dipole antenna and the electroformed copper horn which focusses the laser radiation onto the antenna.

3.3.2 Dipole Antennas on Thin Substrates

For a dielectric substrate of thickness t , relative dielectric constant ϵ_r , and electromagnetic radiation of wavelength λ , the dimensionless effective thickness of the substrate t_{eff} is defined by the relation:

$$t_{\text{eff}} = \frac{\sqrt{\epsilon_r} t}{\lambda} \quad (3.0)$$

We use MKS units, with the dielectric constant written as $\epsilon = \epsilon_r \epsilon_0$,

ϵ_0 is the permittivity of free space, and ϵ_r is the relative dielectric constant. Mizuno, Daiku, and Ono⁶³ performed a microwave modelling experiment at 10 GHz for the case where $t_{\text{eff}} < 1$. Their main results are summarized in Fig. 3.8. If α is defined to be the resonant length of a dipole antenna on the dielectric substrate divided by its resonant length in free space, then α decreases for increasing effective thickness, t_{eff} , for a given value of ϵ_r up to $t_{\text{eff}} = 0.15$. This result is shown in Fig. 3.8(a) for several values of ϵ_r , up to an effective thickness of $t_{\text{eff}} = 0.6$. The reduction factor α was found to be constant for $t_{\text{eff}} > 0.15$, for a given ϵ_r , and these values of α are plotted against ϵ_r in Fig. 3.8(b). The antenna power pattern was also measured, Fig. 3.8(c), for the E-plane and H-plane. (The E-plane is the plane defined by the electric field vector, and the vector from the center of the dipole to the maximum of the power pattern. The H-plane is defined analogously.⁶⁴) Note that the E-plane power pattern differs only somewhat from that of a dipole in free space, having only ~30% more power directed into the substrate, at the maximum perpendicular to the substrate, than in the free space case. The H-plane pattern, however, departs strongly from the cylindrical symmetry of the free-space dipole pattern, having considerable power radiated into the plane of the substrate. Here, the waves are trapped as surface waves by total internal reflection at the substrate interfaces.

3.3.3 Power Patterns of Current Elements and Dipoles

Rutledge and Muha⁶⁵ have calculated the power pattern of a current element on a dielectric half-space, using a physical argument based on

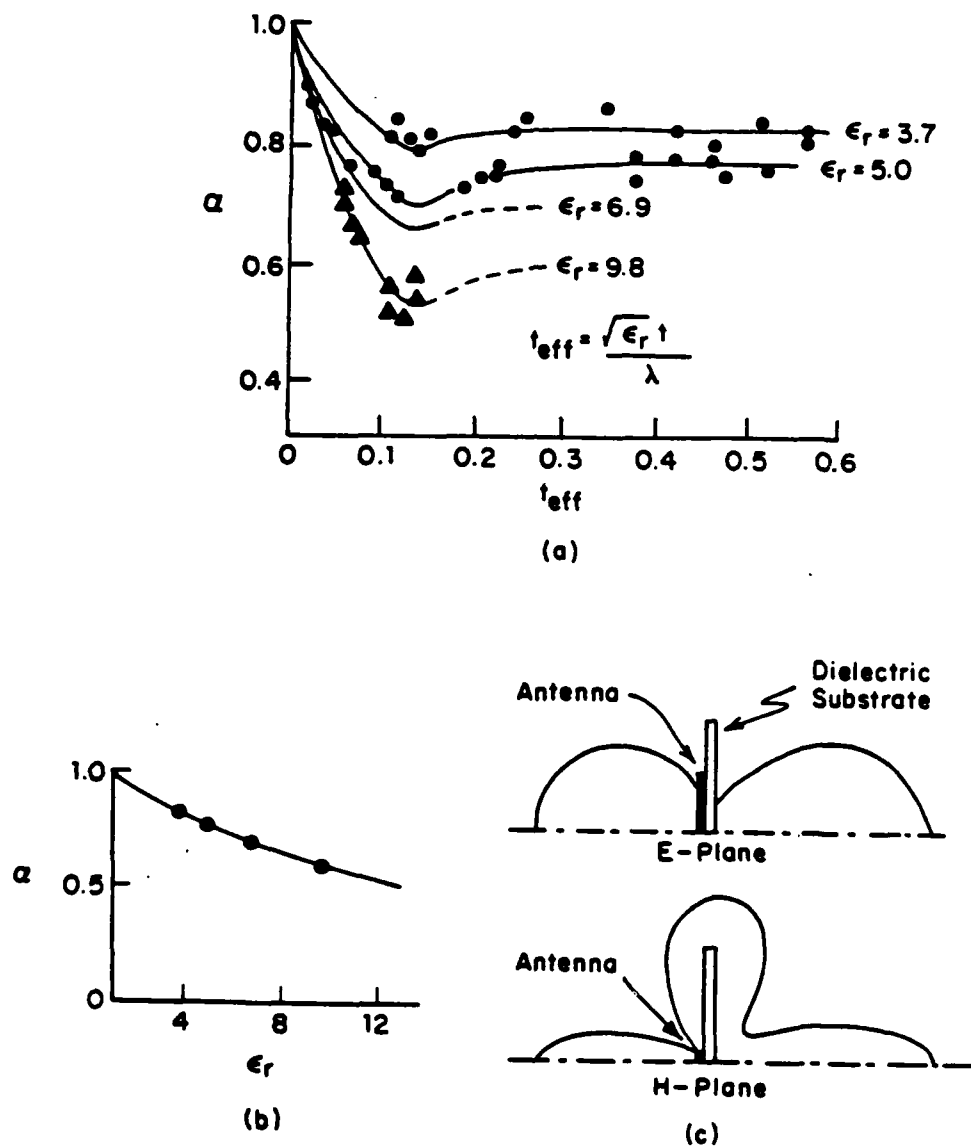


FIG. 3.8 (a) Reduction factor, α , as a function of the effective thickness, t_{eff} , for different values of ϵ_r . (b) Values of α for $t_{\text{eff}} > 0.15$ for the values of ϵ_r in (a). (c) E-plane and H-plane antenna patterns for a dipole antenna on a thin substrate. [Adapted from Ref. 63.]

the Lorentz reciprocity theorem.⁶⁶ They showed that the current element radiates much more strongly into the dielectric than into air (or vacuum). The discussion which follows is closely based on the analysis of Rutledge and Muha (Ref. 65), and analyses presented in Refs. 66-67. The reader is urged to study these articles for a more complete analysis than is presented here. Readers who prefer to forgo the discussion presented here are urged to skip to the answers, Eqs. (3.3)-(3.7), which are plotted in Fig. 3.9(b).

The Lorentz reciprocity theorem, as stated by Ballantine, applies to the situation of two antennas, A_1 and A_2 , located at positions O_1 and O_2 , respectively, and having arbitrary orientations. Consider first A_1 to be a transmitting antenna and A_2 a receiving antenna, and assume that A_1 transmits with some average power P . If A_2 is considered to be a transmitting antenna and A_1 a receiving antenna, and A_2 transmits with the same average power P , as A_1 did previously, then the phase and intensity of the electric field at the receiver A_1 is the same as that produced before at A_2 , when A_2 was the receiver and A_1 was the transmitter. This result is independent of the electrical properties of the intervening media, i.e. conductivity, inhomogeneity, stratification, and so on. It is also independent of the specific forms of the antennas.⁶⁶

This theorem is particularly useful in cases where it is desired to calculate the far-field power pattern of a transmitting antenna, in a

situation where a direct calculation is difficult due to the presence of ground planes or dielectric discontinuities located near the antenna. The antenna could then be considered as a receiving antenna, and the electric field at the antenna produced by the far-field (essentially plane wave) power pattern of another antenna could be calculated. From this electric field the power pattern can be calculated.

This theorem can be applied to the situation of a current element at an air (or vacuum)/dielectric interface, shown in Fig. 3.9(a). We wish to calculate the far-field pattern of the current element situated at the dielectric interface, I_1 . We calculate the pattern for the plane perpendicular to the current element axis, i.e. the H-plane. The current element, I_1 , produces an electric field E_1 , in the far-field at an angle θ_a . In order to calculate the power pattern, we consider the current element I_1 as a receiver, and compute the electric field E_2 at I_1 from the current element I_2 located at E_1 . The reciprocity theorem stated above says that if the two currents I_1 and I_2 are equal then the electric fields E_1 and E_2 are equal. The variation of E_2 with angle θ_a gives the power pattern (for the H-plane) in the air. If I_2 were placed deep inside the dielectric, the reciprocity theorem could be used in a like manner to compute the H-plane pattern in the dielectric.

In order to get an intuitive understanding of the problem, consider a plane wave incident on the dielectric from the air at normal incidence, $\theta_a = 0$. θ_d is the angle of refraction. If n is the index of refraction of the dielectric, then the ratio of the transmitted electric field to that of the incident field is $2/(n+1)$. For large n this ratio

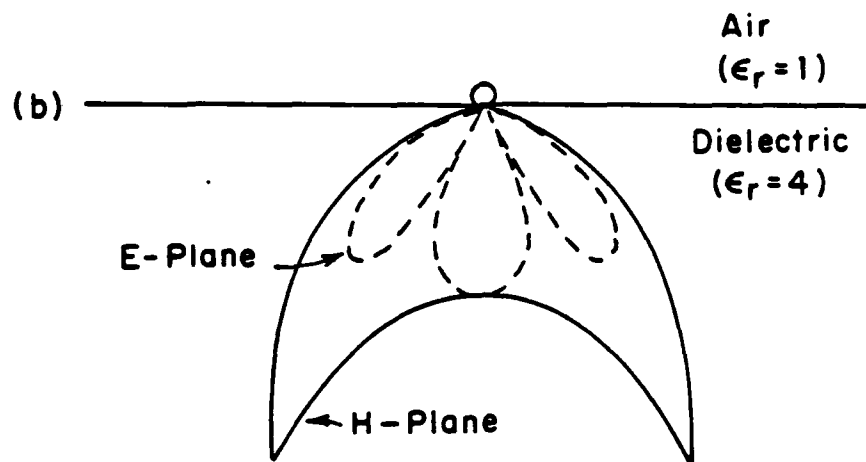
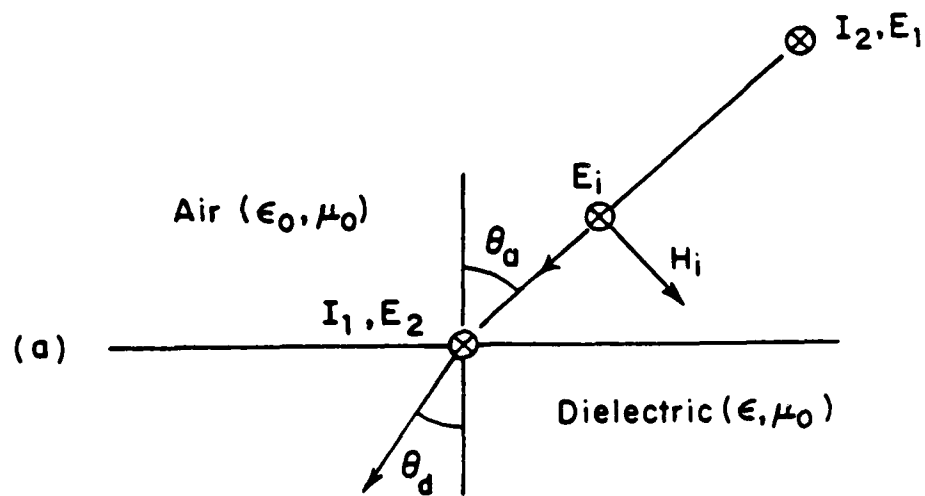


FIG. 3.9 (a) Current element at an air-dielectric interface. (b) E-plane and H-plane power patterns from this current element. [Adapted from Ref. 65.]

is $\sqrt{2}/n$ and is small. If the plane wave were incident from the dielectric side of the interface, the ratio of the transmitted electric field to the incident electric field is large, $\sqrt{2}n/(n+1)$, or for large n the ratio is $\sqrt{2}$. The average power density of the waves is given by the Poynting vector $\langle \vec{S} \rangle = (1/2) \text{Re}(\vec{E} \times \vec{H})$, which becomes $S = (1/2) Z^{-1} |E|^2$, where $Z = (\mu/\epsilon)^{1/2}$, the wave impedance of the medium. For most dielectrics, $\mu = \mu_0$, and $\epsilon = \epsilon_r \epsilon_0$, so that $Z = (\epsilon_r)^{-1/2} Z_0 = Z_0/n$ using $n = (\epsilon_r)^{1/2}$, and $Z_0 = (\mu_0/\epsilon_0)^{1/2} = 377 \Omega$ the wave impedance of free space.

The transmitted electric fields, by the reciprocity theorem, are equal to the radiated far-fields produced by the current element at the interface when it is considered as a transmitting antenna. Therefore, the power density in the far-field on the air side is $S_a = (1/2Z_0) |E_i|^2 (2/n)^2$ where E_i is the incident electric field, whereas on the dielectric side the power density is $S_d = (n/2Z_0) |E_i|^2 2^2$. The ratio of the far-field power density in the dielectric to that of the power density in the air is $S_d/S_a \approx n^3/1$. The antenna at the interface radiates much more power into the dielectric than the air.

This argument can be generalized to angles other than the substrate normal. Rutledge and Muha have done this; we will briefly sketch their calculation for the power pattern on the air side. The electric field E_2 at the substrate interface at I_1 is calculated assuming I_2 is the radiator (transmitter). The incident electric field is

$$E_i = \frac{j \omega \mu_0 h}{4\pi r} e^{-jk_0 r} \quad (3.1)$$

where h is the length of the current element. The field E_2 is the

incident electric field E_i times the transmission coefficient τ , for the electric field perpendicular to the plane of incidence

$$\tau = \frac{2 \cos \theta_a}{\cos \theta_a + n \cos \theta_d} \quad (3.2)$$

Note for $\theta_a=0$, $\theta_d=0$, the transmission coefficient becomes $\tau=2/(n+1)$, the transmission coefficient for normal incidence discussed above. As in the previous discussion, reciprocity says that the electric field E_2 at I_1 due to I_2 is equal to the field E_1 at I_2 is $I_1=I_2$. The power pattern of I_1 is $S_a(\theta_a)=(1/2Z_0)|E_1|^2=(1/2Z_0)|E_i\tau|^2$. If we define $\beta=(2/Z_0)[\omega\mu_0 I_h/4\pi r]^2$; then

$$S_a(\theta_a) = \beta \left(\frac{\cos \theta_a}{\cos \theta_a + n \cos \theta_d} \right)^2 \quad (3.3)$$

is the H-plane pattern in the air. For the H-plane pattern in the dielectric, θ_d becomes the angle of incidence, θ_a is the angle refraction, so that the transmission coefficient τ is now given by:

$$\tau = \left(\frac{2n \cos \theta_d}{\cos \theta_a + n \cos \theta_d} \right) \quad (3.4)$$

The power density is $S_d(\theta_d)=(n/2Z_0)|E_i\tau|^2$ where τ is given by Eq. (3.4) and E_i as in Eq. (3.1). The power pattern is

$$S_d(\theta_d) = \beta n \left(\frac{n \cos \theta_d}{\cos \theta_a + n \cos \theta_d} \right)^2 \quad (3.5)$$

in the dielectric.

The E-plane patterns can be calculated in a similar manner, and we simply state the results. Rutledge and Muha found

$$S_a(\theta_a) = \beta \left(\frac{\cos \theta_a \cos \theta_d}{n \cos \theta_a + \cos \theta_d} \right)^2 \quad (3.6)$$

for the E-plane pattern in the air, and

$$S_d(\theta_d) = \beta n \left(\left| \frac{n \cos \theta_a \cos \theta_d}{n \cos \theta_a + \cos \theta_d} \right|^2 \right) \quad (3.7)$$

for the E-plane pattern in the dielectric. Equations (3.3), (3.5), (3.6), and (3.7) are plotted in Fig. 3.9(b) for $n=2$, the index of fused quartz. Note that no power is radiated along the plane of the substrate in this case since it was assumed the substrate was infinitely thick. There is a null in the power pattern at the interface, implying a weak coupling between antennas if they were made into arrays.

The power patterns for resonant dipoles on thick substrates have been calculated and measured by Brewitt-Taylor and Rees⁶⁷, and are only slightly different from the patterns for the current element. Figs. 3.10(a) and 3.10(b) display their calculated patterns for the H-plane and E-plane, respectively for two different dielectric constants. The major difference between the calculated patterns for the dipole as compared to the current element is that in the E-plane pattern, the dipole has a slightly larger central lobe than the current element (for the $\epsilon_r = 4$ case the only one we could use for direct comparison from the figures). Brewitt-Taylor and Rees also note that the resonant frequency follows roughly as \bar{n}^{-1} from that of the free space dipole, where $\bar{n} = [(\epsilon_r + 1)/2]^{1/2}$, consistent with the resonant length measurements of Mizuno Daiku, and Ono.⁶³ The peak admittance is proportional to \bar{n} , results consistent with the microwave modelling measurements of Rutledge and Muha on bow-tie antennas.⁶⁵

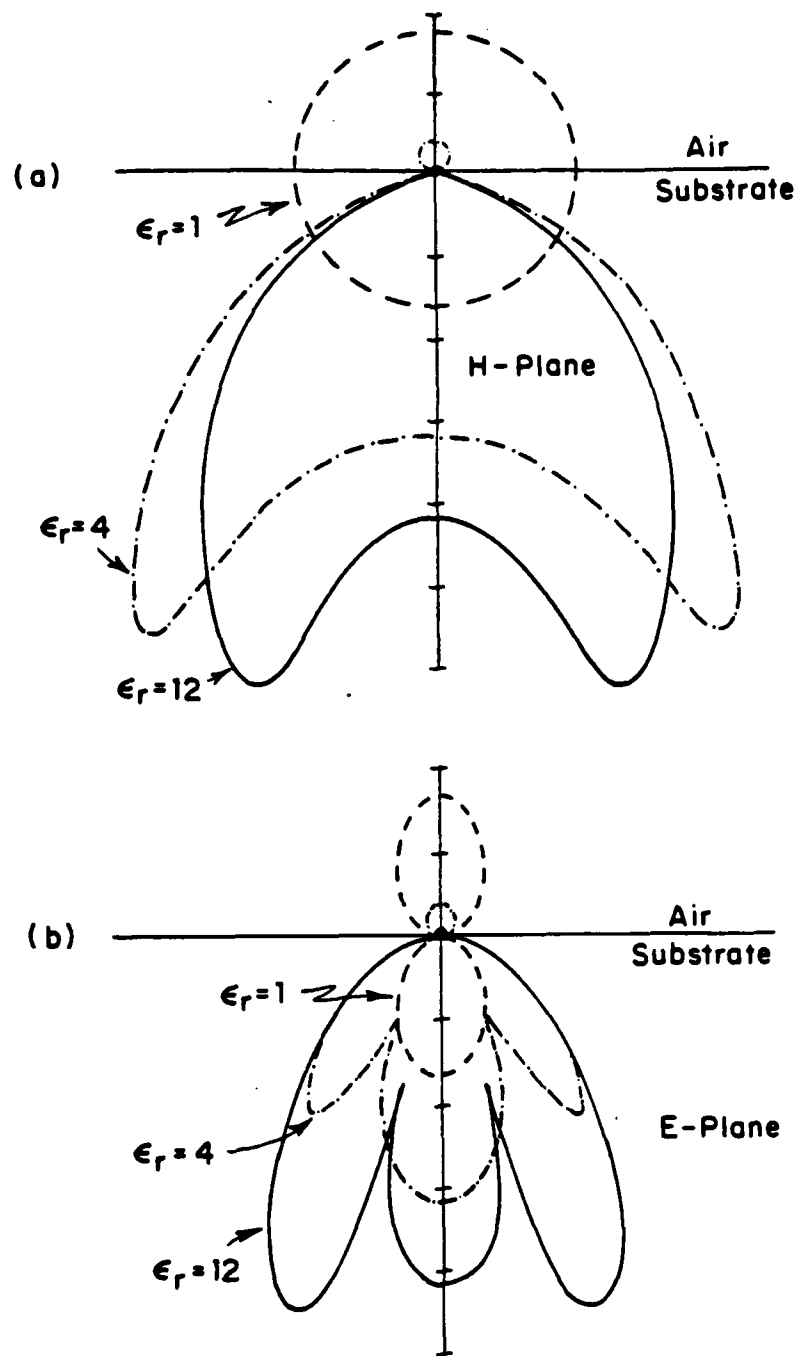


FIG. 3.10 (a) H-plane power pattern of a resonant dipole antenna at an air-dielectric interface for different values of ϵ_r . (b) E-plane power pattern of the resonant dipole of (a) for the same values of ϵ_r . [Adapted from Ref. 67]

3.3.4 Design Decisions

In this work, radiation from a FIR laser source was focussed by an $f/4$ TPX lens and an electroformed copper cone through the back-side of the sample substrate, containing a small-area tunnel junction at the center of the substrate. Fig. 3.11 illustrates the complete coupling arrangement, seen in cross-section, as viewed in the transverse optical access dewar.

The antenna was fabricated following the design rules developed by Mizuno, Daiku, and Ono⁶³. Z-cut crystal quartz substrates, 2.54×10^{-2} cm thick, were used. Single crystal quartz has an index $n = 2.34$ in the 100 μm to 1.2 mm wavelength region of interest to this experiment. The effective thickness was, $t_{\text{eff}} = 1.2$, for the 496 μm methyl fluoride (CH_3F) laser line; it decreases to $t_{\text{eff}} = 0.48$ for the 1.22 mm isotopic methyl fluoride ($\text{C}^{13}\text{H}_3\text{F}$) laser line. The antenna length was shortened to 77% of its free space resonant length (0.48λ) to 0.37λ , or $l_{\text{res}} = 183$ μm for the 496 μm line and $l_{\text{res}} = 451$ μm for the 1.22 mm line. Figure 3.12(a) displays a dipole antenna of 182 μm length, and 5 μm linewidth. At its center is a small-area junction, at a magnified scale in Fig. 3.12(b). This particular junction had a resistance of 24Ω , an area of 2.4×10^{-8} cm^2 , and critical current density, J_c , of 1.1×10^3 A/cm^2 at $T = 1.4$ K.

A conical horn with a short cylindrical waveguide section was used as a feed for the dipole antenna, completing the coupling of the junction to the FIR laser source. The design of this horn was based on

Detail of Transverse Optical Access Dewar

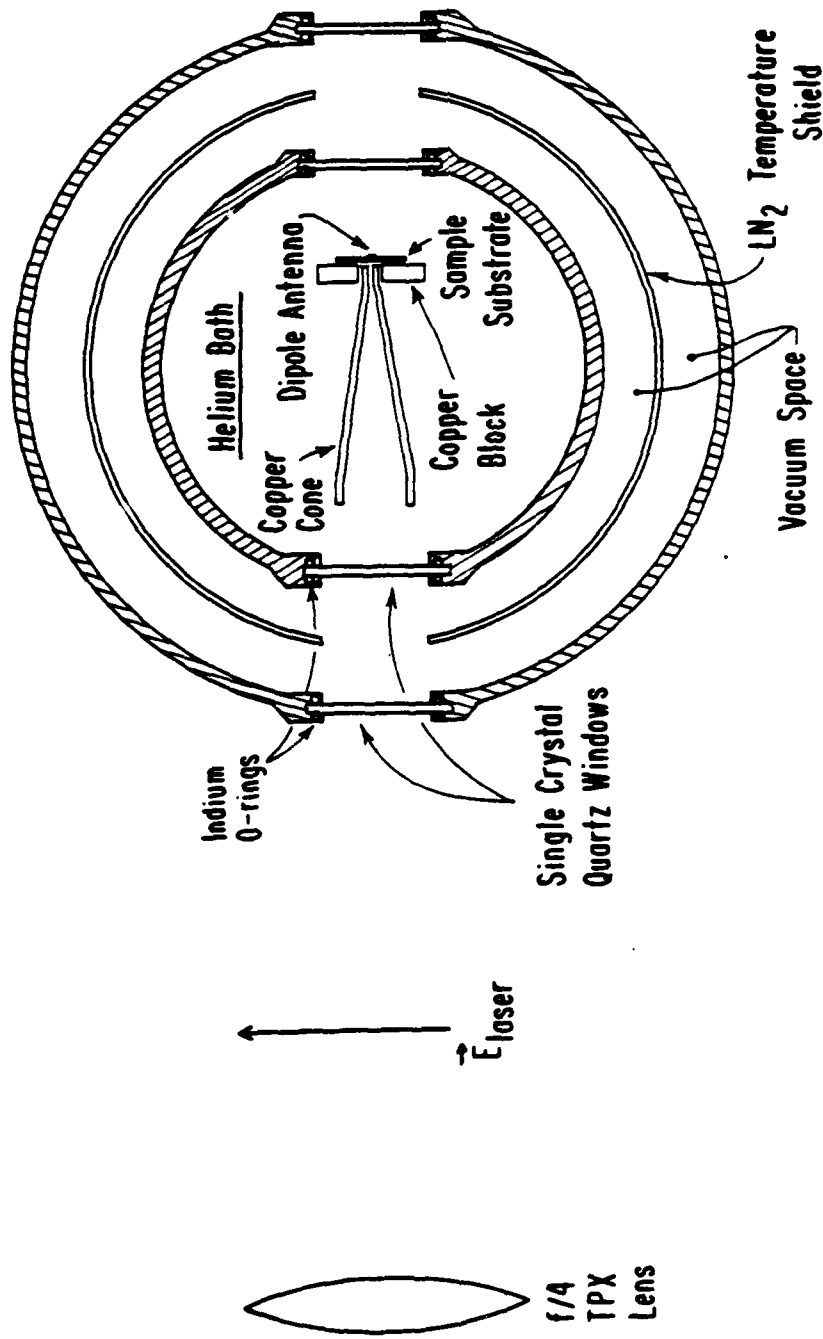
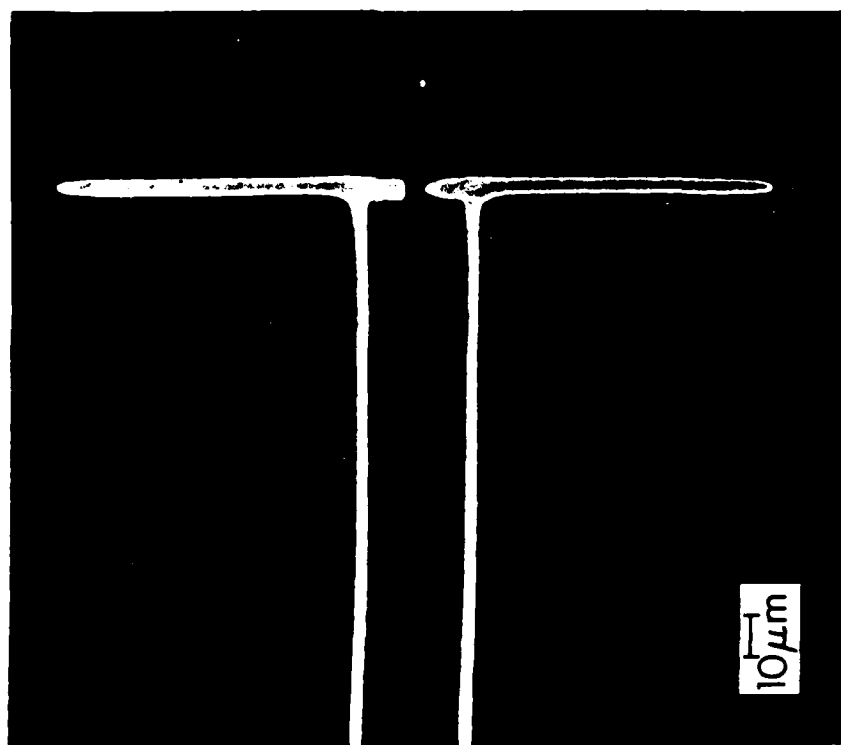
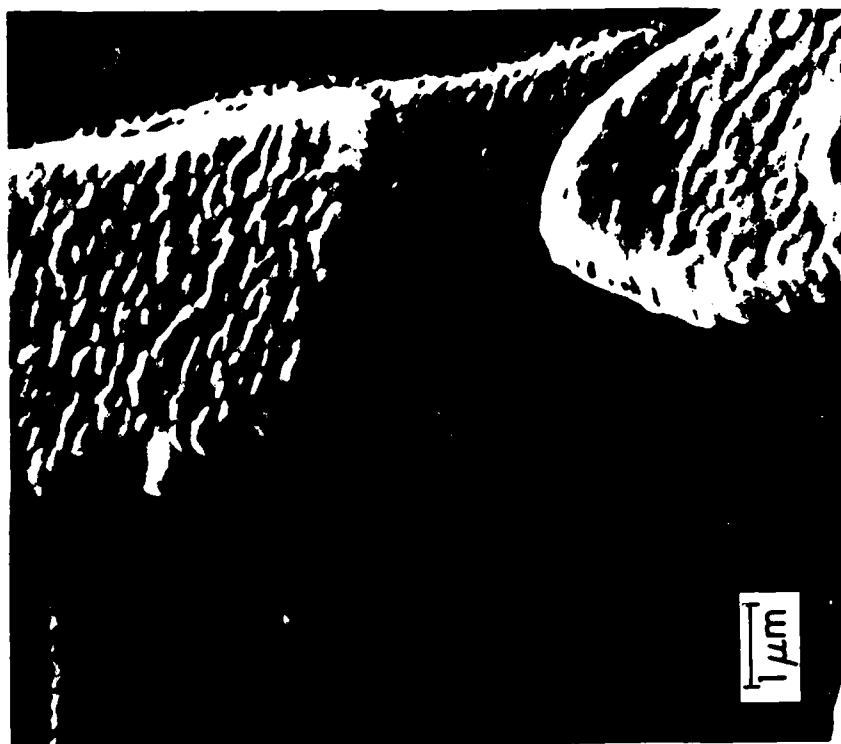


FIG. 3.11 Detail of transverse optical access dewar. FIR laser radiation is focussed by the TPX lens onto the cone, through the back side of the substrate, onto the junction-antenna structure.

FIG. 3.12 (a) SEM micrograph of a typical sample with a dipole antenna of $\sim 183 \mu\text{m}$ length and $\sim 5 \mu\text{m}$ line width. At the center of the dipole is the tunnel junction. (b) Close-up of the junction region in (a).



work of Blaney at the National Physical Laboratory in Great Britain.⁶⁹ The horn had a conical section 35 mm in length, an opening 11.4 mm in diameter, and an opening angle of $\sim 18^\circ$. The waveguide section was 7 mm long and 0.79 mm in diameter. This cone was fabricated by electrodeposition of copper on a polished stainless steel mandrel, in order to keep the surface roughness to a minimum. The cone has a calculated gain of 29 db, or a factor of 760, over that of an isotropic radiator.⁷⁰ The waveguide section had a cut-off wavelength of 1.35 mm for the TE_{11} mode, the lowest order or dominant mode. Cut-off wavelengths for some higher order modes are 1.03 mm for the TM_{01} mode, 0.81 mm for the TE_{21} mode, 0.65 mm for the TM_{11} and TE_{01} modes, etc.⁷¹ Therefore although the waveguide could only operate in the fundamental mode at the 1.22 mm laser line, unfortunately at shorter wavelengths, such as the strong 496 μm line, several modes could be excited at once.

In the usual operation of a horn, an adjustable tuning stub is inserted in the waveguide section about $3\lambda_g/4$ in front of the device, usually a point contact. (λ_g is the wavelength of the mode in the guide.) A moveable plunger terminates the waveguide behind the point contact. A variation on this scheme, in which only a moveable plunger was used to tune out the point contact reactance, performed successfully at 0.66 mm at the NPL, achieving a reasonable coupling efficiency of $\sim 10\%$.⁶⁹

In this work no attempt was made to resonate out the junction reactance by either tuning stubs or plungers. The coupling arrangement, used in this experiment, in which the radiation is focussed through the

back-side of the substrate, takes advantage of the effect of the dielectric substrate on the antenna pattern. During a run the cone could be rotated about the center of the dewar to optimize the coupling of the radiation to the junction.

The FIR radiation came from the optically pumped FIR laser built by D. Weitz.⁷² The characteristics of this laser have been thoroughly described before, but will be discussed briefly in the following section.

3.4 Far-infrared Laser Source

3.4.1 Introduction

In the thirteen years since the first observation of FIR lasing action in an optically pumped molecular gas laser by Chang and Bridges⁷³, over 1300 laser lines have been reported.^{74,75} Optically pumped FIR lasers have become a reliable source of radiation in the 40 μm to 2000 μm wavelength region. The laser used in this work has been documented in detail in connection with earlier work on point contacts, so we will only briefly discuss its theory, design, operation and performance.

3.4.2 Qualitative Theory

The theory of the FIR laser can be understood most simply in terms of the energy level diagram of a specific molecule. Since the symmetric top molecule, methyl fluoride, CH_3F , has been thoroughly studied^{73,76,81} we will begin by presenting a diagram of its energy levels relevant to the FIR laser process, Fig. 3.13. The state of the molecule is described by three quantum numbers, assuming only the ν_3 or C-F bond stretching vibrational mode is allowed: ν , the vibrational quantum number, J related to the total angular momentum, and K , the axial component of the angular momentum, where $K = 0, \pm 1, \pm 2, \dots, \pm J$.⁷³ Methyl fluoride molecules in the $\nu = 0, J = 12, K = 2$ state are excited by the 9P(20), 9.55 μm CO_2 pump laser to the $\nu = 1, J = 12, K = 2$ excited state. The lasing transition is between the $J = 12$ and $J = 11$ rotational states.⁷³ This transition produces the 604 GHz, 496 μm laser

Energy Level Diagram for Optically-Pumped CH_3F FIR Laser

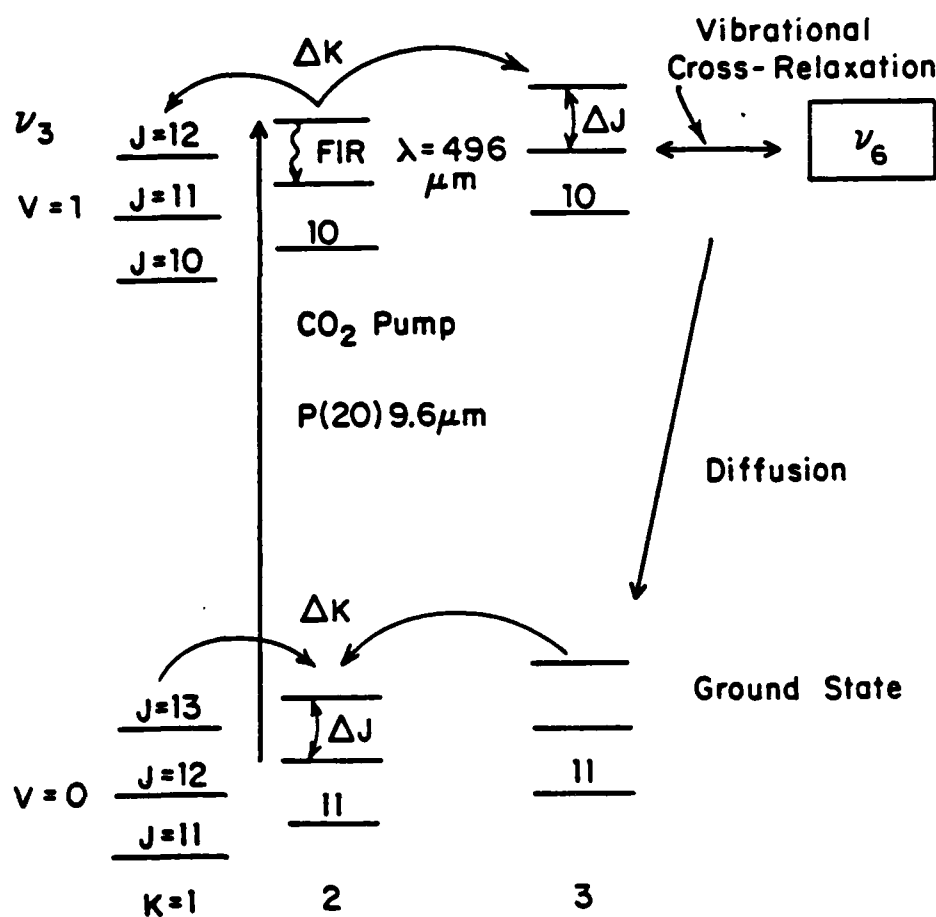


FIG. 3.13 Methyl fluoride energy-level diagram. The CO_2 pump line coincides with the $\nu=0 \rightarrow 1$, $J=12$, $K=2$ transition. The 496 μm FIR lasing transition is the $\nu=1$, $K=2$, $J=12 \rightarrow 11$ transition. ΔK denotes rotational quantum number changing transitions which tend to destroy the population inversion of the lasing level, as does ΔJ . Vibrational mode changing collisions also destroy the population inversion. Molecules relax back into the ground state by collisions with the cavity walls. [Adapted from Ref. 80.]

line, one of the strongest FIR laser lines reported in the literature, and the line used most in this work.

The FIR output power is limited by fundamental factors, such as various relaxation rates of the molecule out of its excited state, and the Manley-Rowe⁸² limit on single photon energy down conversion processes. Experimentally controllable factors such as the fraction of pump power absorbed in the lasing gas, the fraction of pump power lost due to absorption in the walls and mirrors of the cavity, cavity losses of the FIR beam, and transmissivity of the FIR output coupling mirror, also limit the FIR output efficiency.⁷⁹⁻⁸¹ The expression for the theoretical maximum output power of the FIR laser in terms of the input pump power, P_p , pump frequency ν_p , and output frequency ν_{FIR} is:

$$P_{\text{FIR}} = \frac{1}{2} \left(\frac{h\nu_{\text{FIR}}}{h\nu_p} \right) P_p \quad (3.8)$$

and the efficiency η is given by $\eta = P_{\text{FIR}}/P_p$. The factor 1/2 comes from the fact that the degeneracies of the upper and lower lasing sub-levels are approximately equal since the molecules are in high rotational states; this means that for every two molecules excited only one can contribute to the FIR output by emitting a photon and decaying to the lower state, thereby destroying the population inversion necessary for lasing action. The factor $h\nu_{\text{FIR}}/h\nu_p$ is the Manley-Rowe condition, limiting the maximum power to the ratio of output photon energy to the input photon energy, as in a one-photon in, one-photon out process.

This maximum theoretical laser efficiency is $\eta_{\max} = 9.6 \times 10^{-3}$ at $\lambda = 496 \text{ } \mu\text{m}$. The measured efficiency for this laser is only ~7-10 % of the maximum,⁷² which is approximately the same as the efficiency measured by other workers.⁷⁹

Experimentally, the FIR cavity losses can be limited to a few percent by a careful design of the FIR cavity, while allowing a reasonable fraction of the FIR power to be coupled out. A highly-overmoded dielectric waveguide cavity with external mirrors has low propagation losses for the linearly polarized EH_{11} cavity mode,⁸³ which transforms to the TEM_{00} free space gaussian mode.⁸⁴ Losses due to absorption of the pump beam by molecules in the excited state can be minimized by keeping the lasing gas to low pressures. The fraction of pump power absorbed is usually small, due to the low pump absorption coefficients ($\alpha = 0.01 \text{ m}^{-1}$ for CH_3F)⁷⁹. It would be possible to increase the pump absorption by increasing the pressure, but this also increases the rate at which excited atoms are thermalized by rotational quantum number changing collisions, effectively limiting the pressure to ~100 mtorr. In practice as long a cavity as practicable is used to increase the pump absorption. The relaxation rate, γ_v , of molecules in the excited vibrational state to de-excite and return to the vibrational ground state after lasing is slow compared to the rotational cross-relaxation of molecules within the excited vibrational band. The lower-laser-state lifetime is effectively $(\gamma_v)^{-1}$, and therefore decreasing this lifetime would increase the output power. Practical solutions are to decrease the diameter of the cavity⁸¹, thereby reducing

AD-A137 186

A FAR-INFRARED LASER STUDY OF SMALL-AREA
SUPERCONDUCTING TUNNEL JUNCTIONS(U) HARVARD UNIV
CAMBRIDGE MA DIV OF APPLIED SCIENCES W C DANCHI OCT 83

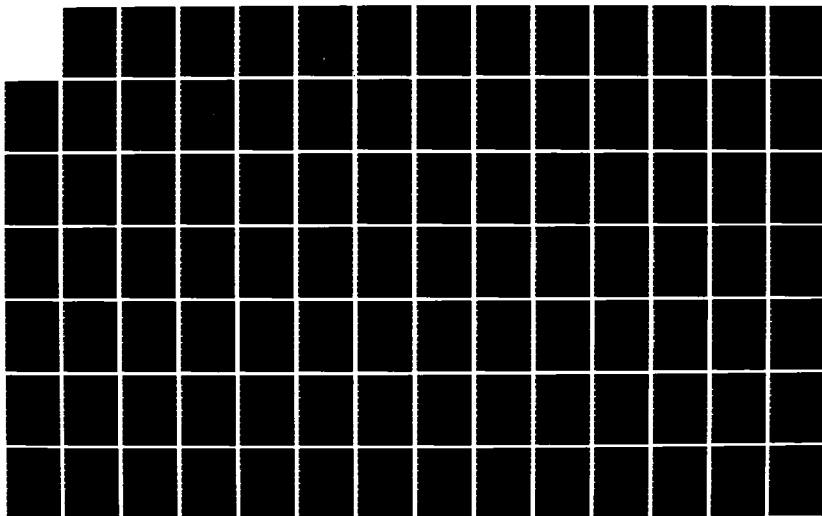
2/3

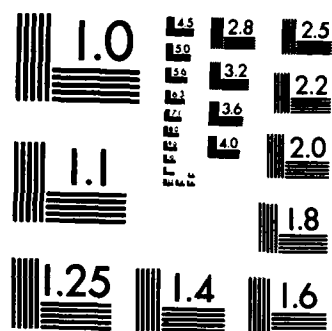
UNCLASSIFIED

DAS-TR-22 N00014-83-K-0303

F/G 20/12

NL





MICROCOPY RESOLUTION TEST CHART
NATIONAL BUREAU OF STANDARDS-1963-A

the diffusion time for molecules to reach the walls and de-excite, or to introduce a buffer gas to collisionally de-excite the molecules.⁸⁵

3.4.3 Operation and Performance

Fig. 3.14 displays the complete FIR laser system. A modified commercial CO₂ laser⁸⁶ provided the pump beam. The pump laser had a 12 mm diameter, 1.8 m long cavity, with the active region enclosed by two ZnSe Brewster angle windows. This laser had been modified by using an ~20 cm longer cavity than usual for increased output power, and by the removal of the output coupling mirror from the end of the laser cavity, and its replacement by a second Brewster angle window. A 75 lines/mm grating was used to tune the laser to a single line, and also served as one end mirror. The output coupling mirror was mounted on a piezo-electric transducer (PZT) stack for fine tuning of the operating frequency, and was semi-transparent with a 20 m radius of curvature. The laser was mounted on a granite slab and enclosed by a metal cover for stability against frequency drift due to thermally induced cavity length changes. ⁷²

In the typical operation of the laser, 12-25 W of output power could be achieved over the 9.5 μ m band, and 20-50 W in the 10.5 μ m band with a nearly Gaussian output beam.

The single most important condition for a stable, single-line, Gaussian output beam was that the Brewster windows were clean. After ~100 hours of operation, the laser would not operate on a single line,

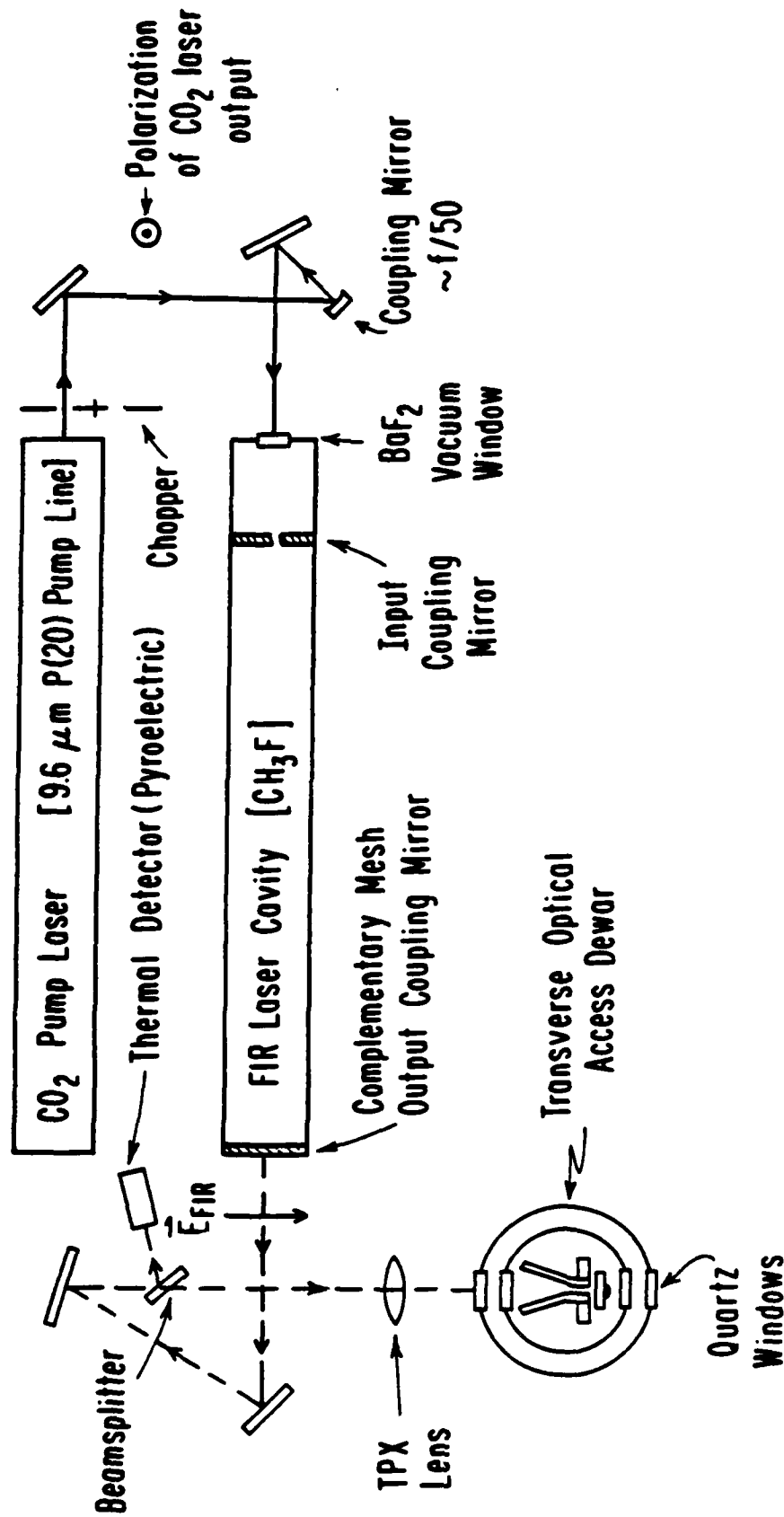


FIG. 3.14 Optically-pumped FIR laser set-up.

but would instead lase on 2-3 lines at once with a diminished and unstable output power. At this time, the windows were removed from the laser and ultrasonically agitated for ~1/2 hour in laboratory detergent, followed by a 15 minute ultrasonic agitation in distilled water, and blown dry with pure nitrogen gas. If the mode shape, and power, and stability were not drastically improved by this treatment the old windows were removed and discarded. New ones were installed on the Brewster mounts, cleaned with the procedure noted above, and installed on the laser.

The FIR cavity consisted of a 38 mm diameter, 3 m long Pyrex pipe with two flat end mirrors. The CO₂ laser beam was focussed into the FIR cavity by an f/50 coupling mirror through the BaF₂ window, and through the 3 mm diameter hole in the input coupling mirror (flat) mounted at the end of the dielectric waveguide. This mirror was mounted on a translation stage between 2 stainless steel bellows vacuum seals. This mirror and also the output coupling mirror were on gimbal mountings for adjustment of the cavity finesse (essentially the cavity quality factor Q). The mirror could be translated to adjust the cavity length to the proper resonant FIR cavity mode. The output coupling mirror consisted of an Al thin-film, capacitive (or complementary) mesh on a 2 mm thick, 1.75 inch diameter, optically polished single crystal quartz flat. The capacitive mesh output mirrors were made by evaporating 3000 Å Al through Ni electroformed meshes onto the quartz flats.^{72,87} The mesh sizes were chosen according to the FIR laser line desired, for example, a 100 lines-per-inch Ni mesh was used to make the output

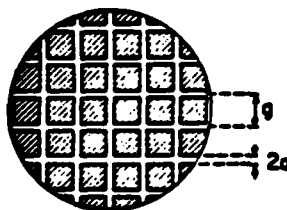
Table 3.1

FIR Laser Lines and Mesh Constants

FIR Wavelength (μm)	FIR Frequency (GHz)	Lasing Gas	Pump Line	Output Pol. ¹	Capacitive Mesh Consts. ² $g(2a)\mu\text{m}$	Mesh Constants ³ (lines/inch)
118.8	2523	CH_3OH	9P(36)	\perp	76(21)	333
148.5	2018	CH_3NH_2	9P(24)	\perp	76(21)	333
170.6	1758	CH_3OH	9P(36)	//	76(21)	333
202.4	1481	CH_3OH	9P(36)	//	76(21)	333
233.9	1282	H_2H_4	10R(8)	//	212(36)	120
328.5	912.7	DCOOH	10P(22)	\perp	212(36)	120
393.6	761.6	HCOOH	9R(18)	\perp	212(36)	120
415	722	CH_2CF_2	10P(14)	-	847(60)	30
432.5	692.9	HCOOH	9R(20)	\perp	254(27)	100
496.1	604.3	$\text{C}^{12}\text{H}_3\text{F}$	9P(20)	\perp	254(27)	100
554.4	541.0	CH_2CF_2	10P(14)	-	847(60)	30
890.0	336.8	CH_2CF_2	10P(22)	//	847(60)	30
1222	245.4	$\text{C}^{13}\text{H}_3\text{F}$	9P(32)	//	847(60)	30

¹ The output polarization is referred to that of the input CO_2 polarization:
 \perp = perpendicular, // = parallel, - = unknown.

² Capacitive mesh constants are given in terms of g , the mesh period, and $2a$, the distance between adjacent Al squares.



³ The period of Ni electroformed mesh used to fabricate the Al capacitive mesh.

coupling mirror for the $496\text{ }\mu\text{m}$, methyl fluoride laser line. For completeness, Table 3.1 displays strong CW FIR laser lines, the lasing gas used, CO_2 pump line, and FIR output polarization relative to the CO_2 polarization, and capacitive mesh constants. The capacitive mesh mirrors have a high reflectivity at the CO_2 pump frequency, proportional to the area coverage of the Al squares which make up the mesh. The pump radiation not reflected by the Al is absorbed in the quartz flat. The reflectivity of the cavity at the output frequency could be altered by using output couplers with different mesh constants.

The FIR radiation is transformed from the EH_{11} cavity mode to the TEM_{00} gaussian free space mode upon transmission through the output coupling mirror. The radiation is reflected by two mirrors and then a reflected beam from the single crystal quartz (flat) beamsplitter feeds the thermal detector.⁸⁸ The transmitted beam is focussed by an $f/4$ lens of TPX or polyethylene, through room temperature and liquid helium temperature single crystal quartz windows onto the electro-formed copper feed horn, as described above.

The FIR laser performed best when the laser room was warm, $\sim 80^\circ\text{ F}$, and when the CO_2 laser had been warmed up for 2-3 hours before injecting its beam into the FIR cavity. The FIR cavity was always operated in a sealed off mode at the pressure which gave the maximum output power. Under these conditions the FIR output power was very stable, having long term drifts of at most $\sim 10\%$ in 24 minutes of operation, using only this passive stabilization scheme. Short term fluctuations were $\sim 2-3\%$, measured with a 0.3 sec time constant. Fig. 3.15 displays the output

power measured over a 24 minute period. Long term drifts were associated with FIR cavity length changes, while short term fluctuations were connected with CO₂ cavity length changes or gross disturbances such as opening or closing the door of the laser room.

Finally, proper alignment of the CO₂ pump laser injection optics was crucial to the stable operation of the FIR laser. A HeNe laser was used for alignment. The alignment procedure began with the alignment of the HeNe laser and CO₂ laser beams. A pin-hole made out of asbestos sheet was first aligned with the pump laser, close to the end of the laser, and the position of the spot from the laser beam on another asbestos sheet about 10' from the end of the CO₂ laser was noted. A removeable mirror was then placed at the end of the CO₂ laser, and the HeNe laser beam was aligned with the center of the hole in the first asbestos sheet and the spot on the second sheet. The HeNe laser was then sent through the injection optics of the FIR laser. The flat injection mirror at the end of the cavity, and the focussing mirror, both mounted on gimbals and adjusted by micrometer screws, were adjusted so the HeNe laser beam went through the center of the input coupling hole through the center of the FIR cavity, and onto the center of the output coupling mirror. The output coupling mirror was partially transmitting so the HeNe beam could be seen as a bright, ~1 cm diameter circular spot. There was never any need to remove the coupling mirror during the alignment. If the light transmitted through the output coupler appeared diffuse, or shaped like a crescent or a line, then most likely the HeNe beam suffered one or more reflections with the walls of

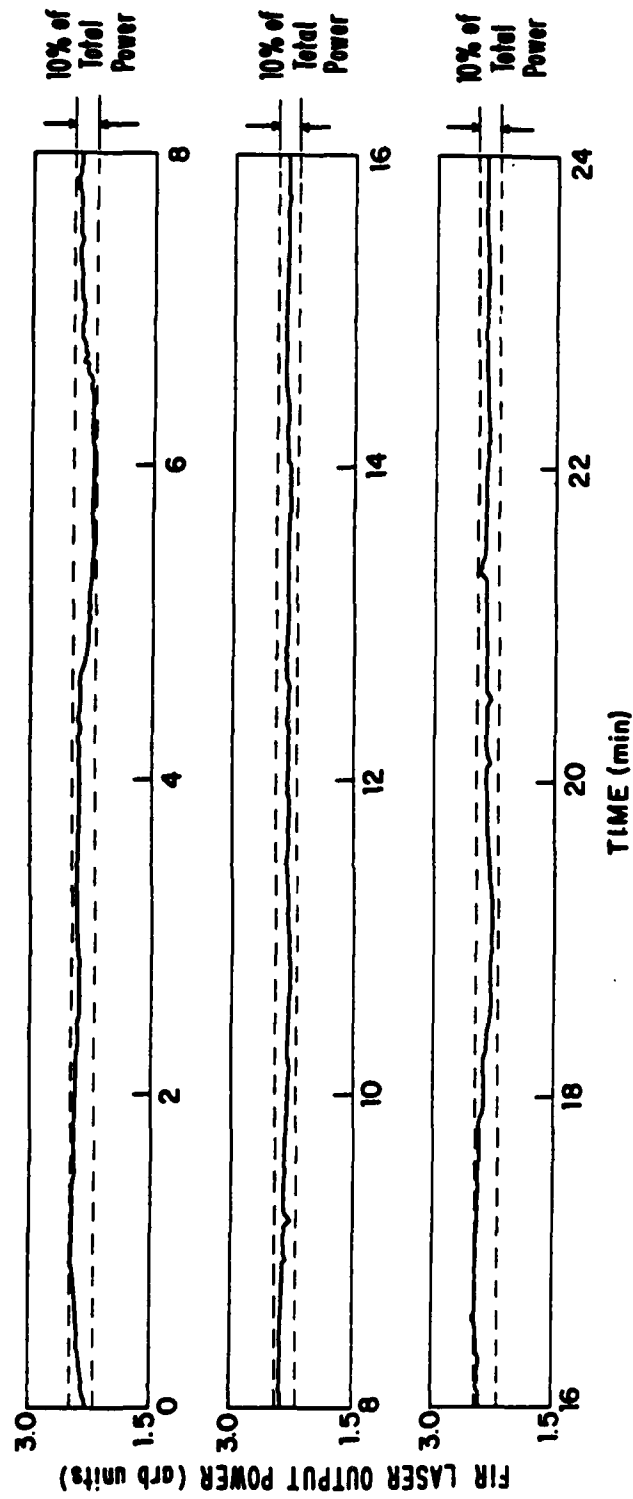


FIG. 3.15 A 24 minute recording of the free-running FIR laser output power.

the FIR cavity before reaching the mirror. If there were transmitted "satellites" in addition to the main spot, then the cavity mirrors were not parallel to each other. The tilt on the mirrors was adjusted until there was only one bright spot at the center of the output mirror.

After this procedure was completed and the CO₂ pump laser was injected into the FIR cavity, the FIR cavity length was adjusted until there was a little FIR output power. The output power could then be maximized by adjusting the pressure, input coupling optics, PZT bias voltage, and pump power.

Before I-V curves of the irradiated junction were taken, the FIR laser was adjusted for maximum power and stability. I-V curves could then be taken at different laser powers by inserting mylar or plexiglass absorbers at the output of the FIR laser.

CHAPTER IV

DATA ANALYSIS

4.1 Introduction

The junctions described in Chapter III provide an ideal test of the frequency-dependent theory of superconductivity, because of their small area and nearly ideal dc I-V characteristics, and the relative reproducibility of these characteristics from junction to junction. We begin this Chapter with analysis of the dc characteristics of low resistance junctions which were the first small-area junctions successfully fabricated in our lab. Their excellent dc properties and microwave response to 4.3 mV with 10 GHz radiation demonstrated that these junctions could be expected to work in the far infrared. The results of the FIR measurements are presented in the following sections, beginning with the analysis of the ac Josephson effect data in Section 4.3. The photon-assisted tunneling data and analysis is presented in Section 4.4. Section 4.5 ends the Chapter with an analysis of the effects of noise on the dc and FIR response of the junctions, and attempts to treat the whole I-V curve, including the ac Josephson effect, the photon-assisted tunneling effect, and noise.

The theoretical discussions of Chapter II provide the framework within which we will analyze the data. The dc characteristics analyzed in the Section below had resistances of $12\ \Omega$ or less, and had high $I_c R_n$ products. Higher resistance samples ($16\text{--}1600\ \Omega$) were used in the FIR measurements.

4.2 DC Characteristics

Figure 4.1 displays the dc I-V characteristics of a low resistance ($R_n \sim 2.4 \Omega$), high current-density ($J_c \sim 1 \times 10^4 \text{ A/cm}^2$), tunnel junction at four selected temperatures. At 4.2 K the I-V curve is non-linear due to the presence of the superconducting Pb electrode and normal Sn electrode, i.e. the junction is a superconductor-insulator-normal metal (SIN) junction at 4.2 K. Below 3.8 K, i.e., the T_c of Sn, the junction develops a critical current, labeled I_c in the Figure. Additional structure appears from the gap of Sn, now growing, at $\Delta_{Pb} + \Delta_{Sn}$ and at $\Delta_{Pb} - \Delta_{Sn}$, as labeled in Fig. 4.1. The structure at the difference of the gaps is due to thermally excited quasiparticles at the gaps of Pb and Sn, which provide an increase in the conductance of the junction, at a voltage in which the thermally excited quasiparticles of the Sn can tunnel into empty states in the Pb, and vice versa. The two I-V curves, one at $T=3.6 \text{ K}$ the other at $T=3.3 \text{ K}$, serve to illustrate the temperature dependence of the gap structure. At the lowest temperature, $T=1.4 \text{ K}$, the structure from the difference of the gaps disappears due to the freezing out of the thermally excited quasiparticles as the temperature approaches zero, $T \rightarrow 0$. We now only observe the structure from the sum of the gaps $\Delta_{Pb} + \Delta_{Sn}$, which arises from "pair breaking," so does not require any thermal quasiparticles.

Experimentally, the gap of Sn as a function of temperature, $\Delta_{Sn}(T)$, as well as the critical current, $I_c(T)$, can be measured from the I-V curves. We have measured these structures on the I-V curves of low resistance junctions, whose parameters are listed in Table 4.1. The

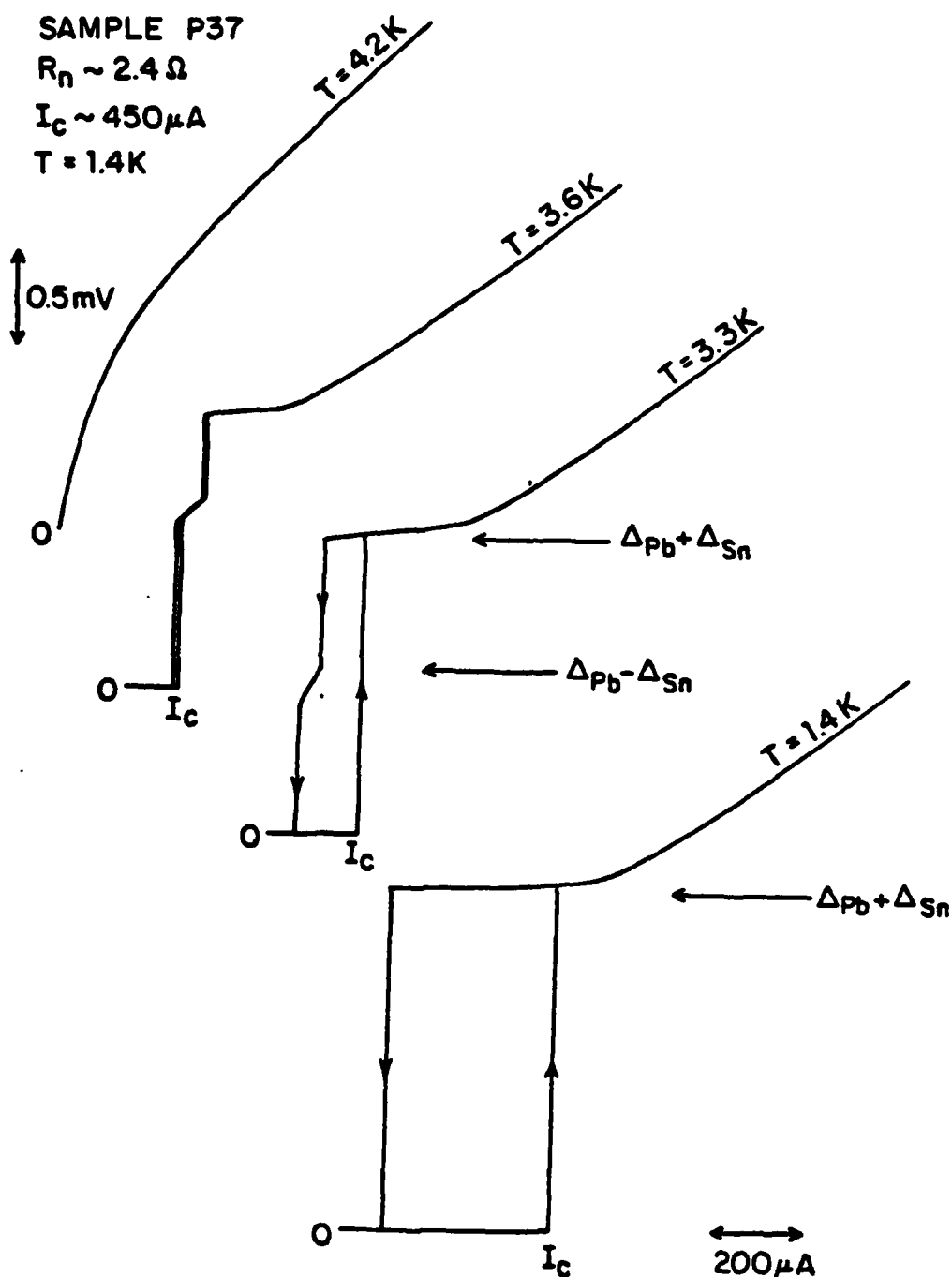


FIG. 4.1 Typical I-V curves of a low resistance ($\sim 2 \Omega$), larger area ($\sim 4.5 \times 10^{-8} \text{ cm}^2$), tunnel junction for decreasing temperatures. Note the gap structure at $\Delta_{Pb} + \Delta_{Sn}$ and $\Delta_{Pb} - \Delta_{Sn}$ at $T = 3.6 K$ and $T = 3.8 K$. At $4.2 K$ the curvature on the I-V is from the gap structure in Pb.

Table 4.1

Parameters of Low Resistance Junctions

Sample	$R_n (\Omega)$	$I_c (\mu A)$ T=1.4k	$A (\mu m^2)$	$I_{Cn} (mV)$ T=1.4k	C (pF)	β_c^1 (est.) ¹	β_c^2 (meas.) ²	$\omega_J (sec^{-1})$ $\times 10^{12}$ (est.) ¹	$\omega_J (sec^{-1})$ $\times 10^{12}$ (meas.) ²	$J_c (A/cm^2)$ (est.)	$J_c (A/cm^2)$ (meas.)
P73	4.0	230	2.0	.92	.053	0.77	0.59	4.1	3.6	1.5×10^4	1.2×10^4
P27	12.5	32	4.6	.43	.12	5.5	1.8	1.6	0.89	2.1×10^3	7.0×10^2
P31	5.0	192	7.0	.96	.19	3.5	2.8	2.0	1.8	3.4×10^3	2.7×10^3
P37	2.4	450	4.5	1.08	.12	1.1	0.95	3.6	3.4	1.1×10^4	1.0×10^4
P47A	3.3	380	1.5	1.25	.040	0.48	0.50	5.3	5.4	2.4×10^4	2.5×10^4
P47B	2.4	527	1.9	1.26	.050	0.44	0.46	5.5	5.7	2.6×10^4	2.8×10^4
P57B	3.6	356	1.6	1.28	.042	0.55	0.59	4.9	5.1	2.1×10^4	2.2×10^4
P59	1.5	725	6.9	1.09	.18	0.98	0.89	3.7	3.5	1.2×10^4	1.1×10^4

¹ β_c or ω_J (est.) means that these parameters are computed using a critical current, $(I_c)_{est.}$, that is calculated from the nominal $I_c R_n$ product of 1.2 mV, and the sample resistance, R_n . (See text.)

² β_c or ω_J (meas.) means that these parameters are computed from the measured critical current, I_c , in Column 3 of this Table. (See text.)

eight samples shown in the table had resistances R_n , ranging from 1.5 Ω to 12.5 Ω , areas, A , from 1.5-6.9 (μm)², and current densities, J_c , from 2×10^3 - 2.6×10^4 A/cm². Table 4.1 also displays $I_c R_n$ products at $T=1.4$ K which range from 0.40 to 1.28 mV, the lowest (0.40 mV) was for the highest resistance sample, while for samples below 4 Ω , the $I_c R_n$ products were high, >1.0 mV, and did not correlate with sample resistance. Finally the table also displays estimates of the junction capacitances C , in pF, as well as the Stewart-McCumber parameter, $\beta_c = (2eI_c R_n^2 C) / \hbar$, and the Josephson plasma frequency $\omega_J = (2eI_c / \hbar C)^{1/2} = (\beta_c)^{1/2} / R_n C$.

In Table 4.1 the capacitance of each junction is estimated from the formula $C = \epsilon_r (\epsilon_0 A / t)$ where A is the junction area, t is the oxide thickness, ϵ_r is the dielectric constant, and ϵ_0 is the dielectric permittivity of vacuum. The area, A , is the geometrical area of the junction, estimated from SEM micrographs, and does not include estimates of parasitic capacitances such as the extra overlap of the Pb layer on the Ge insulating layer visible in the SEM micrograph of Fig. 3.12(b). The relative dielectric constant, $\epsilon_r = 6$ for SnO, is estimated from the ratio of the wave velocity in the oxide to that in free space, \bar{c}/c , for Sn-SnO-Sn junctions, as measured by other authors.^{37,89} For the oxide thickness, t , we use $t = 20 \text{ \AA}$ as a nominal value.¹⁸

The most poorly known junction parameter in Table 4.1 is the junction capacitance, and it is hard to put accurate bounds on its value. The area is known to ~20%, limited by the accuracy of the calibration of the length scale on the SEM (<10%), and the accuracy of

measuring the area from the SEM micrographs, probably another 10%. The relative dielectric constant, ϵ_r , and the dielectric oxide thickness, t , are the most difficult parameters to quantify because the measurements of \bar{c}/c upon which these values are based are for large-area, low current-density junctions of Sn-SnO-Sn, and the measurements were accurate only to ~ 300 GHz, a factor of two lower in frequency than our usual operating frequency of 604 GHz.^{37,89} Our junctions are made of Sn-SnO-Pb. The dielectric layer may contain PbO and other Pb oxides in unknown quantities. There may be also other at present unknown parasitic effects. We estimate that the ratio of ϵ_r/t , is known only to $\sim 20\%$, giving a total potential error of $\sim 40\%$ on the values of the capacitances.

The Stewart-McCumber parameter, β_c , and the plasma frequency, ω_J , are quantities derived from the critical current, capacitance, and resistance. $\beta_c \sim C$ and is therefore known only to $\sim 40\%$, whereas $\omega_J \sim C^{-1/2}$, and is known to $\sim 20\%$. The measured critical current, I_c , and normal resistance, R_n , are known to $\sim 1\%$, and limited by the accuracy of the gains of the amplifiers used (PAR 113).⁹⁰ β_c and ω_J are shown with estimated values based on nominal $I_c R_n$ product of 1.2 ± 0.1 mV, taken from the mean of the $I_c R_n$ products of the five samples, P37-P59. This value of the $I_c R_n$ product, 1.2 mV, is close to the theoretical value, 1.30 mV, computed from Eq. (2.2b), assuming $\Delta_{Pb}(0) = 1.31$ meV, and $\Delta_{Sn}(0) = 0.57$ meV. The measured values of ω_J and β_c correspond to the measured I_c 's of the junctions at $T = 1.4$ K. The estimated critical current density, $J_c(\text{est.})$, is based on the estimated $I_c R_n$ product, while the measured

critical current density, $J_c(\text{meas.})$, was calculated from the actual measured I_c which may be low relative to the nominal value due to premature switching triggered by noise.

Keeping these parameters in mind, Fig. 4.2 displays the squares of the measured values of the gap of Sn plotted against the liquid He bath temperature, determined from the bath pressure (regulated) using NBS pressure-temperature charts. The square of the Sn gap, $(2\Delta_{\text{Sn}})^2$, should be proportional to $T_c - T$, which can be seen from the BCS expression for the superconducting energy gap near T_c , Eq. (4.1),

$$\Delta(T) \approx 1.74\Delta(0) (1-t)^{1/2} \quad \text{for } T \approx T_c \quad (4.1)$$

where $t=T/T_c$. This equation says $[2\Delta_{\text{Sn}}(T)]^2 = [2(1.74)\Delta_{\text{Sn}}(0)]^2 (1-T/T_c)$ so that the slope of the $[2\Delta_{\text{Sn}}(T)]^2$ versus T is $-(3.48\Delta_{\text{Sn}}(0))^2/T_c$, and $\Delta_{\text{Sn}}(0)$ can be determined from the slope, given T_c , where T_c is determined from the temperature at which the gap extrapolates to zero. The data from three of the four samples lie on the same line, and give $T_c(\text{Sn})=3.79\pm0.1$ K, and $\Delta_{\text{Sn}}(0)=0.56\pm0.03$ meV. One sample shown has $T_c=3.81\pm0.01$ K and $\Delta_{\text{Sn}}(0)=0.47\pm0.03$ meV. As is clear from Fig. 4.2, most of the samples have T_c 's and $\Delta_{\text{Sn}}(0)$'s which are very close to (and consistent with) with nominal values used by other workers.^{21,37,93}

The critical current divided by its zero temperature value, $I_c(0)$, when plotted against $t=T/T_c$, in the absence of fluctuations should have the same functional form for all junctions having electrodes of the same materials. This conclusion can be drawn examining Eq. (2.22a) for $I_c(T)$ for a junction made of two electrodes with equal gaps, and

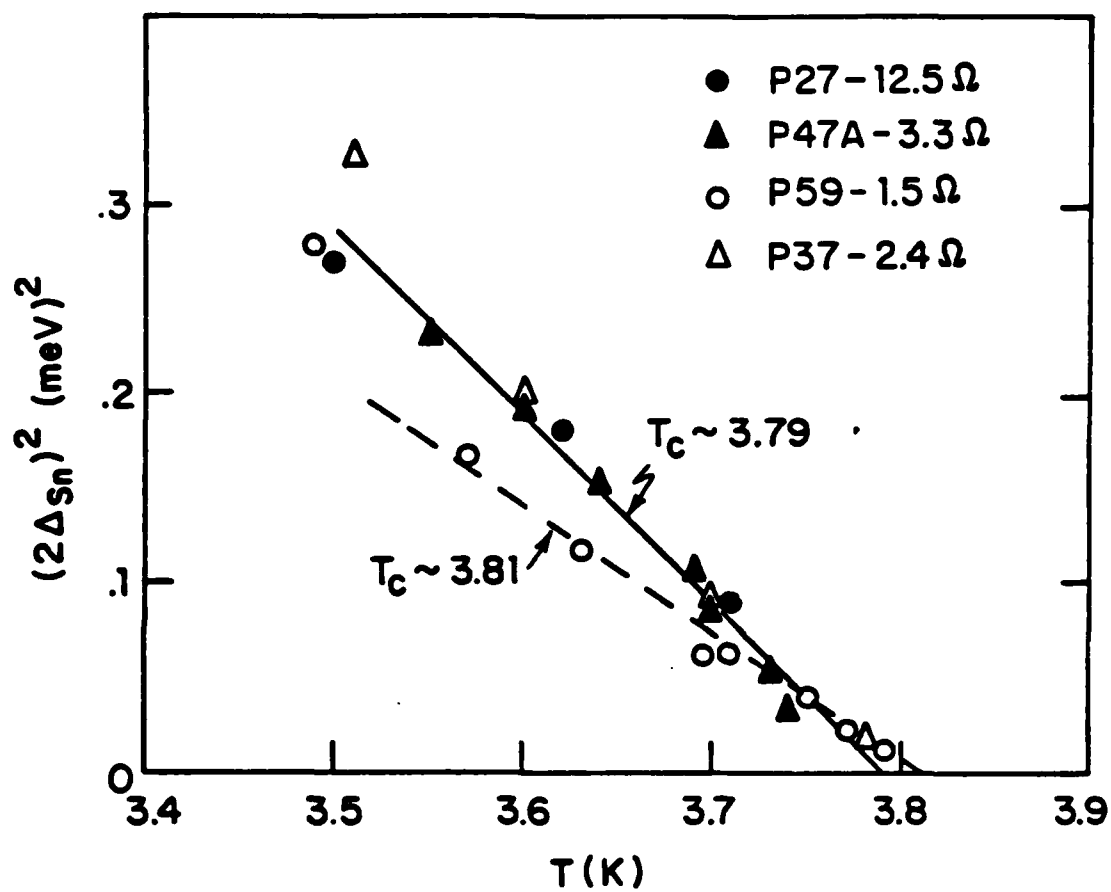


FIG. 4.2 The square of $2\Delta_{Sn}$, measured from data such as that presented in Fig. 4.1, versus the temperature T .

dividing it by $I_c(0)$. A similar result holds if the gaps are different. Fig. 4.3(a) displays $I_c(T)/I_c(1.4K)$ versus $t=T/T_c$ for the four junctions of Fig. 4.2. It is very clear that the data from all the samples lie on the same line, i.e. the solid line in the Figure. This curve is the theoretical curve plotted earlier in Chapter 2 as Fig. 2.2(b), computed from the Ambegaokar-Baratoff results.¹⁷ Fig. 4.3(b) illustrates the same data as Fig. 4.3(a) but the critical current, $I_c(T)$, for each junction is normalized to the estimated zero temperature value, $I_c(0)$, which is computed from the nominal $I_c R_n$ product of 1.2 mV and the sample resistance, R_n . The nominal $I_c R_n$ product is taken from the average of $I_c R_n$ products of samples P37-P59 of Table 4.1. The error on the data points on the vertical scale is ~8%, coming from the estimate for $I_c(0)$. Fig. 4.3(b) brings out how the low resistance samples, i.e. $R < 10 \Omega$, have $I_c R_n$ products consistent with expectations based on theory, but if $R > 10 \Omega$, the $I_c R_n$ products are low. This trend continues for the higher resistance junctions actually tested in the FIR.

Table 4.2 displays the dc characteristics of the samples measured in the FIR, the results of which will be presented in the next section. The analysis of the errors of the various measured quantities of Table 4.1 applies as well to Table 4.2. The $I_c R_n$ products vary from the highest values of ~0.9 mV for a junction of resistance of ~16 Ω , decreasing to a value of ~0.10 mV for junctions with resistance $> 300 \Omega$. This fall-off of the $I_c R_n$ product with increasing junction resistance is shown in Fig. 4.4, where the solid circles represent the I_c and R_n data

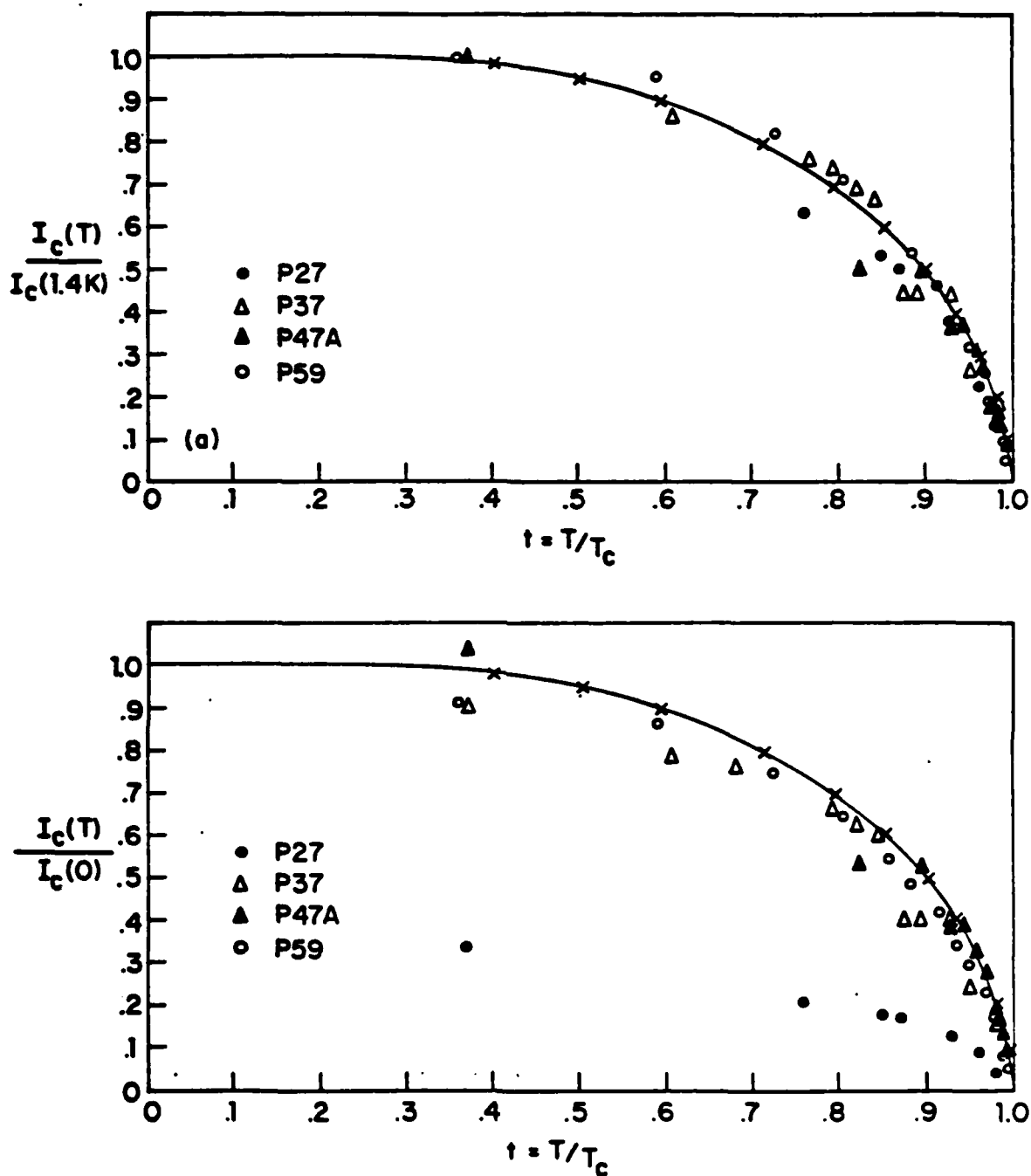


FIG. 4.3 (a) The critical current at a temperature T , normalized to the critical current at 1.4 K, $I_c(T)/I_c(0)$, versus the reduced temperature, $t=T/T_c$. (b) The critical current at a temperature T , normalized to the estimated zero temperature critical current, $I_c(0)=1.2\pm0.1$ mV, $[I_c(T)/I_c(0)]_{\text{est.}}$ versus $t=T/T_c$.

Table 4.2
Parameters of High Resistance Junctions Measured in the Far-Infrared

Sample	Laser line (μm)	Type of Junction: (n, or E)	$R_n(\Omega)$	$I_c(\mu\text{A})$	$I_c R_n(\text{mV})$	$C(\text{pF})$	θ_c^1 (est.) ¹	θ_c^1 (meas.) ²	$\omega_j(\text{sec}^{-1}) \times 10^{12}$ (est.) ¹	$\omega_j(\text{sec}^{-1}) \times 10^{12}$ (meas.) ²	$J_c(\text{A/cm}^2)$ (est.)	$J_c(\text{A/cm}^2)$ (meas.)
P73	496	R	16.4	55	2.2	.90	.058	3.5	2.6	2.0	3.3×10^3	2.5×10^3
P81	496	R	24	25.8	2.4	.62	.064	5.6	7.5	1.5	2.1×10^3	1.1×10^3
P89	496	R	176	1.5	0.40	.26	.011	7.0	1.6	1.4	1.7×10^3	3.8×10^2
P91	496	R	331	0.27	1.7	.10	.045	63	5.4	0.46	1.9×10^2	1.6×10^1
P91	1222	R	330	0.50	2.4	.17	.064	77	11	0.42	1.5×10^2	2.1×10^1
P97	1222	R	156	1.5	1.9	.23	.05	28	5.5	0.68	4.0×10^2	7.9×10^1
B11	496	E	1.6×10^3	0.08	0.93	.13	.025	146	15.6	0.30	8.1×10^1	8.6

¹ θ_c or ω_j (est.) means that these parameters are computed using a critical current, $(I_c)_{\text{est.}}$, that is calculated from the nominal $I_c R_n$ product of 1.2 mV, and the sample resistance, R_n . (See text.)

² θ_c or ω_j (meas.) means that these parameters are computed from the measured critical current, I_c , in Column 5 of this Table. (See text.)

of Table 4.2. The dashed line indicates the roughly constant $I_c R_n$ products (~ 1.2 mV) of the low resistance samples. The solid line and open circles represent the results of a computer simulation which is presented in Section 4.5.2. Critical current densities (est.) varied from ~ 80 A/cm² for the 1600 Ω sample, to about ~ 3000 A/cm² for the 16 Ω sample. Areas ranged from $\sim 0.4 \times 10^{-8}$ cm² to $\sim 2.4 \times 10^{-8}$ cm².

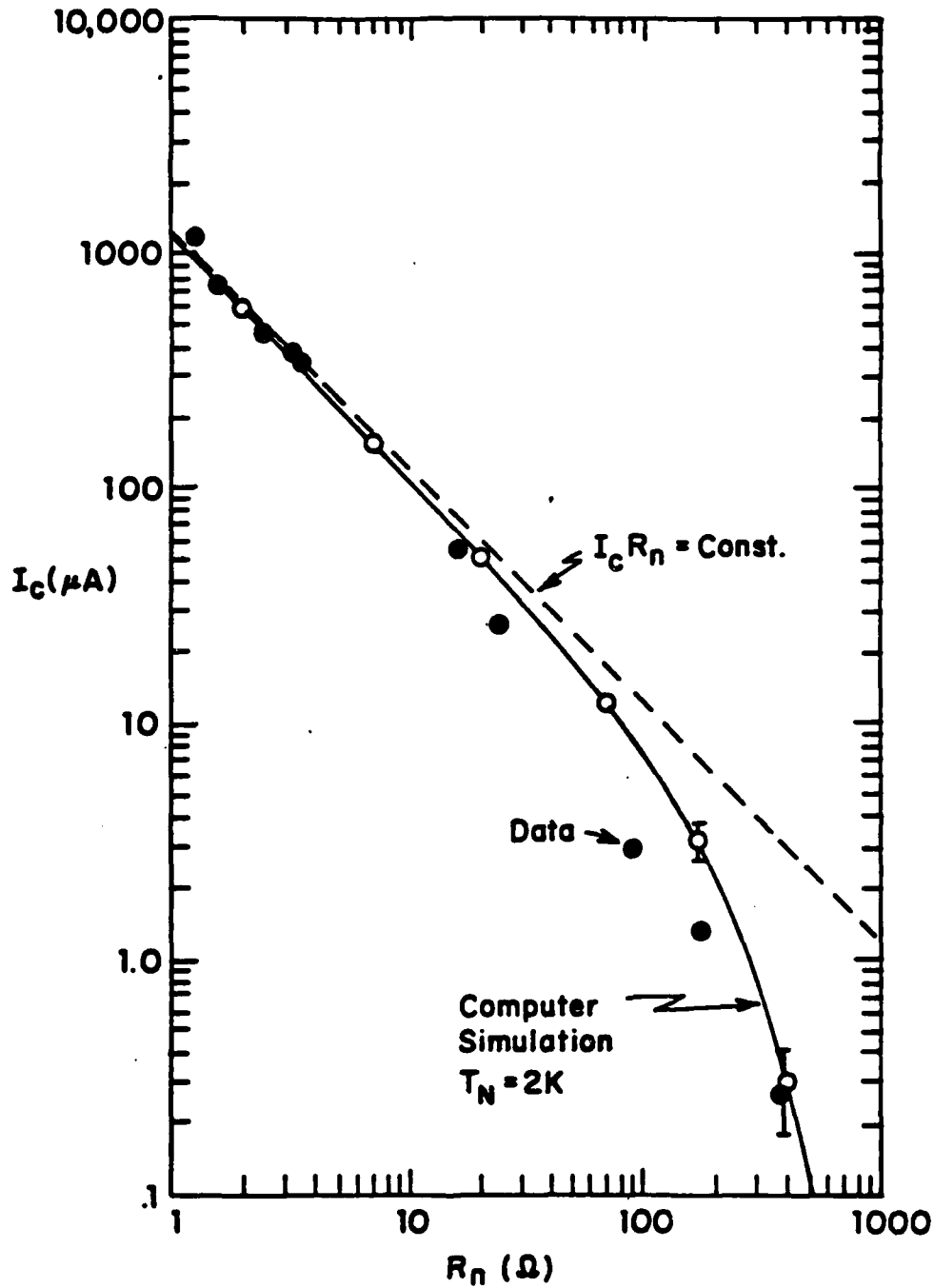


FIG. 4.4 Critical current, I_c , vs. the normal resistance, R_n , for the junctions studied in this work. Data shown by solid circles falls below the dashed line, $I_c R_n = 1.2 \text{ mV}$ for $R_n > 10 \Omega$. The computer simulation, solid line and open circles, closely follows the data. Error bars indicate bounds of simulated I_c for a given R_n . (See text.)

4.3 AC Josephson Effect Analysis

The excellent dc properties of the junctions discussed in the last section encouraged us to fabricate junctions of higher resistances, and to attempt to couple the FIR laser radiation to them, using the FIR laser and coupling arrangement described in Chapter III, illustrated by Fig. 3.11 and Fig. 3.14.

Typical I-V curves for increasing laser powers for two different junctions are shown in Fig. 4.5. In the low resistance large-area junction (Sample P73, $A \sim 2.2 \times 10^{-8} \text{ cm}^2$, $R \sim 16 \Omega$), we find flat steps, free of noise rounding, which fit the RSJ step shape very well. The low impedance of these junctions unfortunately causes a severe mismatch between junction and antenna so only a small fraction of the FIR power is coupled into the junction and only a few steps are observed.¹¹ In the particular junction shown in Fig. 4.5(a), we observe four Josephson steps and one photon-assisted tunneling step, when the maximum available normalized voltage $2\alpha = 2eV_L / \hbar\omega_L = 1.6$ is coupled.

The behavior of a high resistance small-area junction (Sample P89, $R \sim 176 \Omega$, $A \sim 0.4 \times 10^{-8} \text{ cm}^2$) is quite different and is shown in Fig. 4.5(b). Here 2α as high as 8.4 was obtained from the same laser power, and seven Josephson steps and six photon-assisted tunneling steps were observed. In this case the steps are affected by noise, which causes marked rounding and also a slight tilt (i.e. observable differential resistance) in the steps. The coupling of the radiation to the junction is good; it produces steps at voltages as high as 8.75 mV, which is comparable to the performance (12.5 mV) obtained by Weitz et al.⁹⁴,

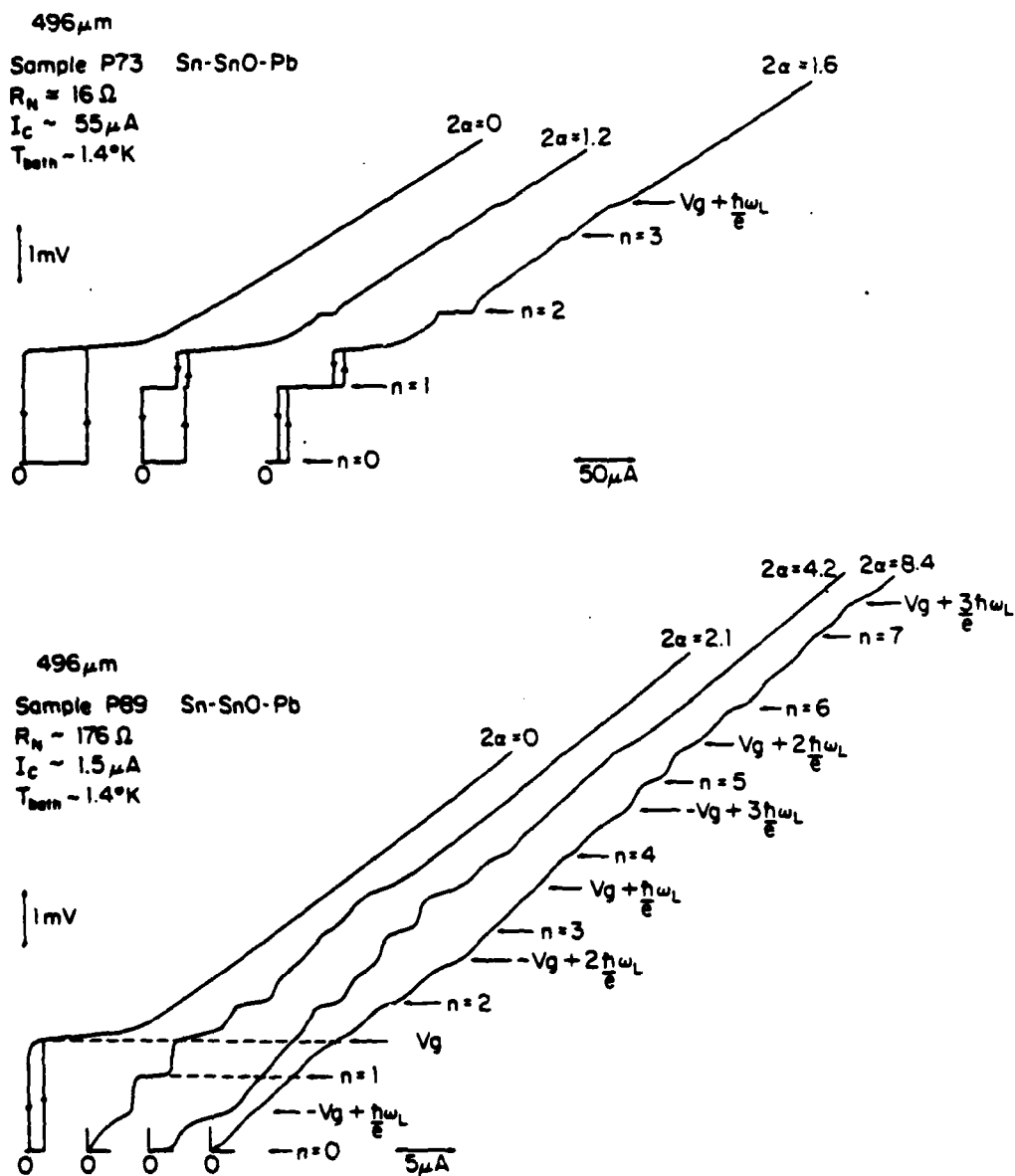


FIG. 4.5 (a) Typical I-V curves of a low-resistance sample for increasing laser powers. Here, $V_g = (\Delta_{\text{Pb}} + \Delta_{\text{Sn}})/e$. (b) Typical I-V curves of a high-resistance junction for increasing laser powers. Note the decrease in the critical current and its subsequent increase. The voltage of the first Josephson step is indicated by a dashed line; the I-V curves were taken at power levels given by the maximum of this step width and at subsequent zeroes. The current step at the gap is also identified by dashed lines.

using point contacts with long wire antenna structures and the same laser source. As a consequence of the well-characterized tunneling properties of these junctions it is possible to identify other features, such as the photon-assisted tunneling steps, not previously reported in the FIR spectral range. We find six steps originating from the gap structures at $V_g = (\Delta_{pb} + \Delta_{sn})/e$ and $-V_g$. They occur at voltages $V = \pm V_g + n(\hbar\omega_L/e)$, where n is an integer, as expected from the discussion of Section 2.3. The structure of these photon-assisted tunneling steps, Fig. 4.5(b), will be analyzed in detail in the next section. The response of the junction at 4.2 K has been studied as well. At this temperature the junction is an SIN junction so the Josephson steps are absent, allowing us to follow the variation of the photon-assisted steps with power.

Another simple qualitative observation is that the coupling of the junction to the FIR laser source is sensitive to the polarization of the incident electric field, the coupling being strong when the polarization of the FIR laser output is parallel to the antenna axis, the solid line in Fig. 4.6, and nearly zero when the polarization is perpendicular to the antenna axis, shown by the dashed line of Fig. 4.6. This observation demonstrates the expected coherent coupling of the focussed beam into the antenna and excludes any sort of diffuse parasitic coupling.

The variation of the step widths with the laser power can be studied. We have analyzed it in the same way as Weitz et al.¹², by plotting the observed step half-widths (normalized to the critical

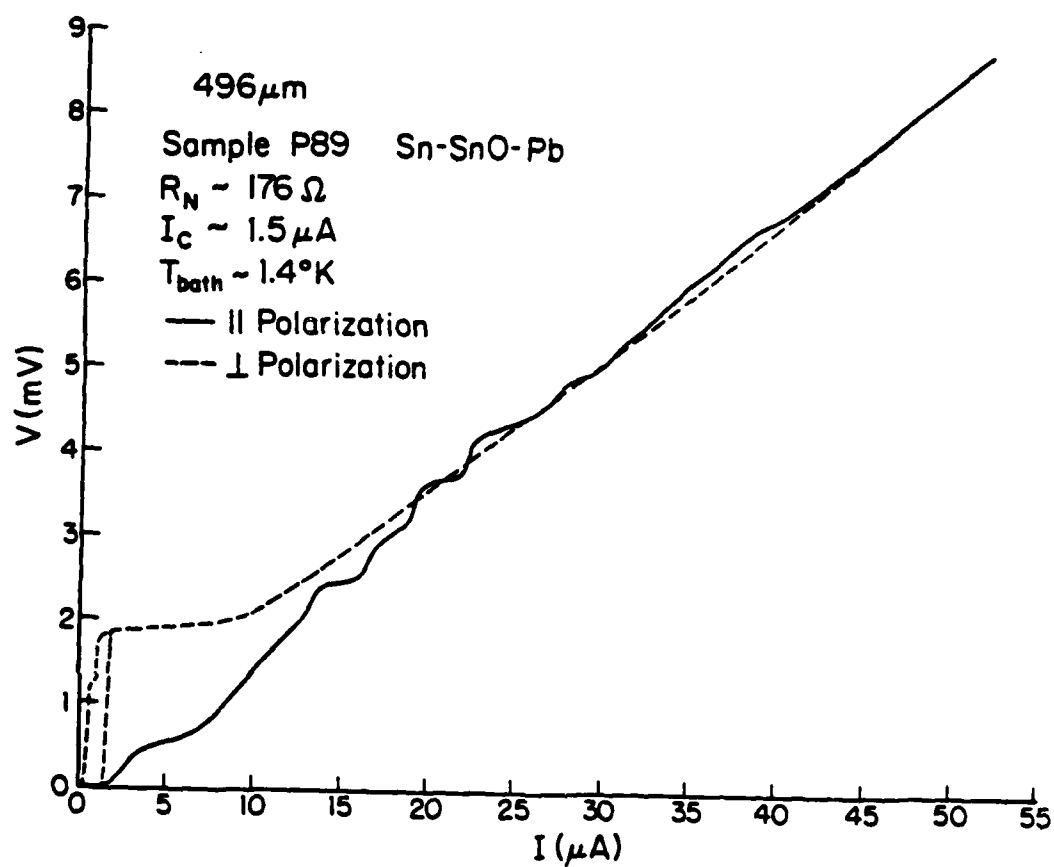


FIG. 4.6 Effect of the polarization of the FIR laser output relative to the antenna axis. Parallel polarization, //, couples well, whereas perpendicular polarization, \perp , does not, as expected. (See text.)

current in the absence of radiation) versus the normalized laser radiation voltage 2α . To obtain 2α from the square root of the power level measured on the reference thermal detector, we have chosen a single scaling factor for all steps for a given junction to take into account the coupling efficiency to that junction.

The frequency-dependent theory predicts that the half-width of the n th Josephson step is given by the n th term of the second sum in Eq. (2.29), at the voltage $V_0 = n(\hbar\omega_L/2e)$. The result is

$$I_n = \left| \sum_{k=-\infty}^{\infty} J_k(\alpha) J_{n-k}(\alpha) I_{J1}(|2k-n| \frac{\hbar\omega_L}{2e}) \right| \quad (4.2)$$

where for the moment we ignore the photon-assisted tunneling effect, and where ω_L is the laser frequency and I_{J1} is the pair response function defined by Eq. (2.18). This response function calculated by Werthamer⁹ for a tunnel junction with electrodes composed of two different superconductors at $T=0$ is

$$I_{J1}(\frac{\hbar\omega}{e}) = \begin{cases} \frac{1}{eR_n} \frac{2\Delta_1\Delta_2}{\Delta_1+\Delta_2} \frac{1}{(1-x^2)^{1/2}} K((\frac{\delta^2-x^2}{1-x^2})^{1/2}) & 0 \leq x \leq \delta \\ \frac{1}{eR_n} \frac{2\Delta_1\Delta_2}{\Delta_1+\Delta_2} \frac{1}{(1-\delta^2)^{1/2}} K((\frac{\delta^2-x^2}{1-\delta^2})^{1/2}) & \delta \leq x \leq 1 \\ \frac{1}{eR_n} \frac{2\Delta_1\Delta_2}{\Delta_1+\Delta_2} \frac{1}{(x^2-\delta^2)^{1/2}} K((\frac{1-\delta^2}{x^2-\delta^2})^{1/2}) & x \geq 1 \end{cases} \quad (4.3)$$

where $x = \hbar\omega/(\Delta_1+\Delta_2)$ and $\delta = |\Delta_1-\Delta_2|/(\Delta_1+\Delta_2)$, and R_n is the resistance of the

tunnel junction. To normalize Eqs. (4.3) to the critical current, we observe that if $\omega=0$, then

$$I_{J1}(0) = I_c(0) = \frac{1}{eR_n} \left(\frac{2\Delta_1\Delta_2}{\Delta_1+\Delta_2} \right) K(\delta) \quad (4.4)$$

which is the expression computed by Ambegaokar and Baratoff¹⁷, and Anderson⁹⁵, Eq. (2.22b). For superconducting electrodes made from identical superconductors, $\delta=0$, and Eq. (4.4) reduces to

$$I_c(0) = I_{J1}(0) = \pi\Delta(0)/2eR_n \quad (4.5),$$

the zero temperature limit of the expression

$$I_c(T)R_n = (\pi\Delta(T)/2e)\tanh(\Delta(T)/2kT), \text{ Eq. (2.22a).}$$

Inserting Eq. (4.4) into Eq. (4.3) we obtain:

$$I_{J1} \left(\frac{\hbar\omega}{e} \right) = \frac{I_c(0)}{K(\delta)} \begin{cases} \frac{1}{(1-x^2)^{1/2}} K\left(\left(\frac{\delta^2-x^2}{1-x^2}\right)^{1/2}\right) & 0 \leq x \leq \delta \\ \frac{1}{(1-\delta^2)^{1/2}} K\left(\left(\frac{x^2-\delta^2}{1-\delta^2}\right)^{1/2}\right) & \delta \leq x \leq 1 \\ \frac{1}{(x^2-\delta^2)^{1/2}} K\left(\left(\frac{1-\delta^2}{x^2-\delta^2}\right)^{1/2}\right) & x \geq 1 \end{cases} \quad (4.6)$$

where $x=\hbar\omega/(\Delta_1+\Delta_2)$ and $\delta=|\Delta_2-\Delta_1|/(\Delta_1+\Delta_2)$ and K is the complete elliptic integral of the first kind. Weitz et al.¹² and Hamilton²² use a slightly different notation for the pair response function $I_{J1}(\hbar\omega/e)$.

They define a new pair response function, I_p which is a function of the Josephson frequency $\omega_0 = 2eV_0/\hbar$. Their $I_p(\omega_0)$ can be obtained from our $I_{J1}(\hbar\omega/e)$ by replacing the dummy frequency variable ω in Eq. (4.6) by half the Josephson frequency $\omega_0/2$. With this change of variables Eq. (4.2) is:

$$\frac{I_n}{I_c} = \frac{1}{I_c} \left| \sum_{k=-\infty}^{\infty} J_k(\alpha) J_{n-k}(\alpha) I_p(|2k-n|\omega_L) \right| \quad (4.7)$$

which is Eq. (7) of Weitz, et al.¹² There is a logarithmic singularity (Riedel peak) in $I_{J1}[(\hbar\omega/e)=V_0]$ at the voltage corresponding to the gap voltage, i.e. when $V_0=(\Delta_1+\Delta_2)/e$. This corresponds to a Josephson frequency ω_0 of $2eV_0/\hbar=\omega_0=\omega_L$, or $\omega_0=\omega_L=[2(\Delta_1+\Delta_2)/\hbar]$.

Eq. (4.7) is easily evaluated on the computer, and we use the notation $W_n(2\alpha)$ for the step half-width divided by the critical current at the normalized voltage 2α , $(I_n/I_c)=W_n(2\alpha)$. The half-width of the n th Josephson step, calculated from the RSJ model is $(I_n/I_c)_{RSJ}=J_n(2\alpha)$ which we obtain from Eq. (2.35). The functions $W_n(2\alpha)$ and $J_n(2\alpha)$ are compared with the step width data for the low resistance sample of Fig. 4.5(a) in Fig. 4.7.

We obtain good agreement between theory and experiment for the $n=0$ and $n=2$ steps, but the predictions of the Werthamer theory and RSJ model are indistinguishable for the low values of 2α which were attainable. For the $n=1$ step, the Werthamer theory predicts an appreciably larger step than the RSJ model, but the data fall somewhat below both predictions. This discrepancy may be related to the apparent need to

SAMPLES P73, P81 Sn-SnO-Pb
 $\lambda = 496 \mu\text{m}$ $T_{\text{bath}} \sim 1.4^\circ\text{K}$

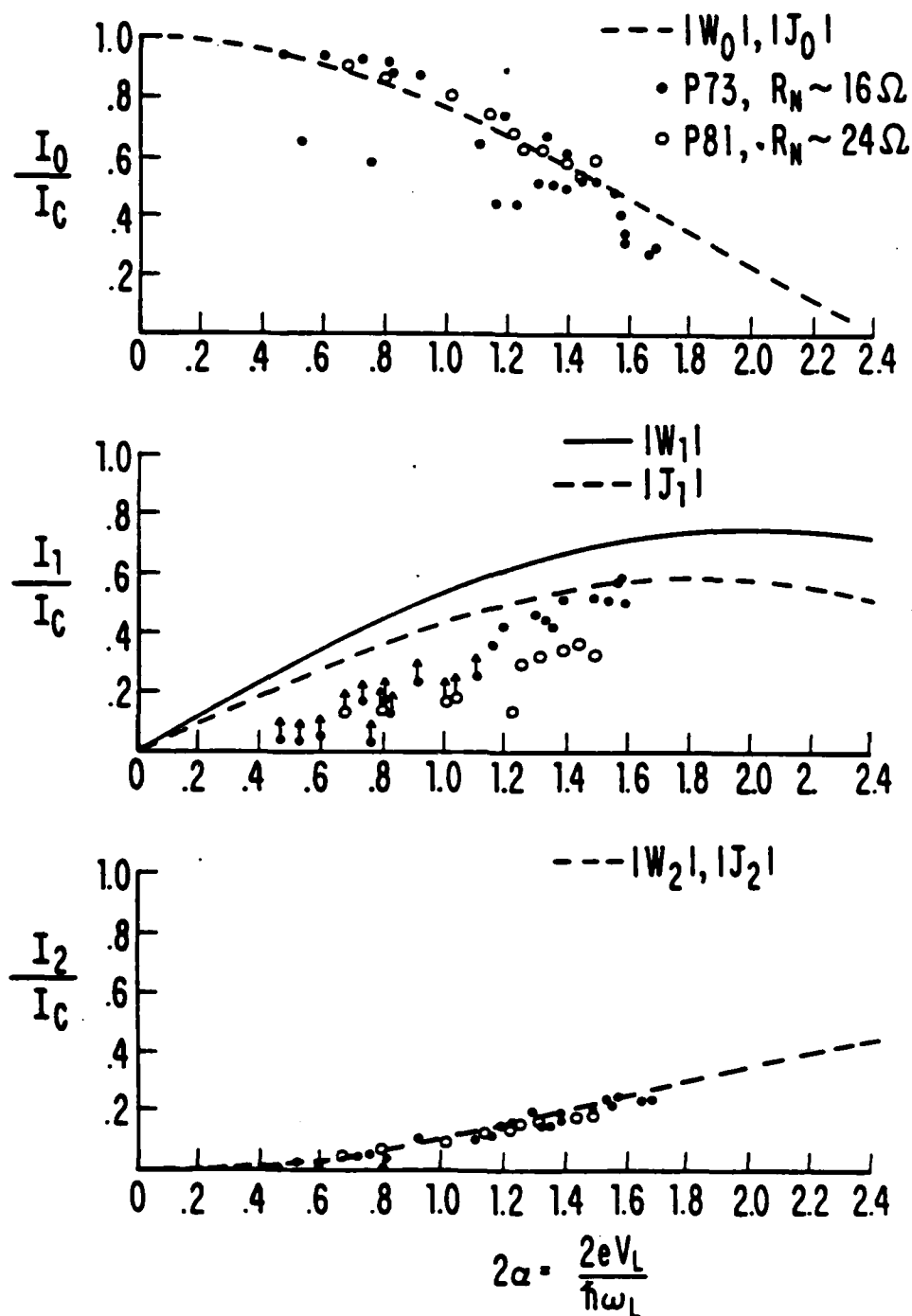


FIG. 4.7 Normalized step width as a function of the laser voltage in the junction compared with the Bessel function $|J_n|$ dependence and the Werthamer theory $|W_n|$, for a composite of data from two low resistance junctions. The data with arrows are from hysteretic steps and may underestimate the intrinsic width (see text).

exceed a threshold power level before the $n=1$ step appears, whereas the theoretical dependence is simply linear in 2α . Similar effects had been seen earlier in some point contact data. It presumably is related to the fact that the voltage on the $n=1$ step falls in the hysteretic part of the I-V curve below the energy gap voltage. We define the full width of the hysteretic step as the current separation between the jump up from the step in increasing current and the jump down from the step in decreasing current. Premature jumps triggered by noise, could cause the measured width to underestimate the intrinsic width of these hysteretic steps. These statements will be discussed more fully in the last section of this chapter, Section 4.5.

With the high-impedance junctions, such as the one shown in Fig. 4.8, larger values of 2α were obtained, allowing more steps to be seen. This permitted a more complete test of the comparative quality of the fit to the Werthamer theory and to the Bessel function dependence of the RSJ model. However, the predictions of the two models actually differ rather little, because neither the signal frequency nor its harmonics are very near the Riedel peak frequency for a Sn-Pb junction, and the scatter of the data in these measurements limits our ability to discriminate between the two. Still the Werthamer theory appears to give a slightly better fit to the observed positions of the zeroes of the step size. Neither theory fits the zeroth step very well. This step goes to zero more quickly than predicted by either theory; the same was true of the point-contact data of Weitz et al.¹² It may be due to the fact that the zeroth step width is reduced by square-law

$\lambda = 496 \mu\text{m}$
 SAMPLE P89 Sn-SnO-Pb
 $R_N \sim 176 \Omega$ $T_{\text{bath}} \sim 1.4^\circ\text{K}$

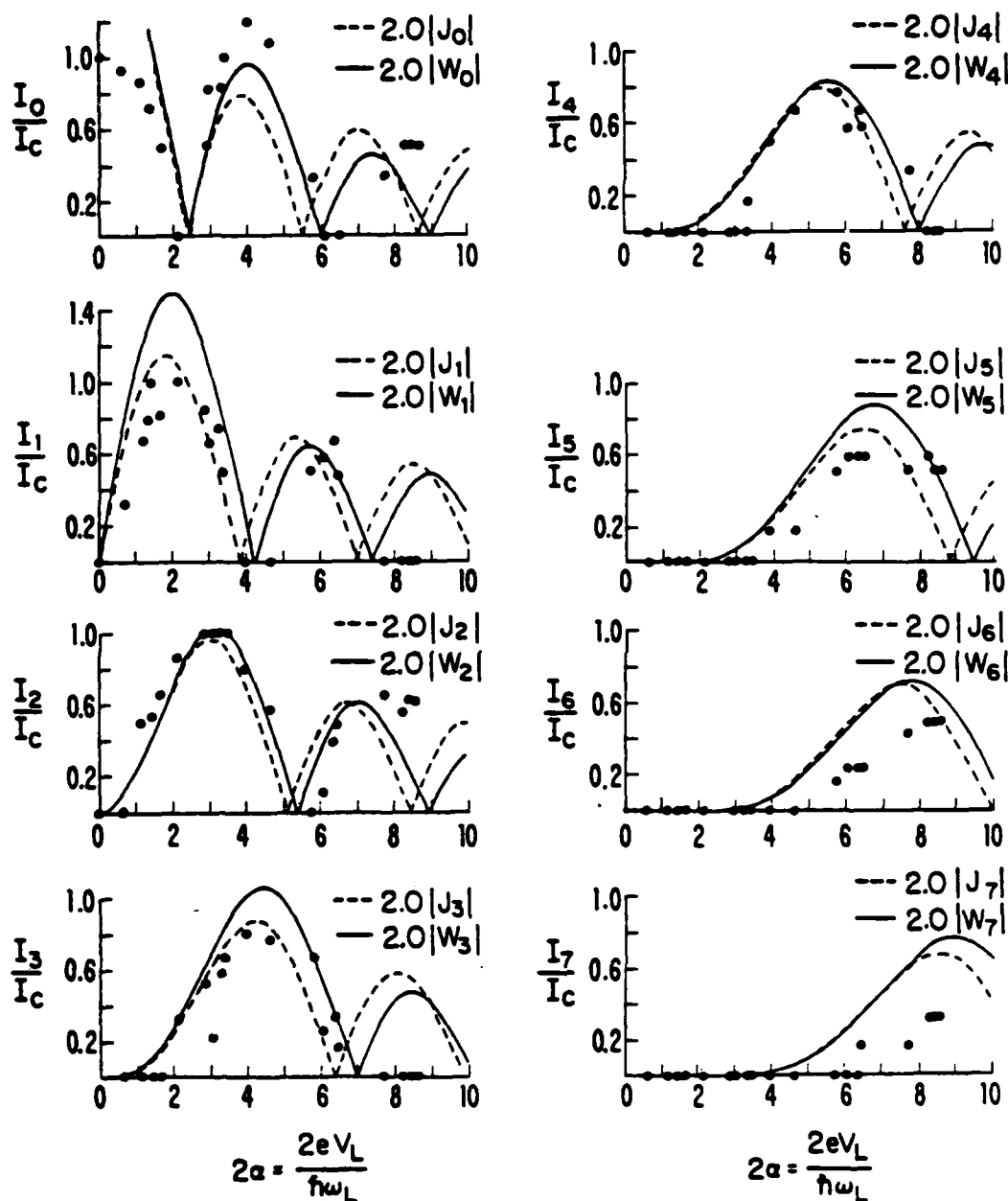


FIG. 4.8 Normalized step width as a function of the laser voltage in the junction compared with the Bessel function $|J|$ dependence and the Werthamer theory, $|W|$. The data is from a high-resistance (176Ω) junction. The theoretical widths have been multiplied by a scale factor of 2.0, as described in the text.

detection of noise at all frequencies in addition to the effect of the laser radiation. In making the fits of the absolute step widths to both models, a scaling factor of ~ 2.0 was required. We attribute the need for this scaling factor to an underestimate of the normalizing denominator I_c because of the above-mentioned noise and fluctuation effects in these high-resistance junctions, in which the nominal $I_c R_n$ product is well below the theoretical value.

The power dependence of the step half-widths was also measured using the 1.22 mm FIR laser line on a high resistance junction ($R_n \sim 156 \Omega$). The radiation was coupled to the junction by an antenna proportionately longer than the antenna for the 496 μm laser line. The step widths are plotted against $|W_n|$ and $|J_n|$ in Fig. 4.9. Constant scaling factors of 2.0 were also used in this Figure. The quality of the agreement between the data and the Bessel and Werthamer functions was very similar to that obtained with the 496 μm line. Surprisingly, the first step was much smaller than expected from either theoretical prediction, for unknown reasons. The second lobe of the power dependence of the zeroth step, as well as all the other steps, were in good agreement with the two (scaled) predictions, which were not all that different at the power levels obtained.

The constant scaling factors, exceeding unity, used in the fits for both the 1.22 mm and the 496 μm data, contrasts with the observations of Weitz et al.¹², on point contacts, in which the corresponding scale factors were less than unity, becoming more so with the higher steps, presumably due to increasing heating effects at the higher voltages. As

$$\lambda = 1.22 \text{ mm}$$

Sample P97

Sn-SnO-Pb

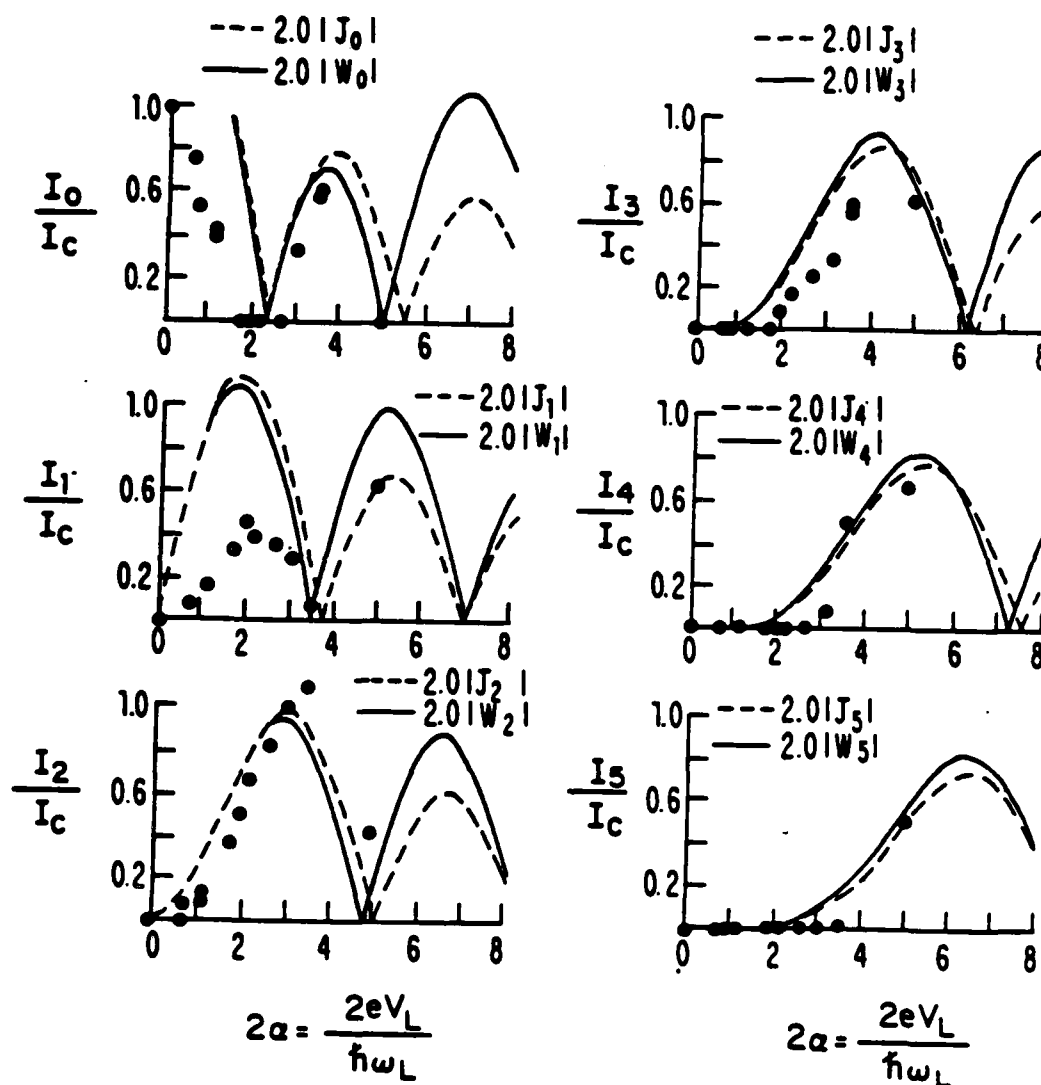
 $R_N \sim 156 \Omega$ $T_{\text{bath}} \sim 1.4^\circ \text{K}$ 

FIG. 4.9 Normalized step width as a function of laser voltage in the junction compared with the Bessel function dependence, $|J|$, and the Werthamer theory, $|W|$. The data shown is from a 156Ω junction irradiated by 246 GHz laser radiation. The theoretical widths have been multiplied by scale factors of 2.0 as described in the text.

mentioned in Section 2.5, even with all known corrections, the magnitude observed in point contacts was about a factor of 2 smaller than predicted by the theory. It is satisfying that our tunnel junctions give step widths which fit the theory with less need for corrections. This might be expected because the theory was derived for a tunnel junction, not a point contact, as shown in Section 2.2. Heating effects are reduced in the tunnel case because the voltage drop occurs across a high-resistance barrier rather than in a metallic constriction with high-conductivity.

Throughout this analysis we have left out the photon-assisted tunneling steps which have a rather drastic effect on the shape of the I-V curves, as seen in Figs. 4.5(a) and (b). In the following section we will analyze the photon-assisted tunneling steps, neglecting the Josephson steps for the junctions studied at 1.4 K, and in the last section of the chapter we will try to put the ac Josephson effect, photon-assisted tunneling effect, and noise rounding together in the analysis.

4.4 Photon-Assisted Tunneling Analysis

The photon-assisted tunneling effect comes from the first term of Eq. (2.29), derived originally by Tien and Gordon before Werthamer, and is written below for convenience as Eq. (4.8):

$$I(V_0) = \sum_{k=-\infty}^{\infty} J_k^2(\alpha) I_{qp}(V_0 + k(\frac{\hbar\omega_L}{e})) \quad (4.8)$$

As mentioned in Section 2.2, the Tien-Gordon result is that, upon irradiation of the junction, the dc I-V curve will have the form of a weighted sum of the dc I-V curves obtained without the radiation, each displaced in voltage by $k(\hbar\omega_L/e)$, and appearing with weight $J_k^2(\alpha)$. In physical terms, an electron in one electrode with energy $k\hbar\omega_L$ less than the lowest available state in the second electrode will tunnel through the barrier upon absorbing k photons of energy $\hbar\omega_L$; this will increase the current at a voltage corresponding to $\pm V_g + k(\hbar\omega_L/e)$, where V_g is the gap voltage, i.e., Δ/e for the SIN case and $(\Delta_1 + \Delta_2)/e$ for the S_1IS_2 case. The parameter α is, as before, $\alpha = eV_L/\hbar\omega_L$, where V_L is the laser radiation voltage across the junction.

In order to compare our data with this theory, we fitted the I-V curves obtained at different values of α , using theoretical curves calculated by digitizing the experimental dc I-V curves obtained at $\alpha=0$, and then using Eq. (4.8) to compute the I-V curve for a given α . The constant of proportionality (for a given sample and frequency) between the square root of the thermal power meter reading and the parameter α was determined both by fitting Eq. (4.8) and by fitting the theoretical α -dependence of the Josephson step widths. Since these two independent

methods gave results consistent to 5%, we are quite confident of our internally calibrated determination of α from the power meter reading. As can be seen in Fig. 4.10, the Tien-Gordon theory (dashed lines) gives a good fit to the PAT steps, and, although Eq. (4.8) completely ignores the Josephson effect, it gives a good account of the entire I-V curve shape except for the Josephson steps themselves.⁹⁶

We also applied similar analysis to data obtained at $T=4.2$ K, where the Josephson effect is absent because $T > T_c(\text{Sn})$. I-V curves for those SIN junctions, without and with radiation are shown in Fig. 4.11. The agreement between theory and experiment is very good, so that on the scale of Fig. 4.11(a), one can not distinguish between the theoretical and experimental curves. To be able to discern any differences, in Fig. 4.11(b) we compare the experimentally determined dV/dI with the theoretical expression. For $\alpha=0$, a large peak, reflecting the nonlinearity at $V=V_g$, is obtained, and for $\alpha \neq 0$, minima and maxima occur with period $\hbar\omega_L/e$. The position and magnitude of the maxima and minima agree well with the theory [dashed lines in Fig. 4.11(b)]

An important parameter characterizing detection efficiency is the current responsivity R , defined by Tucker as

$$R = \Delta I / (\frac{1}{2} V_L I_L) \quad (4.9)$$

Here ΔI is the change in the dc current upon irradiation of the junction, and the FIR power dissipated in the junction is $1/2 V_L I_L$ where I_L is the current at the FIR frequency. This responsivity reaches its quantum limit $e/\hbar\omega$ when for each photon absorbed an additional electron

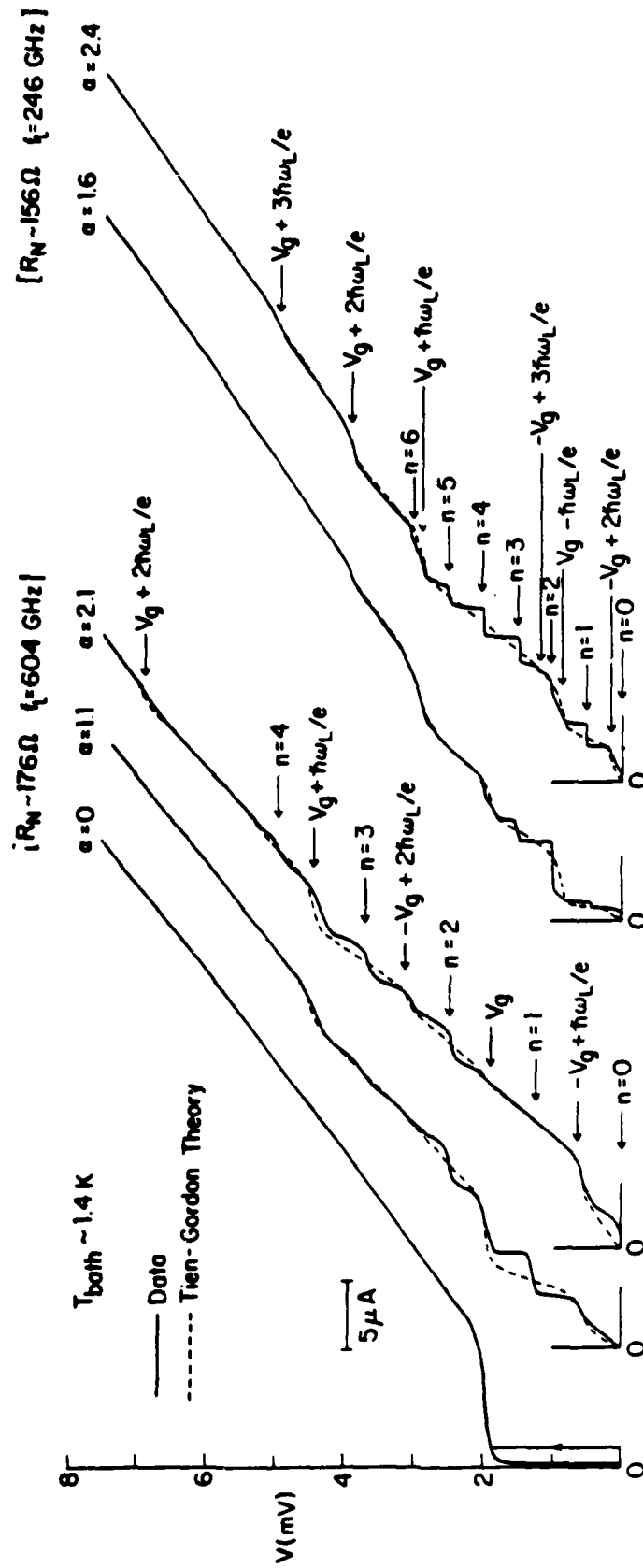


FIG. 4.10 I-V curves of two different junctions, each with suitable antenna length, irradiated at 604 and 246 GHz at 1.4 K. The dashed curves are obtained from the Tien-Gordon theory. This accounts for the photon-assisted tunneling steps at $\pm V_g \pm k\hbar\omega_L/e$ [where k is an integer and $V_g = (\Delta_{\text{BP}} + \Delta_{\text{SP}})/e$], leaving only local voltage displacements near the Josephson steps labeled by $n=0, 1, 2, \dots$.

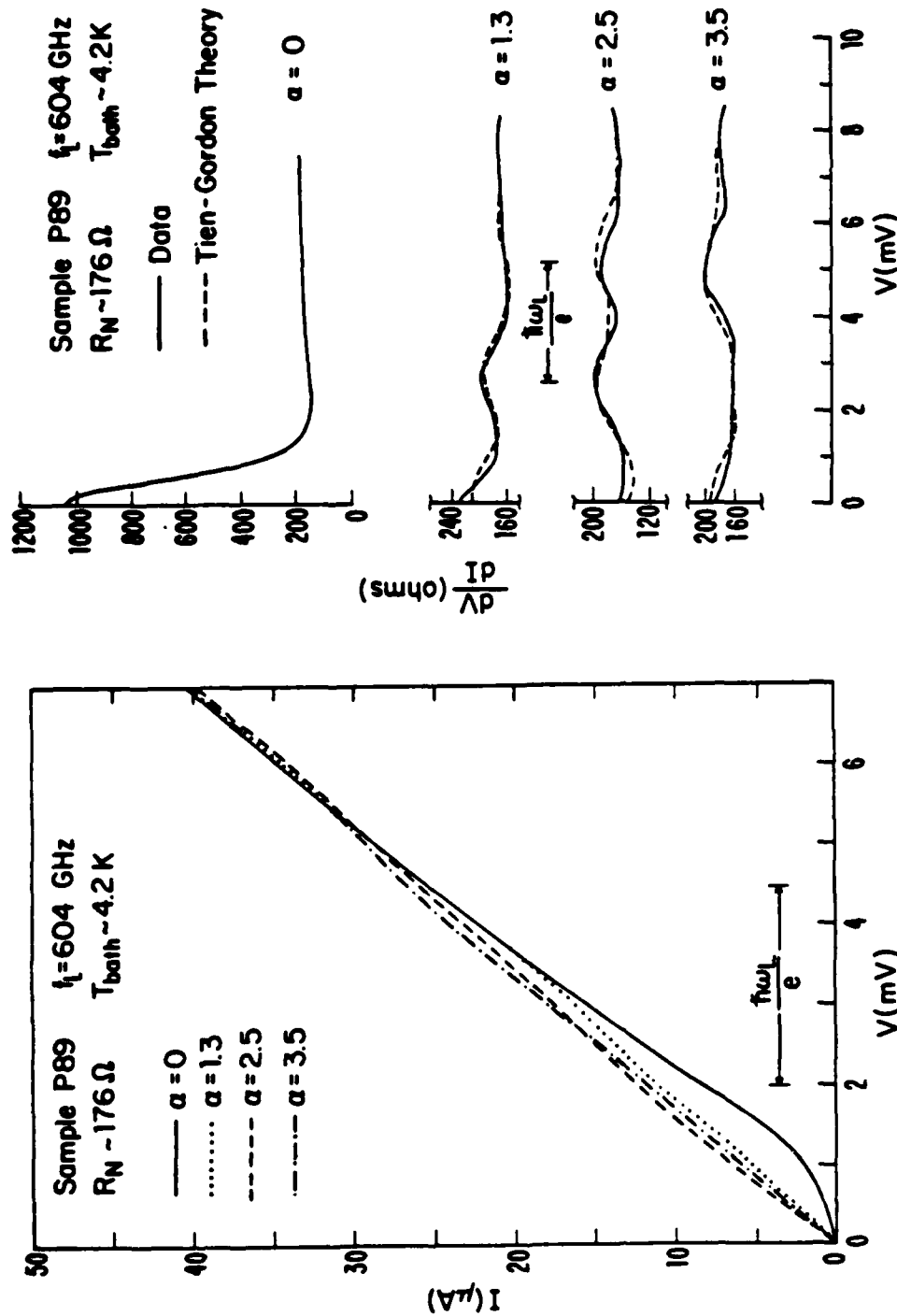


FIG. 4.11 (a) Superposed dc I-V curves for different values of the normalized FIR laser-induced voltage $\alpha = eV/\hbar\omega_L$ for a 176Ω junction at 4.2 K and a laser frequency of 604 GHz . Note that $\hbar\omega_L/e = 2.5 \text{ mV}$, which is indicated on the Figure by a bar. (b) Comparison between the voltage dependence of dV/dI computed theoretically for various FIR power levels and that obtained by digital differentiation of the experimental I-V curves in (a).

tunnels through the barrier. Before evaluating R , we compare the measured ΔI with the one computed using Eq. (4.8). This is done in Fig. 4.12 where we plot the measured changes in current at $T=4.2$ K for a 176Ω junction irradiated at 604 GHz. Also shown is the calculated ΔI versus α^2 , which is proportional to the radiation power, $1/2(\alpha^2/R)(\hbar\omega_L/e)^2$, that would be dissipated in the junction if it had its normal resistance. It is evident that the theory fits well the experimental variations of ΔI with laser power. Similar results were also obtained for $f_L=246$ GHz and for junctions of different resistances.

The theoretical responsivity in the limit of low power is then calculated from the dc I-V curve using the Tucker result⁹⁷

$$R = \frac{e}{\hbar\omega} \frac{I_{qp}(V+\hbar\omega/e) - 2I_{qp}(V) + I_{qp}(V-\hbar\omega/e)}{I_{qp}(V+\hbar\omega/e) - I_{qp}(V-\hbar\omega/e)} \quad (4.10)$$

Here, the numerator and the denominator are proportional to the quantum generalizations of d^2I/dV^2 and dI/dV , respectively. In Fig. 4.13, we plot R as a function of the bias voltage for a junction irradiated at 604 GHz. Using either experimental data or the theoretical $I_{qp}(V)$ for $T=4.2$ K, which differ hardly at all, we find that the highest computed responsivity is $0.47 (e/\hbar\omega)$. This maximum occurs at V_g , where we expect the nonlinearity to be greatest. For comparison, we show, in solid circles, the experimentally inferred values of R found from the initial slopes in Fig. 4.12, and we also plot (dashed line) R as a function of V as estimated from the data in Fig. 4.11 by assuming ΔI is linear in α^2 out to $\alpha=1.3$. In both procedures we obtain the incident power from

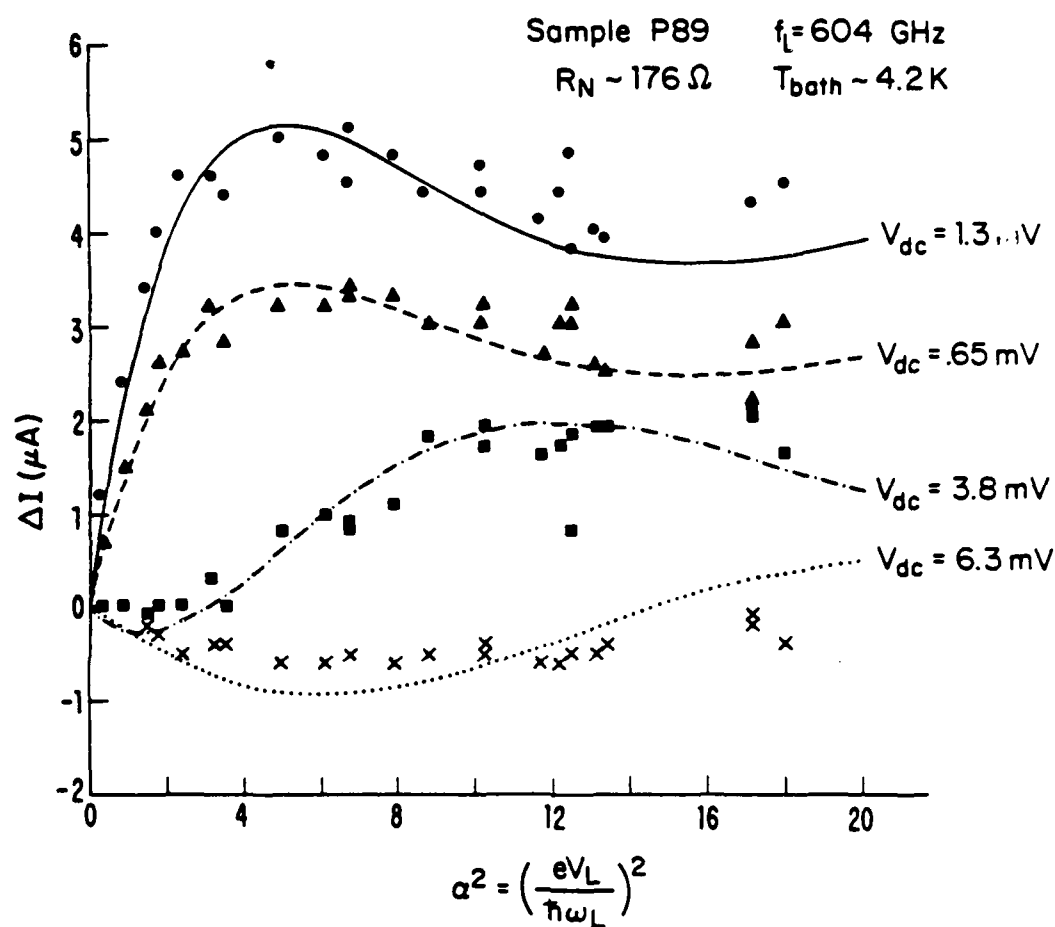


FIG. 4.12 Change in the dc current with laser power (α^2) at selected dc bias voltages. Points are experimental data; curves are computed theoretically from the zero-power I-V curve.

the value of α^2 by assuming that the conductance at f_L is given by the Tucker relation⁹⁷

$$I_L/V_L = (e/2\hbar\omega_L) [I_{qp}(V+\hbar\omega_L/e) - I_{qp}(V-\hbar\omega_L/e)].$$

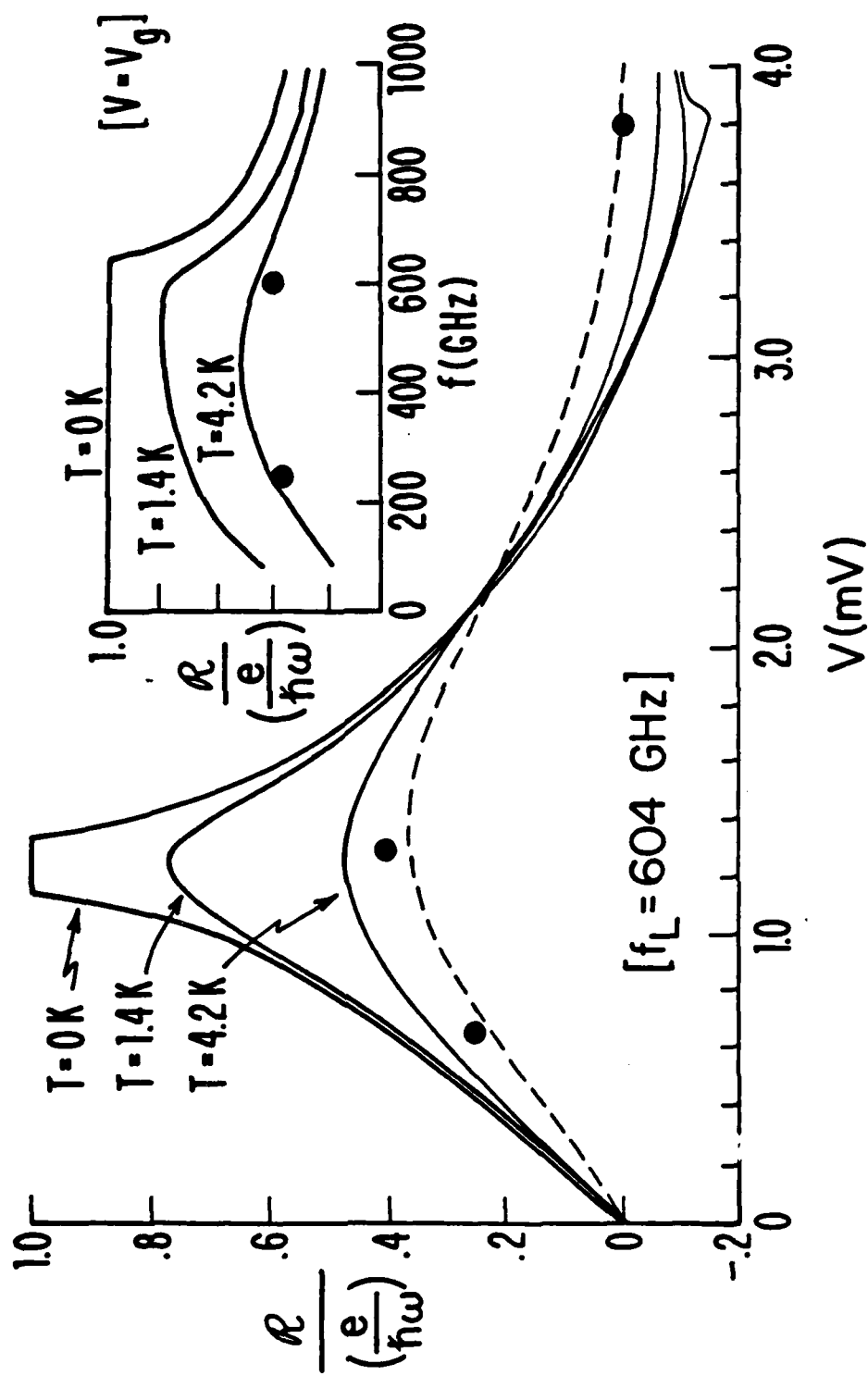
No large error should result from this assumption, since this theoretical conductance never differs from $1/R_n$ by more than a factor of 2.

There is good agreement among these various theoretical and experimental results. In addition, we show curves for $T=0$ and 1.4 K, computed using the theoretical I-V curves for a SIN junction; note that R reaches the quantum limit at $T=0$ over a small voltage range. Clearly there is an advantage in cooling the SIN junction to lower temperatures; for example, at $f_L=604$ GHz, the computed value of $R/(e/\hbar\omega)$ increases from 0.47 at 4.2 K to 0.75 at 1.4 K.

The frequency dependence of R , as predicted by Eq. (4.10) for a junction biased at V_g , is plotted in the inset of Fig. 4.13. At $T=0$, R has the full quantum limited value up to the gap frequency, where $\hbar\omega=2\Delta$. At higher frequencies R decreases rapidly, reflecting the fact that the nonlinearity of a SIN junction is limited to an energy range $\sim 2\Delta$. For $T>0$, R falls below the quantum limit at all frequencies. There is good agreement between the theory and our results at $f_L=256$ and 604 GHz.

It is worth mentioning that the remarkable agreement between the Tien-Gordon theory, which assumes a voltage-biased junction, and our

FIG. 4.13 Plot of current responsivity normalized to the quantum limit ($e/h\omega$) vs. dc bias voltage. Solid curves are computed for a frequency of 604 GHz from theoretical zero-power I-V curves. The experimental points are computed from the initial slopes of ΔI vs. α^2 at 4.2 K from Fig. 4.11. Dashed curve shows responsivity at 4.2 K estimated from data in Fig. 4.10. Inset shows computed frequency dependence of $R/(e/h\omega)$ at $T=0$, 1.4 and 4.2 K, for a bias of $V=V_g$, and experimental points at 246 and 604 GHz at 4.2 K.



findings is presumably due to the presence of sufficient junction capacitance to cause a voltage biasing for ac, although the junction is current biased at dc. This effective voltage biasing can also explain the agreement between the values of α determined from the Josephson effect data, and the values of α determined independently from the photon-assisted tunneling data.

4.5 Noise Effects

As noted in Section 4.3, noise rounding effects are unimportant in our lower resistance, higher critical current-density junctions. That is, the $I_c R_n$ product computed using the nominal I_c is close to the theoretical value for a Sn-Pb junction, as shown in Table 4.2 and Fig. 4.4. Moreover, the Josephson steps are flat and fitted very well by the simple RSJ form without noise rounding, as is illustrated in Fig. 4.14, which shows a step at 2.5 mV in a 16 Ω junction.⁹⁸

This situation is in clear contrast with that which prevails in the higher resistance junctions which give the best coupling to the radiation. In these the nominal $I_c R_n$ product falls increasingly below the theoretical value as R_n increases, the discrepancy reaching a factor of ~ 0.1 in a 381 Ω junction, as shown previously in Fig. 4.4. The systematic nature of the deviation suggests a fundamental origin, and we presume that this is a reduction of the apparent I_c by noise rounding.

Given the large depression of the dc critical current by noise currents, it is obvious that they would be expected to affect the higher Josephson steps as well. For example, if the effects of noise in narrowing the finite voltage steps were significantly less than that on the zero-voltage step, it could account for the need to scale up the ratios I_n/I_c by a factor of ~ 2 in Figs. 4.8 and 4.9. Model calculations reported below support this hypothesis. In addition to narrowing and rounding the steps, the noise gives them appreciable differential resistance, i.e. they are not flat.

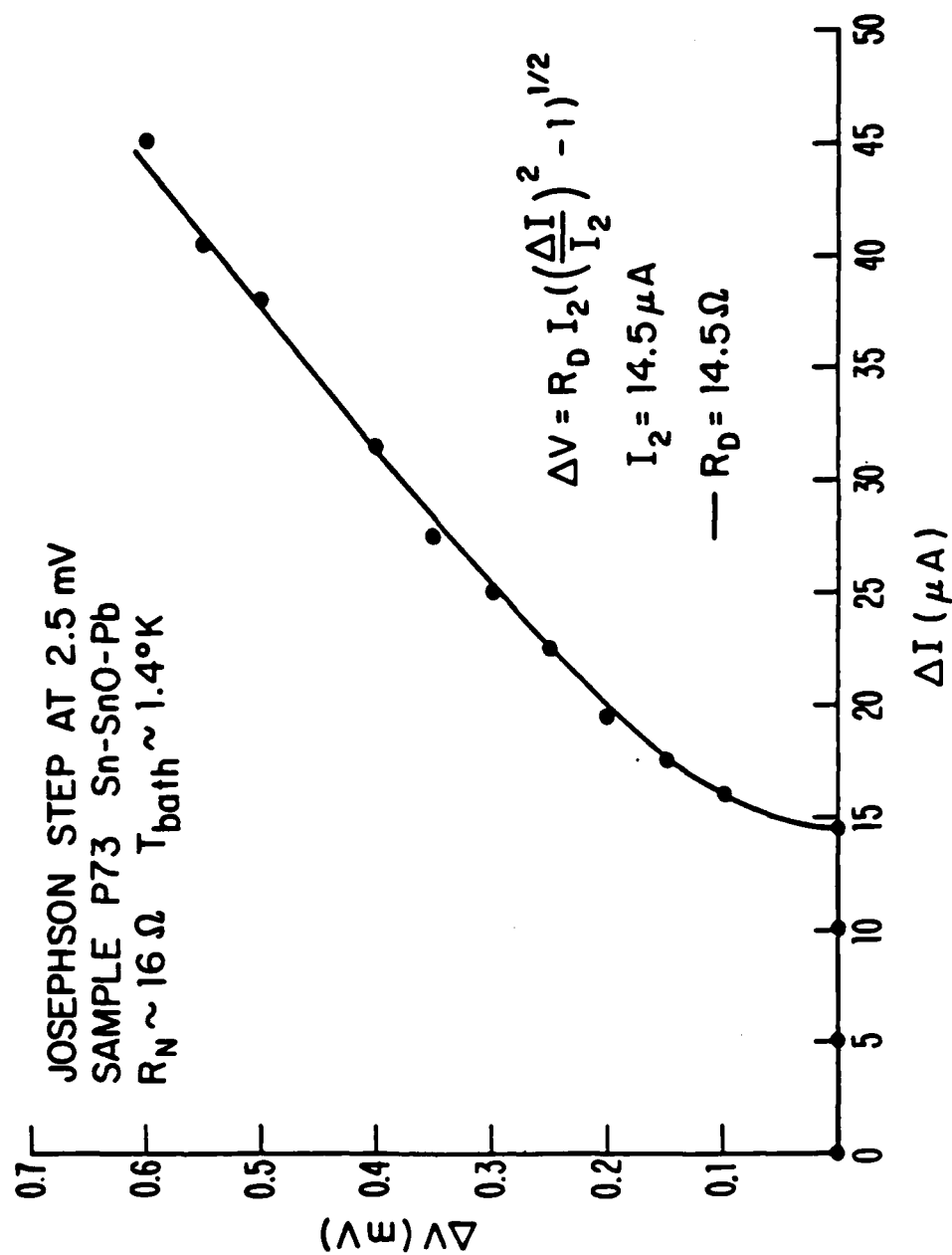


FIG. 4.14 Fit to the shape of the 2nd Josephson step on a 16Ω junction illuminated with 604 GHz laser radiation.

In this section we will examine the effects of noise based on two distinct approaches, first using the analytic result of Lee appropriate to noise rounding on low (but finite) β_c junctions, to determine by curve fitting an approximate noise temperature for a representative Josephson step on the 176 Ω junction.⁹⁸ The remainder of the section is devoted to a computer simulation of a capacitively shunted tunnel junction with a noise current.

4.5.1 The Lee Analytic Approximation

The Lee result³⁵ is valid in the limit of $\beta'_c < 1$. In the limit of zero capacitance, it reduces to the result of Ambegaokar and Halperin³⁴ which was used earlier to analyze the noise rounding observed with point contacts. Lee's result is displayed in Chapter II as Eqs. (2.49) and (2.50), and will not be reprinted here. The integrals T_1 and T_2 of Eq. (2.50) were evaluated numerically using Simpson's rule on an LSI-11 microcomputer.

We remind the reader that the Lee result we use describes the noise rounding of a step in terms of RSJ model parameters appropriate to that step, i.e., the unfluctuated step half-width, I_n^0 , the dynamic resistance at the step center in the absence of radiation, R_d , and so on (see Section 2.4). The usual β_c parameter for the dc current bias case, $\beta_c = 2eI_c R_n^2 C / \hbar$, is replaced by $\beta'_c = (2eI_n^0 R_d^2 C) / \hbar$. Since $\beta'_c \sim 2$ in our junctions, on the 4th step, at the power level studied ($2\alpha = 4.7$), the approximation for $\beta'_c < 1$ is not strictly applicable, but we assume

nonetheless that this approach will give at least a rough indication of the effect of noise on the steps. In fitting our data on the 4th step at 604 GHz (i.e., 5.0 mV), we assumed a value for R_d , the dynamic resistance near the step, given by the experimental curve, and used C , T_{eff} , and I_n^0 (the width of the n th step in the absence of fluctuations) as parameters. For example, as shown in Fig. 4.15 we obtain reasonable fits for the 4th step in a $176 \, \Omega$ junction using various combinations of $C \sim 0.01$ - 0.015 pF, $T_{\text{eff}} \sim 20$ - 25 K, and $I_4^0 \sim 2.2$ - 2.5 μ A, but wider excursions in these parameter values gave significantly poorer fits. This fitted value of I_4^0 is in reasonable accordance with the value computed using the Werthamer theory (Eq. (4.7)) and the nominal $I_C R_n$ (~ 1.2 mV) determined in low R_n junctions at 1.4 K. The agreement between the fitted I_4^0 and the one calculated from the Werthamer theory is significant because the measured $I_C R_n$ product is 0.26 mV, almost a factor of 5 lower, and because there was no need to scale the fitted step width by the factor of ~ 2 used in Figs. 4.8 and 4.9. This result supports our hypothesis that the scaling factors of ~ 2 came from an underestimate of the normalizing denominator in the step width fits, I_C , which is reduced by noise and fluctuation effects. The capacitance used is based on estimates determined from the sample geometry (Table 4.2 and Section 4.1).

These results are rather interesting because the noise temperatures found $T_{\text{eff}} \sim 20$ - 25 K are significantly higher than found in earlier work¹² on point contacts, in which the corresponding temperatures were $T_{\text{eff}} \sim 10$ - 15 K, also on the 4th Josephson step from the 496 μ m laser line

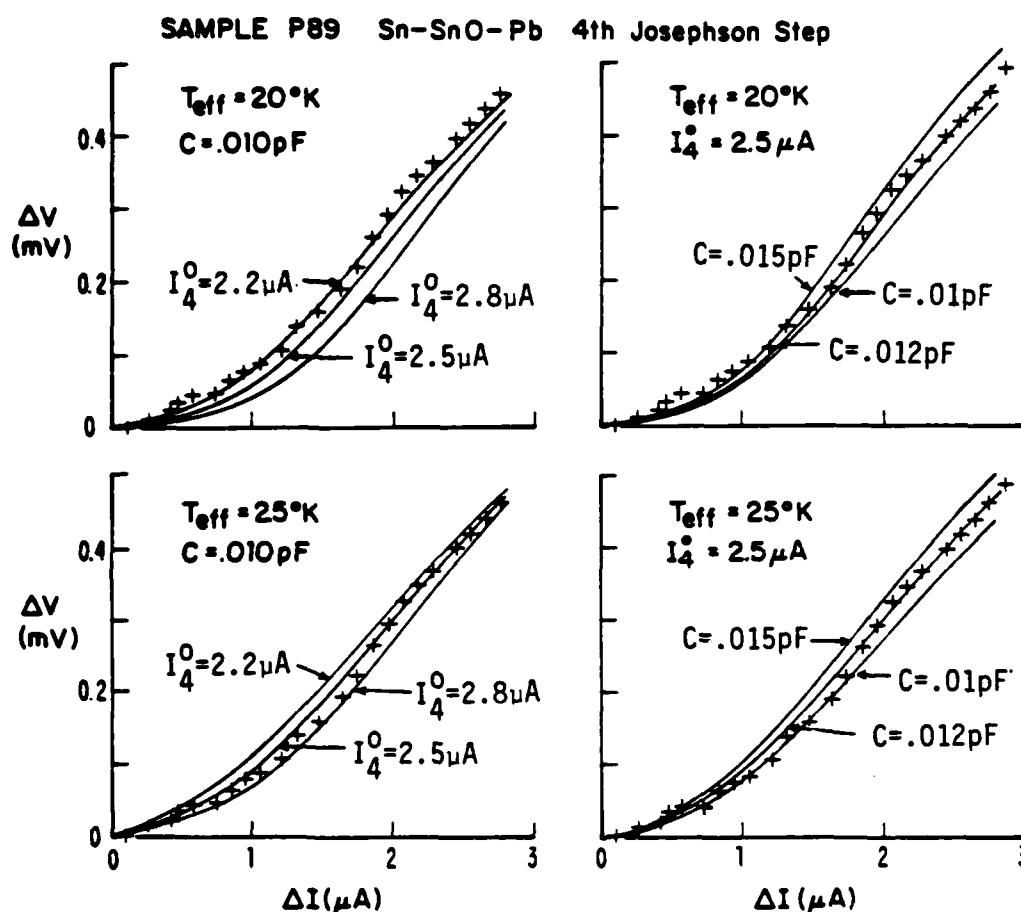


FIG. 4.15 Fits to the shape of the 4th Josephson step on a 176Ω sample at 604 GHz for different values of the fitting parameters I_4^0 , T_{eff} , and C .

using the same laser set-up on a point contact of similar resistance. (The theoretical result used in that earlier analysis was the $\beta_c=0$ limit of Eq. (2.49), which should be appropriate for a point contact.) The origin of this difference is that in a tunnel junction, shot noise gives a mean-square noise current, $\langle i_N^2 \rangle = 2eI_{qp} = 4kT_{eff}/R_n$, implying $T_{eff} = eV/2k \approx 29K$ for $V = 5.0$ mV (4th Josephson step at 604 GHz), whereas for a point contact, metallic heating gave $T_{eff} = \frac{1}{2}(T_{bath} + \frac{\sqrt{3}}{2\pi} \frac{eV}{k}) \approx 10K$ for the 4th step at 5.0 mV (604 GHz). Therefore, the large difference between the two observed noise temperatures is due to the different physical processes which give rise to the noise temperatures.

4.5.2 Computer Simulations

We turn now to our computer simulation analysis of noise effects in these junctions. Our approach is a phenomenological one in which we take the generalized RSJ model presented in Eq. (2.46), and solve it numerically on the computer for the situations relevant to the experimental results discussed in Section 4.3. We reprint this Equation here to aid in the discussion that follows:

$$\frac{d^2\phi}{d\tau^2} + g\left(\frac{d\phi}{d\tau}\right) + \sin\phi = \rho_{dc} + \rho_L \sin\Omega\tau + \hat{\rho}_N \quad (4.11)$$

where $g(d\phi/d\tau)$, the nonlinear tunneling current normalized to the critical current, is a function of the normalized frequency $d\phi/d\tau$. On the right hand side of Eq. (4.11) ρ_{dc} is the normalized dc bias

current, the time τ is normalized to the inverse plasma frequency $(\omega_J)^{-1}$, $\rho_L \sin \Omega \tau$ is the ac current source, and $\hat{\rho}_N$ is a Langevin noise term. Although it is possible to use the full nonlinear quasiparticle tunneling curve to model $g(d\phi/d\tau)$, we have chosen instead to approximate it as follows: for voltages below $eV = \Delta_{Sn} + \Delta_{Pb}$ we use an adjustable linear leakage resistance R_L which models the usual experimental observation of excess leakage current below the gap rise. Above $eV = \Delta_{Sn} + \Delta_{Pb}$ we use the full BCS quasiparticle I-V curve for $T=0$, since we will be considering experimental results far below T_C . In this manner execution times are made faster, but the results of the simulation, as we will show, provide adequate quantitative comparison to the experimental results.

The noise term on the right hand side of Eq. (4.11), $\hat{\rho}_N$, is treated in a white noise approximation with the following auto-correlation function:

$$\langle \hat{\rho}_N(\tau') \hat{\rho}_N(\tau + \tau') \rangle = \frac{2}{\beta_C} \frac{R_n}{(\hbar/e^2)} \frac{d\phi}{d\tau} \coth \left(\frac{R_n}{2(\hbar/e^2)} \frac{\gamma}{\sqrt{\beta_C}} \frac{d\phi}{d\tau} \right) \hat{\delta}(\tau) \quad (4.12)$$

where $\beta_C = 2eI_C R_n^2 C / \hbar$, $\gamma = \hbar I_C / ekT_N$, and $d\phi/d\tau$ is the dimensionless rate of change of the phase, while $\hat{\delta}(\tau)$ is a dimensionless δ function. In this calculation we are assuming that the fluctuations are coming from the normal resistance, R_n , i.e. we approximate the quasiparticle part of the I-V curve, $I_{qp}(V)$ by V/R_n , for the noise term (i.e. $\hat{\rho}_N$ on the right hand side of Eq. (4.11)). This is in contrast to our use of a

non-linear quasiparticle resistance on the left hand side of Eq.

(4.11). Eq. (4.12) is the current-current auto-correlation function in normalized units, coming from the power spectrum of Eq. (2.44), that is

$$\langle \hat{I}_N(t) \hat{I}_N(t+\tau) \rangle = 2eI_{qp}(V) \coth\left(\frac{eV}{2kT}\right) \delta(\tau) \quad (4.13)$$

where $V=V(t)$ is the instantaneous voltage, and $V=(\hbar/2e)d\phi/dt$. Eq.

(4.13) is converted to Eq. (4.12) by dividing both sides of the Eq. by I_C^2 , and by dividing the δ function by $(\omega_J)^{-1}$ to obtain a dimensionless δ function, besides assuming $I_{qp}(V)=V/R_n$.

Eq. (4.11) is solved numerically for the case of a current sweep by using a 4th order Runge-Kutta algorithm¹⁰⁰, which we describe only briefly here. The quantities we wish to solve for are the phase, ϕ at a time τ , which we denote by $V_1(\tau)=\phi(\tau)$, and the rate of change of the phase, $V_2(\tau)=\dot{\phi}(\tau)$, given a dc bias current, ρ_{dc} , rf drive current $\rho_L \sin\Omega\tau$, and noise current, $\hat{\rho}_N$. The method we use involves splitting the 2nd order equation of Eq. (4.11) into two simultaneous first order equations, and then applying the Runge-Kutta algorithm for each. The two first order equations are

$$\dot{V}_1 = f_1 = f_1(V_1=\phi, \tau) = V_2 \quad (4.14)$$

$$\dot{V}_2 = f_2 = f_2(V_1, V_2=\dot{\phi}, \tau) = \rho_{dc} + \rho_L \sin\Omega\tau + \hat{\rho}_N - g(V_2) - \sin V_1$$

$$(4.15)$$

The equations for V_1 and V_2 are solved for by the Runge-Kutta algorithm, which we illustrate with V_2 . We take $\tau_i = ih$, $\tau_{i+1} = \tau_i + h$, where i is an integer greater than zero so that

$$V_2(\tau_{i+1}) = V_2(\tau_i) + \frac{h}{6}(k_1 + 2k_2 + 2k_3 + k_4) \quad (4.16)$$

where the k_i are given by

$$\begin{aligned} k_1 &= f_2(\tau_i, V_1(\tau_i), V_2(\tau_i)) \\ k_2 &= f_2(\tau_i + \frac{1}{2}h, V_1(\tau_i + \frac{1}{2}h), V_2(\tau_i) + \frac{1}{2}hk_1) \\ k_3 &= f_2(\tau_i + \frac{1}{2}h, V_1(\tau_i + \frac{1}{2}h), V_2(\tau_i) + \frac{1}{2}hk_2) \\ k_4 &= f_2(\tau_i + h, V_1(\tau_i + h), V_2(\tau_i) + hk_3) \end{aligned} \quad (4.17)$$

A similar set of equations applies to $V_1 = \phi(\tau)$. The current is incremented in fractions of the critical current, usually $\Delta\rho_{dc} = 0.01$. (A value of $\rho_{dc} = 1$ is the critical current in normalized units.) At the initial current level, i.e. $\rho_{dc} = 0.01$, the algorithm starts with $\tau_0 = 0$, and with the initial conditions for the phase and derivative of the phase, $V_1 = \phi(0) = 0$, and $V_2 = \dot{\phi}(0) = 0$. The time increment, h , is in units of the inverse of the plasma frequency, and is typically 0.04. The algorithm waits for a period of time to permit initial transients to die out, and then the average voltage is calculated by the average of V_2 divided by $(\beta_c)^{1/2}$, i.e. $V/I_c R_n = (\beta_c)^{-1/2} d\phi/d\tau$. After this the current is incremented and the algorithm calculates $\phi = V_1$ and $\dot{\phi} = V_2$ at the new current point, using the last value of V_1 and V_2 from the

previous current point. The total averaging time for each current point in units of inverse plasma frequency, $(\omega_J)^{-1}$, is given by $\tau_{av} = [2\pi/\Omega h][\tau_{total} - \tau_{wait}]$, typically $\sim 10^4 - 10^5$, where $\Omega = \omega_L/\omega_J$ as before, and h is the time increment.

The noise term, $\hat{\rho}_N$, is calculated at each point in time in the following way. First, the average is taken of 12 numbers, x_i , selected from the interval $[0,1]$ by a pseudo-random number generator. This procedure produces an approximately gaussian distribution with mean of $1/2$ and width $1/12$. The mean is shifted to zero by subtracting $1/2$ from this average, and the width is adjusted to give the required mean-squared current noise from Eq. (4.12)^{31,101}. In this discrete version then the noise current at a time τ_i is denoted by $(\rho_N)_i$:

$$(\rho_N)_i = \left[\left(\frac{2}{h\beta_c} \right) \left(\frac{R_n}{(\hbar/e^2)} \right) \frac{d\phi}{d\tau} \coth \left(\frac{R_n}{2(\hbar/e^2)} \frac{\gamma}{\sqrt{\beta_c}} \frac{d\phi}{d\tau} \right) \right]^{1/2} \times \left(\sum_{k=1}^{12} (x_k - 1/2) \right) \quad (4.18)$$

The discretizing of the time variable causes the δ function $\hat{\delta}(\tau)$ to become, $\hat{\delta} \rightarrow (1/h)\delta_{i,0}$, where $\delta_{i,0} = 1$ if $i=0$ ($\tau_i = \tau_0 = 0$), and is zero otherwise, where h is the size of the time step.

We can now examine the results of the simulation beginning with the dc case. The method summarized by Eqs. (4.11)-(4.18) is applied now to the situation where there is no rf current, only dc current and noise, to determine the effect of noise on the critical current. For a noise temperature of 2 K, Fig. 4.4 shows that this computation reproduces the observed fall-off of the $I_c R_n$ product with increasing R_n . The solid

circles in Fig. 4.4 are the data from Table 4.2, while the open circles are the results of the simulation. For low resistance, low β_c junctions, the $I_c R_n$ products are approximately constant shown by the dashed line in the Figure. On the other hand, for the high-resistance junctions measured the critical currents are considerably lower than expected from the behavior observed with the low resistance junctions, in agreement with the simulated behavior shown by the open circles and the solid line. The error bars on the calculated points, at the high R end of the curve, are equal to the variance of the I_c 's from the 5 runs with the simulation. Note that the agreement is good for junctions ranging in resistance over two orders of magnitude. The deviation of the simulated curve from the data may be due to the relatively short averaging time of the simulation (~ 10 μ sec to sweep from zero current to the critical current) relative to that on the laboratory scale (~ 10 secs to sweep from zero current to the critical current). Therefore, the fast sweep rate used in the simulation may underestimate the effect of the noise. It is assumed that the capacitance does not vary from junction to junction in the simulation, whereas in fact the capacitances do vary by a factor of ~ 5 , which may also explain the observed deviation between the simulation and the data.

The simulation produces an I-V curve with the shape shown in Fig. 4.16(a) closely reproducing the observed switching behavior in Fig. 4.16(b). The dashed lines in Fig. 4.16(a) indicates the computed I_c for this junction; the variance on the computed I_c is given by the dotted lines in the Figure. In the simulation the switching from the

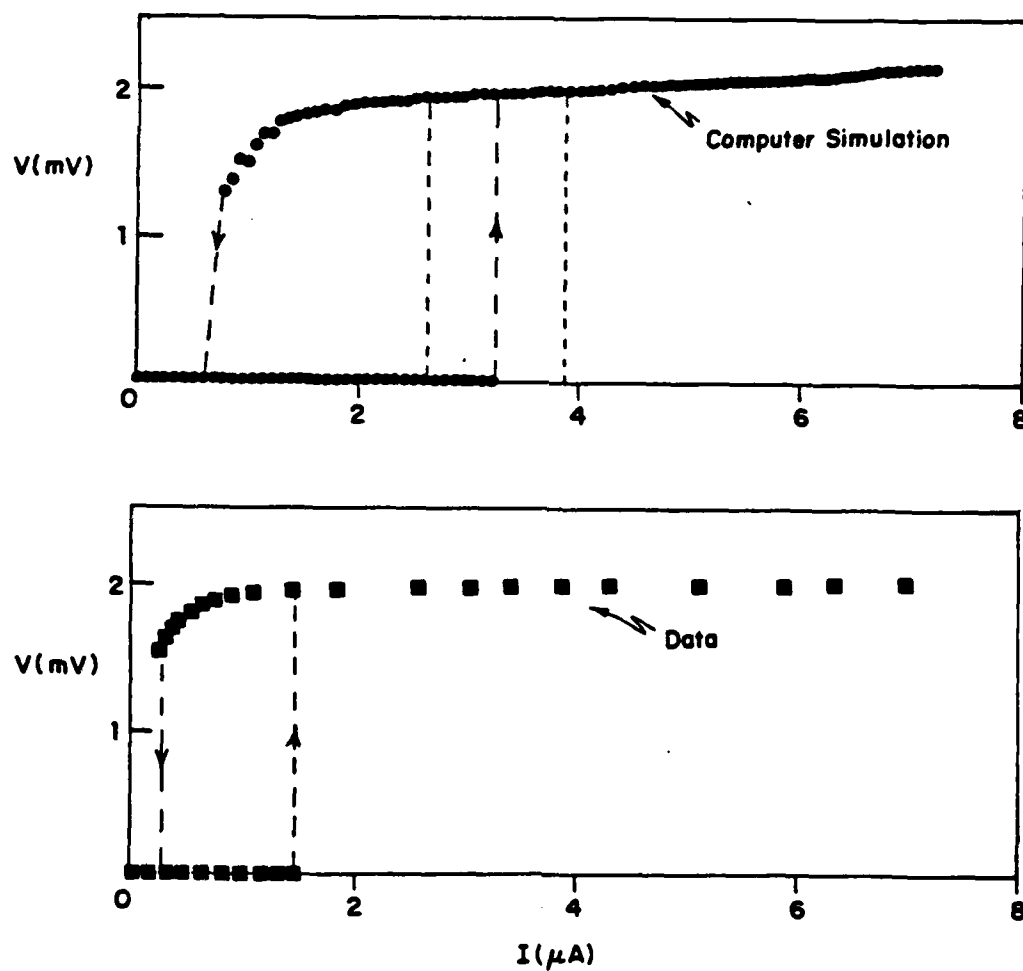


FIG. 4.16 (a) Simulated I-V curve with noise but no ac currents. Switching at critical current shown by dashed lines. Critical currents from simulation (for 5 runs) fall within bounds indicated by dotted lines (see text). (b) I-V curve from the 176Ω junction (data). The noise temperature used in the simulation is $T_N=2K$, while the bath temperature is $1.4K$.

non-zero voltage state to the zero-voltage state occurs at a higher current level than the data, perhaps due to the assumed leakage resistance of 10 times the normal resistance, which may be too low, as may the assumed noise temperature of 2K.

We now simulate the effects of the laser radiation on the junctions. Fig. 4.17(a) shows the simulated critical current with laser power divided by the zero power critical current (in the absence of noise), while Fig. 4.17(b) displays the full-width of the first step, also in the absence of noise. Fig. 4.17(b) is labelled with I_{ab} where the step width is measured only by the distance in current from the point a to the point b, shown by the inset of the Figure, i.e. the portion of the step on the upsweep. I_{db} labels the maximum width of the step, the region in current from d to b in the inset of the Figure. We find for the finite capacitance case, $\beta_C \sim 6-7$, studied in the Figure, that the step widths, I_{db} , are adequately described by the Bessel function step width formula used before for a voltage biased (dc and ac) RSJ model junction:

$$I_n/I_C = J_n(2\alpha) \quad (4.19)$$

for the step half-widths. In order to make a comparison with the experimental data or the simpler voltage biased RSJ model, a relationship must be found between $2\alpha = 2eV_L/\hbar\omega_L$, the normalized ac voltage in the junction (e.g. fitted from the data), and I_L/I_C , the normalized ac current used in the RSJ model simulation. For the finite capacitance case a simple relationship between the two has been found:

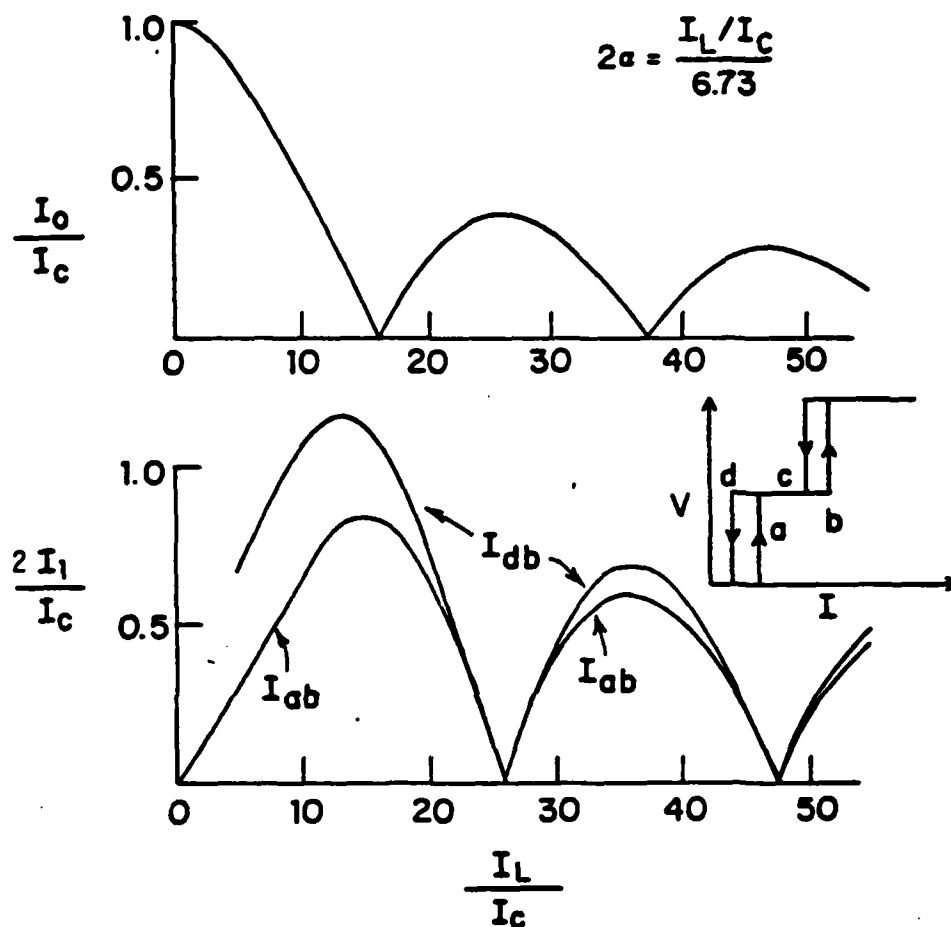


FIG. 4.17 Zeroth and first step simulated behavior for a junction with rf and dc bias but no noise. (a) Zeroth step half-width normalized to the critical current. (b) First step full-width normalized to I_c . Note that if the width of the upsweep is taken, I_{ab} , the width is underestimated, whereas I_{db} , the full-width of the step including the downsweep reproduces the Bessel function behavior.

$$2\alpha = \frac{I_L/I_C}{\Omega(\Omega^2 + \beta_C^{-1})^{1/2}} \quad (4.20)$$

where $\Omega = \omega_L/\omega_J$, and $\beta_C = (2eI_C R_n^2 C)/\hbar$, as before. In Fig. 4.17 the Bessel functions, $J_0(2\alpha)$ for the zeroth step, and $2J_1(2\alpha)$ for the first step full-width, both normalized to the critical current, are indistinguishable from the lines drawn, for $2\alpha = (I_L/I_C)/6.73$. This result was predicted by Braiman et al.¹⁰² for a resistively shunted junction model with $G(V) = 1/R_n$, for the limit of $\Omega \gg 1$. This latter condition is only marginally satisfied by the sample in Fig. 4.17. Fig. 4.17(b), together with the experimental results of Fig. 4.7, indicate that it is the width of the fully hysteretic step that is of importance, justifying the procedure used earlier for the analysis in Section 4.2 and Fig. 4.6.

If noise is included in the simulation of the zeroth step, at the maximum of the first hump of the Bessel function, J_0 , that is at $2\alpha = 4.0$, or $I_L/I_C \sim 27$, the step is rounded somewhat. Fig. 4.18 plots the simulated zeroth step I-V at this power level. Plotted with the simulation is the computed noise-reduced critical current at zero laser power. The error bars indicate the limits on the computed critical current. With the 2 K noise temperature chosen, the step width divided by this critical current is about 0.5, which is roughly the expectation for the step width ratio without noise. If the noise temperature used is higher (in fact up to ~ 10 K), enough to suppress the fluctuated critical

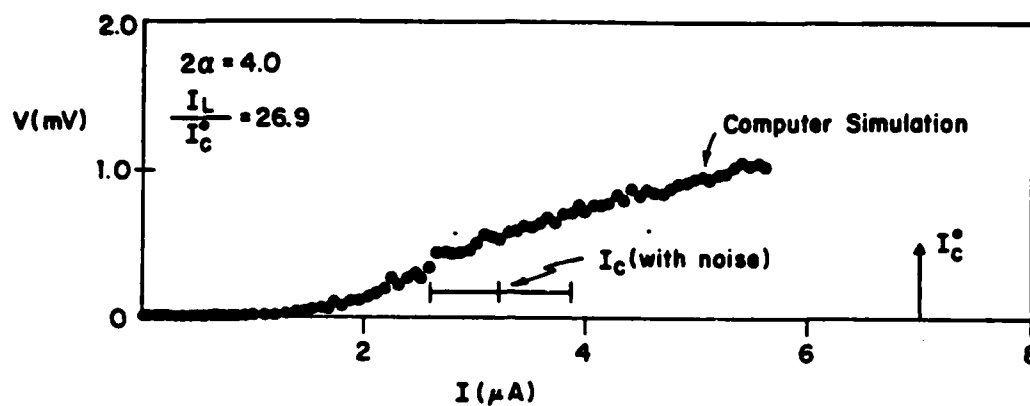


FIG. 4.18 Simulated step at $2\alpha=4.0$ Arrow labeled by I_c^0 is the unfluctuated critical current estimated from the nominal $I_c R_0$ product (see text). The critical current with noise is also shown, as well as the estimated errors on the simulated critical current, i.e., the error bars drawn.

current closer to the measured value or the averaging time in the simulation is longer, the size of the zeroth step at $2\alpha=4$ does not change significantly, even though the critical current at $\alpha=0$ is reduced much more. The simulated critical current without laser power can be reduced enough so that the ratio of the noise rounded zeroth step-width at $2\alpha=4.0$ to the noise rounded critical current is roughly unity. This would justify the scaling factor of ~ 2.0 for the Bessel and Werthamer functions used in the analysis in Section 2.2.

We can now attempt to model the effects of noise on the complete I-V curve of a junction at a particular laser power. We choose $2\alpha=4.0$, the power level used in the Fig. 4.18. We create a simulated tunnel junction I-V curve complete with photon-assisted tunneling steps and noise rounded ac Josephson steps in the following way. Using the simulation, we create a noise rounded I-V curve with only Josephson steps. We subtract off the smooth background as a function of voltage from this I-V curve, leaving only the local current displacements from the ac Josephson steps. A simulated I-V curve with only photon-assisted tunneling steps is created from the dc quasiparticle I-V curve for this particular choice of 2α following the procedure described in Section 4.4. This I-V curve is very similar to the dashed curve for the 176Ω junction at $\alpha=2.1$ shown in Fig. 4.9. The local current displacements from the ac Josephson effect are added as a function of voltage to the I-V curve with only the photon-assisted tunneling steps, creating an I-V curve with both photon-assisted steps and ac Josephson steps. The results of this procedure are shown in Figs. 4.19(a)-(c). In Fig.

4.19(a) we show the experimental I-V curve at $\alpha=2$ we are simulating. The simulated I-V curve is shown in dashed lines next to the experimental I-V curve (Fig. 4.19(b)), while Fig. 4.19(c) plots the simulated I-V curve (dashed lines) on top of the experimental I-V curve shown in the solid lines. It is remarkable how similar the simulation is to the actual data. The differences between the simulation and the data, particularly at the 3rd step, are most likely due to the fact that the simulation does not include any effects of the frequency dependence of the step widths. That the two effects should add in current at each voltage is precisely the expected behavior from the Werthamer result for a voltage biased junction, i.e., as in Eq. (2.29), further confirming that the finite capacitance of the junction makes it appear approximately voltage biased.

We can apply the above procedure to the situation of the 4th step, analyzed previously with the simple result of Lee (Fig. 4.14), which ignores photon-assisted tunneling. Fig. 4.20 displays the results of the procedure. All four curves show the 4th step, measured from the center of the step, with the data shown as a solid line, and the simulation as the solid circles. The power level is $2\alpha=4.0$ for the upper curves, while $2\alpha=5.75$ for the lower curves. Note that while the upper left I-V curve fits the data very well, the lower left simulated curve lies below the data. The difference at the higher power level could be due to the presence of a photon-assisted tunneling step distorting the I-V curve. To test this conjecture, on the right half of Fig. 4.20 are I-V curves measured from the step center where

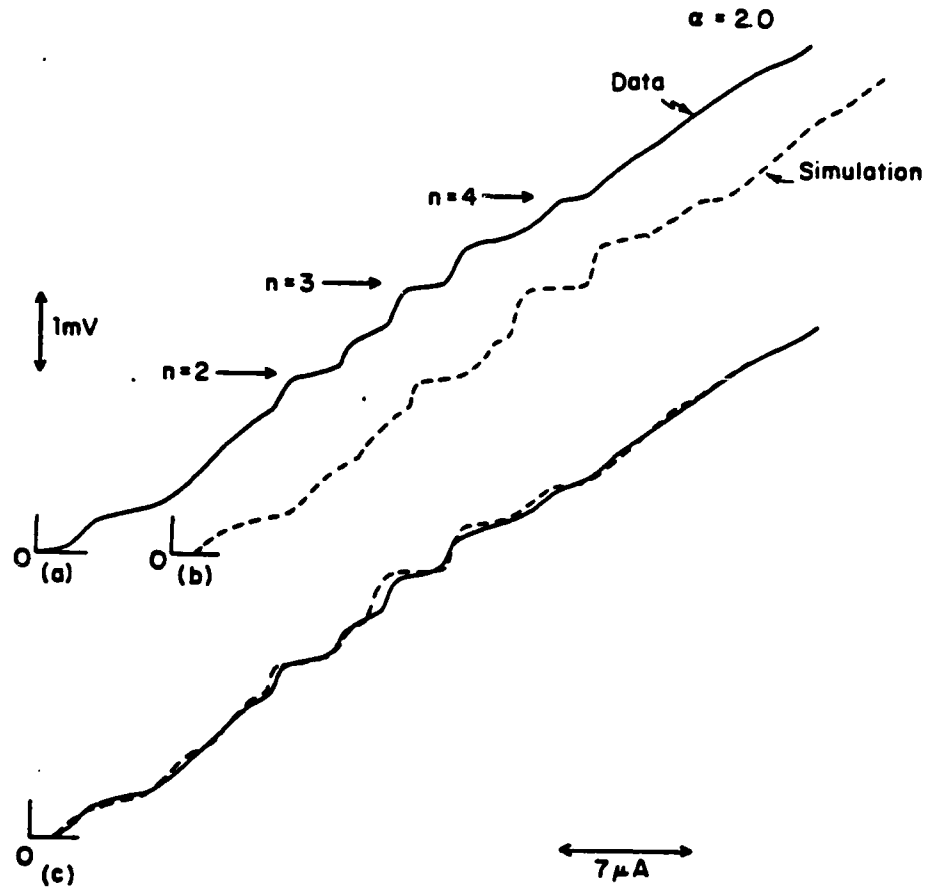
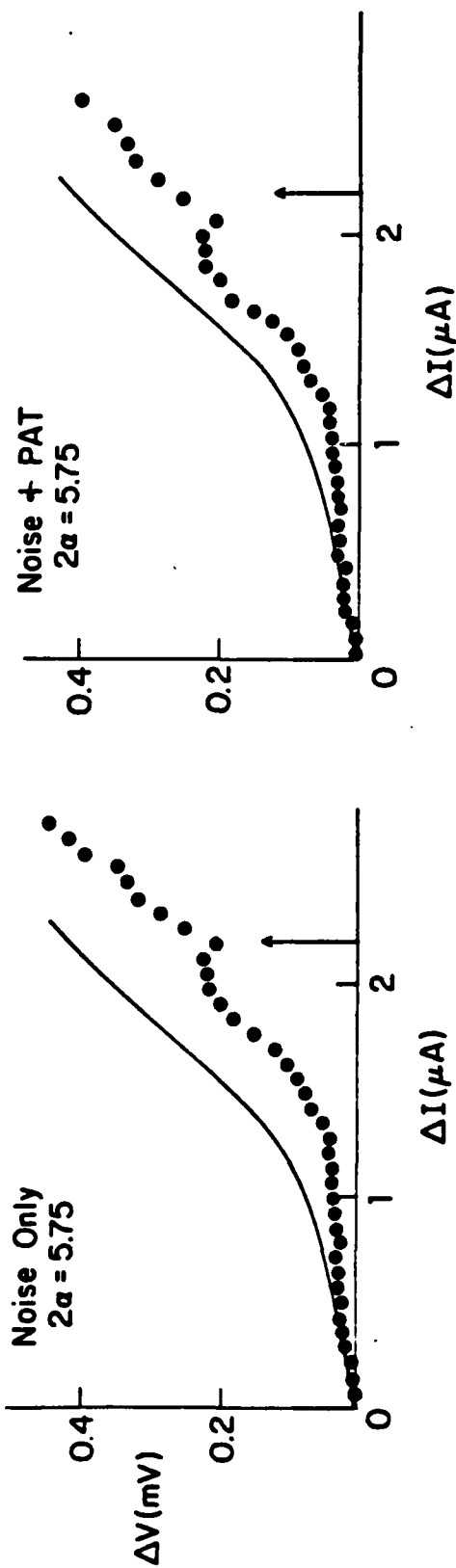
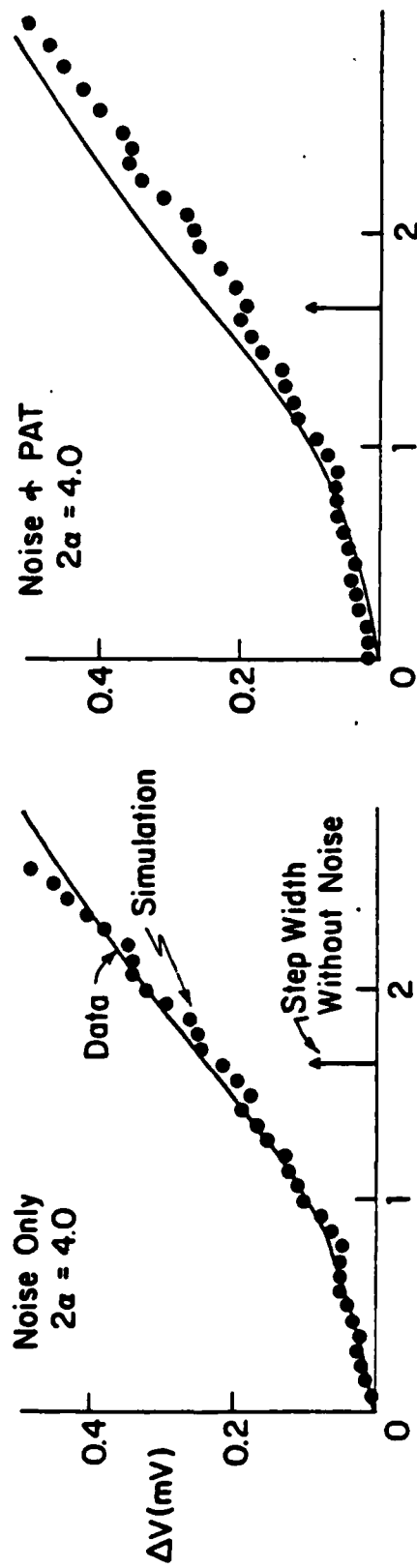


FIG. 4.19 (a) I-V curve of a $176\ \Omega$ junction at $\alpha=2.0$; Josephson steps are labelled by the integers $n=2$, $n=3$, and $n=4$. (b) Simulation of the data shown in (a), which includes noise and photon-assisted tunneling steps (see text). (c) Simulation, dashed lines in (b), compared with data from (a) illustrating the excellent quality of the fit.

FIG. 4.20 Fourth Josephson step fits at two laser power levels, $2\alpha=4.0$ and $2\alpha=5.75$. On the left are the simulated step shapes, measured from the step center, solid circles, compared with the data, solid line. On the right is the same data, but the simulation now includes the photon-assisted tunneling effect (see text). The quality of fit for $2\alpha=4.0$ is worsened while the fit at $2\alpha=5.75$ is improved, giving roughly the same quality of fit.

4th ac Josephson Step



simulations now include the effects of the photon-assisted tunneling steps in addition to the noise. The resulting fit to the step data with $2\alpha=4.0$ is worse, the simulation lying below the data, while for $2\alpha=5.75$ the simulation lies much closer to the data, the net result being that both fits are of roughly comparable quality.

It is rather remarkable that we have obtained such good fits to the data for both the fall-off of the $I_c R_n$ with increasing junction resistance and the rounding of the Josephson steps with a model as simple as the RSJ model that we have used. We have made two simplifications which, on the face of it, do not appear to be physically correct. First, we have taken the voltage in the noise term, $\hat{\rho}_N$, of Eq. (4.11-4.13) to be the instantaneous voltage. This would seem to be a problem because the noise power spectrum from which the noise term, $\hat{\rho}_N$, was calculated, was derived for the case of a constant dc bias voltage, so that it would seem appropriate to use an average voltage to calculate the noise term. However, we replaced the voltage-dependent (shot) noise term in the computer simulation ($\langle i_N^2 \rangle \sim 2eV/R_n$) by a Johnson noise term ($\langle i_N^2 \rangle = 4kT_{\text{eff}}/R_n$) at an elevated temperature, $T_{\text{eff}} = eV/2k \sim 30\text{K}$, appropriate to the 4th step at 5.0 mV (604 GHz), and found that the simulated step shape with this noise temperature was nearly identical to that simulated before with the voltage-dependent noise term. Also, $V(t) = \bar{V}$ on the 4th step, since $I \gg I_c$, so for this reason the instantaneous voltage should be no problem in the simulation. Second, we used the normal resistance to model the noise below the gap which contrasts with the theoretical expectation from Section 2.4 of using the sub-gap leakage resistance to model the noise for voltages below the gap. The junctions, however, are well coupled to external fields through the

antenna, which has a resistance of roughly the normal resistance, so the fact that we are using the normal resistance for the noise below the gap may not be a bad approximation to reality. We have also tried using the sub-gap leakage resistance for the noise, and for the typical sub-gap leakage resistance of $10R_n$ we found that we could model the reduction in the critical current with a noise temperature of ~ 30 K. This noise temperature seems unreasonably high. In any case we have found rather remarkable agreement between our data and the RSJ simulations used, which gives some credibility to the method.

4.5.3 Discussion

Before concluding this Chapter we would like to pause briefly to point out some recent analytic approaches to the problem of noise in junctions, which go beyond the now classic results presented in Section 2.4.

In a recent paper, Ben-Jacob et al.¹⁰³, have examined the effects of shot noise on the non-zero voltage state of a hysteretic junction and found a distribution of fluctuations that is non-symmetric in that positive fluctuations are more probable than negative ones. This is not surprising since the shot noise power spectrum shows increased noise power with increasing voltage. Their results are confined to the hysteretic region of the junction I-V curve, and are applicable for $\beta_c > 1.6$, but not too large, and can be tested by observing the transition rate to the zero voltage state from the non-zero voltage state.

Büttiker, Harris and Landauer¹⁰⁴ have extended the treatment of the noise activated escape of a particle out of a metastable well (e.g. the transition out of the zero voltage state of a junction as in Fig. 2.4), given originally by Kramers, and applied to superconducting tunnel junctions by Lee for the extreme underdamped case ($\beta_C \gg 1$), to a broader range of β_C 's. Their results are applicable to shunted junctions with $\beta_C > 44$, a condition satisfied by only three of the seven junctions studied.

The theoretical developments cited above are applicable to shunted junctions and only in certain limits of parameters. These analyses have not been extended to the case of a junction with the full nonlinearity of the quasiparticle I-V curve, nor a junction which is driven by a FIR or microwave source. The most encouraging approaches are those recently developed by Caldeira and Leggett¹⁰⁵, Chakravarty¹⁰⁶, and Ambegaokar Eckern, and Schon¹⁰⁷. These approaches were developed for the problem of the transition out of the zero voltage state where thermally activated processes are frozen out, and depend on complicated functional integral formalisms. These treatments, however, can take the full nonlinearity of the quasiparticle I-V curve into account, but physically intuitive results, or results for junctions driven by high frequency sources are not yet available.

We conclude this section and the chapter by noting that we have found rather remarkable agreement between the theory of the tunnel junction described in Chapter II, and our data, at the highest frequency yet reported for a thin-film, fabricated superconducting tunnel junction.

CHAPTER V

SUMMARY AND CONCLUSIONS

In this chapter, we will summarize the main results of this work, as well as briefly discuss experiments which could be done in the future to extend this work or to resolve some of the questions which are at present still open.

We have photolithographically fabricated small-area Sn-SnO-Pb superconducting tunnel junctions which have nearly ideal dc characteristics. We have coupled submillimeter laser radiation to these junctions by fabricating them at the centers of dipole antennas which are resonant at the wavelength used ($\lambda=496 \mu\text{m}$ or $\lambda=1.22 \text{ mm}$).

In a high resistance junction ($R_n \sim 176 \Omega$), with a submicron area ($A \sim 0.4 (\mu\text{m})^2$), we have coupled enough radiation to observe seven ac Josephson steps, up to a voltage of 8.75 mV, a result comparable to that observed in point contacts ($\sim 12.75 \text{ mV}$). In addition to this, six photon-assisted tunneling steps have been observed on this same junction, an effect not observed in previous work with point contacts, although it is expected from the microscopic (Werthamer) theory of the tunnel junction. We have systematically studied the power dependence of the widths of the Josephson steps at $\lambda=496 \mu\text{m}$ (604 GHz) and at $\lambda=1.22 \text{ mm}$ (246 GHz) and find reasonable agreement with both the RSJ model and the Werthamer (voltage-biased frequency-dependent) theory, which are not all that different at the laser frequencies tested thus far.

In addition, we have systematically studied the photon-assisted tunneling effect at 246 and 604 GHz at 1.4 K ($T < T_c(\text{Sn})$) where the

Josephson effect is present, and also at 4.2 K where it is absent. We find good agreement with the Tien-Gordon (Werthamer) theory. We infer that the responsivity of these junctions approaches the quantum limit at low temperatures for photon energies less than 2Δ .

We have studied the effects of noise on the behavior of these junctions. We have observed that noise systematically reduces the measured $I_c R_n$ product (at 1.4 K) with increasing junction resistance. Noise also rounds and produces a slight tilt on the ac Josephson steps of high resistance tunnel junctions. The Josephson step rounding has been interpreted in two ways: First, using a simple analytic result of P. A. Lee,³⁵ applicable to low β_c junctions, based on the RSJ model of the tunnel junction with reasonable estimates of junction parameters, we have found good fits to the Josephson step rounding with noise temperatures of roughly 20-25 K, which is thought to reflect the shot noise which is not included in this model. Second, we have developed a computer simulation to study the effects of noise on the tunnel junctions. This simulation uses an RSJ model which has been modified to include the nonlinear quasiparticle I-V in the junction dynamics. The simulation includes ac current sources, and a noise current source which, for simplicity, is that expected theoretically for the junction in the normal state, and models shot noise behavior at high voltages and thermal noise at low voltages. The simulation produces dc I-V curves which look quite close to the measured I-V curves. Using a noise temperature of ~ 2 K, we reproduced the observed fall-off of the $I_c R_n$ products with increasing junction resistance. The noise rounding behavior of the steps is also modelled well by the simulation, if the effects of the

photon-assisted tunneling steps are included.

The general agreement between our data and the theoretical predictions of the frequency-dependent (Werthamer) theory of superconductivity is excellent. None the less, there is a need to extend this work beyond its present limits. An original goal of the work was to measure the frequency dependence of the ac Josephson effect above the superconducting energy gap. We have had partial success towards this goal, since we have successfully coupled FIR laser radiation into the junction at $\hbar\omega_L/2e = 0.51$ mV, and $\hbar\omega_L/2e = 1.25$ mV from the 246 GHz and 604 GHz laser lines, respectively. The higher frequency is still only $\sim 2/3$ of the gap. Two significant questions still remain. What is the frequency dependence of the Josephson effect above the gap? Secondly, will the simple Tien-Gordon (Werthamer) photon-assisted tunneling result still work as well at 1-2 THz as it does at 0.6 THz?

Now that we have shown that it is possible to couple submillimeter laser radiation into a thin-film, photolithographically fabricated junction, one should attempt to couple radiation into a single junction over a wide range of FIR laser lines. To do this we must have an antenna which has a response which is substantially frequency-independent.

The bow-tie antenna is such an antenna. This antenna has been shown to work well in the frequency range of interest to us (0.246-2.5 THz)^{60,65}. The bow-tie antenna has a constant input impedance over the desired frequency range, and being a planar antenna is easily fabricated photolithographically. The impedance of the bow-tie antenna depends on bow

angle; it is lower for larger bow angles, as is shown in Fig. 5.1. The theory for the antenna impedance (solid line) agrees well with values measured (crosses) in a 10 GHz microwave modelling experiment.⁶⁵ A bow angle of -90° gives an almost purely resistive impedance of $\sim 100 \Omega$ if it were on a fused quartz substrate. As shown in this work, it is feasible to fabricate a small-area junction of roughly this impedance, for good matching.

A second improvement would be to successfully fabricate junctions of smaller area and higher current-density than fabricated thus far in our lab. All but one of the junctions measured in the FIR were fabricated using the resist-aligned technique discussed in Chapter 3. We attempted to fabricate smaller area, edge-aligned junctions with the Sn-Pb metal system which worked so successfully with the resist-aligned junctions, but we had relatively little success. These fabrication problems may be due to some metallurgical problem which is not understood by us at present. The simplest course of action would be to try another metal system, such as PbIn-Pb (20 weight percent In) which was used with good success at Bell Labs.⁴⁶ The smallest area junction which could be made using the edge-aligned technique and our present day $2 \mu\text{m}$ linewidth contact lithography is $\sim 0.2 (\mu\text{m})^2$. A junction of reasonable resistance ($R_n \sim 20\text{--}50 \Omega$) could then be expected to have current densities in the range of $\sim 5\text{--}2 \times 10^4 \text{ A/cm}^2$, an order of magnitude higher than the current densities of the junctions studied in this work. A further increase in current density (or decrease in junction area) could be expected to come from a decrease in the minimum linewidth by the use of either deep UV

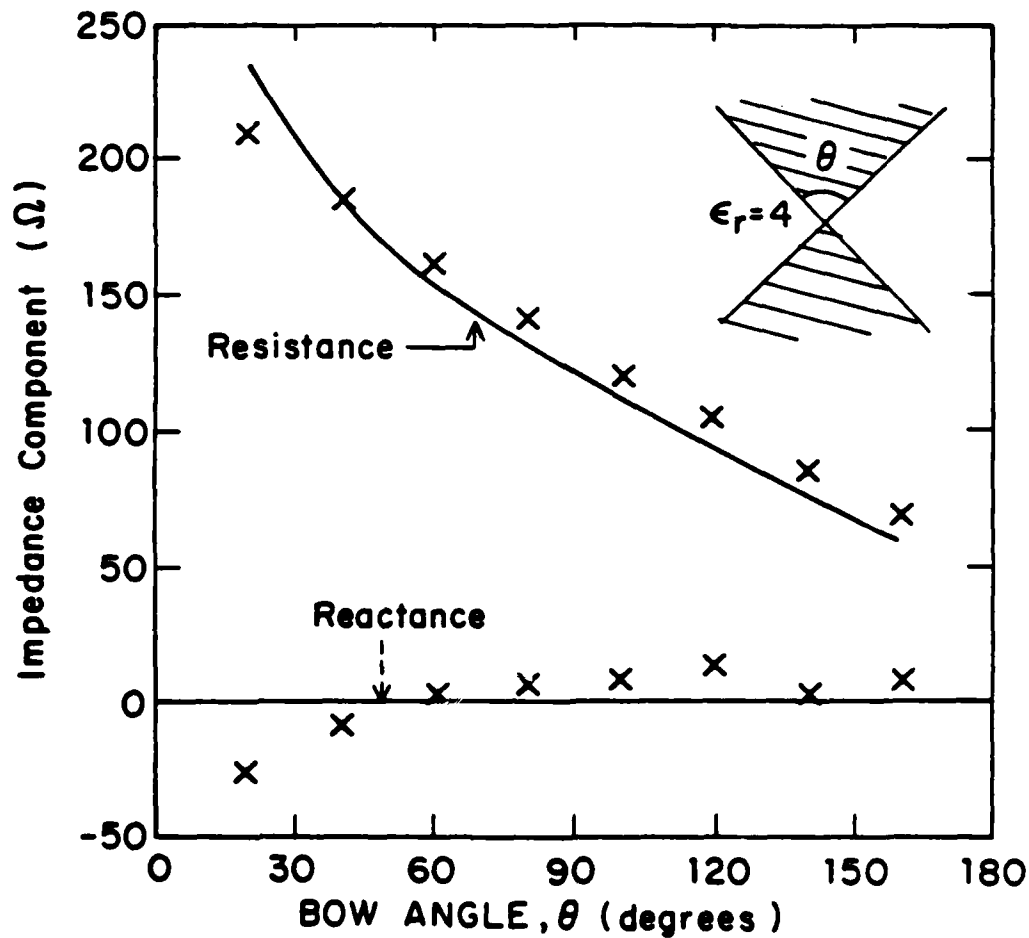


FIG. 5.1 Input impedance of a bow-tie antenna as a function of bow angle for an antenna on a fused quartz substrate. Solid lines are calculated values, crosses are values measured from a 10 GHz microwave modelling experiment. [After Ref. 65.]

contact lithography (minimum linewidth $\sim 0.2-0.3 \mu\text{m}$)¹⁰⁸ or the use of electron beam exposure of a two-layer electron-beam resist system (minimum linewidth $< 0.1 \mu\text{m}$).¹⁰⁹ A group at Bell Labs has fabricated superconducting tunnel junctions with areas below $0.01 (\mu\text{m})^2$ ¹¹⁰, a factor of roughly 50 smaller in area than the smallest junction we have studied. Clearly there is considerable room for improvement in junction fabrication.

A third area where the experiment can be improved is concerned with the question of whether external noise gives rise to the somewhat above bath ($\sim 2 \text{ K}$) noise temperatures which were shown to be able to cause the low $I_C R_n$ products of the high resistance junctions. The experiments were not carried out in an electromagnetically shielded room. It would be beneficial to construct an electromagnetic shield around the optical dewar.

Of practical significance, this work has shown that the inferred responsivity of these junctions, when viewed as a direct detector, approaches the quantum limit of one electron transferred across the barrier for each photon absorbed. It is desirable to study the performance of SIS and SIN mixers and direct detectors in the submillimeter wavelength region. At this time at least two groups are preparing to study SIS mixers operating in the submillimeter wavelength region with quantum limited performance, as described below.

At Caltech, an SIS (PbIn-Pb) mixer designed for 250 GHz has a measured noise temperature of 350 K at 250 GHz and has been studied up to 400 GHz where it has a noise temperature of $\sim 2000 \text{ K}$.¹¹¹ The 350 K

noise temperature is still considerably higher than the quantum limit of $T_N = \hbar\omega_L/e \sim 12$ K for 250 GHz, but it is the lowest reported mixer noise temperature at this frequency. The mixer block is machined from a single piece of copper. It uses a circular waveguide (0.97 mm diameter) fed by a corrugated horn, and an adjustable backshort for tuning.^{111,112} The junctions were fabricated on 0.1 mm thick quartz substrates which fit into a groove in the mixer block which spanned the waveguide. This scheme could be extended to higher frequencies by using a smaller diameter waveguide and so on. A group at U. C. Berkeley is using a different approach for a 600 GHz mixer in which a Nb-Si-Nb SNAP junction is coupled to the signal and local oscillator sources through a long-wire antenna mounted in a corner cube. The long-wire antenna is designed to touch a gold pad on top or near the tunnel junction to couple the radiation to the junction while the junction reactance is tuned out with an open circuited transmission line.¹¹³ Both approaches have good potential for yielding quantum-limited heterodyne mixing performance.

In summary, we have performed the first measurements of thin-film superconducting tunnel junctions in the submillimeter wavelength region of the spectrum. Our data agrees well with the fundamental theory of the tunnel junction. Considerable work remains to be done to extend this work to still higher frequencies and to develop practical SIS mixers which can operate in this frequency range.

APPENDIX A
DETAILED SAMPLE FABRICATION PROCEDURES

A.1 Introduction

This appendix describes in detail the complex procedures needed to make small-area superconducting tunnel junctions. The first section provides complete details of the photolithographic procedures used in fabricating the samples. The second section is a thorough description of the thin film evaporation techniques, while the third section details the substrate cleaning procedures. The Appendix ends with formulas for the etches used throughout this work.

A.2 Photolithographic Procedures

A. Photography

1. Prepare black-tape patterns on transparent acetate sheets.
 - 250x scale for $\times 10$ microscope reduction.
 - 1250x scale for $\times 50$ microscope reduction.
 - Note: a $\times 10$ reduction produces $\sim 5 \mu\text{m}$ minimum linewidths, while $\times 50$ reduction produces 1-2 μm minimum linewidths. No microscope reduction (i.e. $\times 1$) produces 20 μm minimum linewidths, due to the

grain size of the film.

- The black tape regions on the pattern become clear on the film. Clear regions on the emulsion will expose photoresist producing clear regions on a substrate. Therefore black regions on the film will determine where metal is in the sample because the metallization is done using a lift-off technique.

2. Details of photography.

- Film type - Kodalith Ortho film type 6556 with the red ester base, bulk roll.
- f/22 aperture on camera.
- 1-7 second exposure time.
- Developer concentrations, for 1600 ml total; make up 800 ml Kodalith Fineline developer A using 107.4 gm of powder, make up 800 ml Kodalith Fineline developer B from 53.7 gm powder by mixing with distilled water. Temperature of solutions should be 20 ° C. Mix solutions only just before film development since the mixed developer is good only for 1-2 hours.
- Shoot film 63" from the lightboard.
- Film process.

Develop 2:45

Stop 0:10 - Kodak Indicator Stop Bath

Fix 2:00 - Kodak Rapid Fixer

Rinse 10:00 in running water

Dip in Photo-flo and hang dry.

- Result-- +25 reduction of original pattern with black and white reversed.
- Ultimate resolution of film $\sim 5 \mu\text{m}$ or 200 lines/mm.

B. Intermediate Masking Step

1. Use glass microscope slides cut into 1" x 1" pieces.
2. Clean with standard cleaning procedure.
3. Coat with 1000 \AA ⁰Cr, using Cr plated Tungsten rod evaporation source.
4. Coat with 1.5 μm AZ 1350J photoresist, spun on at 5500 RPM, baked at 80⁰ C for 20-25 min.
5. Contact print by putting 1" x 1" substrate into contact with emulsion. The emulsion and photoresist must be in contact. Sandwich glass and emulsion between two glass plates. Expose for 90 seconds at a distance of 2' from the UV lamp.
6. Develop photoresist in high-resolution make-up developer -- 5 parts distilled water to 1 part developer (AZ 351) -- for a total of 30 - 60 secs. There should be no photoresist scum on the surface of the Cr, i.e. it should look quite shiny.
7. Clean in photoresist stripper solution.

8. Store in tightly sealing containers.

C. Projection steps.

1. Contact print pad mask onto 2" x 2" x 0.060" low reflectivity Cr, master mask blank, coated with 0.5 μ m AZ 1350B photoresist.
2. Expose, develop, rinse, and blow dry with pure nitrogen.
3. Projection:
 - Attach light source to projection attachment of microscope.
 - Adjust microscope optics so light can travel thru projection attachment onto substrate.
 - Set lamp power supply to 10 V.
 - Use 8x objective.
 - Expose 35-40 secs.
 - Attachment dial 12-14 mm setting.
 - Put substrate into perfect focus, then lower microscope stage slightly so that projected pattern is slightly out of focus to attempt to focus the UV radiation on top of the photoresist.
 - Always use red filter when inspecting photoresist.
4. Develop 30-60 secs., rinse, dry.

5. Inspect in microscope, if OK go on to the next stage, otherwise strip photoresist, and recoat mask blank with 0.5 μm AZ 1350B photoresist, then go back to step 3.
6. If OK etch Cr.
7. Strip, clean, recoat with 0.3 μm AZ 1350B photoresist, bake 20-25 min., let it sit in air for 20 min. to regain lost humidity.
8. +50 projection thru microscope
 - 40x objective on microscope
 - Lamp on 5 V.
 - Expose for 10 secs.
 - Focus as before.
9. Develop, inspect, and etch if good.
10. Expose large dots, using 8x objective, to indicate proper sample orientation during evaporation sequence.
11. Etch Cr, clean mask, and store in mask storage box.

D. Working Copies

1. Using cleaned Master Mask, contact print Master onto a 2" x 2" x 0.010" flexible 0.5 μm thick photoresist coated low reflectivity Cr mask blank.
2. Expose for 60 secs., develop, rinse, dry.

3. Inspect, clean if OK, and this mask will become a working copy, otherwise recoat and repeat steps 1 and 2.
4. Store in clean, tightly sealing containers.

E. Preparation of Sample Substrates

1. 1" x 0.5" x 0.010" z-cut, optically polished, single crystal quartz substrates.
2. Clean using standard cleaning procedure, described in Section IV.A below.
3. Coat with 1.5 μm , AZ 1350J photoresist, bake at 80⁰ C for 20-25 min.
4. Expose for 2.5-3.0 min. at a distance of 2' from the UV lamp.
5. Deposit 500 \AA ⁰Al from Tungsten boat source, using diffusion-pumped evaporator at a base pressure of 3×10^{-6} torr, with liquid nitrogen trap filled.
6. Coat with 1.0 μm AZ 1370 photoresist, bake at 70⁰ C for 20 min.
7. Substrates are ready now for contact printing.
8. Store in tightly sealing sample storage boxes.

F. Contact Printing Procedure

1. Insert sample into depression in plexiglass contact printing sample holder so that substrate

surface is nearly at the same height as the surrounding plastic. See Figure A.1.

2. Position flexible working mask over substrate, Cr side down, center pattern over substrate.
3. Open vacuum valve so substrate and mask are tightly held together. Check for good contact--look for dirt particles lifting mask away from the substrate.
4. Expose for 90 seconds at 2' from the lamp.
5. Close the vacuum valve, remove the substrate from the holder, repeat for other prepared substrates.

G. Developing Procedure

1. Develop the top layer until the photoresist is entirely removed and the Al layer looks shiny in such areas, rinse, and dry.
2. Inspect to make sure the photoresist is completely removed. Optional.
3. Etch Al layer until Al is entirely removed from the places uncovered by step 1, rinse, and dry.
4. Develop the bottom layer until a few seconds after the quartz substrate looks shiny, i.e. in areas that only had the bottom layer of photoresist remaining, watch the photoresist slowly develop away until it appears that

Plexiglass Contact Printing Sample Holder
(not to scale)

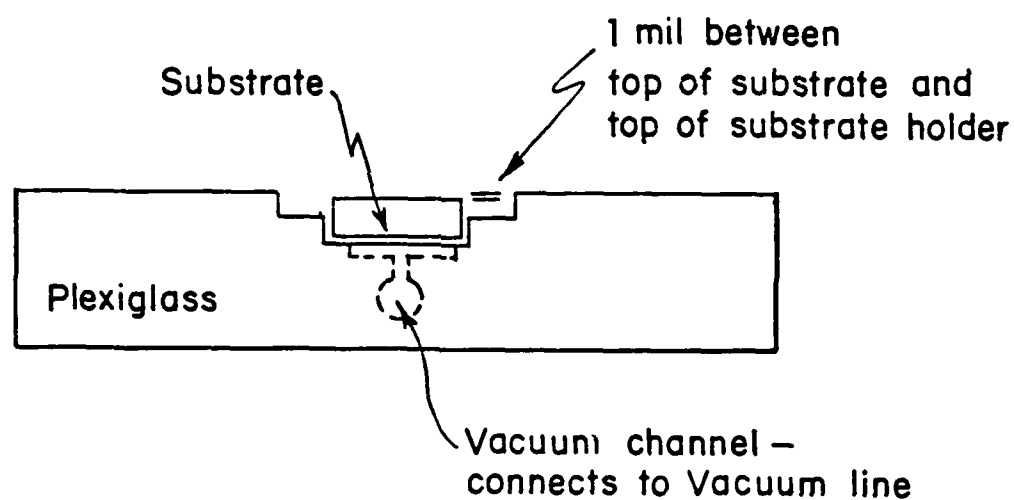


FIG. A.1 Illustration of cross-section of plexiglass contact printing sample holder. Substrate sits in slot in holder with substrate surface 1 mil=0.025 inches below the top of the holder. A vacuum is applied so that the mask is pulled into hard contact with the substrate.

the substrate is clean, hold the substrate in the developer a few seconds longer, rinse quickly, dry.

5. Etch the Al layer again. This is done to make it possible to see the undercut when the sample is placed under the microscope for inspection.

6. Inspect, if sample needs more of an undercut then repeat steps 4 and 5.

7. If OK, store the sample in clean room storage boxes until needed for the evaporation sequence.

8. Note:

- Developer is the high resolution make-up mentioned above.

- It is important that all the photoresist is removed from the surface of the quartz.

- Usually 9 out of 10 substrates could be used in the evaporation sequence.

A.3 Evaporation Procedures

A. Use of Cryopump evaporator -- before evaporation.

1. Bake out molecular sieve the night before using the evaporator.
2. Base pressure should be $2-4 \times 10^{-7}$ torr before beginning.
3. Check glow discharge apparatus, look for shorts.
4. Center of glow discharge wire should be directly under the sample holder, but should be 2-3" wider than the sample holder all the way around. The wire should be at a negative potential with respect to ground. The base plate of the evaporator should be grounded.
5. The digital thickness monitor crystal should be tested for thickness of accumulated metal, replaced if necessary.
6. Check metals -- make sure there is enough.
 - a. Use only etched high-purity, 99.999-99.9999 %, Pb. The Pb is etched in an acetic acid/peroxide/distilled water solution detailed in etch section of this Appendix. Dip Pb in etch, rinse quickly in distilled water, then in methanol. Keep in methanol until ready to put in evaporator.

Dry with clean room wipers or dry nitrogen gas.

- b. Sn does not need to be etched, but should also of very high purity.
- c. Ge does not need to be etched either, also high purity.

7. Put clean metals in clean tungsten boat sources.
Boat sources should be cleaned by ultrasonic agitation in Methanol before inserting into evaporator.
8. Sample holder should be reasonably clean; if too much metal has been evaporated onto it, it should be disassembled, etched in copper etch, rinsed with distilled water, and methanol, and blown dry with nitrogen gas.

B. Evaporation

1. Put sample in sample holder, screw onto bottom of liquid nitrogen pot, rotate into position for Sn evaporation.
2. Rough pump evaporator to 30-50 mtorr.
3. Close rough pump, begin pumping with cryopump.
4. In ~1 hour pressure should be in mid 10^{-7} range.
5. When pressure is $3-4 \times 10^{-7}$, begin liquid nitrogen flow to the liquid nitrogen pot.

In 1/2 hour, the pot should be nearly at liquid nitrogen temperature.

6. Keep liquid nitrogen flowing while depositing metal films.
7. Evaporate Sn at 100-200 A/sec for a total thickness of 1000-1500 Å when corrected for the angle of the substrate with respect to the source. Base pressure of the evaporator should be $2-4 \times 10^{-7}$ torr. The boat should be slowly heated until the pressure begins to rise in the chamber; at this time the shutter should be opened and the rate should be adjusted if necessary.
8. Rotate substrate to proper angle for Ge evaporation.
9. Evaporate Ge, only need 300-500 Å when corrected for the angle of the evaporation.
10. Rotate the substrate to the proper angle for the Pb evaporation.
11. Close gate valve, bleed in pure oxygen, until the pressure is 30 mtorr. Wait 1 minute.
12. Pump out chamber with cryopump for 2-3 minutes, until at the proper base pressure.
13. Close gate valve, bleed in 30 mtorr of oxygen, wait 1 minute, turn on glow discharge. Voltage should be 1.1 kV, current 12-15 mA, and the color should be gray-green. Continue discharge

for 45-75 secs., depending on junction resistance desired. Pressure should drop to about 20 mtorr, and the current should fall 2-4 mA, as the oxygen is consumed.

14. Open gate valve, chamber pressure should go down rather quickly to base pressure, $2-4 \times 10^{-7}$ torr. Evaporate Pb $100-200 \frac{\text{\AA}}{\text{sec}}$ to make a total thickness of $3000-4000 \text{\AA}$ when corrected for the evaporation angle.
15. Turn off liquid nitrogen flow, blow nitrogen gas thru the liquid nitrogen lines for about 1/2 hour to warm up sample holder.
16. Wait until sample holder has warmed up.
17. Take sample out of holder, put holder back in the evaporator, and pump down to a high vacuum. Evaporator should always be left under high vacuum condition, except when samples are inserted or removed from the evaporator.

C. Sample

1. Photoresist should be removed by soaking the sample in acetone for 1/2 hour, followed by rinsing it with acetone, then methanol, and blowing it dry with nitrogen.

2. Inspect sample, photograph, run if OK.

A.4 Cleaning Procedures

A. Simple Procedure

If the substrates are basically clean, i.e. as they come from the supplier, then the simple cleaning procedure is all that is called for:

1. Insert substrates into Teflon holder.
2. Ultrasonically agitate in Trichloroethylene (TCE) for 10 mins.
3. Ultrasonically agitate in Acetone for 10 mins.
4. Ultrasonically agitate in Methanol for 10 mins.
5. Blow dry with nitrogen gas.

B. Procedure for Dirty, But Not Coated Substrates

Some times it is helpful initially soak the samples in a ~2% solution of Micro cleaner and distilled water heated to near boiling or boiling, for 1/2 hour. ultrasonically agitated for 10 mins., and blown dry with nitrogen gas. Steps 1-5 above are then followed.

C. Procedure for Coated Substrates

If the samples had been used before, there are two possibilities:

1. If covered by photoresist, the substrates should be soaked in photoresist remover, which is nearly boiling, for 20 mins., rinsed with distilled water, and blown dry.
2. If the substrates have metal films on them they should be soaked in Aqua Regia for 1/2 hour until the films are removed, rinsed, and dried.
3. After completing C1 or C2 above then steps A1-A5 above should be followed.

The photoresist stripper is 1 part Shipley Photoresist Remover 1112A to 2 parts distilled water.

A.5 Etches

In the formulas which follow all proportions are by volume unless otherwise noted.

Aluminum:

84	H_3O_4	Phosphoric Acid
6	H_2O	Distilled Water
5	CH_3COOH	Acetic Acid
5	HNO_3	Nitric Acid

Aqua Regia:

1	HNO_3	Nitric Acid
3	HCl	Hydrochloric Acid
3	H_2O	Distilled Water

Copper:

1	HNO_3	Nitric Acid
3	H_2O	Distilled Water

Chrome:

165 gm	NH_4CeNO_3	Ceric Ammonium Nitrate
43 ml	$HClO_4$	Perchloric Acid (70%)
	H_2O	Distilled Water to make 1 liter solution

Lead:

1	CH_3COOH	Acetic Acid
1	H_2O_2	Hydrogen Peroxide
	H_2O	Distilled Water if dilute solution desired

APPENDIX B

OTHER DATA AND ANALYSIS

B.1 Introduction

In this Appendix we will discuss experimental results which were obtained either prior to (and in preparation for) the experiments which comprise the bulk of this work, or which were completed after the major part of the work was completed. Section B.2 discusses experiments performed on very low resistance ($R_n \sim 0.1 \Omega$), larger-area ($A \sim 5-20 \times 10^{-8} \text{ cm}^2$) junctions fabricated at Bell Laboratories in Holmdel, NJ. Results of far-infrared (FIR) measurements on edge-aligned tunnel junctions ($A < 10^{-8} \text{ cm}^2$), with point-contact or microbridge type I-V curves, are reported in Section B.3. The Appendix ends with Section B.4 which describes results from experiments with small-area SNAP⁴⁷ junctions fabricated at Sperry Research Laboratories.

B.2 Low Resistance Junctions Fabricated at Bell Labs

When the construction of the cryopumped evaporation system at Harvard was nearing completion, the author of this report made a set of tunnel junctions at Bell Labs using tunnel junction evaporation/oxidation facilities available there. Photoresist stencils for this work were made, however, at Harvard.

The Bell Labs (Holmdel) evaporation system was constructed out of a bakeable stainless steel chamber pumped by a mechanical roughing pump

from atmospheric pressure to the millitorr range and an ion pump at high vacuum. Contamination from the mechanical roughing pump was prevented from migrating to the chamber by the presence of a molecular sieve trap and a liquid nitrogen cold trap in the roughing pump lines. A mass spectrometer was attached to the chamber to monitor the gases in the chamber and to detect contaminants. To minimize the adsorption to the chamber of water vapor and other contaminants from the atmosphere, the chamber was always kept under high vacuum, except when samples were transferred into or from the chamber. A liquid nitrogen baffle was mounted in the chamber to help pump the water vapor.¹¹⁵

The stencils used were fabricated using the commercial mask described in Section 3.2.1 of Chapter 3, and the photoresist exposure/development sequence summarized in Fig. 3.3. These Sn-Pb junctions were made using the simple overlap technique (Fig. 3.5) with areas ranging from $\sim 5\text{-}20 \times 10^{-8} \text{ cm}^2$, and resistances from $\sim 0.10\text{-}2.0 \Omega$. The Sn film was typically $\sim 1000 \text{ \AA}$ thick, while the Pb film was somewhat thicker, $\sim 2000 \text{ \AA}$. These films were evaporated from metal shot in resistively heated boat sources onto room temperature sapphire substrates onto which the photoresist stencils had been previously prepared. The Sn film was oxidized by glow discharge in pure oxygen at 7 millitorr for times ranging from 7-60 seconds, producing junctions with current densities $\sim 10^4\text{-}10^5 \text{ A/cm}^2$, and resistances and areas noted above.

The I-V characteristics at selected temperatures of a typical sample prepared in the above manner is shown in Fig. B.1. This

particular junction has an area of $\sim 12 \times 10^{-8} \text{ cm}^2$, $R_n \sim 0.35 \Omega$, and $I_c(1.4 \text{ K}) = 2.3 \text{ mA}$. The capacitance, C , is estimated to be $C \sim 0.32 \text{ pF}$, $\beta_c = (2eI_c R_n^2 C / \hbar) \approx 0.30$ at 1.4 K , and the $\omega_J = (\beta_c)^{1/2} / R_n C \sim 5.2 \times 10^{12} (\text{sec}^{-1})$. β_c and ω_J are computed using the actual measured I_c , not from an inferred zero temperature I_c . See the discussion in Chapter 4, Section 4.2 for more details on this question.

Fig. B.1 shows I-V curves at six temperatures, $T = 4.2, 3.61, 3.31, 3.07$, and 1.4 K . We observe that at 3.61 K , the junction switches at I_c from the zero voltage state to the structure at $\Delta_{pb} - \Delta_{Sn}$, and then at a higher current level, to the structure at $\Delta_{pb} + \Delta_{Sn}$. At higher currents still, there is a decrease in voltage as a function of current, until a point is reached where the voltage again begins to increase with increasing current, i.e. the normal resistance is being approached. This trend is continued at lower temperatures, $T < 3 \text{ K}$, shown in the second set of I-V curves. Note that the second set is plotted with a scale that is $1/2$ as sensitive as the first set of I-V curves. Similar data was obtained by Yeh and Langenberg¹¹⁶ on Sn-SnO-Sn junctions. Fig. B.2 shows an I-V curve from Yeh and Langenberg at 1.3 K , displaying qualitatively the same type of gap depression observed in our data. On the I-V curve at 1.4 K , the lowest temperature reached in this experiment, the I-V curve of a high resistance ($R_n \sim 1600 \Omega$), low current-density junction is plotted in dashed lines for comparison. The I-V curve from the high resistance junction is scaled by multiplying the measured current of the high resistance at a particular dc voltage by

AD-A137 186

A FAR-INFRARED LASER STUDY OF SMALL-AREA
SUPERCONDUCTING TUNNEL JUNCTIONS(U) HARVARD UNIV
CAMBRIDGE MA DIV OF APPLIED SCIENCES W C DANCHI OCT 83

3/3

UNCLASSIFIED

DAS-TR-22 N00014-83-K-0383

F/G 20/12

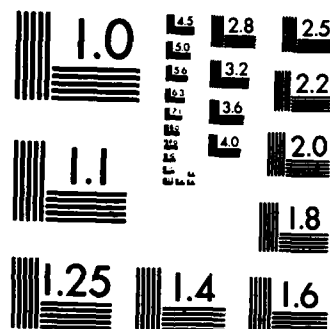
NL

END

FILED

1984

10/12



MICROCOPY RESOLUTION TEST CHART
NATIONAL BUREAU OF STANDARDS-1963-A

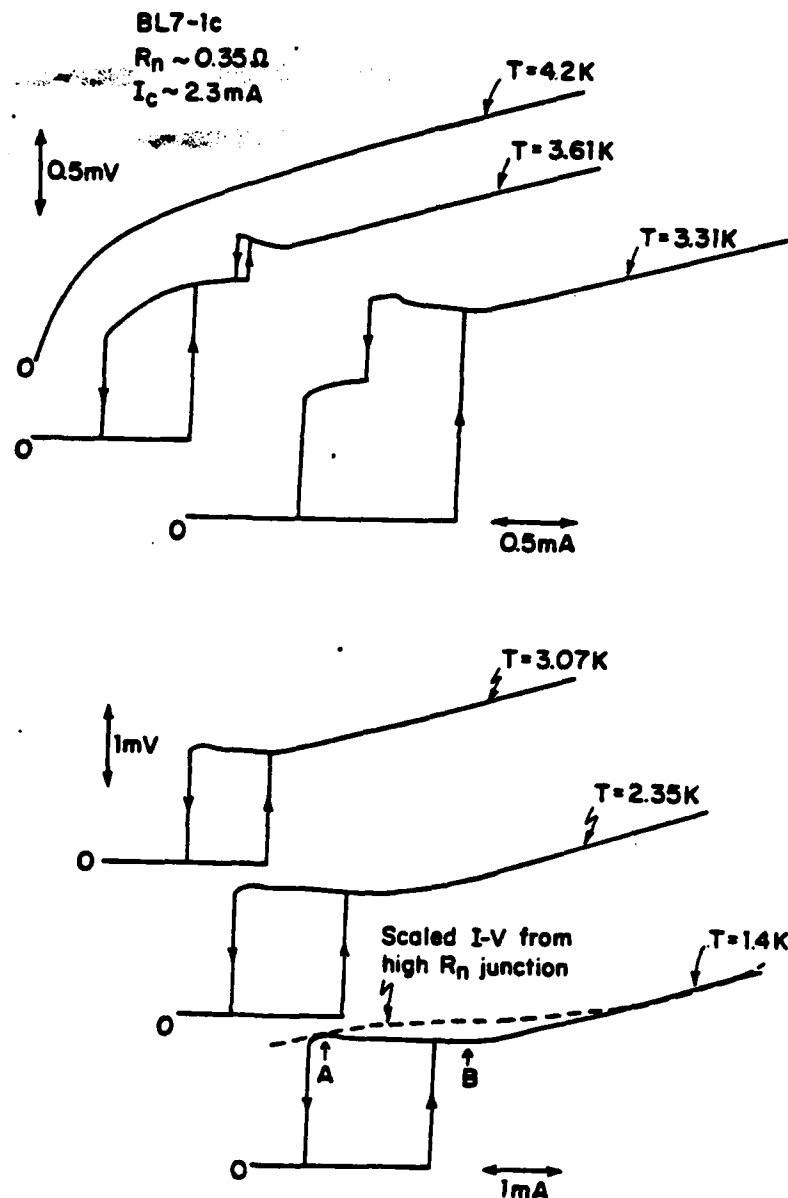


FIG. B.1 A typical high current-density sample showing depressed gap structure from quasiparticle injection at 6 temperatures. At 1.4 K a scaled I-V curve from a high-resistance junction is drawn in dashed lines for comparison (see text). The three upper curves are drawn with a scale twice as sensitive as the lower three curves.

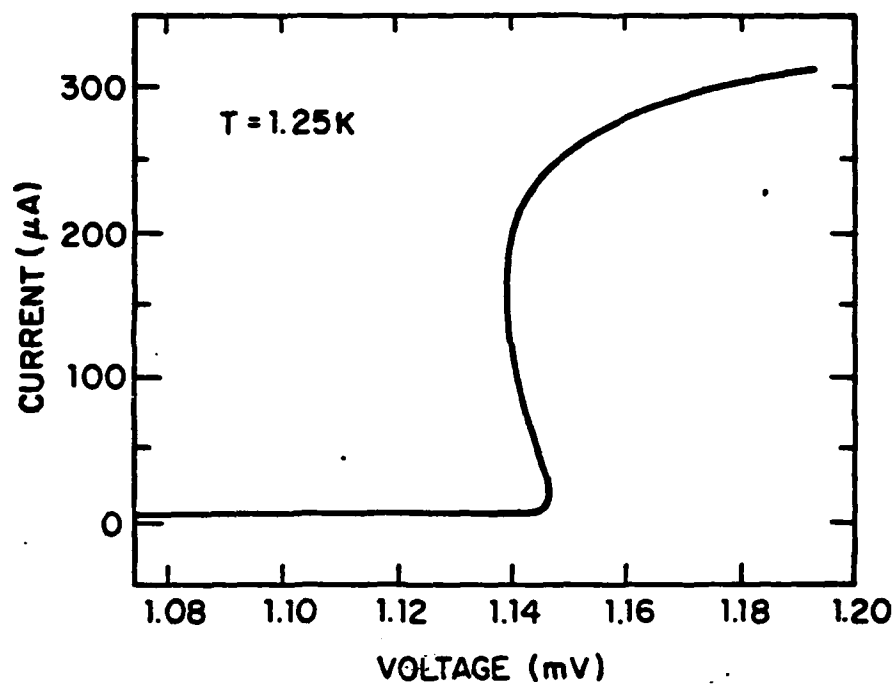


FIG. B.2 An I-V curve for a Sn-SnO-Sn junction (Ref. 116) showing the same sort of gap depression phenomena observed in this work on Sn-SnO-Pb junctions.

the ratio of the resistances at voltages just above the gap region, i.e., $I_{\text{scaled}} = I_{\text{high}} R \times (1400 \Omega / 0.29 \Omega)$. As can be clearly seen the voltage at the sum of the gaps is rather low, ~ 1.75 mV, near the point at which the junction switches from the non-zero voltage state to the zero voltage state, and decreases to a minimum of ~ 1.68 mV before increasing again. This is in contrast to the behavior seen on the high resistance junction which has approximately the same voltage at the point the low resistance junction has gap structure at ~ 1.75 mV, point A in the Figure. As the current is increased the voltage is increased slightly to ~ 1.90 mV, at point B, giving a maximum difference of $\sim 280 \mu\text{V}$. At higher current levels the curves match onto each other. The voltage difference between the two curves, δV_g , is plotted as a function of current in Fig. B.3.

The behavior described above has been studied extensively by Yeh and Langenberg.¹¹⁶ The difference, $-\delta V_g$, is interpreted by them as coming from gap depression due to the heavy quasiparticle injection in the low-resistance junction at the gap edge, and quantitatively described in terms of phenomenological equations developed by Rothwarf and Taylor.¹¹⁷ These equations relate the excess quasiparticle density above the gap compared to the number of thermally excited quasiparticles as a function of the current injected. The gap depression is related to the excess number of quasiparticles by the T^* model of Parker¹¹⁸ and the μ^* model of Owen and Scalapino¹¹⁹, which give equivalent results for the low temperature, 1.4 K, of the sixth I-V. Fig. B.3 (for $I \leq 3\text{mA}$) looks rather like Fig. 5 of Ref. B.4 reproduced as Fig. B.4 here in which $-\delta V_g$ is as we defined it above, and JG is proportional to the current. The

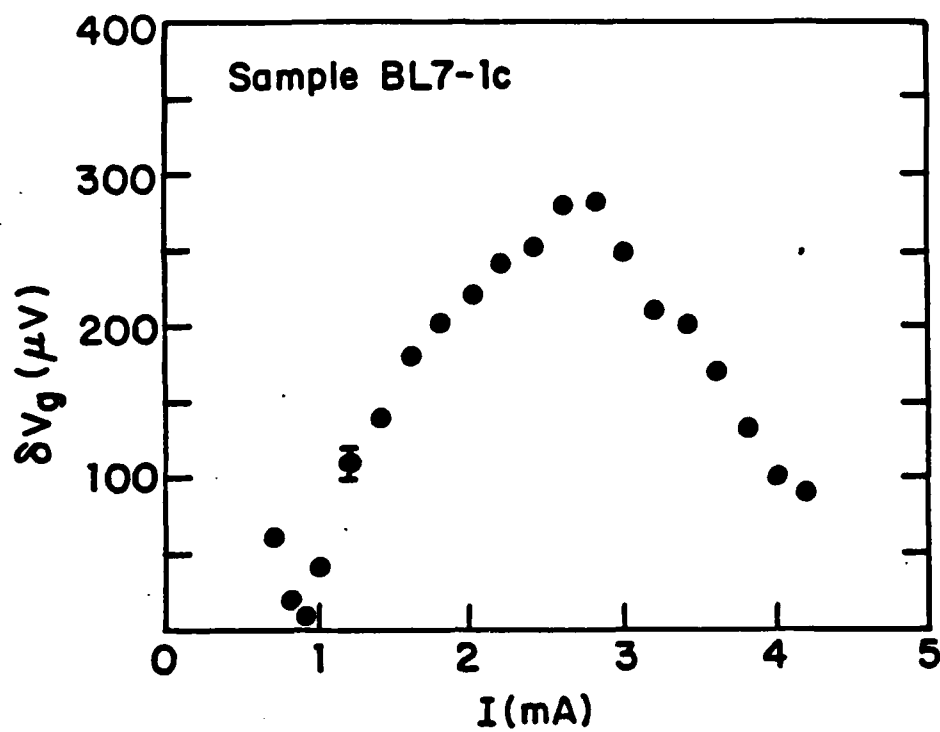


FIG. B.3 Voltage difference, V_g , between the dashed curve and solid curve in Fig. B.1 at $T=1.4$ K versus the current in the junction.

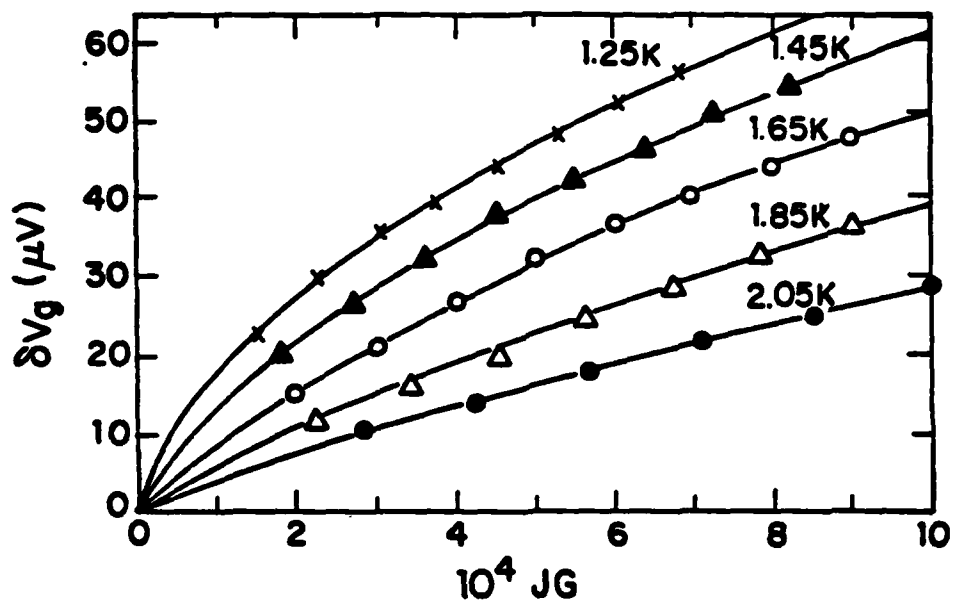


FIG. B.4 Voltage difference, $-\delta V_g$, between gap structure of low resistance and high resistance junctions, computed in the same way as Fig. B.3 for the Sn-SnO-Sn junctions of Ref. 116 as a function of JG , which is proportional to the current through the junction. There is clearly a great deal of similarity between this curve and Fig. B.3.

solid lines in Fig. B.4 are fits from the non-equilibrium model described above. Unlike Yeh and Langenberg, we will not carry the analysis any further.

Qualitatively their I-V curves and ours are similar, although the gap depression seen by them is roughly a factor of ~ 5 less than seen in our data. This might be due to the higher current-density of our junctions, $\sim 10^4$ A/cm² compared to the current-density of their junctions, $\sim 10^2$ A/cm².

The analysis above was not pursued further because this sort of behavior, while interesting, was not expected in the high resistance, smaller-area junctions which were to be used in the FIR work. Non-equilibrium behavior, such as seen here, may become important in very high current-density, extremely small-area junctions ($A < 10^{-9}$ cm²) junctions which may be studied in the FIR in the future.

B.3 Point-Contact Edge-Aligned Junctions

The successes with the resist-aligned junction technique reported in Chapter IV motivated us to attempt to use the edge-aligned junction technique to produce junctions with areas smaller than the smallest junctions fabricated thus far, $A \sim 0.4 \times 10^{-8}$ cm². The edge-aligned junctions held the promise of junctions with areas, $A \sim 0.2 \times 10^{-8}$ cm², a factor of two or more smaller in area, which would significantly increase the power coupled at the frequencies used thus far, and would enable us to more easily couple to higher frequencies, $\hbar\omega_L > 2(\Delta_{pb} + \Delta_{sn})/e$.

We fabricated a series of junctions using the edge-aligned junction technique discussed in Section 3.2.4. Of six junctions fabricated, only one was a proper tunnel junction, displaying the kind of I-V curve expected from tunneling theory. That junction had a resistance of $\sim 1600 \Omega$ and was reported in Section 4.2. Parameters for the remaining junctions are listed in Table B.1. These junctions had resistances ranging from $\sim 0.55 \Omega$ to $\sim 75 \Omega$. All but the 0.55Ω junction had some sort of gap structure at $(\Delta_{\text{Pb}} + \Delta_{\text{Sn}})/e$, and all had excess currents^{12,28} of $\sim 0.8 I_c$. In simple terms an "excess current" exists if the linear high-voltage I-V extrapolates to a non-zero current at zero voltage, instead of extrapolating to zero current at zero voltage like a resistor or a tunnel junction would. This behavior is characteristic of a metallic weak link like the point contacts of Weitz et al.¹² The $I_c R_n$ products were mostly much higher than $I_c R_n = 1.3 \text{ mV}$, expected from tunneling theory. The average $I_c R_n$ was $\sim 1.7 \text{ mV}$.

Figure B.5 displays the I-V characteristics of the lowest resistance sample $R_n \sim 0.55 \Omega$, at two power levels, $2\alpha=0$, and the highest power coupled, $2\alpha=0.8$, where $2\alpha=2eV_L/\hbar\omega_L$, as usual. This I-V curve is linear, with little, if any, gap structure. The low sample resistance causes a large impedance mismatch between the sample and antenna, which explains why the coupled power is so low. However, the critical current is depressed to about 75% of its zero power value and a clear Josephson step is seen at 1.25 mV .

I-V curves for a series of laser power levels for a junction with $I_c R_n$ product close to the theoretical value of 1.3 mV , are shown in Fig.

Table B.1

Parameters of Point Contact Type Junctions
(T=1.4 K)

Sample	$R_n(\Omega)$	$I_c(\mu A)$	$I_c R_n(mV)$
B-5	14.4	86	1.2
B-7	0.55	3.4×10^3	1.9
B-13	2.0	800	1.6
B-15	75	23	1.7
B-17	27	69	1.9

Sample B-7

$R_n \sim 0.55 \Omega$

$I_c \sim 3.4 \text{ mA}$

$T = 1.4 \text{ K}$

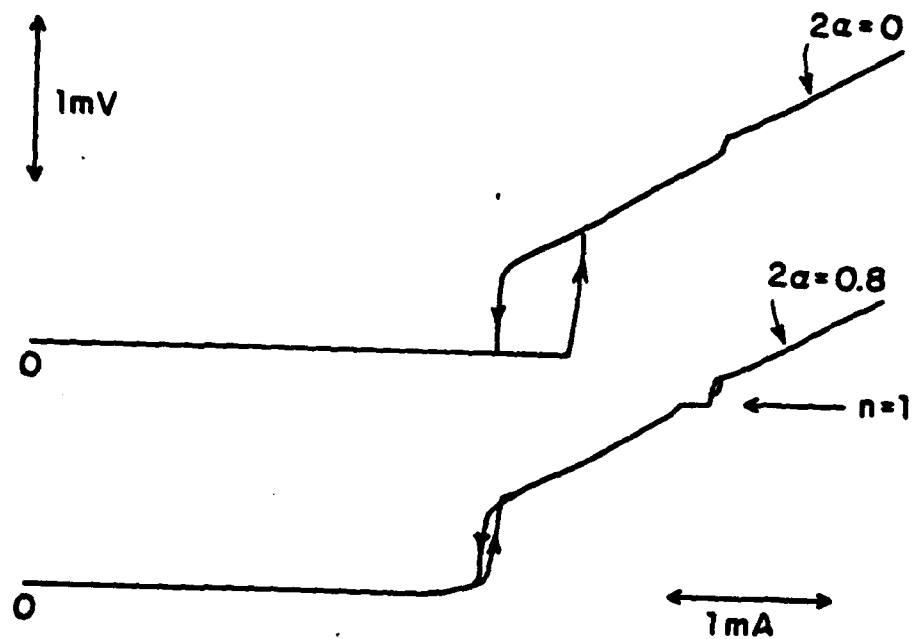


FIG. B.5 I-V curves of a 0.55Ω edge-aligned point contact type sample at $2\alpha=0$, and $2\alpha=0.8$, the maximum power coupled to the junction, where $2\alpha=2eV_j/\hbar\omega_L$. The curve at $2\alpha=0.8$ clearly shows a step at 1.25 mV, labelled $n=1$.

B.6. This junction has strong gap structure at $V_g = (\Delta_{Pb} + \Delta_{Sn})/e$, and has structure at lower voltages, possibly subharmonic gap structure.¹²⁰ More power is coupled into this low β_c , non-hysteretic junction, and a total of five steps are seen at the highest power coupled, $2\alpha = 6.7$. A new feature on these I-V curves, not seen previously with point contacts in the FIR, is a half-harmonic step at ~ 0.61 mV, labelled $n=1/2$ in the Figure. With the exception of the half-harmonic step these I-V curves are remarkably similar to the point contact I-V curves of Weitz et al.¹²

The large amount of power coupled to the junction makes it possible to make further comparisons with point contact data by plotting the step half-widths versus the normalized ac voltage, 2α , as had been done previously in the analysis in Section 4.3. Fig. B.7 shows the step widths for this sample compared with the Bessel function, $|J_n|$, and Werthamer function predictions, $|W_n|$. In order to obtain good fits with the step width data, these theoretical step width dependences had to be multiplied by scaling factors less than unity which decreased in magnitude with increasing voltage. The scaling factors decreased from ~ 0.4 - 0.6 for the zeroth and first steps to ~ 0.1 - 0.2 for the fourth and fifth steps. Weitz et al.¹² observed somewhat larger scaling factors which varied from ~ 0.5 - 1.0 for the zeroth and first steps and decreased to ~ 0.2 for the fifth step. These results can be contrasted with the low resistance, $R_n \sim 20 \Omega$, tunnel junctions of Chapter IV which showed no need for any scaling factors, or the higher resistance junctions in which the scaling factors were greater than unity and had little dependence on voltage.

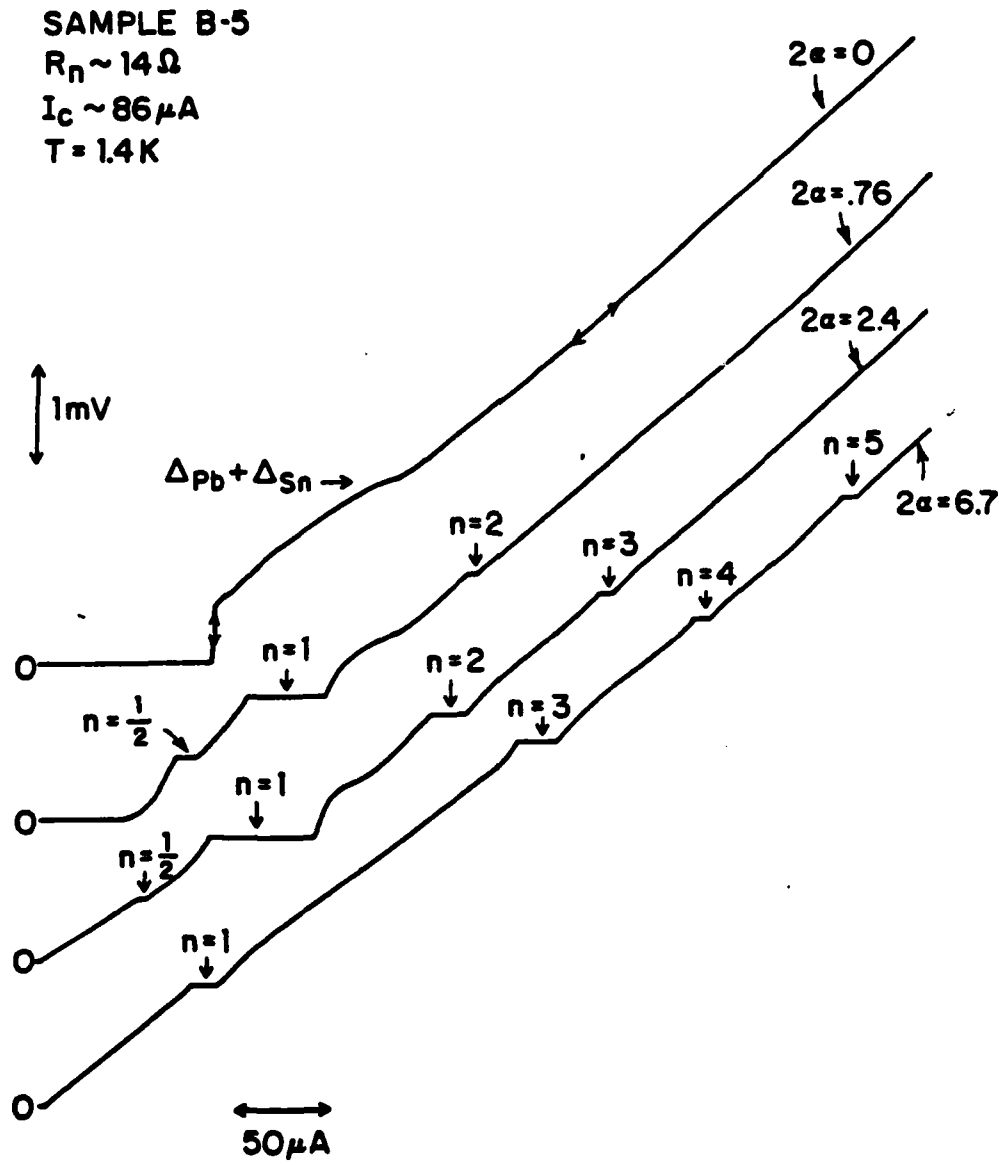


FIG. B.6 I-V curves at several laser powers for a 14Ω point contact edge-aligned sample showing gap structure at $(\Delta_{pb} + \Delta_{Sn})/e$ at $2\alpha=0$, and up to five Josephson steps at $2\alpha=6.7$. Note the presence of the half harmonic step, labelled $n=1/2$, not previously seen in point contact data in the FIR.

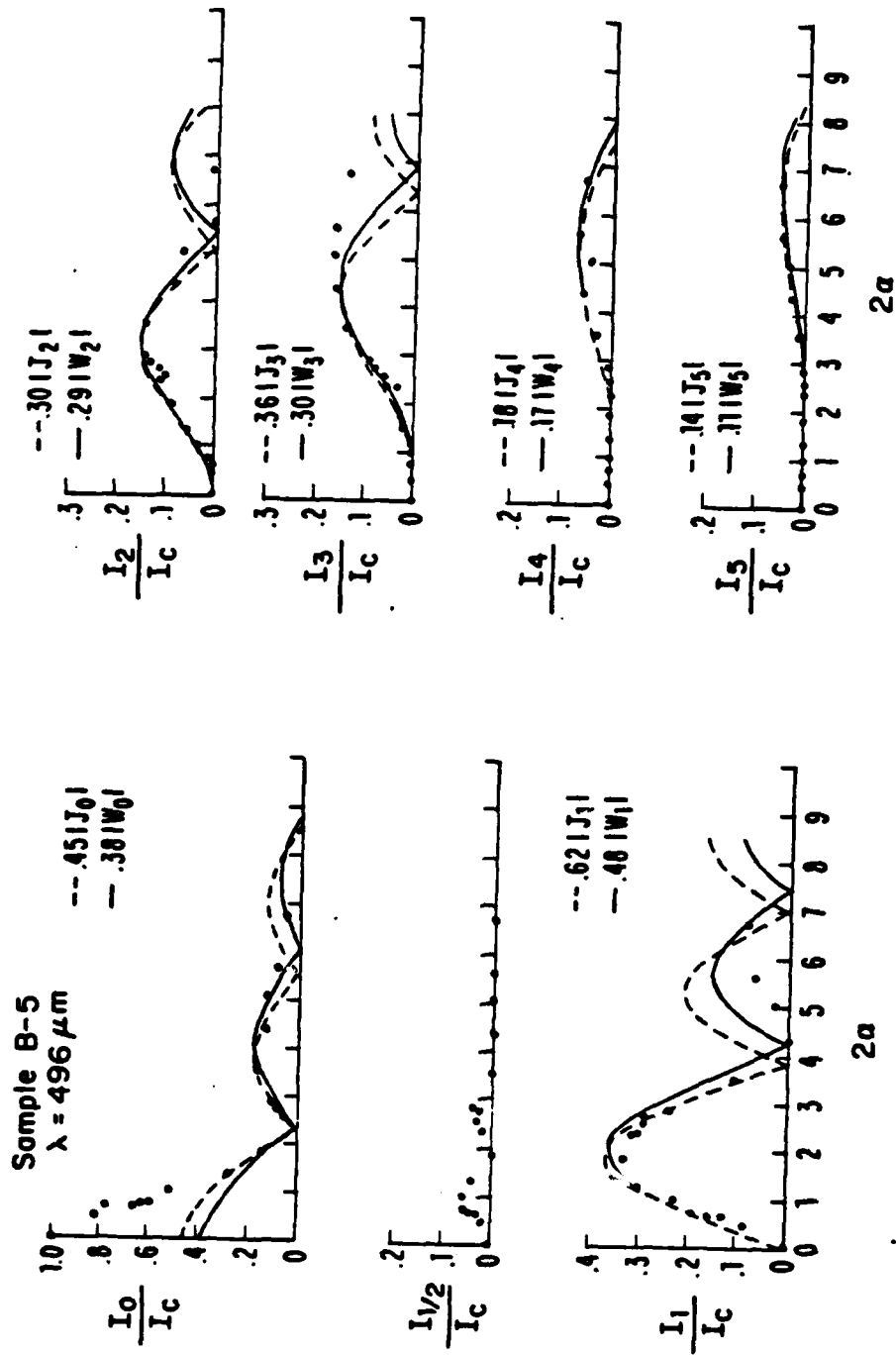


FIG. B.7 Step-widths as a function of normalized laser induced voltage in the junction, 2α , for the steps shown in Fig. B.6. Solid lines are scaled Werthamer functions, $|W|$, and the dashed lines are scaled Bessel functions, $|J|$. Note that these scaling factors are less than unity, in contrast to the scaling factors greater than unity in the data in Chapt. IV (see text), and that the $n=1/2$ step widths remain unfitted.

We leave the $n=1/2$ step unfitted because the Werthamer theory and the simple voltage-biased RSJ model do not provide for a subharmonic step. The presence of this step may be due to the much higher capacitance of the tunnel junction as compared to the point contact. It may also be due to the impedance seen by the junction at the laser frequency which may be much higher than the junction impedance, giving a bias which may approach a current bias. Braiman et al.¹⁰² have predicted the existence of these subharmonic steps under similar conditions but did not provide any analytic expressions with which to fit data.

An approximate value of $(2\alpha)_{\max}$ for each junction can be determined from the power dependence of the step widths. These values of $(2\alpha)_{\max}$ are plotted in Fig. B.8, which shows an approximately linear relationship between $(2\alpha)_{\max}$ and R_n , as indicated by the solid line in the Figure. This relationship implies that the source impedance at the laser frequency must be much larger than the junction impedance, on the order of 200 Ω .

The data described above are interesting, and further analysis might be beneficial, but we did not pursue it any further because we were trying to get away from the problems of point contacts, rather than inventing a planar-fabricated point contact. A planar point contact would be less well-cooled than the three dimensional structure of a regular point contact, and would be expected to have a lower high-frequency limit.^{120,121} The reason why the Sn-Pb edge-aligned junctions were seldom real junctions must have something to do with the soft

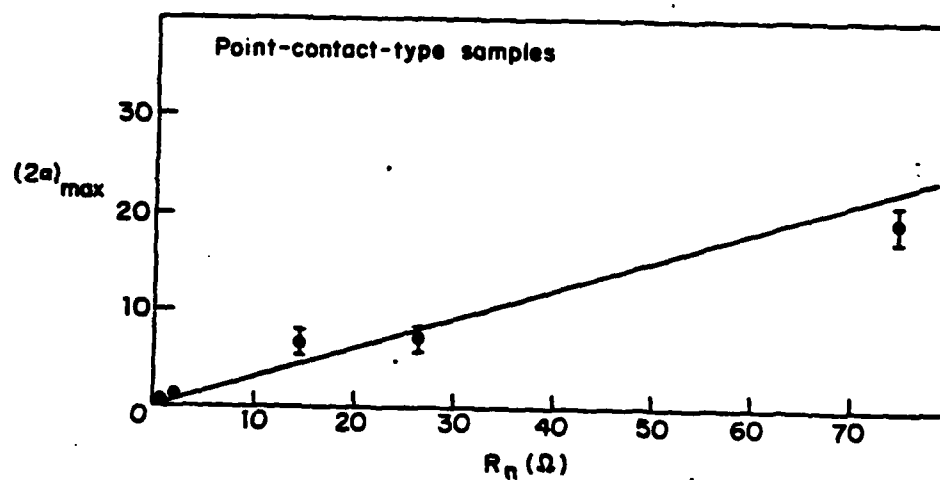


FIG. B.8 Maximum value of the normalized laser induced voltage in the junction, $2\alpha=2eV/\hbar\omega_L$, versus the normal resistance, R_n . The solid curve is drawn to show the approximate linear dependence of 2α on normal resistance, R_n (see text).

materials used. Howard et al.⁴⁶ reported resist-aligned junctions of Sn-Pb, but the edge-aligned junctions were of PbIn-Pb. Further work is clearly needed to fabricate smaller area junction which have low-hysteresis tunneling I-V curves.

B.4 SNAP Junctions

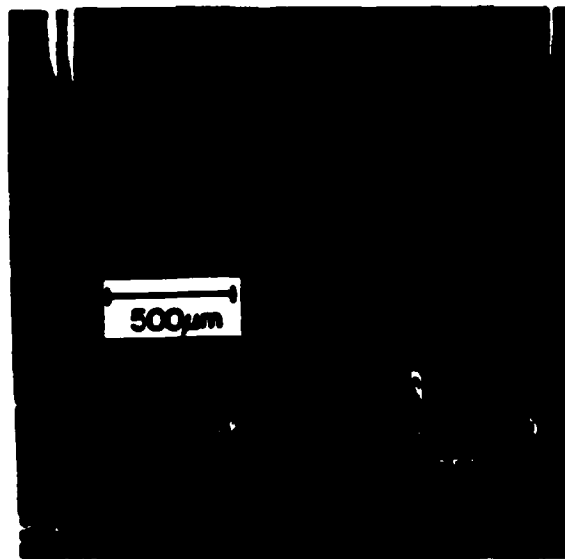
The soft-metal junctions fabricated at Harvard and used in all the work reported thus far are unable to cycle between room temperature and liquid He temperature more than a few times. Technology based on refractory metals such as Nb provide the best hope for the robust, thermally-cyclable type of junctions needed for practical applications. In this vein we have collaborated with Sperry Research Labs in order to test the suitability of Nb junctions for high frequency (FIR) applications, such as for SIS heterodyne mixers.

The results at 604 GHz which will be described below are for junctions fabricated by the selective niobium anodization process (SNAP)⁴⁷ developed at Sperry Research Labs. The SNAP process begins with a clean polished Si wafer, upon which are sputtered successive layers of Nb, amorphous Si (α -Si), and Nb. The wafer now is essentially one gigantic tunnel junction which can be stored for several months without any deterioration. The wafer is then coated with photoresist, which is exposed and developed, leaving areas uncovered which are to be anodized. Areas which are covered by the photoresist become the tunnel junctions which will be either tested singly, or through later wiring steps will

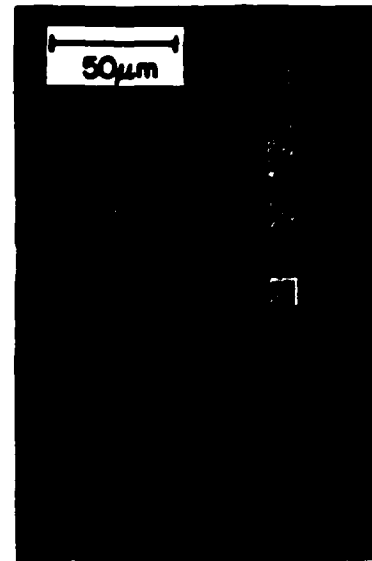
be combined to form logic circuits. The anodization process proceeds until the entire layer not covered by the photoresist is converted to niobium oxide. Next, a contact is made to the non-anodized niobium upper electrode in which the anodized Nb isolates the upper and lower contacts. A second insulating layer can also be deposited before the upper Nb contact is made.

Fig. B.9 displays a SNAP junction at the center of a $\sim 180\text{ }\mu\text{m}$ long dipole antenna for coupling to the FIR laser source. Fig. B.9(a) shows one-half of a 2 mm by 4 mm long chip upon which the SNAP junction, its antenna, and dc leads are fabricated. The antenna is the top of the "T" in the top part of the Figure. At the bottom of the Figure pads can be seen to which gold wires have been attached, which connect to larger pads which are connected to wires in the dewar insert (described in Section 3.4.1). Fig. B.9(b) is a close-up of the antenna of $10\text{ }\mu\text{m}$ linewidth. To the left are the dc leads. At the center of the antenna is the junction, shown from two views in Figs. B.9(c) and (d). Fig. B.9(c) is taken with the SEM stage tilted, while Fig. B.9(d) shows a view with the SEM stage in the normal position. The small square at the center of the region is the tunnel junction. Outside the tunnel junction there is a larger square (of $\sim 3 \times 3\text{ }\mu\text{m}^2$ area) which has Nb, Si, and anodized Nb, while outside this square, in addition to the Nb, Si, and anodized Nb, there is a layer of SiO. Therefore, looking from the inside of the smallest square and going outward, the upper Nb layer (contact layer) is in contact with Nb, then Nb_2O_5 , then SiO. The tunnel junction has an area of $\sim 1\text{ }\mu\text{m}^2$. The specific capacitance of the α -Si barrier has

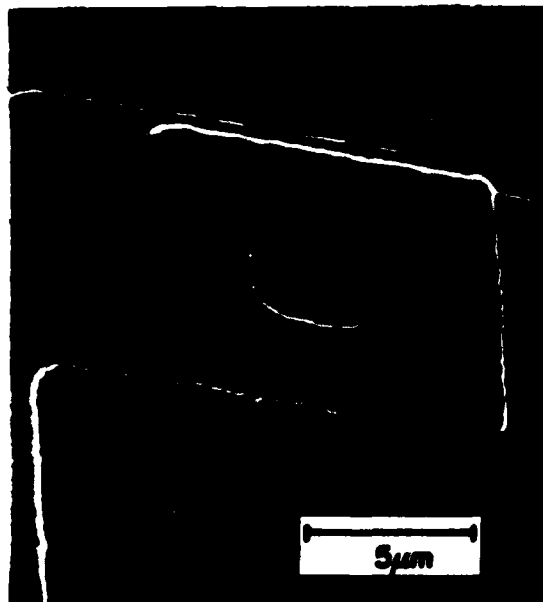
FIG. B.9 SEM micrographs of a SNAP junction. (a) Low magnification view of sample, displaying dc leads--vertical parallel lines in the Figure--and pads to which gold wires are bonded. (b) Close-up of antenna region of (a), showing 10 μm linewidth antenna, $\sim 180 \mu\text{m}$ long. The junction is at the center of the antenna, dc leads are to the left of the center. (c) Close-up of junction region at the center of (b) taken with SEM stage tilted. The junction is the smallest area at the center of the two larger squares. (d) Close-up of junction region but without a tilt on the SEM stage, the junction is the $\sim 1 \mu\text{m}$ by $\sim 1 \mu\text{m}$ region at the center of the Figure (see text).



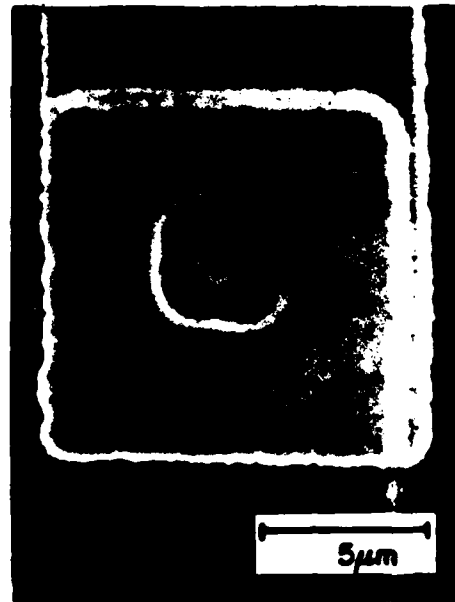
(a)



(b)



(c)



(d)

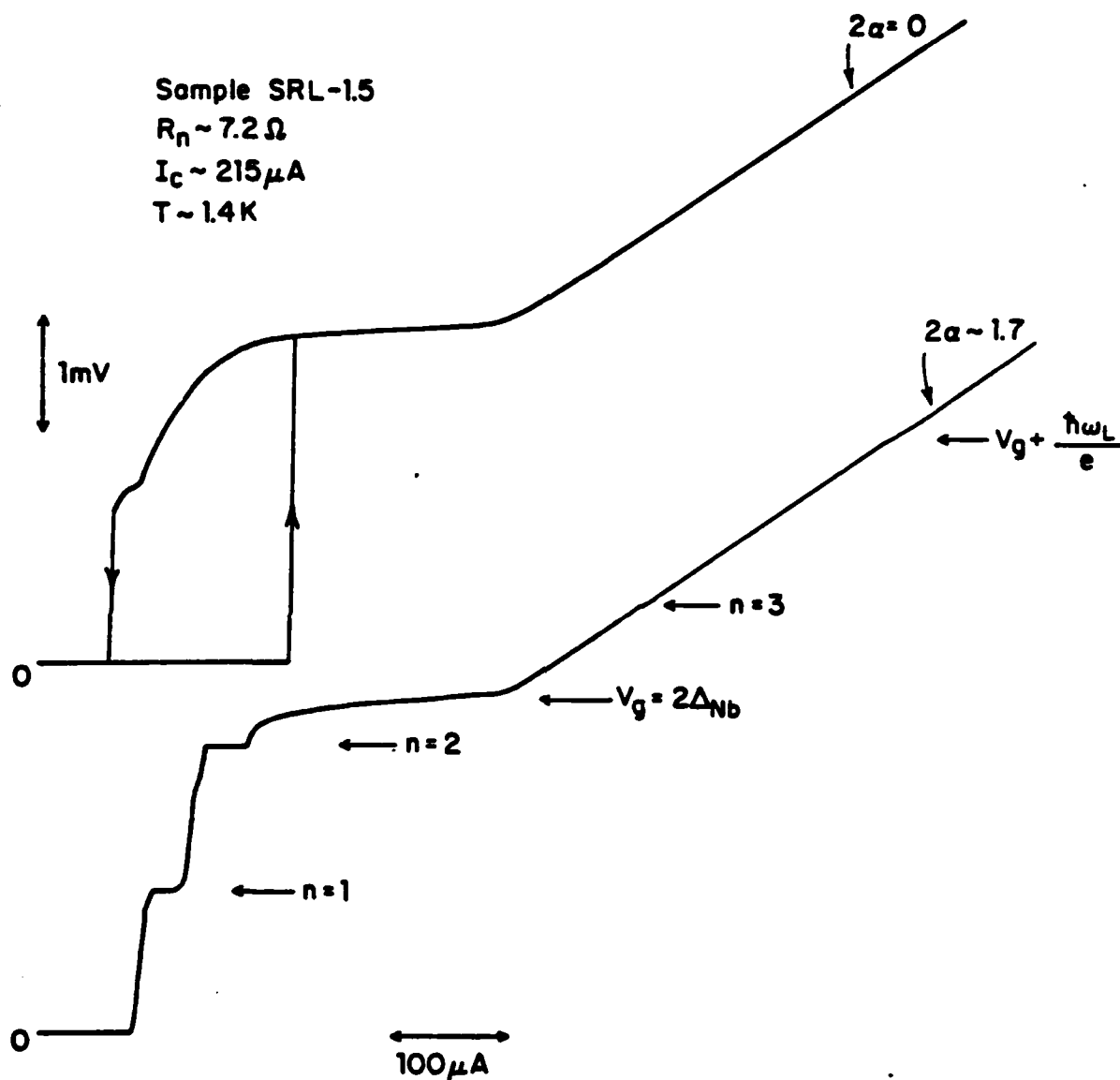


FIG. B.10 I-V curves of the SNAP junction in Fig. B.9 irradiated with 604 GHz ($\lambda = 496 \mu m$) laser radiation, at normalized laser induced voltages, $2\alpha = 0$, and the highest voltage coupled, $2\alpha = 1.7$. We see three Josephson steps at $V = n(\hbar\omega_L/2e)$ where n is an integer, and a single photon-assisted tunneling step at $V_g + (\hbar\omega_L/e)$ where $V_g = 2\Delta_{Nb}$, as labelled in the Figure.

been measured¹²² and is $2.5 \text{ pF}/\mu\text{m}^2$, giving the junction a capacitance of $\sim 2.5 \text{ pF}$.

The junction shown in Fig. B.9 has a resistance of $\approx 7 \Omega$, and a critical current, I_c , of $215 \mu\text{A}$ at 1.4 K . Fig. B.10 displays I-V curves at two power levels of the $496 \mu\text{m}$ laser line: $2\alpha=0$, and at the highest power reached, $2\alpha=1.7$. When $2\alpha=0$, we clearly see the expected gap structure at $V_g=2\Delta_{\text{Nb}}=2.9 \text{ mV}$. The leakage current below the gap is much larger than seen with the Sn-Pb junctions used previously. At $2\alpha=1.7$, we observe that the critical current is depressed to about 35% of its zero-laser-power value. Two steps are easily seen, labelled $n=1$ and $n=2$ in the Figure, while a third small step is barely visible, labelled by $n=3$. A small, photon-assisted tunneling step is seen at $V_g+(\hbar\omega_L/e)\approx 5.4 \text{ mV}$. This step may perhaps be so small because of the large leakage current seen on this particular sample.

The variation of the step widths with power has been measured and is shown in Fig. B.11. None of the steps fit the expected Bessel function, $|J_n|$, or Werthamer function, $|W_n|$, power dependences very well. This plot was made by scaling the laser power meter reading to the value of 2α which would give the observed zeroth step size at this maximum power. The same scaling factor was used for the first and second steps as had been done in Section 4.3. Data from two temperatures is shown where the crosses denote the data at 4.2 K , and the solid circles show the data at 1.4 K . Unfortunately the first and second step widths are very much smaller than expected from either the Bessel functions or

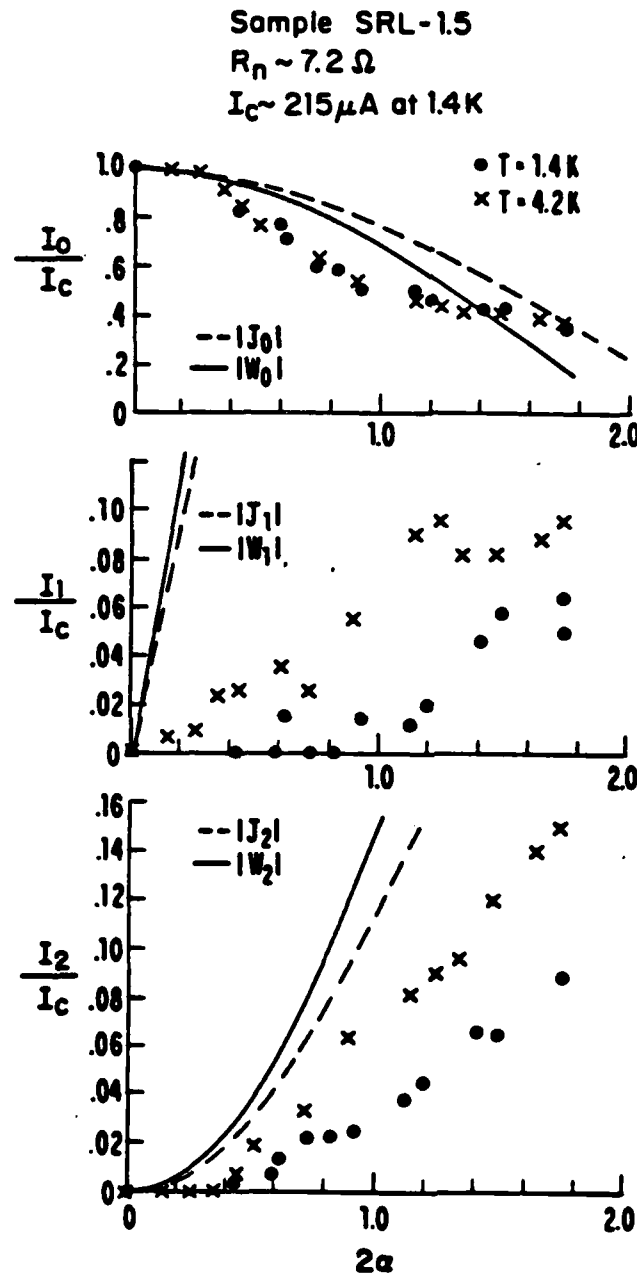


FIG. B.11 Step half-widths as a function of normalized laser induced voltage, $2a$, for the Josephson steps of Fig. B.10, at two temperatures $T=4.2$ K (crosses), and $T=1.4$ K (solid circles). Solid line denotes Werthamer function fits, $|W|$, and dashed lines denote Bessel function fits, $|J|$. The data for the first and second Josephson steps lie considerably below the theoretical curves but for reasons which are unknown at present.

Werthamer functions. Approximate scaling factors for these functions are ~ 0.1 - 0.2 for the first step, and ~ 0.5 for the second step. This situation is much different than seen in Section 4.3 with Sn-Pb junctions of roughly comparable capacitance and resistance in which the Bessel or Werthamer functions were not scaled. The need for these scaling factors may be related to the rather large leakage current observed which is not expected from tunneling theory. It may be also due in part to the fact that both steps are in the hysteretic region of the I-V. There is more of a temperature dependence in the step widths than expected with nearly a factor of two difference in the step size at the highest power level for both the first and second step. We know of no simple reason for this at present.

We conclude by noting that we have been able to couple 604 GHz laser radiation into a SNAP junction, and that we have observed up to three Josephson steps and one photon-assisted tunneling step. The step widths for the first and second steps are considerably smaller than expected. Further work is needed to explain why this is true. It would also be desirable to work with junctions with areas, $A < 1 \mu\text{m}^2$, and with higher resistance to decrease the impedance mismatch between the junction and the antenna, in order to increase the power coupled to the junction.

REFERENCES

1. J. Bardeen, L. N. Cooper, and J. R. Schrieffer, Phys. Rev. 108, 1175 (1957).
2. T. H. Geballe and J. K. Hulm, Scientific American 243, 138 (Nov. 1980).
3. G. F. Hardy and J. K. Hulm, Phys. Rev. 87, 884 (1953); B. T. Matthias, T. H. Geballe, S. Geller, E. Corenzwit, Phys. Rev. 95, 1435 (1954); J. E. Kunzler, E. Buchler, F. S. L. Hsu, and J. Wernick, Phys. Rev. Lett. 6, 89 (1961).
4. I. Giaever, Phys. Rev. Lett. 5, 147 (1960); Phys. Rev. Lett. 5, 464 (1960).
5. B. D. Josephson, Phys. Lett. 1, 251 (1962).
6. J. Matisoo, IBM Journal of Research and Development 24, 113 (1980).
7. A. H. Dayem and R. J. Martin, Phys. Rev. Lett. 8, 246 (1962).
8. P. K. Tien and J. P. Gordon, Phys. Rev. 129, 647 (1963).
9. N. R. Werthamer, Phys. Rev. 147, 255 (1966).
10. P. L. Richards, in Semiconductors and Semimetals, Vol. 12, R. K. Willardson and A. C. Beers, Eds., New York: Academic Press 1977, Chpt. 6; IEEE Trans. Electron Devices, ED-27, 1909 (1980); see also T. G. Phillips and G. J. Dolan, Physica 109 and 110 B+C, 2010 (1982).
11. W. C. Danchi, F. Habbal, and M. Tinkham, Appl. Phys. Lett. 41, 883 (1982).
12. D. A. Weitz, W. J. Skocpol, and M. Tinkham, Phys. Rev. B18, 3282 (1978).
13. D. A. Weitz, W. J. Skocpol, and M. Tinkham, J. Appl. Phys. 49, 4873 (1978).
14. W. C. Danchi, M. Octavio, F. Habbal, and M. Tinkham, unpublished.
15. J. Bardeen Phys. Rev. Lett. 6, 57 (1961).
16. M. H. Cohen, L. M. Falicov, and J. C. Phillips, Phys. Rev. Lett. 8, 316 (1962).
17. V. Ambegaokar and A. Baratoff, Phys. Rev. Lett. 10, 486 (1963); Errata, Phys. Rev. Lett. 10, 104 (1963).

18. A. Barone and G. Paterno, Physics and Applications of the Josephson Effect, New York: John Wiley and Sons, 1982, Chpt. 1.
19. See for example, V. Ambegaokar in Superconductivity Vol. 1, R. D. Parks, Ed., New York: Marcel Dekker, Inc., 1969, Chpt. 5.
20. E. Riedel, Z. Naturforsch, 19A, 1634 (1964).
21. E. P. Balsalmo, G. Paterno, A. Barone, P. Rissman, M. Russo, Phys. Rev. B10, 1881 (1974).
22. C. A. Hamilton, Phys. Rev. B5 912 (1972).
23. C. A. Hamilton and S. Shapiro, Phys. Rev. Lett. 26, 426 (1971).
24. S. A. Buckner, T. F. Finnegan, and D. N. Langenberg, Phys. Rev. Lett. 28, 150 (1972); see also S. A. Buckner and D. N. Langenberg, J. Low Temp. Phys. 22, 569 (1976).
25. D. A. Weitz, W. J. Skocpol, and M. Tinkham, Phys. Rev. Lett. 40, 253 (1978).
26. See for example, G. E. Blonder, M. Tinkham, and T. M. Klapwijk, Phys. Rev. B25, 4515 (1982).
27. R. E. Harris, Phys. Rev. B11, 3329 (1975); Phys. Rev. 13, 3818 (1976); J. Appl. Phys. 48, 5188 (1977).
28. W. C. Stewart, Appl. Phys. Lett. 12, 277 (1968); J. Appl. Phys. 45, 452 (1974).
29. D. E. McCumber, J. Appl. Phys. 39, 3113 (1968).
30. R. E. Harris, Phys. Rev. B10, 84 (1974).
31. See for example, Y. W. Lee, Statistical Theory of Communication, New York: John Wiley and Sons 1960, Chpt. 1.
32. A. J. Dahm, A. Denenstein, D. N. Langenberg, W. H. Parker, D. Rogovin, and D. J. Scalapino, Phys. Rev. Lett. 22, 1416 (1969).
33. D. Rogovin and D. J. Scalapino, Ann. Phys. 86, 1 (1974).
34. V. Ambegaokar and B. I. Halperin, Phys. Rev. Lett. 10, 486 (1969).
35. P. A. Lee, J. Appl. Phys. 42, 325 (1971).
36. W. H. Henkels and W. W. Webb, Phys. Rev. Lett. 26, 1164

(1971).

37. T. Fulton and L. N. Dunkleberger, Phys. Rev. 89, 4760 (1974).
38. R. F. Voss and R. A. Webb, Phys. Rev. Lett. 47, 265 (1981).
39. A. O. Caldeira and A. J. Leggett, Phys. Rev. Lett. 46, 211 (1981); see also, V. Ambegaokar, U. Eckern, and G. Schon, Phys. Rev. Lett. 48, 1745 (1982).
40. L. D. Jackel, J. P. Gordon, E. L. Hu, R. E. Howard, L. A. Fetter, D. M. Tennant, R. W. Epworth, and J. Kurkijarvi, Phys. Rev. Lett. 47, 697 (1981).
41. D. A. Weitz, W. J. Skocpol, and M. Tinkham, Infrared Phys. 18, 647 (1978)
42. G. Vernet, J. C. Heneaux, and R. Adde, IEEE Trans. Micro. Theory and Tech. MTT-25, 473 (1978).
43. P. Crozat, G. Vernet, and R. Adde, Appl. Phys. Lett. 32, 506 (1978).
- 43a. J. H. Claassen, Y. Taur, and P. L. Richards, Appl. Lett. 25, 759 (1974).
44. G. J. Dolan, Appl. Phys. Lett. 31, 337 (1977).
45. L. N. Dunkleberger, J. Vac. Sci. Tech. 15, 88 (1978).
46. R. E. Howard, E. L. Hu, L. D. Jackel, L. A. Fetter, and R. H. Bosworth, Appl. Phys. Lett. 35, 879 (1979).
47. H. Kroger, L. N. Smith, and D. W. Jillie, Appl. Phys. Lett. 39, 280 (1981).
48. GCA/D. W. Mann "3600 Software Manual Appendix B: 3600 Pattern Generator Mag Tape Formats," GCA Corporation, IC Systems Group, Santa Clara, CA.
49. C. A. Mead and L. Conway, in Introduction to VLSI Systems Addison-Wesley Publishing Co., Reading, MA, 1980, Chpt. 4.
50. D. J. Frank, Ph. D. Thesis, Harvard University, 1982, unpublished, and Div. of Appl. Sci., Technical Report No. 20, Tinkham Series June 1983.
51. A product of Shipley Co., Newton, MA.
52. H. I. Smith, F. J. Bachner, and N. Efremow, J. Electrochem. Soc. 118, 821 (1971).

53. L. M. Matarese and K. M. Evenson, Appl. Phys. Lett. 17, 8 (1970).
54. K. Mizuno, R. Kuwahara, and S. Ono, Appl. Phys. Lett. 26, 605 (1975).
55. P. L. Richards and A. Yariv, unpublished.
56. J. G. Small, G. M. Elchinger, A. Javan, A. Sanchez, F. J. Bachner, and D. L. Smythe, Appl. Phys. Lett. 24, 275 (1974).
57. R. A. Murphy, C. O. Bozler, C. D. Parker, H. R. Fetterman, P. E. Tannenwald, B. J. Clifton, J. P. Donnelly, and W. T. Lindley, IEEE Trans. Micro. Theory and Tech. MTT-25, 494 (1977).
58. B. J. Clifton, R. A. Murphy, and G. D. Alley, Conf. Digest, 4th Int. Conf. on Infrared and Millimeter Waves and Their Applications, IEEE Cat. No. 79, CH 1384-7 MTT, 1979, p. 84.
59. T. L. Hwang, D. B. Rutledge, and S. E. Schwarz Appl. Phys. Lett. 34, 9 (1979).
60. D. P. Neikirk, D. B. Rutledge, M. S. Muha, H. Park, and C-X. Yu, Appl. Phys. Lett. 40, 203 (1982).
61. Y. Yasuoka, M. Heiblum, and T. K. Gustafson, Appl. Phys. Lett. 34, 823 (1979).
62. D. B. Rutledge, S. E. Schwarz, T-L. Hwang, D. J. Angelakos, K. K. Mei, and S. Yokota, IEEE J. of Quantum Electron. QE-16, 508 (1980).
63. K. Mizuno, Y. Daiku, and S. Ono, IEEE Trans. Micro. Theory and Tech. MTT-25, 470 (1977).
64. E. A. Wolff, Antenna Analysis, New York: John Wiley and Sons, Inc., 1965, p. 7.
65. D. B. Rutledge and M. S. Muha, IEEE Trans. Antennas and Prop., AP-30, 535 (1982).
66. S. Ballantine, Proc. IRE 16, 513 (1928).
67. C. R. Brewitt-Taylor, D. J. Guntton, and H. D. Rees, Electronics Lett. 17, 729 (1981).
68. L. C. Robinson, Methods of Experimental Physics, Vol. 10, New York: Academic Press, 1973, Chpt. 3, p. 92.
69. T. G. Blaney, "A Theoretical and Experimental Study of Josephson Frequency Mixers for Heterodyne Reception in the

- Submillimeter Wavelength Range," National Physical Laboratory Report No. 89/0382, March 1978.
70. W. C. Jakes, Jr., in Antenna Engineering Handbook, H. Jasik, Ed., New York McGraw-Hill, Inc., 1961, Chpt. 10.
 71. G. C. Southworth, Principles and Applications of Waveguide Transmission, New York Van Nostrand and Co., 1950, Chpt. 5.
 72. D. A. Weitz Harvard University, Div. of Appl. Sci., Technical Report No. 14, Tinkham Series, May 1978.
 73. T. Y. Chang and T. J. Bridges, Optics Comm. 9, 423 (1970).
 74. D. J. E. Knight, "Ordered List of Far-infrared Laser Lines," National Physical Laboratory, Report QU-45, Sept. 1982.
 75. M. Rosenbluth, R. J. Temkin, and K. J. Button, Appl. Optics 15, 2635 (1976).
 76. T. Y. Chang, IEEE Trans. Micro. Theory and Tech. MTT-22, 983 (1974).
 77. J. R. Tucker, Conf. Digest., Int. Conf. on Submillimeter Waves and Their Applications, Atlanta, June 1974, p. 17.
 78. D. T. Hodges, J. R. Tucker, and T. S. Hartwick, Infrared Phys. 16, 175 (1976).
 79. D. T. Hodges, F. B. Foote, and R. D. Reel, Appl. Phys. Lett. 29, 662 (1976).
 80. T. A. DeTemple and E. J. Danielwicz, IEEE J. of Quant. Electron. QE-12, 40 (1976).
 81. D. T. Hodges, F. B. Foote, and R. D. Reel, IEEE J. of Quant. Electron. QE-13, 491 (1977).
 82. J. M. Manley and H. E. Rowe Proc IRE 44, 904 (1956).
 83. E. A. J. Marcatili and R. A. Schmeltzer, Bell Sys. Tech. J. 43, 1783 (1964).
 84. R. L. Abrams IEEE J. Quant. Electron. QE-8, 838 (1972).
 85. T. Y. Chang and C. Lin, J. Opt. Soc. Am. 66, 362 (1976).
 86. Apollo Lasers Model 550L.
 87. D. A. Weitz, W. J. Skocpol, and M. Tinkham, Optics Lett. 3, 13 (1978).

88. Pyroelectric Detector--Molelectron Model P4-73.
89. T. C. Wang and R. I. Gayley, Phys. Rev. B18, 293 (1978).
90. Princeton Applied Research Corp., Low Noise Preamplifier, Model 113.
91. NBS Pressure-temperature chart.
92. M. Tinkham, Introduction to Superconductivity, New York: McGraw-Hill Co., Inc., 1975, p. 35.
93. See for example Ref. 18, p. 200.
94. D. A. Weitz, W. J. Skocpol, and M. Tinkham, Appl. Phys. Lett. 31, 227 (1978).
95. P. W. Anderson, in: Lectures on the Many-Body Problem, Ravello-1963, Vol. 2. Ed. E. R. Caianello, New York: Academic Press, 1964, p. 115.
96. F. Habbal W. C. Danchi, M. Tinkham, Appl. Phys. Lett. 42, 296 (1983).
97. J. R. Tucker, IEEE J. of Quantum Electron. QE-15, 1234 (1979).
98. W. C. Danchi, F. Habbal, and M. Tinkham, IEEE Trans. Magn. MAG-19, 498 (1983).
99. See Fig. 6 of Ref. 12.
100. J. L. Devore, Probability and Statistics for Engineers and Scientists, Monterey, CA: Brooks/Cole Publishing Co., 1982, p. 199
101. Handbook of Applicable Mathematics, Vol. III: Numerical Methods, Ed. R. F. Churchhouse, New York: John Wiley and Sons., 1981, p. 321.
102. Y. Braiman, E. Ben-Jacob, and Y. Imry, in Proceedings of the IC SQUID Conference, Berlin, 1980, Ed. H. D. Halbohm, New York Walter de Gruyter and Co., 1980, p. 783.
103. E. Ben-Jacob, D. J. Bergman, Y. Imry, B. J. Matkowsky, and Z. Schuss, Appl. Phys. Lett. 42, 1045 (1983).
104. M. Büttiker, E. P. Harris, and R. Landauer, Phys. Rev. B28, 1268 (1983).
105. A. O. Caldeira and A. J. Leggett, Phys. Rev. Lett. 46, 211 (1981).
106. S. Chakravarty, Phys. Rev. Lett. 49, 681 (1982).

107. V. Ambegaokar, U. Eckern, and G. Schön, Phys. Rev. Lett. 48, 1745 (1982).
108. Karl Suss America, Inc., Mask Aligner Model SUSS-MJB3-UV200.
109. R. E. Howard, E. L. Hu, L. D. Jackel, P. Grabbe, and D. M. Tennant, Appl. Phys. Lett. 36, 596 (1980).
110. E. L. Hu, L. D. Jackel, and R. E. Howard, IEEE Trans. on Electron Dev. ED-28, 1382 (1981).
111. E. C. Sutton, submitted to IEEE Trans. Micro. Theory and Tech.
112. G. J. Dolan, R. A. Linke, T. C. L. G. Sollner, D. P. Woody, and T. G. Phillips, IEEE Trans. Micro. Theory and Tech. MTT-29, 87 (1981); see also T. G. Phillips and D. P. Woody, Ann. Rev. Astron. Astrophys. 20, 285 (1982).
113. A. D. Smith, P. L. Richards, and L. N. Smith, private communication.
114. L. Jackel, E. Hu, R. Howard, L. Fetter, and D. Tennant, IEEE Trans. Magn. MAG-17, 295 (1981).
115. L. Fetter, private communication.
116. J. T. C. Yeh and D. N. Langenberg, Phys. Rev. B17, 4303 (1978).
117. A. Rothwarf and B. N. Taylor, Phys. Rev. Lett. 19, 27 (1967).
118. W. H. Parker, Phys. Rev. B12, 3667 (1975).
119. C. S. Owen and D. J. Scalapino, Phys. Rev. Lett. 28, 1559 (1972).
120. T. M. Klapwijk, G. E. Blonder, and M. Tinkham, Physica 109 and 110 B+C, 1657 (1982); see also M. Octavio, Ph.D. Thesis, Harvard University, Div. of Appl. Sci., Technical Report No. 13, Tinkham Series, Jan. 1978, p. 149.
121. M. Tinkham, M. Octavio, and W. J. Skocpol, J. Appl. Phys. 48, 1311 (1978).
122. H. Kroger, D. W. Jillie, and J. B. Thaxter, Proc. of the Ninth International Cryogenic Engineering Conf., Kobe, Japan, p. 363, 1982.

ACKNOWLEDGEMENTS

The work described in this report owes much to the many people with whom I have interacted during my stay at Harvard. I would particularly like to thank Prof. M. Tinkham, who has provided support and encouragement throughout this project, and who has taught me much about the importance of thoroughness of analysis and clarity of presentation. Prof. W. J. Skocpol was instrumental in helping me to get started when I was a beginning graduate student in the research group. The tunnel junction oxidation technique reported here owes its success to a three-day visit I spent with him and Drs. L. Jackel, R. Howard, E. Hu, and Mr. L. Fetter at Bell Telephone Laboratories in Holmdel, NH, where Dr. Skocpol has been employed since leaving Harvard. I am grateful to Dr. Fawwaz Habbal with whom much of this work was done; he has taught me that perseverance and patience are important components to success in experimental physics. From Drs. A. D. Smith and D. A. Weitz I have learned how to operate and maintain the far-infrared laser system that was used in this work. Dr. L. N. Smith of Sperry Research Laboratories was most helpful by providing us with the Nb-Si-Nb tunnel junctions reported in Appendix B. While a graduate student nearing completion of his work, Prof. Chris Lobb gave me my first small research project when I was a first-year graduate student, and has since then always provided me with encouragement.

Several graduate students in the research group have helped me considerably during the course of this research. David Abraham, acting in behalf of the group, bought the evaporator which was used in this work. He also did much of the early design and assembly for it. Alice White generated the computer tape from which the first mask I used was made. Dave Frank and Greg Blonder always provided helpful answers to my electronics questions. Juan Aponte was a good office mate and shared with me his thoughts on photolithographic techniques.

Louis DeFeo, our talented machinist, always did an excellent job building the many mechanical stages, sample and substrate holders, and other precision mechanical parts used in this work, even when under considerable time pressure.

Finally, my wife Lisa has provided me with an enormous amount of love and support throughout this work, and it is to her this work is dedicated.

This work was supported in part by Joint Services Electronics Program Contract No. N00014-75-C-0648 and Office of Naval Research Contract No. N00014-83-K-0383.

DISTRIBUTION LIST FOR ONR ELECTRONIC AND SOLID STATE SCIENCES

Director Advanced Research Projects Agency Attn: Technical Library 1400 Wilson Boulevard Arlington, Virginia 22209	Commandant, Marine Corps Scientific Advisor (Code AX) Washington, D.C. 20380	Air Force Cambridge Research Laboratory L.G. Hanscom Field Technical Library Cambridge, Massachusetts 02138
Office of Naval Research Electronics Program Office (Code 427) 800 North Quincy Street Arlington, Virginia 22217	Naval Ordnance Station Technical Library Indian Head, Maryland 20640	Harry Diamond Laboratories Technical Library Connecticut Avenue at Van Ness, N.W. Washington, D.C. 20438
Office of Naval Research Code 105 800 North Quincy Street Arlington, Virginia 22217	Naval Postgraduate School Monterey, California 93940 Attn: Technical Library (1 copy) Elect. Engin. Depart. (1 copy)	U.S. Army Research Office Box CM, Duke Station Durham, North Carolina 27706
Director Naval Research Laboratory 4555 Overlook Avenue, S.W. Washington, D.C. 20375 Attn: Technical Library (6 cps) Code 5200 (1 copy) 5210 (1 copy) 5270 (1 copy) 6400 (1 copy)	Naval Missile Center Technical Library (Code 5632.2) Point Mugu, California 93010	Director U.S. Army Engineering Research and Development Laboratories Fort Belvoir, Virginia 22060 Attn: Technical Documents Center
Office of the Director of Defense Research and Engineering Office of the Assistant Director Electronics & Physical Sciences The Pentagon, Room 3D1079 Washington, DC 20301	Naval Electronics Laboratory Center San Diego, California Attn: Technical Library (1 copy) Code 2300 (1 copy) 2600 (1 copy) 4800 (1 copy)	Director National Bureau of Standards Attn: Technical Library Washington, D.C. 20234
Defense Documentation Center (12 cps) Cameron Station Alexandria, Virginia 22314	Naval Undersea Center Technical Library San Diego, California 92132	Naval Research Laboratory 4555 Overlook Avenue, S.W. Washington, D.C. 20375 Attn: Code 5300 (1 copy) 7100 (1 copy) 7900 (1 copy)
Commanding Officer Office of Naval Research Branch Office 536 South Clark Street Chicago, Illinois 60605	Naval Weapons Laboratory Technical Library Dahlgren, Virginia 22448	Naval Electronics Laboratory Center San Diego, California 92152 Attn: Code 2100 (1 copy) 2200 (1 copy)
San Francisco Area Office Office of Naval Research 50 Fell Street San Francisco, California 94102	Naval Ship Research and Development Center Central Library (Codes L42 and L43) Washington, D.C. 20007	C.C. Klick Superintendent Materials Sciences Division Naval Research Laboratory 4555 Overlook Avenue, S.W. Washington, D.C. 20375
Commanding Officer Office of Naval Research Branch Office 1030 East Green Street Pasadena, California 91101	Naval Surface Weapons Center White Oak Laboratory Silver Spring, Maryland 20910 Attn: Technical Library (1 copy) Code 200 (1 copy) 212 (1 copy)	Naval Research Laboratory 4555 Overlook Avenue, S.W. Washington, D.C. 20375 Attn: Code 5220 (1 copy) 5230 (1 copy) 5250 (1 copy) 5260 (1 copy) 5270 (1 copy) 5500 (1 copy)
Commanding Officer Office of Naval Research Branch Office 495 Summer Street Boston, Massachusetts 02210	Deputy Chief of Naval Operations (Development) Technical Analysis and Advisory Group (Code MOP-077D) Washington, D.C. 20350	Naval Electronics Laboratory Center San Diego, California 92152 Attn: Code 2500 (1 copy) 4000 (1 copy)
New York Area Office Office of Naval Research 115 Broadway 5th Floor New York, New York 10003	Commander Naval Air Systems Command Washington, D.C. Attn: Code 310 (1 copy) 360 (1 copy)	Office of Naval Research (2 cps) 800 N. Quincy Street Arlington, Virginia 22217 Attn: Code 430 (2 copies)
ODDRAZ Advisory Group on Electron Devices 201 Varick Street New York, New York 10014	Commander Naval Electronics Systems Command Washington, D.C. 20360 Attn: Code 304 (1 copy) 310 (1 copy)	Naval Research Laboratory 4555 Overlook Avenue, S.W. Washington, D.C. 20375 Attn: Code 5400
Naval Air Development Center Attn: Technical Library Johnsville Warminster, Pennsylvania 18974	Naval Surface Weapons Center Attn: Library Dahlgren, Virginia 22448	Naval Electronics Laboratory Center San Diego, California 92152 Attn: Code 3000 (1 copy) 5000 (1 copy) 5600 (1 copy)
Naval Weapons Center China Lake, California 93555 Attn: Technical Library (1 copy) Code 6010 (1 copy)	Air Force Office of Scientific Research Attn: Electronic and Solid State Science Division Department of the Air Force Washington, D.C. 20333	Air Force Office of Scientific Research Mathematical and Information Sciences Directorate 1400 Wilson Blvd. Washington, D.C. 20333
Naval Research Laboratory Underwater Sound Reference Division Technical Library P.O. Box 8337 Orlando, Florida 32806	Air Force Weapon Laboratory Technical Library Kirtland Air Force Base Albuquerque, New Mexico 87117	
Navy Underwater Sound Laboratory Technical Library Fort Trumbull New London, Connecticut 06320	Air Force Avionics Laboratory Air Force Systems Command Technical Library Wright-Patterson Air Force Base Dayton, Ohio 45433	

... ..

FILMED

02 - 84